

**POLITECHNIKA WARSZAWSKA**

**WYDZIAŁ MECHATRONIKI**

# Rozprawa doktorska

**Mgr inż. Marcin Michałowski**

**Rozwój mikroskopii sił atomowych na potrzeby projektowania  
mikrourządzeń mechanicznych**

**Promotor:**

**dr hab. inż. Sergiusz Łuczak, prof. uczelni**

**Promotor pomocniczy/Kopromotor:**

**dr inż. Dariusz Jarząbek**

**WARSZAWA**



**Słowa kluczowe:**

*mikroskopia sił atomowych (AFM), nanotrybologia, badania powierzchniowe, MEMS*

**Streszczenie**

Podstawą niniejszej pracy jest cykl recenzowanych publikacji zawierający artykuły z czasopism indeksowanych, referat konferencyjny oraz rozdział monografii specjalistycznej. Przewodnik ten podsumowuje tematykę tych prac, opisuje mój wkład w poszczególnych publikacjach, a także omawia prace, których realizacja umożliwiła ich powstanie. Pod koniec opisujano przyszłe planowane prace, zarówno te będące już na etapie recenzji napisanych prac, a także te będące w początkowej fazie.

Tematem niniejszej rozprawy jest rozwój mikroskopii sił atomowych (ang. Atomic Force Microscopy – AFM) w aspekcie opracowania nowych metod badawczych oraz narzędzi dla wspierania projektowania mikrosystemów (ang. Microelectromechanical Systems – MEMS). Zawarte w tej pracy metody uwzględniają:

- Nowe procedury badawcze – takie jak modyfikacja techniki wyznaczania sztywności i sprężystości badanego materiału metodą krzywej zbliżania. Metoda ta została zastosowana między innymi do próbek biologicznych w celu opracowania mikro-protezy ucha środkowego. Drugą innowacją jest zmiana procedury badawczej pętli tarcia oraz krzywej zbliżania w celu wyznaczenia energii zrywania i ścinania polimerów w celu optymalizacji procesu wytwarzania za pomocą litografii nanodrukowej.

- Wytwarzanie nowego typu sond pomiarowych do specjalnych zastosowań, czyli wytrawianie sond o wymiarach i materiale końcówki dostosowanych do specyficznych zastosowań, np. do doboru odpowiedniej pary trącej.
- Nowe obszary, w których mikroskopia sił atomowych pozwoliła uzyskać wyniki o większej wiarygodności niż dotychczas stosowane metody, przykładowo dzięki badaniu strzemiączka ucha ludzkiego w jego fizjologicznym zakresie odkształceń, co oznacza stukrotnie mniejsze przemieszczenia niż podczas wcześniejszych przeprowadzonych badań opisanych w literaturze przedmiotu.
- Opracowanie numerycznych modeli symulacyjnych, zarówno ogólnego modelu tarciowego, który można zastosować dla różnorodnych powierzchni współpracujących w mikrosystemach (MEMS), a także modeli specyficznych np. dla zrywania maski w procesie litografii nanodrukowej.

Przedstawiłem także przeglądową analizę metod pomiarowych stosowanych przy wyznaczaniu własności mechanicznych dla różnych grup materiałów. Omówiłem też zagadnienia dotyczące kalibracji oraz modeli kontaktowych w mikroskopii sił atomowych.

## **Keywords:**

*Atomic Force Microscopy (AFM), nanotribology, surface measurements, MEMS*

## **Abstract**

The basis of this work is a set of reviewed publications, including papers published in JCR journals, one reviewed conference proceedings paper and one co-authored book chapter. The presented review sums up the topic of these publications, my contribution to these publications and the research that led to its realization. At the end of the review I discuss works planned in the future, including both publication that is currently under review and projects being at an early stage of development.

The topic of this review is development of Atomic Force Microscopy (AFM) in terms of novel methods and instruments to support design of Microelectromechanical Systems (MEMS). The methods included in this work refer to:

- They include novel testing procedures, such as modification of Force-Distance Curve (FDC) procedure in order to obtain stiffness and Young modulus of biological samples in order to develop micro prosthesis of human middle ear. Second modification is modifying both friction-loop procedure and FDC in order to measure adhesion energy and shear energy of polymers to optimize the fabrication process of nano-imprint lithography (NIL).
- Fabrication of new cantilevers for special purposes, which is realized by etching cantilever beams and attaching spherical tips, with dimensions and tip material selected for particular purpose, e.g. selection of a friction-pair.

- New areas of application of atomic force microscopy, which allowed one to achieve more reliable results than previous methods. For example, while studying human middle ear AFM allowed measurements to be performed within physiological deflection range, which is 100 times smaller than it has been done so far.
- Development of simulation models for both general purposes and specific applications. A universal model that simulates frictional contact between any two surfaces that could operate within a MEMS device and a specific model which simulates a peel off during nano-imprint lithography.

A guide to a selection of measurement method to be applied for particular purpose is also included, as well as a discussion of problems of atomic force microscopy such as calibration and applications of various contact models.

## **Spis treści**

1.	WSTĘP	9
1.1.	Dotychczasowa praca naukowa .....	9
1.2.	Wprowadzenie do tematyki.....	14
2.	PRZEWODNIK PO PUBLIKACJACH	17
2.1.	Wykaz publikacji stanowiących rozprawę.....	17
2.2.	Sondy badawcze z końcówkami badawczymi sferycznymi milimetrowej średnicy ...	20
2.3.	Wykorzystanie mikroskopii sił atomowych w symulacyjnym modelu tarcia.....	22
2.4.	Badania energii odrywania maski w procesie NIL .....	25
2.5.	Badania powierzchni polikrystalicznych uzyskiwanych metodą LPCVD.....	27
2.6.	Przegląd metod badawczych w badaniach biomateriałów .....	28
2.7.	Badania warstwy grafenowej naniesionej na metalowych powierzchniach .....	31
2.8.	Badania strzemiączka ucha ludzkiego.....	31
3.	PRZYSZŁE PRACE	35
4.	PODSUMOWANIE	38
5.	BIBLIOGRAFIA	39
6.	PUBLIKACJE NAUKOWE STANOWIĄCE PODSTAWĘ PRZEWODNIKA	47



## **1. Wstęp**

### **1.1. Dotychczasowa praca naukowa**

Jestem absolwentem Wydziału Mechatroniki Politechniki Warszawskiej, na którym uzyskałem zarówno tytuł zawodowy inżyniera w 2011 r. jak i później magistra w 2012 r. Obie prace realizowałem w Zakładzie Konstrukcji Urządzeń Precyzyjnych pod kierunkiem prof. Zygmunta Rymuzy. Pierwszym moim kontaktem z mikroskopią sił atomowych był staż w Białoruskiej Akademii Nauk w 2009 roku, od kiedy zacząłem też pracować w czystym laboratorium na Wydziale Mechatroniki. Prace w czystym laboratorium kontynuuję do dnia dzisiejszego. W latach 2010 oraz 2011 skonstruowałem wraz z zespołem własny mikroskop sił atomowych, co było tematem mojej pracy inżynierskiej.

### **Projekty Europejskie**

W czasie swojej pracy naukowej uczestniczyłem jako wykonawca w kilku projektach europejskich:

1. *Creating and disseminating novel nanomechanical characterisation techniques and standards* (Nanoindent), realizowany w latach 2008-2011, z moim udziałem w latach 2010-2011. W projekcie tym brało udział 15 partnerów z 12 krajów, a polski zespół stanowiły 4 osoby.

2. *Development of wear resistant coatings based on complex metallic alloys for functional applications* (AppliCMA), realizowany w latach 2008-2011, z moim udziałem w latach 2010-2011, z udziałem 18 partnerów z 8 krajów, polski zespół natomiast stanowiły dwie osoby pod kierownictwem prof. Zygmunta Rymuzy.

3. *3-Scale modelling for robust-design of vibrating micro sensors* (3SMVIB), realizowany w latach 2012-2016 przy udziale 6 partnerów z 3 krajów; w zespole z Politechniki Warszawskiej było dwóch wykonawców pod kierownictwem prof. Rymuzy. W końcowej fazie realizacji projektu przejąłem funkcję kierownika z powodu nagłej śmierci prof. Rymuzy (mojego ówczesnego opiekuna naukowego).

### *Projekt Nanoindent*

W ramach projektu Nanoindent pracowałem nad opracowaniem standardowej procedury badań indentacji przy wykorzystaniu mikro-tryboskopów. W przypadku naszego laboratorium był to tryboskop firmy Hysitron umożliwiający testy indentacji oraz badania

metodą zarysowania (scratch testing) w zakresie sił od 20  $\mu\text{N}$  do 10 mN. Wyniki tych badań umożliwiły analizowę między innymi wpływu chropowatości powierzchni na wyniki pomiaru twardości: zarówno wartości średniej oraz rozrzutu wyników. Pozwoliły też ocenić mocniejsze i słabsze strony często używanych wgłębników (Berkovitch, CubeCorner, Spherical), jak np. fakt, że dla badań metodą zarysowania najbardziej uzasadnione jest stosowanie końcówek sferycznych o promieniu zaokrąglenia od 2 do 5  $\mu\text{m}$ , których kalibracja może odbywać się poprzez proces nanoindentacji. Projekt ten wpłynął też istotnie na końcową postać normy ISO 14577 dotyczącej metod pomiaru twardości materiałów w mikroskali. Razem z zespołem w projekcie opracowałem także wiele praktycznych wskazówek dotyczących kalibracji, badań indentacyjnych oraz metody zarysowania [1-5].

### *Projekt AppliCMA*

Projekt AppliCMA miał na celu opracowanie powłok ze stopów metali (CMA-Complex Metall Alloys) oraz ich dalszą optymalizację [6-9]. Zakres stosowania tych powłok jest bardzo szeroki i projekt dotyczył opracowania rozwiązań dla narzędzi skrawających, technik lotniczych oraz w litografii nanodrukowej (NIL-Nano Imprinting Lithography). Mój udział w tym projekcie dotyczył oceny przydatności nowo-wytwarzanych powłok dla zastosowań w NIL. Praca ta uwzględniała pomiary energii powierzchniowej, tarcia, adhezji, topografii powierzchni, odporności na zużycie, twardości oraz modułu sprężystości. Projekt ten umożliwił wskazanie tych powłok jako możliwych do zastosowania w rozważanej metodzie wytwarzania. Jednak konieczne w tym celu jest obniżenie adhezji i tarcia, ponieważ adhezja polimetakrylanu metylu (PMMA - często wykorzystywany w technologii NIL polimer) do powłoki CMA jest większa niż siła przyczepności PMMA do podłoża wykonanego z krzemiu, przez co następuje odrywanie polimeru i powstaje większa liczba defektów. W celu zmniejszenia oporów tarcia i adhezji wymagana jest optymalizacja topografii powierzchni. Temat ten był dalej rozwijany, czego efektem jest publikacja [10].

### *Projekt 3SMVIB*

Celem projektu 3SMVIB było zwiększenie wydajności wytwarzania urządzeń MEMS przy zmniejszeniu kosztów produkcji poprzez planowanie procesu wytwarzania w taki sposób, aby na podstawie dobranych parametrów znany był rozrzut uzyskanych właściwości końcowego urządzenia. W tym celu konieczne było opracowanie modelu symulacyjnego, który pozwoliłby przewidzieć właściwości mechaniczne i trybologiczne powstającego urządzenia, zebranie bazy danych właściwości powierzchni uzyskiwanych w wyniku

typowych metod wytwarzania, razem z ich rozrzutem oraz validacja tego modelu. Do moich zadań w ramach tego projektu należał współudział w opracowywaniu modelu symulacyjnego i tworzenie bazy niepewności charakteryzujących różne metody wytwarzania, a także opracowanie jednej z metod walidacji modelu. W wyniku tego projektu powstały dwa modele symulacyjne, duża baza danych oraz liczne publikacje [11-26].

## Projekty krajowe

Oprócz projektów europejskich pracowałem także w projektach o zasięgu krajowym, takich jak *Grafenowe pokrycia specjalnych kół zębatych i łożysk ślizgowych* (Graphtrib) w ramach programu Graf-tech, którego celem było opracowanie oraz przetestowanie grafenowego pokrycia wymienionych w tytule elementów. Był to duży projekt, w którym mój udział polegał na weryfikacji jakości nałożenia grafenu oraz na badaniach właściwości mechanicznych i trybologicznych powłok urządzeń, czego efektem jest praca mojego współautorstwa [P5]. Innymi badaniami w których uczestniczyłem była praca nad protezą strzemiączka ucha, przedstawiona w pracy mojego współautorstwa [P6], która realizowana była w ramach działalności statutowej uczelni, a kontynuowana poprzez grant dziekański w 2016 r. „*Wykonanie biozgodnej membrany z PDMS dla nowej komorowej protezki strzemiączka wraz z pomiarem sztywności membrany*” oraz projekt w konkursie NCN TANGO „*Nowa komorowa protezka strzemiączka*”. W ostatnich latach byłem nie tylko wykonawcą, ale też podjąłem się kierownictwa własnymi projektami, w tym dwoma projektami w ramach grantu dziekana w latach 2014 r. i 2016 r., mającymi na celu opracowanie nowego urządzenia do badań własności reologicznych polimerów, a następnie modernizację i ulepszenie tego urządzenia. Objąłem też kierownictwo w projekcie „*Measurements of viscosity of ultrathinfilms: optimization of the method* (Nanovisc)”, czyli projektu w ramach grantu NCN w konkursie Preludium, którego celem jest weryfikacja różnych metod pomiaru lepkości polimerów. Jego zakończenie planowane jest na październik 2019. W ramach tego projektu prowadzone są badania za pomocą mikroskopu sił atomowych, gdzie przy pomocy metody pętli tarcia można uzyskać informację o lepkości cienkiej warstwy polimeru, zgodnie z teorią przepływu Couette'a [27]. Ta metoda pomiaru porównywana będzie z innymi jak np.: modele lepko-plastyczne wykorzystywane do pomiarów nano-indentacyjnych z pomocą tryboskopu. Modele te zakładają, że odkształcenie podczas indentacji składa się z trzech komponentów: plastycznego, sprężystego oraz lepkościowego, a poprzez dopasowywanie krzywej do tej uzyskanej z pomocą indentacji można wyznaczyć wszystkie te 3 komponenty, gdzie dwa pierwsze mogą zostać równocześnie potwierdzone

modelem Olivera i Pharra [28]. Inną wykorzystywaną metodą będzie zastosowanie masy drgającej napędzanej elementem piezoelektrycznym, którego drugi element oddzielony od pierwszej okładki piezoelektrycznej mierzy drgania wypadkowe. Metoda ta działa analogicznie do badania w makro-skali [29].

### **Współpraca zagraniczna i udział w konferencjach**

W czasie pracy naukowej w Instytucie Mikromechaniki i Fotoniki nawiązywałem współpracę z wieloma zagranicznymi ośrodkami, takimi jak np.: Akademia Nauk w Mińsku, co zaowocowało wspólną publikacją [30], Uniwersytet w Osace (w ramach kilku projektów, które zaowocowały wspólną publikacją [P7]), Uniwersytet w Cork w Irlandii w ramach pracy nad nowymi membranami do zastosowań kosmicznych, Uniwersytet w Bukareszcie, Uniwersytet w Kluż-Napoce, czy Uniwersytet w Liege. Współpraca ta obejmowała także firmy działające w tej branży, jak np. brytyjska firma MicroMaterials. Wyniki moich prac prezentowane były na 18 konferencjach naukowych o zasięgu międzynarodowym, w tym 8 osobiście przeze mnie, przedstawiając różnorodne metody wykorzystywania mikroskopii sił atomowych w takich dziedzinach jak otolaryngologia, bioinżynieria, technologie kosmiczne, urządzenia MEMS czy trybologia. Ponadto byłem głównym organizatorem konferencji 8th International Colloquium on Micro-Tribology, która odbyła się w Warszawie w roku 2017 (uczestniczyło w niej 23 badaczy z 5 różnych krajów oraz 3 przedstawicieli firm specjalistycznych pracujących w tej branży).

### **Szkolenia i rozwój dodatkowy**

W ramach rozwijania swoich kompetencji uczestniczyłem w licznych szkoleniach specjalistycznych z takich dziedzin jak badania mikroskopowe, m.in. „Błąd pomiaru w mikroskopii”, niestandardowe metody w projektowaniu „Design Thinking”, metody nauczania „Warsztaty trenerskie” w CSDiZ (Centrum studiów i doradztwa zawodowego) i wiele innych. W tym czasie uzyskałem też drugi tytuł zawodowy magistra w dziedzinie psychologii pracy oraz stresu.

### **Praca dydaktyczna**

Od marca 2016 roku pracuję na stanowisku asystenta badawczo-dydaktycznego na Wydziale Mechatroniki Politechniki Warszawskiej. W ramach obowiązków dydaktycznych prowadzę zajęcia projektowe oraz laboratoryjne z Podstaw Konstrukcji Urządzeń Precyzyjnych (I stopień), a także wykłady z Mikrorządzeń MEMS (I stopień),

Mikromechatroniki (I stopień), Nanotechnologii (II stopień, wykład w języku angielskim) oraz Zaawansowane Techniki Pomiaru Topografii Powierzchni (II stopień), w ramach których jednym z tematów jest mikroskopia sił atomowych oraz jej różne zastosowania. Prowadzę także zajęcia z Mikro i Nanotechniki (II stopień), na których zapoznaje studentów z różnymi laboratoriami pracującymi w tej dziedzinie w Polsce oraz odwiedzam z nimi te placówki. W pracy dydaktycznej zdobytą wiedzę i doświadczenie przekazuję studentom.

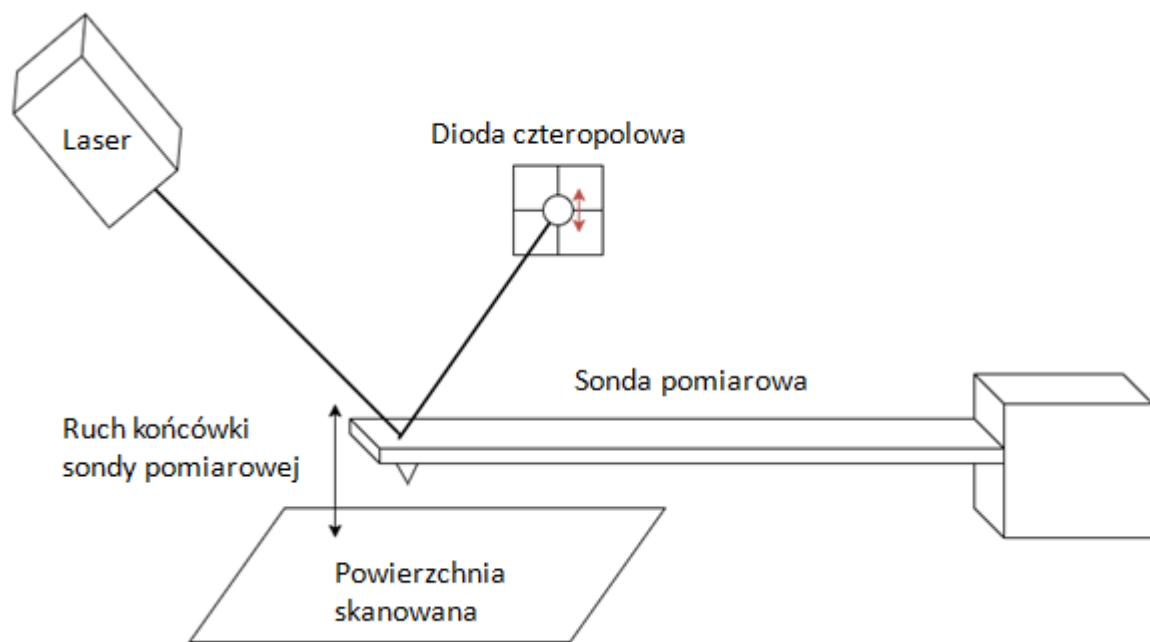
## **Podsumowanie**

Moją dotychczasową pracę w obszarze badawczo-dydaktycznym można podsumować w kilku poniższych punktach:

- brałem czynny udział w 3 projektach europejskich: *Nanoindent*, *AppliCMA*, *3SMVIB*,
- brałem czynny udział w projektach krajowych m.in.: *Graphtrib*,
- kierowałem projektami: *Nanovisc*, *Opracowanie urządzenia do badań reologicznych*,
- współpracowałem z zagranicznymi ośrodkami naukowymi: Akademia Nauk w Mińsku, Uniwersytet w Osace, Uniwersytet w Cork, Uniwersytet w Buchareszcie, Uniwersytet w Cluj-Napoce, Uniwersytet w Liege, firma MicroMaterials,
- prezentowałem swoje prace na 8 konferencjach międzynarodowych, a wyniki moich badań prezentowane były łącznie na 18 konferencjach międzynarodowych,
- byłem głównym organizatorem konferencji międzynarodowej 8th International Colloquium on Micro-Tribology,
- prowadzę zajęcia projektowe, zajęcia laboratoryjne oraz wykłady na Wydziale Mechatroniki Politechniki Warszawskiej,
- jestem współautorem lub jedynym autorem 11 publikacji (wg. WoS).

## 1.2. Wprowadzenie do tematyki

Mikroskopia sił atomowych od swojego powstania w latach 80. ubiegłego wieku [31] prężnie się rozwija pod względem stosowanych urządzeń [32-35], metod badawczych [36-40], czy obszarów zastosowania [41-45]. Podstawowa zasada działania skaningowej mikroskopii sił atomowych pozostaje jednak niezmienna: belka sondy pomiarowej (ang. cantilever) najczęściej zakończona ostrą igłą lub kulką (ang. tip) oddziałuje z powierzchnią badanej próbki (Rys. 1). Może ona zarówno dotykać próbki w tak zwanym trybie kontaktowym lub zostać wprowadzona w drgania ponad powierzchnią w trybie bezkontaktowym. Oddziaływanie pomiędzy końcówką pomiarową a powierzchnią doprowadza do ugięcia belki sondy pomiarowej, co najczęściej mierzone jest przy pomocy odbitego od jej górnej powierzchni promienia lasera, który następnie pada na kilkupolową fotodiodę. Dioda ta może być 2-lub 4-polowa, umożliwiając detekcję odkształcenia belki w 1 lub 2 osiach. Precyzyjne pozycjonowanie sondy względem próbki jest rozwiązywane poprzez wykorzystanie elementu piezoelektrycznego o kształcie tulei podzielonej na 4 niezależne segmenty piezoelektryczne. W ten sposób można zapewnić precyzyjny ruch układu sonda-próbka badana w trzech osiach.



Rysunek 1 Schemat działania mikroskopu sił atomowych

Urządzenie to pozwala na bardziej dokładne obrazowanie powierzchni badanej niż mikroskopia optyczna czy mikroskopia elektronowa, dodatkowo nie ma tutaj ograniczenia wynikającego z konieczności stosowania powierzchni przewodzących, co pozwoliło na jego

wdrożenie w badaniach nad tkankami żywymi [41,43,45]. Oprócz możliwości obrazowania powierzchni, kontakt uzyskiwany pomiędzy końcówką sondy pomiarowej a próbką umożliwia badania sił z dużą rozdzielczością zarówno w kierunku pionowym [46], jak i poziomym [27]. Siły te są mniejsze niż podczas badań nanoindentacyjnych z wykorzystaniem typowych komercyjnych wgłębników. Zalety te doprowadziły do częstszego stosowania tej aparatury badawczej podczas wspierania procesu projektowania, wytwarzania oraz późniejszego badania mikrourządzeń mechanicznych [47-48].

Projektowanie mikrourządzeń mechanicznych obarczone jest licznymi trudnościami, które znacznie komplikują uzyskanie dużej trwałości, a czasem także w ogóle możliwość ich wytworzenia. Do takich największych trudności możemy zaliczyć:

- duże zużycie powierzchni [49],
- duże siły adhezji pomiędzy stykającymi się powierzchniami [50, 51],
- brak znajomości współczynnika tarcia, a w efekcie tego sił tarcia pomiędzy dwoma powierzchniami [52],
- trudności z ustalaniem własności mechanicznych i reologicznych urządzeń, jak np. sztywność konstrukcji [53],
- technologiczność konstrukcji, czyli ograniczenie metod wytwarzania sprawiające, że zaprojektowane urządzenia mogą być niemożliwe do wytworzenia przy obecnym stanie techniki [54].

Brak znajomości dokładnych wartości siły adhezji czy sił tarcia doprowadza do trudności w dobieraniu powłok i odpowiednich chropowatości powierzchni w urządzeniach. Duże siły tarcia i adhezji doprowadzają do szybkiego zużycia powierzchni, a co za tym idzie małej trwałości urządzeń opracowywanych w tej skali. Trudności z pomiarem parametrów mechanicznych doprowadzają do takich problemów jak blokowanie się belek MEMS [50] czy wytwarzanie membran o niskiej trwałości [53]. Zastosowanie mikroskopii sił atomowych może pomóc w projektowaniu mikrourządzeń, jednak istnieją pewne ograniczenia, które należy wziąć pod uwagę. Są to między innymi trudności kalibracyjne tego urządzenia. Wszystkie pomiary topografii próbki, sił adhezji, energii zrywania, współczynnika tarcia i inne wymagają złożonej kalibracji, która do chwili obecnej obciążona jest dużym błędem [55]. Innym problemem jest zakres stosowanych obecnie sond pomiarowych, które jako ostre igły lub kulki o średnicy pojedynczych mikrometrów symulują nierealistyczny kontakt pomiędzy badanymi powierzchniami. Materiały wykorzystywane na końcówki sond

pomiarowych oraz obecnie stosowane metody pomiarowe także nie pozwalają na pomiar wszystkich parametrów wykorzystywanych przy projektowaniu mikrourządzeń. W ramach niniejszej pracy skupiłem się więc na rozwoju mikroskopii sił atomowych w aspekcie wspomagania projektowania mikrourządzeń poprzez rozwój metod pomiaru współczynnika tarcia, pomiaru poszczególnych parametrów mechanicznych oraz zwiększania technologiczności konstrukcji w przypadku urządzeń wytwarzanych metodą litografii nanodrukowej.

## 2. Przewodnik po publikacjach

Przewodnik ten obejmuje 5 publikacji z listy JCR, jeden rozdział z monografii specjalistycznej traktującej o pomiarach własności powierzchni oraz publikację pokonferencyjną.

### 2.1. Wykaz publikacji stanowiących rozprawę

	Publikacja
P1	<b>Michałowski M.</b> , Łuczak S., Cantilevers with spherical tips of millimeter magnitude, <i>Journal of Micromechanics and Microengineering</i> (2019), tom 29, numer 1, no. 017002
P2	<b>Michałowski M.</b> , Simulation model for frictional contact of two elastic surfaces in micro/nano scale and its validation, <i>Nanotechnology Reviews</i> (2018), tom 7, numer 5, str. 355-363
P3	<b>Michałowski M.</b> , Voicu R., Obreja C., Baracu A., Muller R., Rymuza Z., Influence of deposition temperature during LPCVD on surface properties of ultrathin polysilicon films, <i>Microsystem Technologies</i> (2018), tom 24, str. 537-542
P4	Jarząbek D., <b>Michałowski M.</b> , 11 Surface mechanical properties. W: Tanzi M. C. and Farè S. (red.) <i>Characterization of Polymeric Biomaterials</i> , Woodhead Publishing (2017), str. 255-282
P5	<b>Michałowski M.</b> , Tomaszik J., Wiśniewska M. Impact of graphene coatings on nanoscale tribological properties of miniaturized mechanical objects. W: Jabłoński R., Brezina T. (red) <i>Advanced Mechatronics Solutions. Advances in Intelligent Systems and Computing</i> (2016). Springer, Cham, tom 393, str. 501-507
P6	Kwacz M., Rymuza Z., <b>Michałowski M.</b> , Wysocki J., Elastic Properties of the Annular Ligament of the Human Stapes—AFM Measurement, <i>Journal of the Association for Research in Otolaryngology</i> (2015). tom 16, numer 4, str. 433-446
P7	Tochino T., Uemura K., <b>Michałowski M.</b> , Fujii K., Yasuda M., Kawata H., Rymuza Z., Hirai Y., Computational study of the effect of side wall quality of the template on release force in nanoimprint lithography, <i>Japanese Journal of Applied Physics</i> (2015), tom 54, Numer 6S1, no. 06FM06

Tabela 1 Cykl publikacji stanowiących rozprawę

Parametry bibliometryczne publikacji mojego autorstwa i współautorstwa podsumowane są w tabeli 2. Mój uśredniony wkład własny w wymienione publikacje wynosi 69%.

	<b>Rok wydania</b>	<b>Udział własny</b>	<b>Impact Factor 2017</b>	<b>IF z uwzględnieniem udziału własnego</b>	<b>Impact Factor 5-letni 2017</b>	<b>Punkty MNiSW max 2013-2016</b>	<b>Cytowania wg. WOS</b>
<b>P1</b>	<b>2019</b>	<b>90%</b>	<b>1.888</b>	<b>1.699</b>	<b>1.954</b>	<b>35</b>	<b>0</b>
<b>P2</b>	<b>2018</b>	<b>100%</b>	<b>1.904</b>	<b>1.904</b>	<b>1.945</b>	<b>25</b>	<b>0</b>
<b>P3</b>	<b>2018</b>	<b>80%</b>	<b>1.581</b>	<b>1.265</b>	<b>1.330</b>	<b>20</b>	<b>1</b>
<b>P4</b>	<b>2017</b>	<b>50%</b>	-	-	-	<b>3</b>	<b>0</b>
<b>P5</b>	<b>2016</b>	<b>75%</b>	-	-	-	<b>15</b>	<b>0</b>
<b>P6</b>	<b>2015</b>	<b>45%</b>	<b>2.716</b>	<b>1.222</b>	<b>2.859</b>	<b>35</b>	<b>8</b>
<b>P7</b>	<b>2015</b>	<b>40%</b>	<b>1.452</b>	<b>0.581</b>	<b>1.149</b>	<b>20</b>	<b>4</b>
<b>Łącznie</b>		<b>9.541</b>		<b>6.671</b>	<b>9.237</b>	<b>153</b>	<b>13</b>

Tabela 2 Podsumowanie parametrów bibliometrycznych cyklu publikacji

Poniższa tabela natomiast podsumowuje parametry bibliometryczne moich wszystkich publikacji.

<b>Liczba publikacji w WoS</b>	<b>11</b>
<b>Liczba publikacji w Scopus</b>	<b>11</b>
<b>Liczba publikacji w Google Scholar</b>	<b>18</b>
<b>Index Hirsha</b>	<b>3</b>
<b>Łączna liczba cytowań według WoS</b>	<b>19</b>
<b>Łączna liczba cytowań według Scopus</b>	<b>21</b>
<b>Łączna liczba cytowań według Google Scholar</b>	<b>21</b>

Tabela 3 Parametry bibliometryczne całego dorobku publikacyjnego

Tabela 4 zawiera natomiast podsumowanie udziału własnego procentowego wraz z rozwiniętym opisem.

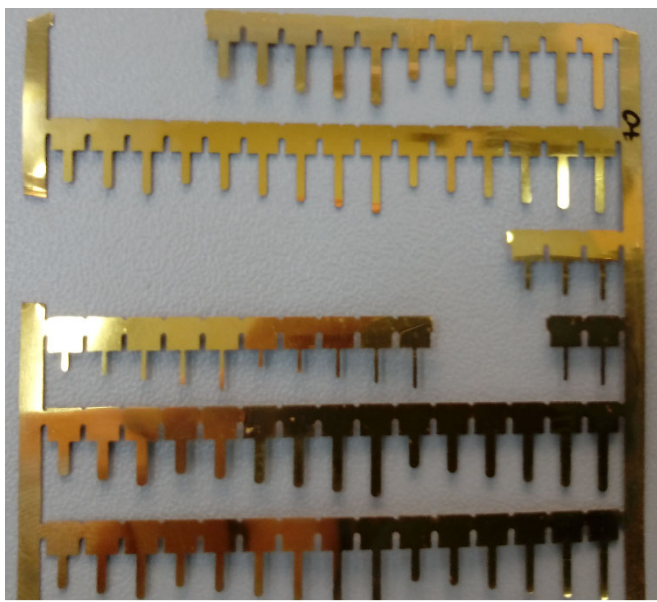
	<b>Udział własny</b>	<b>Opis udziału własnego</b>
<b>P1</b>	<b>90%</b>	Moim wkładem w tę publikację było opracowanie technik badawczych, wskazanie obszarów zastosowań, a także opracowanie treści manuskryptu. Sam pomysł tych sond opracowany został przez innych badaczy wymienionych w tym artykule.
<b>P2</b>	<b>100%</b>	Praca monoautorska
<b>P3</b>	<b>80%</b>	Mój udział w tej pracy dotyczył technik badawczych, przeprowadzenia badań i analizy wyników. Obejmował także przygotowanie ostatecznej treści publikacji.
<b>P4</b>	<b>50%</b>	Moim wkładem w ten rozdział monografii był opis: pomiarów poprzez krzywą siła – przemieszczenie; pomiarów tarciowych; analizy metod kalibracji pionowej; porównanie modeli kontaktu; opis pomiaru lepkości oraz niektórych metod specjalistycznych.
<b>P5</b>	<b>75%</b>	Moim udziałem w tej publikacji był dobór metod pomiaru własności mechanicznych i trybologicznych, przeprowadzenie badań oraz ich analiza, a także opracowanie treści publikacji.
<b>P6</b>	<b>45%</b>	Mój udział w tym artykule polegał na opracowaniu metodyki badawczej, konsultacjach dotyczących przygotowywania próbek, analizie otrzymanych wyników, a także napisaniu części treści ostatecznej publikacji.
<b>P7</b>	<b>40%</b>	Mój udział w tej publikacji polegał na doborze metodyki realizacji pomiarów oraz opracowaniu szczegółowych aspektów nowej metody, uwzględniających takie elementy jak wprowadzanie sondy pomiarowej w drgania pomiędzy poszczególnymi pomiarami w celu usunięcia potencjalnych zanieczyszczeń i fragmentów polimeru. Przeprowadziłem też analizę wyników badawczych, konsultacje modelu oraz końcowej treści manuskryptu.

*Tabela 4 Podsumowanie wkładu własnego autora w poszczególne publikacje zawarte w cyklu*

## **2.2. Sondy badawcze z końcówkami badawczymi sferycznymi milimetrowej średnicy**

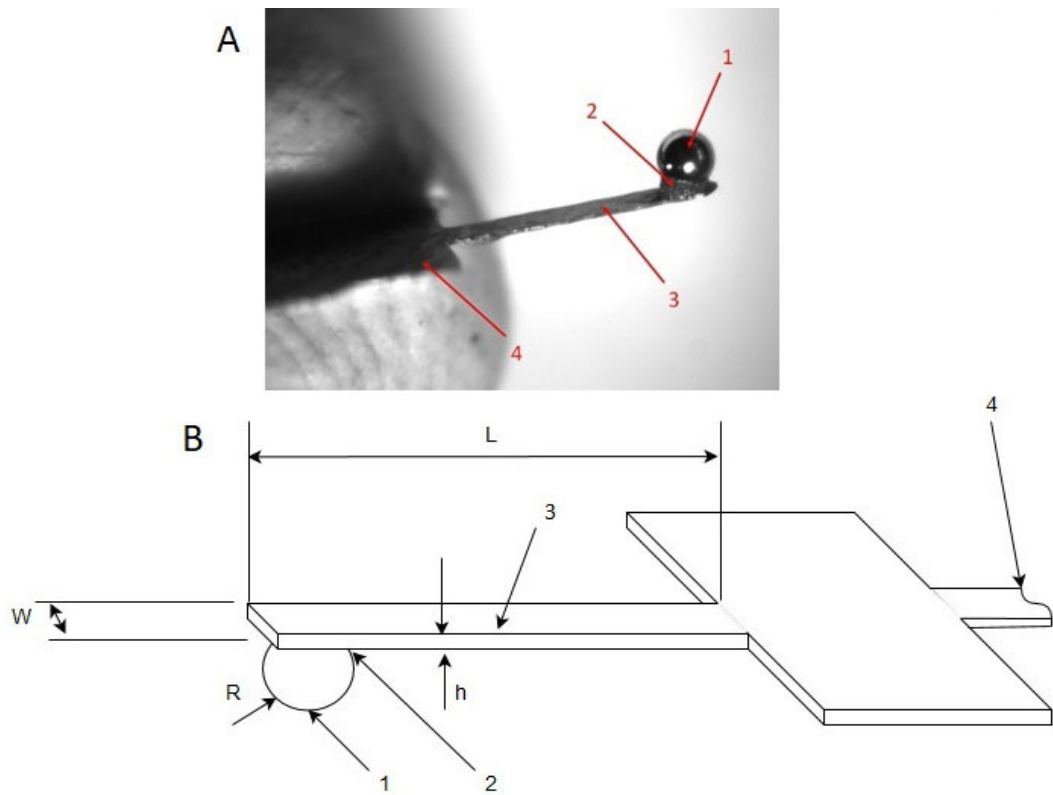
W publikacji [P1] opisałem nowy rodzaj sond badawczych do zastosowania w mikroskopii sił atomowych. Komercyjnie sprzedawane sondy zakończone są najczęściej ostrą igłą, sferą o promieniu kilku mikrometrów lub nie mają żadnej końcówki. Wszystkie te trzy rozwiązania cechują się pewnymi ograniczeniami. Symulowanie styku dwóch powierzchni w ten sposób stwarza pewne ograniczenia topografii tych powierzchni oraz wymusza bardzo małe pole powierzchni styku. Sondy bez końcówki badawczej mogłyby mieć duże pole styku z powierzchnią badaną, jednak ze względu na konstrukcję mikroskopu sił atomowych nie byłoby możliwe odczytanie siły bocznej skutkiem braku skrętu tej sondy. Drugim problemem z komercyjnie stosowanymi sondami jest ograniczona grupa materiałów z jakich są wykonywane ich końcówki pomiarowe. O ile podczas badania topografii powierzchni, czy własności mechanicznych próbki nie jest to istotne, to do badań własności trybologicznych czy adhezyjnych może być potrzebne testowanie konkretnej pary materiałów. Zastosowanie zaproponowanych przeze mnie sond umożliwia uniknięcie tych problemów poprzez pomiary z wykorzystaniem końcówki pomiarowej o większej średnicy wykonanej z różnorodnych materiałów. Ich dodatkowym atutem jest możliwość dobrania różnorodnych materiałów na końcówkę sondy, dzięki czemu różne pary materiałowe mogą być badane. Końcówka ta może też być w ograniczonym stopniu modyfikowana pod względem topografii, a większy niż typowo promień ich zaokrąglenia pozwala zmniejszyć naciski jednostkowe, co jest korzystne w badaniach próbek biologicznych.

Publikacja przedstawia metodę wytwarzania tych sond polegającą na wytrawianiu z cienkiej blachy z brązu berylowego struktury składającej się z dużej liczby zróżnicowanych sond badawczych przyczepionych do jednej wspólnej bazy. Wytrawianie to można przeprowadzać metodą trawienia mokrego z wykorzystaniem odpowiedniej maski. Dzięki wytworzeniu belek sond o różnych wymiarach, zarówno długości jak i szerokości, można uzyskać sondy o sztywności zarówno skrętnej i zginającej zmiennej w szerokim zakresie. Tak wytworzoną strukturę pokrywa się powłoką odbijającą, a poszczególne belki sondy odcina się mechanicznie od bazy (Rys. 2).



Rysunek 2 Zdjęcie bazy wytrawionej z brązu berylowego z przyczepionymi belkami sond pomiarowych

Do poszczególnych belek sond przyklejane za pomocą kleju epoksydowego są kulki będące końcówkami pomiarowymi. Kulki te najczęściej mają średnicę rzędu 0,1 do 1 mm (Rys. 3).

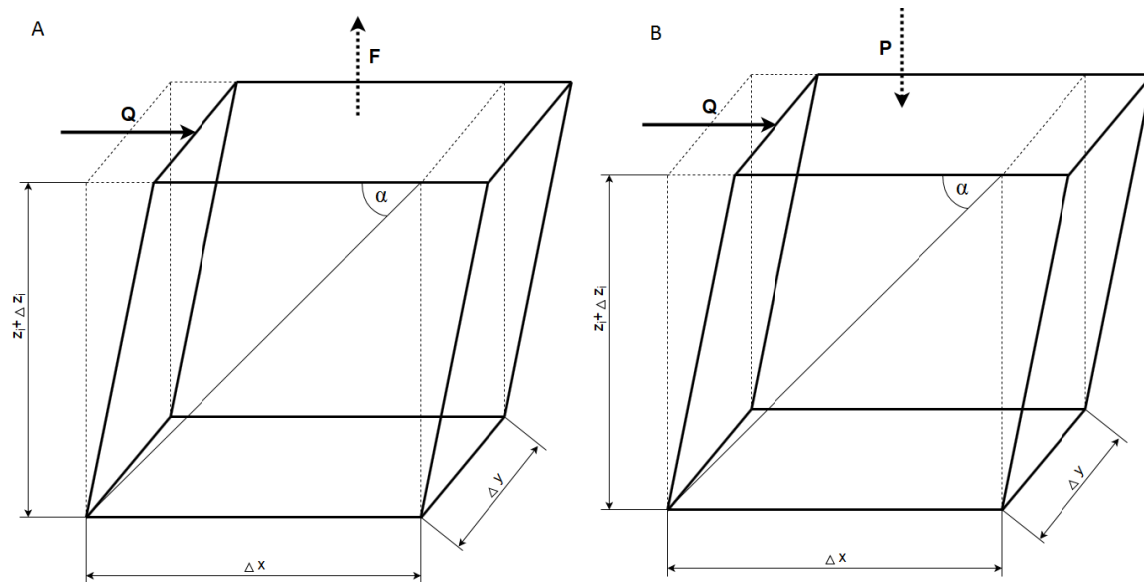


Rysunek 3 A) Zdjęcia przykładowej sondy badawczej 1) końcówka sondy w tym przypadku stalowa kula o średnicy 0,7 mm 2) spoina klejowa łącząca kulkę z belką sondy 3) belka sondy pomiarowej 4) baza sondy, jej mocowanie w mikroskopie sił atomowych B) Schemat opracowanej sondy badawczej L- długość belki, W- szerokość belki, h- grubość belki, R- promień kulki pomiarowej

Oprócz metod wytwarzania sond w publikacji tej opisałem przykładowe oraz potencjalne zastosowania dla nich, uwzględniające badania sił oraz współczynnika tarcia, badania sił adhezji, pomiary lepkości cienkich powłok polimerowych czy badania własności mechanicznych próbek biologicznych.

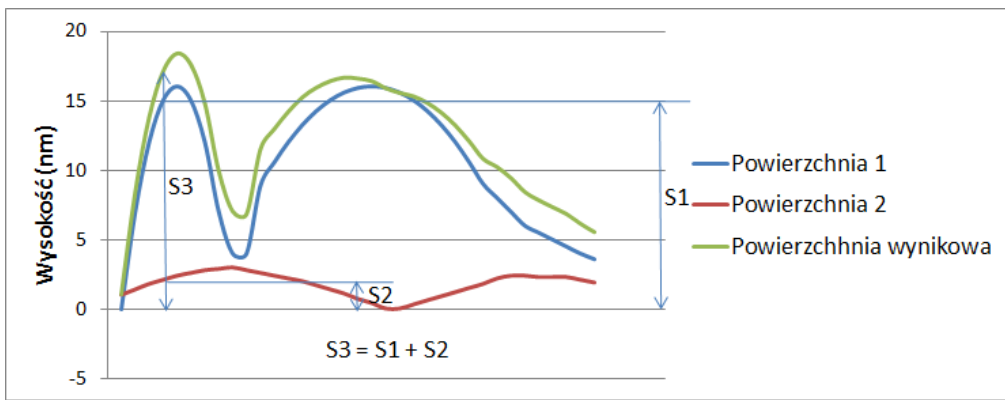
### 2.3. Wykorzystanie mikroskopii sił atomowych w symulacyjnym modelu tarcia

Monoautorska publikacja [P2] przedstawia sposób na wykorzystanie pomiaru topografii z wykorzystaniem mikroskopii sił atomowych wraz z kilkoma innymi parametrami do symulowania kontaktu tarciowego pomiędzy dwoma powierzchniami o złożonym kształcie. Oprócz zebrania danych niezbędnych do przeprowadzenia takiej symulacji ta sama aparatura pomiarowa, po zmianie sondy pomiarowej, może zostać wykorzystana do validacji tego modelu poprzez symulowanie kontaktu kulki o dużej średnicy z powierzchnią próbki. Model symulacyjny wykorzystujący teorię tarcia McClellanda [56] oraz energię kontaktu w postaci przedstawionej przez Leonarda-Jonesa [57] opisuje powierzchnię jako zbiór niezależnych prostopadłościanów, które odkształcają się w kierunku pionowym w wyniku nacisku i sił adhezji, a następnie są ścinane podczas tarcia dwóch próbek o siebie (Rys. 4).



Rysunek 4 Schemat pojedynczego elementu odkształcanego z jego wymiarami  $x, y, z$  wraz z odkształceniem w osi  $z$ ; a) w wyniku adhezji  $F$ ; b) w wyniku nacisku  $P$ ; w obu przypadkach ścinanego przez siłę  $Q$

Druga powierzchnia natomiast modelowana jest jako płaska, dlatego pierwsza powierzchnia stanowi złożenie jej własnej nierówności oraz nierówności powierzchni drugiej (Rys. 5), co ułatwia proces modelowania.



Rysunek 5 Sumowanie nierówności dwóch powierzchni do jednej, druga interpretowana jest jako idealnie płaska

Do zamodelowania kontaktu potrzebna była znajomość topografii, energii powierzchniowej, sprężystości i współczynnika Poissona obu kontaktujących się powierzchni. Wartości te wyznaczyłem wykorzystując mikroskopię sił atomowych, nano-indentację oraz pomiary zwilżalności. Badania przy pomocy mikroskopu sił atomowych pozwoliły na poznanie dokładnej topografii próbki oraz powierzchni kulki sondy pomiarowej z takim krokiem skanowania, jaki docelowo ma być zastosowany w symulacji, w tym przypadku 10 nm. Nanoindentacja pozwoliła wyznaczyć moduł Younga próbek poprzez zastosowanie modelu Olivera i Pharra [28]. Natomiast energia powierzchniowa uzyskiwana jest poprzez pomiar zwilżalności, podczas którego na powierzchni próbki umieszczane są dwie ciecze o różnych składowych energii powierzchniowych: polarnej i dyspersyjnej. Następnie mierząc kąt, jaki kroplatworzyła na powierzchni, możliwe jest obliczenie energii powierzchniowej danego materiału [27]. Po uzyskaniu tych parametrów przeprowadziłem walidację modelu poprzez zamodelowanie kontaktu powierzchni kulki sondy pomiarowej z powierzchnią próbki badanej (Rys. 6) dla kilku różnych próbek. Siła tarcia wyliczana jest w tym modelu jako suma tarcia adhezyjnego i mechanicznego. W każdym punkcie wyliczana jest siła tarcia adhezyjnego lub mechanicznego w zależności od wstępного kontaktu (w każdym punkcie występuje na raz tylko jedna składowa). Następnie jest ona sumowana dla wszystkich modelowanych punktów pomiędzy dwiema powierzchniami. Składowa mechaniczna tarcia wyliczana jest jako:

$$Q_i = \sqrt{\frac{1}{d} 4CGS \frac{8\Delta\gamma}{3} \left( \frac{\varepsilon^2}{2l_{im}^2} - \frac{\varepsilon^8}{2l_{im}^8} \right)} \quad (1)$$

gdzie:

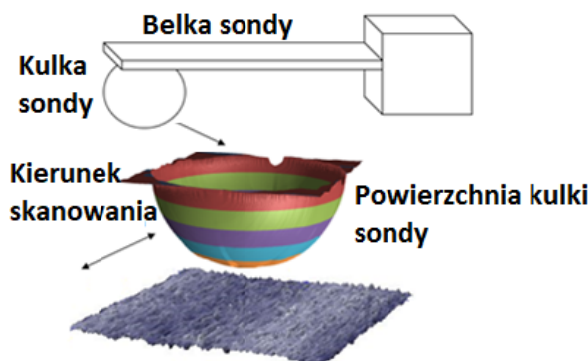
$$C = \frac{\tan\alpha}{\tan^2\alpha+1}, \quad \tan\alpha = \frac{z_i + \Delta z_i}{\Delta x}, \quad \Delta x - \text{bok modelowanego punktu kontaktu (rozdzielcość symulacji)} \\ G = \frac{E}{2(1+v)}, \quad S - \text{powierzchnia góra modelowanego elementu}, \quad l_i - \text{odległość}$$

pomiędzy dwoma powierzchniami w punkcie kontaktu  $i$ ,  $l_{lim}$ - odległość pomiędzy dwoma punktami w momencie nacisku powierzchni na siebie, wyliczana z równowagi sił nacisku i odpychania cząsteczkowego,  $d$  - odległość pomiędzy powierzchnią płaską a powierzchnią odniesienia powierzchni chropowatej,  $\varepsilon$  - odległość międzycząsteczkowa.

Składowa adhezyjna siła tarcia natomiast wyliczana jest jako:

$$Q_i = \sqrt{\frac{1}{z_i + \Delta z_i} 4CGS \frac{8 \Delta \gamma}{3} \left( \frac{\varepsilon^2}{2l_{im}^2} - \frac{\varepsilon^8}{2l_{im}^8} \right)} \quad (2)$$

gdzie  $l_{ia}$ - odległość pomiędzy dwoma punktami, wyliczana z wstępnej odległości powierzchni oraz przyciągania cząsteczkowego



Rysunek 6 Schemat metody walidacji modelu symulacyjnego. Sonda pomiarowa mikroskopu sił atomowych zakończona kulką po doprowadzeniu do kontaktu jest wprowadzana w ruch równoległy względem drugiej powierzchni. Wartość siły tarcie jest mierzona i porównywana z wartościami uzyskanymi za pomocą symulacji

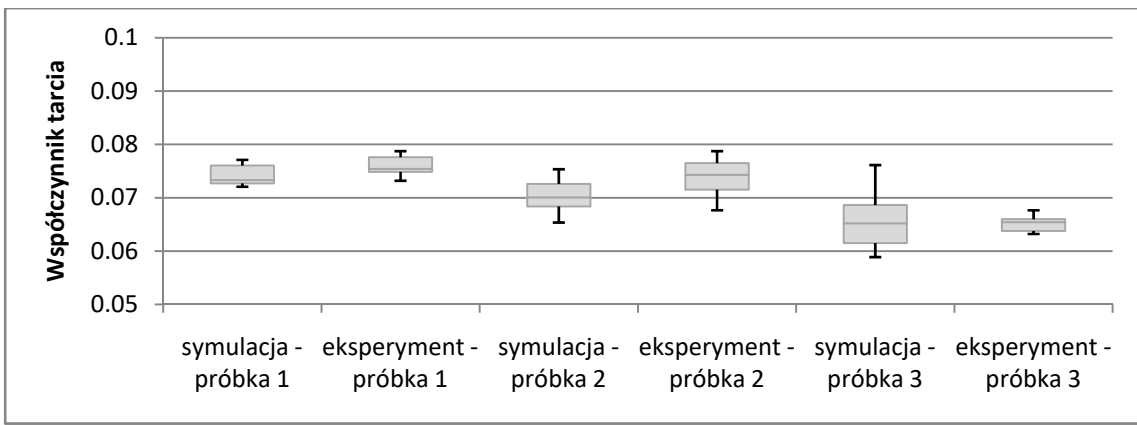
Ostateczny współczynnik tarcia wyliczany jest jako:

$$\mu = \frac{\sum_i Q_i}{N} \quad (3)$$

gdzie:

$N$  – zewnętrzna siła nacisku.

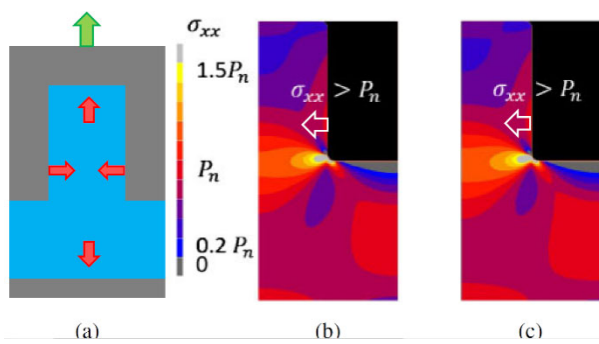
Przeprowadzona w ten sposób przeze mnie walidacja modelu sugeruje poprawność jego działania, a przykładowe porównanie wyników eksperymentalnych z symulacyjnymi zostały zestawione na Rys. 7 razem z ich odchyleniem standardowym.



Rysunek 7 Zestawienie wyników symulacji i eksperymentu w walidacji modelu symulacyjnego, prostokąty przedstawiają zakres od 1 do 3 kwartyla, natomiast linie oznaczają rozstęp wyników. Różnice w rozpięcie poszczególnych symulacji wynikają z większych różnic w chropowatości powierzchni w poszczególnych punktach pomiarowych w próbce 3 niż w 2 i 1

#### 2.4. Badania energii odrywania maski w procesie NIL

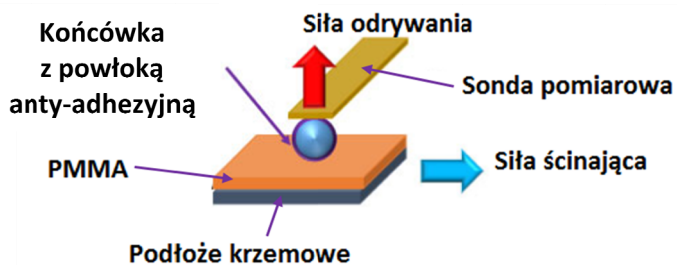
Litografia nanodrukowa (Nano Imprint Lithography - NIL) [58] jest bardzo obiecującą metodą wytwarzania dla systemów MEMS i NEMS ze względu na wysoką rozdzielcość oraz niski koszt procesu. Jednak defekty powstające podczas zdejmowania maski wprowadzają duże ograniczenia w zastosowaniach [59] tej metody. Opracowywanych zostało wiele metod zmniejszania liczby defektów, wykorzystujących np: powłoki anty-adhezyjne [60,61] lub odpowiedni sposób przyłożenia siły podczas odrywania [62,63], jednak wszystkie one dają ograniczone efekty i usunięcie wszystkich defektów nadal nie jest możliwe w technologii NIL. W celu pogłębienia zrozumienia tego problemu opracowany został model MES pozwalający symulować proces zrywania maski [P7]. Model ten skupia się na wpływie kątu docelowej struktury na siłę potrzebną do oderwania maski od rezystu (Rys. 8).



Rysunek 8 Naprężenia pojawiające się w polimerze podczas odrywania maski w kształcie podłużnego prostokątnego elementu, a) schematyczne przedstawienie naprężen, b) naprężenia dla sytuacji, gdy naprężenia ścinające są 10-krotnie większe od normalnych, c) naprężenia dla sytuacji gdy naprężenia ścinające są 20-krotnie większe od normalnych

Do opracowania tego modelu [P7] niezbędne było wyznaczenie parametrów podstawowych, takich jak krytyczne naprężania normalne, naprężenia ścinające interfejsu

pomiędzy materiałami tworzącymi maskę i wytwarzany polimer, oraz obliczenie istotnego stosunku pomiędzy tymi dwiema wartościami. Parametry te są specyficzne dla każdego połączenia materiałów, dla tej analizy wybrałem PMMA jako rezyst, ze względu na docelowe wykorzystanie w technologii NIL oraz kilka różnych powłok anty-adhezyjnych nakładanych na  $\text{SiO}_2$  oraz  $\text{SiO}_2$  bez powłoki. Do pomiaru tych dwóch własności wykorzystana została mikroskopia sił atomowych (Rys. 9).

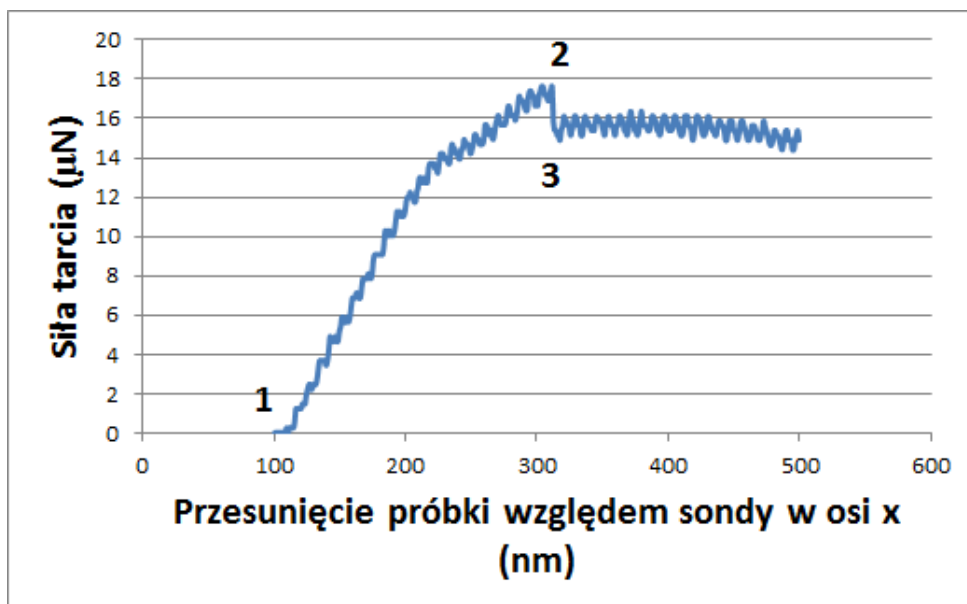


Rysunek 9 Schemat pomiarowy naprężeń normalnych oraz naprężeń ścinających mierzonych na potrzeby modelowania zrywania maski NIL

Do pomiaru naprężeń normalnych wykorzystałem procedurę krzywej siła-przemieszczenie (Force-Distance Curve -FDC) [46]. Procedura ta polega na przybliżaniu końcówki sondy pomiarowej do powierzchni próbki, aż do styku sondy z powierzchnią. Następnie próbka jest obciążana siłą pionową do ustalonej z góry wartości obciążenia, po tym siła jest zmniejszana, a po zmniejszeniu do zera sonda pomiarowa jest odrywana od powierzchni badanej próbki [46]. Podczas tych badań wyznaczałem naprężenia zdefiniowane jako stosunek siły odrywania do pola powierzchni kontaktu pomiędzy kulką sondy pomiarowej a powierzchnią. Naprężenia te, będące wytrzymałością połączenia na rozciąganie, były mierzone zarówno przed jak i po pokryciu sondy powłoką antyadhezyjną. Natomiast w przypadku naprężeń ścinających, czyli wytrzymałości połączenia na ścinanie, mierzone były one poprzez pomiar siły tarcia statycznego na początku ruchu sondy w kierunku skrętnym. Wykonywałem linie pomiarowe o dużym zagęszczeniu punktów, kończąc pomiar na etapie przejścia z tarcia statycznego do tarcia kinetycznego. Na podstawie wychylenia belki sondy z pozycji początkowej do momentu rozpoczęcia poślizgu można przy odpowiedniej kalibracji skrętnej wyznaczyć siłę potrzebną do ścinania połączenia (Rys. 10). Natomiast przy znajomości pola kontaktu kulka sondy-próbka, siłę te można przeliczyć na naprężenia ścinające danej pary materiałów. Kalibracja siły skrętnej przeprowadzana była metodą geometryczną poprzez obliczenie skręcenia belki o znanych wymiarach pod wpływem siły uzyskanej podczas badań [P4]. Pole kontaktu obliczane było natomiast przy

pomocy modelu kontaktowego Johnson-Kendall-Roberts (JKR), który dobrze odzwierciedla kontakt z materiałami polimerowymi [P4, 45].

Dodatkowo podczas tych badań mierzona była także energia zrywania w postaci całki oznaczonej siły zrywania po przemieszczeniu od początku ścinania do momentu poślizgu. Rezultaty te zostały wykorzystane do walidacji wstępnych wyników uzyskanych dzięki wykorzystaniu modelu symulacyjnego [P7].



Rysunek 10 Przykładowy schemat wyniku pomiaru siły tarcia statycznego podczas ścinania pomiędzy kulką sondy pomiarowej a próbką PMMA, 1- skręcanie belki sondy pomiarowej podczas tarcia statycznego, 2- rozpoczęcie poślizgu sondy po powierzchni próbki, punkt zerwania interfejsu, 3- spadek siły tarcia po przejściu z tarcia statycznego na tarcie kinetyczne

## 2.5. Badania powierzchni polikrystalicznych uzyskiwanych metodą LPCVD

W procesie wytwarzania urządzeń MEMS kluczowy jest dobór odpowiednich materiałów oraz ich szczegółowych parametrów wytwarzania. Właściwości materiałowe wpływają na niezawodność urządzeń produkowanych, a mechanizmy tych uszkodzeń są nierzaz zdecydowanie inne niż w makroskali [64, 65]. Na podstawie dotychczasowych badań wiemy, iż wpływ struktury powierzchni na urządzenia jest znaczący w mikroskali [64]. Przeprowadziłem, więc serię badań mającą na celu ustalenie właściwości powierzchniowych oraz trybologicznych próbek uzyskiwanych przy zmienianiu technologii wytwarzania. Pierwsza seria pozwoliła mi wstępnie wybrać optymalny materiał na współpracujące powierzchnie MEMS [17, 20], w czym pomocny był model kontaktowy opisany w artykule mojego autorstwa [P2]. Kolejne serie badawcze pozwoliły mi na wstępny dobór parametrów wytwarzania, czy ocenę zasadności dodatkowych zabiegów takich jak wyżarzanie [13, 24-

26]. Wstępny dobór materiału oraz zakresu parametrów podczas wytwarzania powłok pozwolił mi na bardziej szczegółową analizę próbek uzyskanych metodą chemicznego osadzania przy niskim ciśnieniu (LPCVD) przy zmianie temperatury napylania krzemu polikrystalicznego [P3].

Końcowa analiza parametrów tych próbek uwzględniała pomiar ich dokładnej topografii wraz z wyznaczeniem chropowatości oraz kurtozy, która zgodnie z uzyskanymi wynikami może mieć wpływ na własności adhezyjne oraz tarciowe przy próbkach o zbliżonej chropowatości w rozumieniu najczęściej używanego współczynnika Ra. Uwzględniała ona także analizę siły adhezji, mierzonej poprzez siłę odrywania, pomiędzy badaną powierzchnią a specjalnie w tym celu przygotowaną sondą pomiarową z brązu berylowego z kulką o średnicy 0,35 mm wykonaną z SiO<sub>2</sub>. Badania te przeprowadzane były dodatkowo w różnych warunkach wilgotności powietrza w celu weryfikacji potencjalnego stałego kontaktu dwóch powierzchni w takich urządzeniach jak mikro przełączniki działające w paśmie częstotliwości radiowej (RF-MEMS). Metoda wykonania sond pomiarowych została opisana w rozdziale 2.2 oraz publikacji [P1]. Ostatnie z badań dotyczyło wyznaczenia współczynnika tarcia pomiędzy daną próbką a kulką wykonaną z SiO<sub>2</sub>, które przeprowadzane było metodą pętli tarcia. Metoda ta polega na poślizgu końcówki sondy pomiarowej po próbce dwukrotnie wzduż jednej linii zmieniając zwrot ruchu [27]. Podczas tego poślizgu mierzone jest skręcenie belki sondy pomiarowej pod wpływem siły tarcia. Siła tarcia wyznaczana jest jako połowa różnicy pomiędzy skręceniem sondy podczas przebiegu w dwie strony, pomnożona przez sztywność skrętną sondy.

## 2.6. Przegląd metod badawczych w badaniach biomateriałów

W ostatnich latach opracowywane są w dużej liczbie nowe materiały bio-kompozytowe [66-68], rozwijane są także nowe obszary zastosowań dla nich [69, 70]. Przy rosnącym ich wykorzystaniu w mikro i nano-technologii coraz większy nacisk kładziony jest na ich własności powierzchniowe [71], których wpływ w mikroskali jest dobrze znany [72-74]. W świetle tego potrzebne jest opracowanie dobrej i powtarzalnej metodologii prowadzenia badań powierzchni podczas opracowywania nowych materiałów biokompozytowych. W celu zaspokojenia tej potrzeby, w monografii opisującej biokompozyty zawarto rozdział mojego współautorstwa dotyczący badań powierzchniowych [P4].

W rozdziale tym opisałem najczęściej używane metody do pomiaru adhezji, siły tarcia, lepkości, odporności na zużycie, czy sprężystości materiału zarówno w skali mikro jak i nano.

Pomiary adhezji czy sprężystości opisane są zarówno poprzez wykonywane krzywej siła-przemieszczenie (ang. FDC) oraz bardziej specjalistycznych metod jak pomiar metodą ‘nanowieź’, w której przygotowywana jest próbka składająca się z płaskiej powierzchni z wystającymi elementami o kształcie walców, a następnie te walce obciążane są siłą poprzeczną poprzez końcówkę sondy pomiarowej [75]. Natomiast pomiary siły tarcia czy odporności na zużycie przeprowadzane są przy pomocy pętli tarcia. Na podstawie pomiaru tarcia możliwe jest także uzyskanie lepkości cienkiej warstwy powierzchniowej. Opisane w tym rozdziale są także takie kluczowe aspekty analizy danych jak:

- różne metody kalibracji sondy pomiarowej w mikroskopie sił atomowych w osi pionowej: metoda Sadera, metoda sprężyny referencyjnej czy metoda geometryczna [76-81],
- różne metody kalibracji sondy pomiarowej w mikroskopie sił atomowych w osi poziomej: metodą klinu (ang. wedge) czy z wykorzystaniem specjalistycznych kalibratorów [82-87],
- różne modele kontaktu wykorzystywane w mikroskali oraz ich mocne i słabsze strony, modele rozważane: Hertza, JKR'a, Maugisa, DMT [88-90].

Oprócz badań przeprowadzanych na mikroskopie sił atomowych rozdział ten opisuje także inne metody pomiaru własności mechanicznych powierzchni takie jak nanoindentacja, zarówno w najczęściej wykorzystywanej wersji modelu Olivera i Pharra [28] oraz mniej znanych modeli. Metody te przedstawiane są wraz z ich przykładowymi zastosowaniami. Podsumowaniem rozdziału jest skrótny poradnik sugerujący jaką metodę najlepiej wybrać w celu wyznaczenia konkretnej właściwości powierzchni (Tabela 5).

	<b>Metoda</b>	
<b>Materiały</b>	<b>Wyznaczanie twardości</b>	<b>Wyznaczanie modułu Younga</b>
<b>Materiały twarde (np. ceramiczne)</b>	Mikro- i nano- indentacja za pomocą diamentowego wgłębnika, np. wgłębnika typu Berkovitch	Mikro- i nano- indentacja za pomocą diamentowego wgłębnika typu Berkovitch Metoda „nanowież”
<b>Metale</b>	Mikro- i nano- indentacja za pomocą diamentowego lub szafirowego wgłębnika	Mikro- i nano- indentacja za pomocą diamentowego lub szafirowego wgłębnika,  Metoda „nanowież”
<b>Materiały miękkie (np. polimery)</b>	Pomiary krzywej siła-przemieszczenie (FDC) za pomocą AFM,  Nanoindentacja	Pomiary krzywej siła-przemieszczenie (FDC) za pomocą AFM,  Metoda „nanowieże”
<b>Cienkie powłoki ceramiczne lub metaliczne</b>	Mikro- i nano- indentacja za pomocą diamentowego wgłębnika, np. wgłębnika typu Berkovitch	Mikro- i nano- indentacja za pomocą diamentowego wgłębnika, np. wgłębnika typu Berkovitch
<b>Cienkie powłoki polimerów</b>	Pomiary krzywej siła-przemieszczenie (FDC) za pomocą AFM,	Pomiary krzywej siła-przemieszczenie (FDC) za pomocą AFM,
	<b>Wyznaczanie siły tarcia</b>	<b>Wyznaczanie siły adhezji</b>
<b>Wszystkie materiały</b>	Pomiary pętli tarcia za pomocą AFM	Pomiary krzywej siła-przemieszczenie (FDC) za pomocą AFM,
	<b>Wyznaczanie lepkości</b>	<b>Wyznaczanie własności lepko-sprężystych</b>
<b>Materiały lepko-sprężyste (jednolite oraz cienkie powłoki)</b>	Pomiary pętli tarcia za pomocą AFM	Dynamiczna analiza mechaniczna poprzez nanoindentację

Tabela 5 Przegląd metod, jakie należy zastosować w celu poznania właściwości powierzchni w mikro i nano skali

## **2.7. Badania warstwy grafenowej naniesionej na metalowych powierzchniach**

Praca [P5] była związana z realizacją projektu Graphtrib. We wcześniejszych etapach w tym projekcie określone zostały podłożą, na które można nakładać warstwy grafenowe do zastosowań w kołach zębatych i łożyskach ślizgowych [91] oraz wpływ warunków środowiskowych na powstałe warstwy [92]. Etap przedstawiony w publikacji [P5] dotyczył własności trybologicznych stalowych próbek z powierzchnią grafenową, z miedzą jako materiałem pośrednim, koniecznym ze względu na przyczepność grafenu [91]. Wpływ procesu nakładania powłoki na geometrię próbki przedstawiony został w pracy [93].

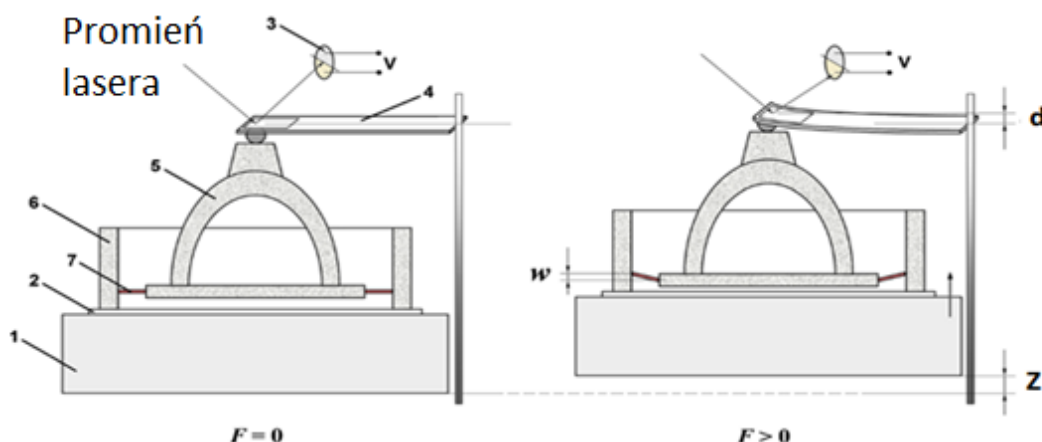
Badania tarcia próbek stal-miedź-grafen przeprowadzone zostały na mikroskopie sił atomowych z sondą pomiarową z doczepioną kulką stalową mającą za zadanie odwzorowanie kontaktu pomiędzy zębami kół zębatych lub łożysk ślizgowych. Sonda pomiarowa z końcówką będącą kulką stalową została wykonana zgodnie z opisem w rozdziale 2.2 oraz publikacji [P1]. Badania przy pomocy pętli tarcia pozwoliły zaobserwować niedokładność nałożonej warstwy miedzi na stal. Można było ją zaobserwować poprzez dwa rozdzielne poziomy tarcia pomiędzy powierzchnią próbki a stalą. Poziomy te zostały ujednolicone po nałożeniu warstwy grafenowej. Równolegle przeprowadzane zostały też pomiary twardości i modułu Younga. Przeprowadzane były one przy sile nacisku rzędu 1,5 mN, co oznaczało głębokość zagłębienia około 200 nm. Przy takiej sile nacisku niezauważalny jest wpływ grafenu na własności sprężyste próbki.

## **2.8. Badania strzemiączka ucha ludzkiego**

W artykule [P6] przedstawiam opcję wykorzystania mikroskopii sił atomowych w biomedycynie. Otoskleroza, czyli choroba kosteczek ucha środkowego, może doprowadzać do utraty słuchu w jednym lub obu uszach. Problem ten dotyczy 1% całej populacji. W celu przywrócenia słuchu stosuje się protezę ‘tłoczkową’, jednak słuch nie zostaje przywrócony w całym paśmie częstotliwości [94-97] i pogarsza się z biegiem czasu [98-99]. W celu opracowania nowej protezy, pozwalającej na przywrócenie słuchu w większym paśmie częstotliwości i w bardziej trwałym sposobie, potrzebna jest dokładna znajomość własności mechanicznych ucha środkowego. Kość ucha środkowego, inaczej strzemiączko, wprowadzana jest w drgania przez błonę bębenkową. Strzemiączko umieszczone w okienku przedsionka przenosi drgania do ucha wewnętrznego, które razem ze strzemiączkiem działa

na zasadzie sprężyny płaskiej. W celu odtworzenia tego mechanizmu niezbędne jest poznanie jego wymiarów, charakterystyki oraz własności mechanicznych. Wykonane wcześniej pomiary na świecie modułu sprężystości więzadłka pierścieniowego, które mocuje strzemiączko do okna przedsionka cechowały się bardzo dużym rozrzutem wyników, od 0,01 MPa do 5,5 MPa [100-102].

W celu poznania charakterystyki oraz własności strzemiączka wykorzystałem mikroskopię sił atomowych, a dokładniej modyfikację jednej z podstawowych metod pomiarowych, jaką jest wykorzystanie krzywej siła-przemieszczenie [46]. Końcówka sondy pomiarowej, w tym przypadku kulka, została umieszczona na wyciętej i przygotowanej uprzednio kości strzemiączka. Powstał w ten sposób układ dwóch umieszczonych szeregowo sprężyn: belki sondy pomiarowej oraz chrząstki okna przedsionka (Rys.11). Analizując układ ten w sposób analogiczny do procesu kalibracji belki pomiarowej ze sprężyną wzorcową [103], ale traktując tę belkę jako sprężynę o znanych parametrach, natomiast próbce pod nią jako badaną, wyznaczyłem charakterystykę tej sprężyny.



Rysunek 11 Schemat układu podczas pomiaru własności strzemiączka ucha-środkowego, 1- piezoelement sterujący przemieszczeniem, 2- podstawa próbki, 3-fotodioda, 4-belka sondy pomiarowej, 5- strzemiączko, 6- okienko przedsionka, 7- więzadło pierścieniowe, w- ugięcie więzadła podczas badania, F- siła pionowa nacisku sondy pomiarowej na próbce, d- ugięcie belki sondy pomiarowej, Z- przesunięcie próbki podczas badania, V- fotodioda odpowiadająca za pomiar ugięcia belki sondy.

Analizując uzyskane wyniki wyznaczyłem sztywność tej sprężyny, która w badanym zakresie ruchu miała liniowy charakter. Kolejnym parametrem potrzebnym do opracowania protezy było wyznaczenie sprężystości materiału. W celu wyznaczenia tej własności potrzebne było założenie o jednorodności więzadłka pierścieniowego stanowiącego mocowanie strzemiączka, a następnie przy użyciu modelu Kirchhoff-Love'a [104] można było wyznaczyć własności mechaniczne materiału, jaki powinna odtwarzać proteza. Po

zastosowaniu tego modelu i przeprowadzeniu niezbędnych przekształceń oraz i przyjęciu warunków brzegowych dochodzimy do zależności na moduł sprężystości [P6]:

$$E = C \cdot \frac{\frac{F}{Z} \cdot k_c}{k_c + \frac{F}{Z}} \quad (4)$$

gdzie:

$k_c$ - sztywność sondy pomiarowej

$$C = \frac{3 \cdot (1 - \nu^2)}{4\pi h^3} \cdot \left[ \frac{(a^2 - b^2) \cdot (3 + \nu)}{1 + \nu} + \frac{4a^2 b^2 (1 + \nu)}{(a^2 - b^2) \cdot (1 - \nu)} \left( \ln \frac{a}{b} \right)^2 \right] \quad (5)$$

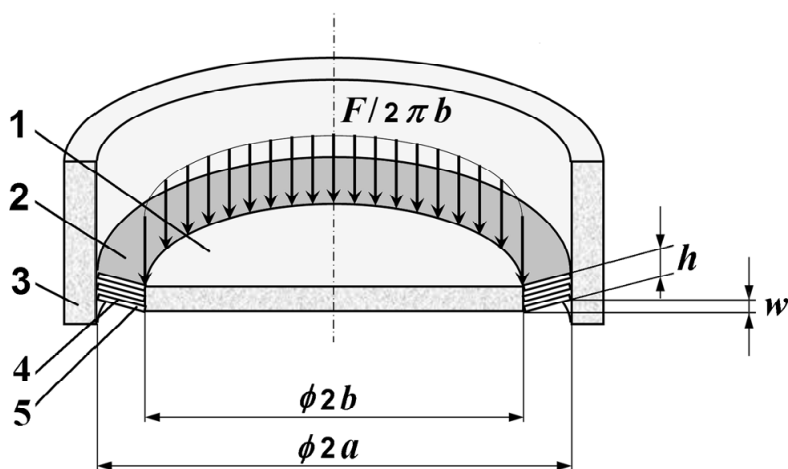
gdzie:

$\nu$  – liczba Poissona więzadłka pierścieniowego

$F$  – siła pionowa nacisku sondy pomiarowej na próbkę (Rys. 11)

$Z$  – przesunięcie próbki podczas badania (Rys. 11)

$a, b, h$  – wymiary elementu (Rys. 12)



Rysunek 12 Uproszczony schemat mocowania strzemiączka w okienku przedsięwzięcia opracowany w celu obliczenia podatności materiału więzadłka pierścieniowego, 1- strzemiączko, 2-więzadło pierścieniowe, 3- okienko przedsięwzięcia, 4- pojedyncze włókno więzadłka, 5-amorficzna substancja łącząca więzadła, a,b,h-wymiary modelowanego elementu, F-siła nacisku wywieranego na element, w-ugięcie więzadła pierścieniowego

Uprzednio stosowane metody badawcze w tym obszarze uwzględniały między innymi: wykorzystanie maszyny wytrzymałościowej. Jednak w tym przypadku membrany te były przemieszczone o około 0,2 mm czyli 2000 razy więcej niż podczas naturalnej pracy [100]. W innym przypadku wykorzystano czujnik siły LVS-5GA, a przemieszczenie sprawdzono przy użyciu interferometru dopplerowskiego. Metoda ta cechowała się trzema ograniczeniami: interferometr wymagał powierzchni odbijającej, więc cała próbka musiała zostać pokryta

powłoką refleksyjną; nacisk był nakładany od dolnej strony strzemiączka czyli odwrotnie w stosunku do tego jak pracuje ona w organizmie żywym; niska rozdzielczość zastosowanego miernika siły. Rozdzielczość ta wynosiła  $10 \mu\text{N}$ , co uwzględniając wyniki z moich badań przekłada się na około  $85 \text{ nm}$  ugięcia strzemiączka, które stanowi 85% całego zakresu fizjologicznego przemieszczenia. Ze względu na niewystarczającą rozdzielczość badania te były przeprowadzane w zakresie do  $50 \text{ mN}$  z końcowym uzyskiwanym przemieszczeniem  $10 \mu\text{m}$ , czyli 100 razy większym niż podczas naturalnej pracy [102].

Wykorzystanie do tego zadania mikroskopu sił atomowych umożliwiło dokładny i wielokrotny powtarzalny pomiar, zarówno kilku próbek jak i wielokrotny test jednej próbki w zakresie fizjologicznego ruchu. Zmniejszyło to niepewność dotyczącą wyznaczenia charakterystyki oraz własności strzemiączka, a także pozwoliło zasugerować odpowiedni materiał dla przyszłej protezy. Kluczową zmianą było jednak przeprowadzenie po raz pierwszy na świecie badań w fizjologicznym zakresie ruchu strzemiączka.

### **3. Przyszłe prace**

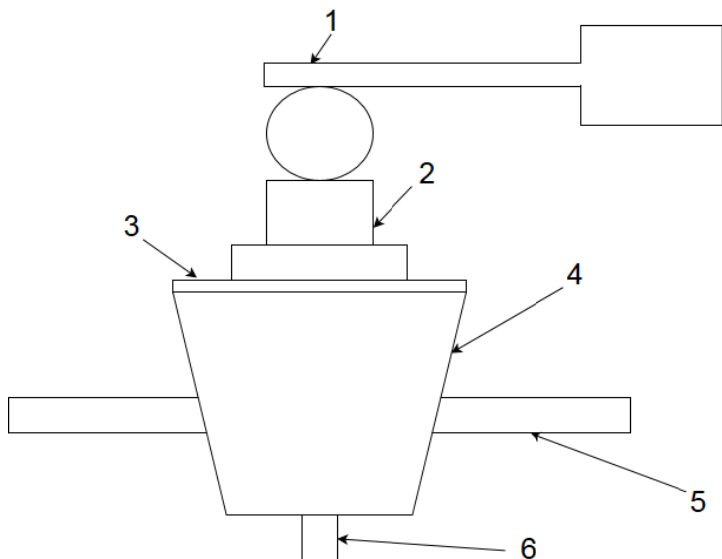
Moje dalsze plany badawcze uwzględniają realizację kilku projektów. Najważniejsze z nich to:

- badania nad powłokami ochronnymi dla krzemu do zastosowań w urządzeniach MEMS; wstępnie przeprowadzone badania z wykorzystaniem siarczku molibdenu, ołowiu, węgla diamentopodobnego i indu dały obiecujące wyniki,
- zaadaptowanie mikroskopii sił atomowych do badań charakterystyki rozruchowej silnika budowanego w technologii MEMS.

Zamierzam także kontynuować prace nad opracowywaniem protezy strzemiączka ucha ludzkiego. W przypadku tego projektu przeprowadziłem już dalsze badania oraz napisałem publikację, która jest obecnie recenzowana. Jej szczegółowy opis przedstawiono poniżej.

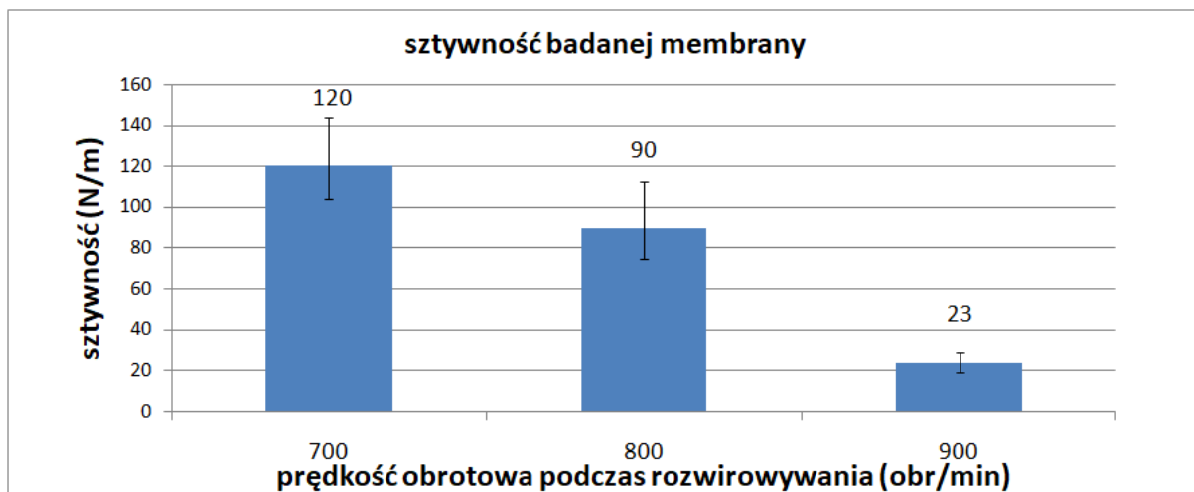
#### **Weryfikacja parametrów protezy ucha środkowego oraz jej metody wytwarzania**

Publikacja ta będzie stanowić kontynuację badań przedstawionych w pracy [P6]. Dalszy etap prac w tym obszarze dotyczył rozwoju prototypu protezy ucha środkowego. Proteza komorowa została wykonana z materiałów o właściwościach odpowiadających wynikom badań przeprowadzonych podczas doświadczeń na strzemiączku ucha [P6]. Membrana z poli(dimetylosilosanu) (PDMSu) została wykonana metodą rozwierowania (ang. spin-coating) i zaczepiona do komory wykonanej z poli(akrylonitryl-co-butadien-co-styrenu) (ABSu). Membrana ta stanowi kluczowy element sprężysty, którego zadaniem jest imitowanie zamocowania więzadłka pierścieniowego i odtwarzanie ruchu strzemiączka, dlatego też niezbędne jest odtworzenie takiej samej sztywności jak we wcześniej przebadanym strzemiączku. Z tego względu wykonanych zostało kilka membran o różnej grubości, poprzez nastawianie różnej prędkości obrotowej w czasie rozwierowania polimeru. Grubość tych membran została zmierzona, a po zmontowaniu prototypu protezy i umieszczeniu go w specjalnie przygotowanej podstawie (Rys. 13) przeprowadzone zostały pomiary jej sztywności.



Rysunek 13 Schemat badanej protezy, 1- sonda pomiarowa z kulką, 2- sztywna płytka imitująca górny fragment strzemiączka, 3-mebrana z polimeru PDMS, 4- komora protezy, 5– mocowanie próbki podczas badań, 6- rurka wychodzącą z protezy, łącząca protezę z uchem wewnętrznym

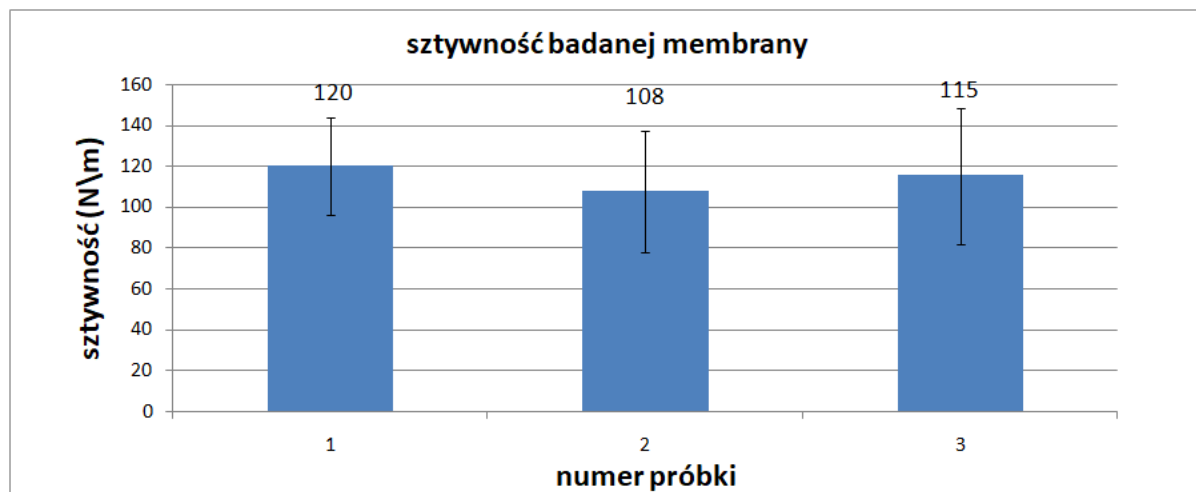
Pomiary te potwierdziły, że przy zmianie prędkości rozwijanego grubość membrany zostaje zmieniona, co z kolei przełoży się na sztywność uzyskaną w końcowej protezie. Rys. 14 przedstawia wartości sztywności uzyskane dla różnych prędkości rozwijanego polimeru.



Rysunek 14 Wyniki pomiarów sztywności membran wytworzonych metodą wirową, przy zastosowaniu różnych prędkości rozwijywania

Badania te pozwoliły wybrać prędkość obrotową, która pozwoli na uzyskanie takiej samej sztywności membrany, jak w naturalnym strzemiączku. Przy danych materiałach jest to 700 obrotów na minutę. Następnie przeprowadzone zostały testy powtarzalności procesu (Rys 15), które wykazały, że proces cechuje się rozrzutem wyników zbliżony do rozrzutu uzyskanego podczas badania strzemiączka. Mój udział w pracy nad tą publikacją polegał na:

przygotowaniu i przeprowadzeniu pomiarów, analizie statystycznej, konsultacji projektu oraz przygotowaniu dużej części tekstu artykułu.



Rysunek 15 Wyniki pomiaru sztywności membran dla kilku próbek wytworzonych metodą wirową przy tej samej prędkości (700 obr/min) dla zweryfikowania powtarzalności procesu

#### **4. Podsumowanie**

W publikacjach [P1-P7] przedstawiłem kilka różnych dróg rozwoju mikroskopii sił atomowych do zastosowań w różnych dziedzinach nauki. Publikacja [P1] przedstawiła koncepcje nowych sond badawczych wraz z opisem metody ich wytwarzania oraz przykładowymi zastosowaniami. Sondy te są tańsze w wytwarzaniu od komercyjnych sond i umożliwiają prowadzanie badań par materiałów dotychczas niemożliwych za pomocą mikroskopii sił atomowych. W publikacji [P2] przedstawiłem sposób na walidację symulacyjnego modelu tarcia pomiędzy dwoma strukturami z wykorzystaniem mikroskopii sił atomowych. Ta metoda walidacji pozwala na sprawdzenie różnorodnych materiałów oraz bardziej złożonych powierzchni niż dotychczas stosowane ostre igły współpracujące z płaską powierzchnią. Ta sama publikacja opisuje model symulacyjny, który można zastosować dla różnorodnych powierzchni stykających się ze sobą w urządzeniach MEMS, a jako dane wejściowe wykorzystuje parametry możliwe do wyznaczenia przy pomocy mikroskopii sił atomowych, między innymi topografię powierzchni. Opisałem także nowe metody umożliwiające pomiar energii ścinania oraz zrywania na potrzeby symulacji naprężeń podczas wytwarzania struktur metodą litografii nanodrukowej [P7]. Metoda ta umożliwiła między innymi przetestowanie różnych powłok antyadhezyjnych oraz dobór parametrów procesu zrywania maski w celu zminimalizowania defektów wytwarzanej struktury. W publikacjach [P3, P5] opisałem sposób wykorzystania nowych sond badawczych do dobrania pary materiałów, jaka była oczekiwana w docelowym mechanizmie, oraz dla zwiększenia sił pomiędzy końcówką sondy a próbką. Przedstawiłem także przekrojową analizę metod dobieranych do poszczególnych zastosowań [P4]. W rozdziale tym opisuje też różne metody kalibracji w mikroskopii sił atomowych, różne metody badawcze oraz ich słabe i mocne strony, a także specjalistyczne metody badawcze, wykorzystujące mikroskop sił atomowych. W pracy [P6] przedstawiłem modyfikację metody krzywej zbliżania w celu poznania kluczowych parametrów, takich jak sztywność oraz moduł Younga próbki biologicznej, jaką jest strzemiączko ucha ludzkiego. Poznanie tych parametrów umożliwiło dobranie wymiarów oraz materiałów do opracowanej protezy komorowej, która może zapewnić przywrócenie słuchu w większym zakresie częstotliwości niż dotychczasowo stosowane metody. Protezy zostały przeze mnie przebadane pod kątem sztywności, dzięki czemu można było dobrać odpowiednie parametry wytwarzania w celu osiągnięcia danej sztywności.

Rozwój mikroskopii sił atomowych przedstawiony w tej pracy wspomógł projektowanie urządzeń takich jak np. proteza komorowa czy przełączniki MEMS. Nowe techniki badawcze

wspierały proces wytwarzania metodą litografii nanodrukowej. Natomiast opracowanie modelu symulacyjnego tarcia oraz nowych sond badawczych wraz z proponowanymi dla nich metodami badawczymi wspomoże przyszłe projektowanie mikrosystemów poprzez zapewnienie lepszej znajomości parametrów, takich jak współczynniki tarcia, siła adhezji czy sztywność fragmentu urządzenia. Prace w wyniku których powstały te publikacje pozwoliły zarówno na rozwój dziedzin do których się one zaliczają, ale także na mój rozwój osobisty oraz rozwój mikroskopii sił atomowych jako bardzo wszechstronnego narzędzia badawczego.

Prace przedstawione w publikacjach [P1-P7] wspomogły projektowanie urządzeń w takich zakresach jak:

- wprowadzenie nowego modelu symulacji tarcia oraz sposób walidacji takich modeli,
- wprowadzenie nowych sond pomiarowych do mikroskopii sił atomowych,
- wspomaganie wytwarzania metodą litografii nanodrukowej,
- Wspomaganie opracowywania protezy strzemiączka ucha wewnętrznego.

Praca ta była współfinansowana przez projekt NANOViSC 2014/15/N/ST8/03664 przyznany w konkursie Preludium przez Narodowe Centrum Nauki.

## 5. Bibliografia

1. Cabibbo M., Ricci, P., True Hardness Evaluation of Bulk Metallic Materials in the Presence of Pile Up: Analytical and Enhanced Lobes Method Approaches, Springer 2013
2. Cabibbo M., Ricci, P., Cecchini, R., Rymuza Z., An international round-robin calibration protocol for nanoindentation measurements, Pergramon-Elsevier Science Ltd 2012
3. Nagy R. M., Kuekemezey I. Istvan, Kassavetis S., Berke P., Delpancke-Ogletree M. P., Logothetidis S., The Effect of Roughness on Nanoindentation Results, Amer Scientific Publishers 2013
4. Beake B.D., Harris A.J., Liskiewicz T.W., Review of recent progress in nanoscratch testing, Maney Publishing 1751-5831 2013
5. Karagiannidis P. G., Kassavetis S. Pitsalidis, Logothetidis S., Thermal annealing effect on the nanomechanical properties and structure of P3HT: PCBM thin films, Elsevier Science Sa 2011
6. Maedar R., Widmer R., Groening P., Correlating scanning tunneling spectroscopy with the electrical resistivity of Al-based quasicrystals and approximants, Amer Physical Soc, 2013

7. Maedar R., Widmer R., Bauer R., Revealing the atomic surface structure of the (100) Y-Al-Ni-Co approximant by low-energy electron diffraction and scanning tunneling microscopy, Amer Physical Soc, 2010
8. Maedar R., Widmer R., Groening P., A comparative scanning tunneling spectroscopy investigation of the (12110)-surface of decagonal Al-Ni-Co and the (100)-surface of its approximant Y-Al-Ni-Co, Iop Publishing Ltd 2010
9. Polishchuk S., Boulet P., Mezin A., Residual stress in as-deposited Al-Cu-Fe-B quasicrystalline thin films, Cambridge Univ Press 2012
10. Stelmachowski J., Rymuza Z., Eisenmenger-Sittner C., Surface properties of AlCuFeB coatings with focus on resolving tribological issues of nanoimprint lithography, RSC Advances, Tom 4, 2014, str. 29474-29478
11. Hoang T.V., Wu L., Paquay S., Obreja C., Voicu R., Muller R., Golinval J.C., Noels L., A probabilistic model for predicting the uncertainties of the humid stiction phenomenon on hard materials, Journal of Computational and Applied Mathematics 289 · February 2015
12. Lucas V., Golinval J.C., Paquay S., Nguyen V.D., Noels L., Wu L., A stochastic computational multiscale approach; Application to MEMS resonators, Computer Methods in Applied Mechanics and Engineering, str. 141-167, 2015
13. **Michałowski M.**, Rymuza Z., Voicu R., Obreja C., Baracu A., Müller R., Nanotribological Behaviour of Polysilicon Films Applied in MEMS Devices, Proceedings of the SAIT Tribology Conference Tribology 2015-11th International Tribology Conference, 10 – 12.03.2015, University of Pretoria Conference Centre, Pretoria, South Africa ISBN 978-0-60543-4 Tribology 2015
14. Voicu R., Obreja C., Baracu A., Avram A., Muller R., Rochet J., Pustan M., MEMS Polysilicon Cantilevers for Vibrational Applications, Conf. 26th Micromechanics and Microsystems Europe Workshop-MME20-23.09.2015, Toledo, Spain, 2015
15. Voicu R., Baracu A., Gavrila R., Obreja C., Danila M., Bita B., Müller R., Material layers investigations for MEMS vibration sensors and biostructures applications, Conf. CSSD-UDJG 4-5.06.2015, Galați, 2015
16. Baracu A., Voicu R., Obreja C., Design and Fabrication of Polysilicon Bridges Used for MEMS Applications, Conf. Micro and Nano Engineering-MNE, 21-24.09.2015, The Hague, The Netherlands. 2015
17. Voicu R., **Michałowski M.**, Rymuza Z., Gavrila R., Obreja C., Müller R., Baracu A. "Design and Analysis of Polysilicon Thin Layers and MEMS Vibrating Structures", Proc. DTIP 2014 - SYMPOSIUM on Design, Test, Integration & Packaging of MEMS/MOEMS, Cannes Côte d'Azur, France, 1-4.04.2014, str. 129-133, 2014
18. Hoang Truong V., Wu L., Arnst M., Golinval J.C., Muller R., Voicu R., Paquay S., Noels L., "A probabilistic model of the adhesive contact forces between rough surfaces in the MEMS stiction context", Book of abstracts of the 6th International Conference on Advanced Computational Methods in Engineering 23–28.06.2014, ACOMEN 2014
19. Lucas V., Wu L., Arnst M., Golinval J.C., Paquay S., Nguyen V.D., Noels L., „Prediction of macroscopic mechanical properties of a polycrystalline microbeam subjected to material uncertainties”, Proc. EURODYN 2014
20. Voicu R., Rymuza Z., **Michałowski M.**, Obreja C., Gavrila R., Müller R., Investigations of surface properties of SiO<sub>2</sub> and Si<sub>3</sub>N<sub>4</sub> thin layers, used for MEMS vibrating structures applications, Proc. Cas 2013, Tom 1, str. 111-114, 2013.

21. Pustan M., Dutescu C., Birleanu C., Rymuza Z., Nanomechanical studies and materials characterization of metal/polymer bilayer MEMS cantilevers, International Journal of Materials Research, Tom 104, str. 408-414, Nr 4, 2013
22. Abetkovskaya S., Chizhik S., Nazaruk P., Stelmachowski J., Rymuza Z., Complex approach to investigate mechanical and tribological characteristics of microcontacting objects for MEMS, Tribology - Materials, Surfaces & Interfaces, Tom 7, str. 83-86, Nr 2, 2013
23. **Michałowski M.**, Nolbert D., Ocupa L., Rymuza Z., Surface topography and adhesive/frictional behavior of sliding surfaces in micro/nanocontacts, Proceedings Conference BALTRIB'2013 / Stulginskis Aleksandras, University, Kaunas /Lithuania, str. 88-92,2013
24. **Michałowski M.**, Rymuza Z., Voicu R., Obreja C., Baracu A., Muller R., AFM studies of stiction properties of ultrathin polysilicon films, Advances in Intelligent Systems and Computing, Springer, str. 347-353, 2016
25. **Michałowski M.**, Rymuza Z., Voicu R., Obreja C., Baracu A., Muller R., Control of tribological properties of ultrathin polysilicon films, Symposium on Design, Test, Integration and Packaging of MEMS/MOEMS, Budapest 2016
26. **Michałowski M.**, Rymuza Z., Voicu R., Obreja C., Baracu A., Muller R., Adhesive and frictional properties of ultrathin polysilicon films, Proceedings of Turkeytrib 7 – 9.10.2015 - 1st international conference on tribology, 2015
27. Bhushan B. Nanotribology and Nanomechanics: An Introduction, Springer-Verlag Berlin Heidelberg, 2018
28. Olesiak S., Oyen M., Ferguson V., Viscous-elastic-plastic behavior of bone using Berkovich nanoindentation, Mechanics of Time-Dependent Materials, Tom 14, str. 111-124, 2010
29. Brinson H. F., Brinson L. C., Polymer Engineering Science and Viscoelasticity – An introduction, Springer, 2008
30. Abetkovskaya S. O., Chizhik S. A., Pogoskaya I.V., Rymuza Z., Jarząbek D., **Michałowski M.**, and Linke J., Determining the Young modulus of nanosize thickness coatings for MEMS from the results of static force spectroscopy, Bulletin of the Russian Academy of Sciences: Physics, Springer, tom 76, str. 1122-1124, nr 9, 2012
31. Binnig G., Quate C. F., Gerber C., *Atomic Force Microscope, Physical Review Letters*. 56: str. 930–933, 1986
32. Yongda Yan, Yanquan Geng, Zhenjiang Hu, Recent advances in AFM tip-based nanomechanical machining, In International Journal of Machine Tools and Manufacture, tom 99, str. 1-18, 2015
33. Kolchuzhin V., Sheremet E., Bhattacharya K., Rodriguez R., In, Mechanical properties and applications of custom-built gold AFM cantilevers, In Mechatronics, tom 40, str. 281-286, 2016
34. Tseytlin Y. M., Chapter 3 - AFM with Higher Mode Oscillations and Higher Sensitivity, In Advanced Mechanical Models of DNA Elasticity, Academic Press, Boston, str. 101-155, 2016
35. Geng Y., Brousseau E., Zhao X., Gensheimer M., Bowen C., AFM tip-based nanomachining with increased cutting speed at the tool-workpiece interface, In Precision Engineering, tom 51, str. 536-544, 2018

36. Jianxun Xu, Yoshitaka Shingaya, Yuliang Zhao, Tomonobu Nakayama, In situ, controlled and reproducible attachment of carbon nanotubes onto conductive AFM tips, In Applied Surface Science, tom 335, str. 11-16, 2015
37. Stetter F., Seok-Hee Hyun, Brander S., Urban J., Thompson D., Hugel T., Nanomechanical characterization of lipid bilayers with AFM-based methods, In Polymer, tom 102, str. 326-332, 2016
38. Jelita Rydel J., Vegter R.H., Rivera-Díaz-del-Castillo P.E.J., Tribocorrosion of bearing steels: A new AFM method to study the material–tribofilm correlation, In Tribology International, tom 98, str. 74-81, 2016
39. Furustig J., Dobryden I., Almqvist A., Almqvist N., Larsson R., The measurement of wear using AFM and wear interpretation using a contact mechanics coupled wear model, In Wear, tom 350–351, str. 74-81, 2016
40. Xiaobin Yue, Dajiang Lei, Hailong Cui, Xiaofeng Zhang, Min Xu, Lingbao Kong, An integrated method for measurement of diamond tools based on AFM, In Precision Engineering, tom 50, str. 132-141, 2017
41. Smolyakov G., Cauquil M., Severac C., Lachaize V., Guilbeau-Frugier C., Sénard J., Galés C., Dague E., Biophysical properties of cardiomyocyte surface explored by multiparametric AFM, In Journal of Structural Biology, tom 198, str. 28-37, 2017
42. Oyarzún D., Linarez Pérez O., Teijelo M., Zúñiga C., Jeraldo E., Geraldo D., Arratia-Perez R., Atomic force microscopy (AFM) and 3D confocal microscopy as alternative techniques for the morphological characterization of anodic TiO<sub>2</sub> nanoporous layers, In Materials Letters, tom 165, str. 67-70, 2016
43. Uchihashi T., Watanabe H., Fukuda S., Shibata M., Ando T., Functional extension of high-speed AFM for wider biological applications, In Ultramicroscopy, tom 160, str. 182-196, 2016
44. Roos W., AFM nanoindentation of protein shells, expanding the approach beyond viruses, In Seminars in Cell & Developmental Biology, 2017
45. Efremov Yu., Bagrov D., Kirpichnikov M., Shaitan K., Application of the Johnson–Kendall–Roberts model in AFM-based mechanical measurements on cells and gel., In Colloids and Surfaces B: Biointerfaces, tom 134, str. 131-139, 2015
46. Cappella B., Dietler G., Force-distance curves by atomic force microscopy, Surface Science Reports Tom 34, str. 1-3, 5-104, 1999
47. Korayem M. H., Kavousi A., Ebrahimi N., Dynamic Analysis of Tapping-Mode AFM Considering Capillary Force Interactions, Scientia Iranica, tom 18, Num 1, str. 121-129, 2011
48. Korayem M. H., Zakeri M., Dynamic Modeling of Manipulation of Micro/Nano Particles on Rough Surfaces, Applied Surface Science, tom 257, Num 15, str. 6503-6513, 2011
49. Tanner D. M., Miller W. M., Peterson K. A., Dugger M. T., Eaton W. P., Irwin L. W., Sentf D. C. Smith N. F., Tangyunyong P. Miller S. L., Frequency dependence of the lifetime of a surface micromachined microengine driving a load, Microelectronics Reliability, tom 39, num. 3, str. 401-414, 1999
50. Yapu Z., Stiction and anti-stiction in MEMS and NEMS, Acta Mechanica Sinica, tom 19, num. 1, str. 1-10, 2003
51. Wolf I., Microsystems Technology: Fabrication, Test & Reliability, red. Boussey J., ISTE Publishing Company, 2003

52. Alsem D. H., Hulst R., Stach E. A., Dugger M. T., Hosson J. Th. M., Ritchie R. O., Wear mechanisms and friction parameters for sliding wear of micron-scale polysilicon sidewalls, Sensors and Actuators A: Physical, tom 163, nr 1, str. 373-382, 2010
53. Kamat S. V., Mechanical properties in MEMS, DRDO Science Spectrum, str. 203-211, 2009
54. Malloy M., Litt L. C., Technology review and assessment of nanoimprint lithography for semiconductor and patterned media manufacturing, Journal of Micro/Nanolithography, MEMS, and MOEMS, Tom 10, 2011
55. Dziekoński C., Dera W., Jarząbek D.M., Method for lateral force calibration in atomic force microscope using MEMS microforce sensor, Ultramicroscopy, Tom 182, str.1-9, 2017
56. McClelland G.M., Friction at weakly interacting interfaces. w: Adhesion and Friction, red. Grunze M., KreuzerH. J., Springer, Berlin, Heidelberg,str. 1–16, 1989
57. Azoroff L., Introduction to Solids, New York, Mc Graw-hill, 1960
58. Chou S. Y., Krauss P., and Renstrom P., J. Vac. Sci. Technol. B 14, 4129, 2012
59. DiBiase T., Ahamdian M., Malik I., Comprehensive defect analysis methodology for nano imprint lithography, Microelectronic Engineering, Tom 4, Nr 5–8, str. 989-993, 2007
60. Bailey T., Choi B., Colburn M., Meissl M., Shaya S., Ekerdt J. G., Sreenivaan S. V., Wilson C. G., Step and flash imprint lithography: Template surface treatment and defect analysis, Journal of Vacuum Science & Technology B 18, 3572, 2000
61. Jung G., Li Y., Wu W., Chen Y., Olynick D. L., Wang S-Y., Tong W. M., Williams R. S., Vapor-Phase Self-Assembled Monolayer for Improved Mold Release in Nanoimprint Lithography, Langmuir 21, 1158, 2005.
62. Nishino T., Fujikawa N., Kawata H., Hirai Y., Evaluation of Demolding Energy for Various Demolding Modes in Embossing Process, Japanese Journal of Applied Physics, Tom 52, Nr 6S, 2013
63. Kitagawa T., Nakamura N., Kawata H., Hirai Y., A novel template-release method for low-defect nanoimprint lithography, Microelectronic Engineering, Tom 123, str. 65-72, 2014
64. Pustan M., Golinalval J., Rochus V., Geometrical effects on the dynamic behaviour of MEMS structures, European Conference on Computational Mechanics ECCM, Paris, 2010
65. Pustan M., Müller R., Golinalval J., Nanomechanical and nanotribological characterization of microelectromechanical system, Journal of Optoelectronics and Advanced Materials Tom 14, Nr 3-4, str. 401 – 412, 2012
66. Etxabide A., Caba K., Guerrero P., A novel approach to manufacture porous biocomposites using extrusion and injection moulding, In European Polymer Journal, Tom 82, str. 324-333, 2016
67. Dumont V., Mansur H., Mansur A., Carvalho S. M., Capanema N. S. V., Barrioni B., R., Glycol chitosan/nanohydroxyapatite biocomposites for potential bone tissue engineering and regenerative medicine, In International Journal of Biological Macromolecules, Tom 93, Part B, str. 1465-1478, 2016
68. Alves N., Silva G., Weber D., Luchese C. Wilhelm E. A., Fajardo A. R., Chitosan/poly(vinyl alcohol)/bovine bone powder biocomposites: A potential biomaterial for the treatment of atopic dermatitis-like skin lesions, In Carbohydrate Polymers, Tom 148, str. 115-124, 2016

69. Bhatti H., Hayat J., Iqbal M., Noreen S., Nawaz S., Biocomposite application for the phosphate ions removal in aqueous medium, In Journal of Materials Research and Technology, 2017
70. Htun Z. L., Ahmad N., Thant A. A., Noor A-F. M., Characterization of CaO-ZrO<sub>2</sub> Reinforced Hap Biocomposite for Strength and Toughness Improvement, In Procedia Chemistry, Tom 19, str. 510-516, 2016
71. Harmata A., Guelcher S., 3 - Effects of surface modification on polymeric biocomposites for orthopedic applications, In Nanocomposites for Musculoskeletal Tissue Regeneration, red. Huinan Liu, Woodhead Publishing, Oxford, str. 67-91, 2016
72. Kang M., Park Y., Kim B., Seo Y. H., Micro- and nanoscale surface texturing effects on surface friction, Applied Surface Science, Tom 345, str. 344-348, 2015
73. Kim Y., Hwang W., Wettability modified aluminum surface for a potential antifungal surface, Materials Letters, Tom 161, str. 234-239, 2015
74. Rahimi M., Afshari A., Fojan P., Gurevich L., The effect of surface modification on initial ice formation on aluminum surfaces, In Applied Surface Science, Tom 355, str. 327-333, 2015
75. Jarzabek D., Kaufmann A., Schift H., Rymuza Z., Jung T., Elastic modulus and fracture strength evaluation on the nanoscale by scanning force microscope experiments, Nanotechnology 25, 2014
76. Hutter J., Bechhoefer J., Calibration of atomic-force microscope tips, Review of Scientific Instruments, Tom 64, str. 1868-1873, 1993
77. Sader J., Larson I., Mulvaney P., White L., Method for the calibration of atomic-force microscope cantilevers, Review of Scientific Instruments, Tom 66, str. 3789-3798, 1995
78. Sader J., Chon J., Mulvaney P., Calibration of rectangular atomic force microscope cantilevers, Review of Scientific Instruments, Tom 70, str. 3967-3969, 1999
79. Gibson C., Watson G., Myhra S., Determination of the spring constants of probes for force microscopy/spectroscopy, Nanotechnology, Tom 7, str. 259-262, 1996
80. Gibson C., Weeks B., Abell C., Rayment T., Myhra S., Calibration of AFM cantilever spring constants, Ultramicroscopy, Tom 97, str. 113-118, 2003
81. Slattery A., Blanch A., Quinton J., Gibson C., Accurate measurement of Atomic Force Microscope cantilever deflection excluding tip-surface contact with application to force calibration, Ultramicroscopy, Tom 131, str. 46-55, 2013
82. Ruan J., Bhushan B., Atomic-scale friction measurements using friction force microscopy. 1. General-principles and new measurement techniques, Journal of Tribology-Transactions of the Asme, Tom 116, str. 378-388, 1994
83. Jarzabek D., Precise and direct method for the measurement of the torsion spring constant of the atomic force microscopy cantilevers, Review of Scientific Instruments, Tom 86, 2015
84. Ogletree D., Carpick R., Salmeron M., Calibration of frictional forces in atomic force microscopy, Review of Scientific Instruments, Tom 67, str. 3298-3306, 1996
85. Varenberg M., Etsion I., Halperin G., An improved wedge calibration method for lateral force in atomic force microscopy, Review of Scientific Instruments, Tom 74, str. 3362-3367, 2003
86. Wang H., Gee M., AFM lateral force calibration for an integrated probe using a calibration grating, Ultramicroscopy, Tom 136, str. 193-200, 2014

87. Mullin N., Hobbs J., A non-contact, thermal noise based method for the calibration of lateral deflection sensitivity in atomic force microscopy, *Review of Scientific Instruments*, Tom 85, 2014
88. Hertz H., Ueber die Beruehrung elastischer Koerper, *Gesammelte Werke*, 1882.
89. Johnson K., Kendall K., Roberts A., Surface energy and contact of elastic solids, *Proceedings of the Royal Society of London Series a-Mathematical and Physical Sciences*, Tom 324, str. 301-313, 1971
90. Derjaguin B., Muller V., Toporov Y., Effect of contact deformations on adhesion of particles, *Journal of Colloid and Interface Science*, Tom 53, str. 314-326, 1975
91. Missala T., Szewczyk R., Kamiński M., Hamela M., Winiarski W., Szałatkiewicz J., Tomasik J., Salach J., Strupiński W., Pasternak I., Borkowski Z., Study on Graphene Growth Process on Various Bronzes and Copper-Plated Steel Substrates. In: Szewczyk R., Zieliński C., Kaliczyńska M. (red.) *Progress in Automation, Robotics and Measuring Techniques. Advances in Intelligent Systems and Computing*, Tom 352. Springer, Cham, 2015
92. Trzcinka K. Missala T., Pasternak I., Strupiński W., Winiarski W., Kamiński M., Szewczyk R., Nowicki M., Investigation of the Functional and Environmental Characteristics of Elements with Graphene Coating. In: Szewczyk R., Zieliński C., Kaliczyńska M. (red.) *Progress in Automation, Robotics and Measuring Techniques. Advances in Intelligent Systems and Computing*, vol 352. Springer, Cham, 2015
93. Tomasik J., Wiśniewska M., Badania wpływu powłok grafenowych na mikrogeometrię powierzchni, *Mechanik* 88, 2015
94. Häusler R., Advances in stapes surgery. In: Jahnke K. (Ed.), *Middle Ear Surgery*. Thieme, New York, str. 105-119., 2004
95. Møller P., Stapedectomy versus stapedotomy. *AdvOtorhinolaryngol*, 2007, Tom 65, str. 169-173, 2007
96. Rizer F. M., Lippy W.H., Evolution of techniques of stapedectomy from the total stapedectomy to the small fenestra stapedectomy. *OtolaryngolClin North Am*, Tom 26, str. 443-451, 1993
97. Vincent R., Sperling N. M., Oates J., Jindal M., Surgical findings and long term hearing results in 3050 stapedotomies for primary otosclerosis: a prospective study with the otology-neurotology database. *OtolNeurotol*, Tom 27, str. 25-47, 2006
98. Lesinski S. G., Causes of conductive hearing loss after stapedectomy or stapedotomy: a prospective study of 279 consecutive surgical revisions. *OtolNeurotol*, Tom 23, str. 281-288, 2002
99. Lesinski S. G., Revision stapedectomy. *CurrOpinOtolaryngol Head Neck Surg*, Tom 11(5), str. 347-354, 2003
100. Sun Q., Gan R. Z., Chang K. H., Dormer K. J., Computer-integrated finite element modeling of human middle ear. *Biomech Model Mechanobiol*, Tom 1(2), str. 109–122, 2002
101. Gan R. Z., Reeves B. P., Wang X., Modeling of sound transmission from the ear canal to cochlea. *Ann Biomed Eng*, Tom 35(12), str. 2180–2195, 2007
102. Lauxmann M. Eiber A., Haag F., Ihrle S., Nonlinear stiffness characteristics of the annular ligament, *J Acoust Soc Am*, Tom 136, str. 1756-1767, 2014
103. Sikora A., Bednarz L., Ekwiński G., Ekwińska M., The determination of the spring constant of T-shaped cantilevers using calibration structures, *Measurement Science and Technology*, Tom 25 (4), 2014

104. Reddy J. N., Theory and analysis of elastic plates and shells. CRC Press, Taylor & Francis, 2014
105. Svintsov A. A., Trofimov O. V., and Zaitsev S. I., J. Vac. Sci. Technol. B tom 25, str. 2435, 2007

## **6. Publikacje naukowe stanowiące podstawę przewodnika**



## Publikacja - P1

Cantilevers with spherical tips of millimeter  
magnitude

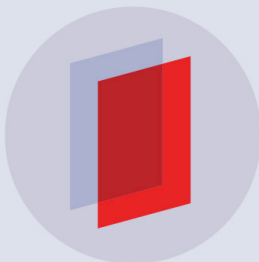
**Michałowski M., Łuczak S.**

TECHNICAL NOTE

## AFM cantilevers with spherical tip of millimeter size

To cite this article: M Michaowski and S uczak 2019 *J. Micromech. Microeng.* **29** 017002

View the [article online](#) for updates and enhancements.



**IOP | ebooks™**

Bringing you innovative digital publishing with leading voices to create your essential collection of books in STEM research.

Start exploring the collection - download the first chapter of every title for free.

This content was downloaded from IP address 194.29.140.92 on 23/11/2018 at 19:43

## Technical Note

# AFM cantilevers with spherical tip of millimeter size

M Michałowski<sup>ID</sup> and S Łuczak<sup>ID</sup>

Faculty of Mechatronics, Warsaw University of Technology, Institute of Micromechanics and Photonics, Warsaw, Poland

E-mail: [m.michalowski@mchtr.pw.edu.pl](mailto:m.michalowski@mchtr.pw.edu.pl)

Received 20 August 2018, revised 19 October 2018

Accepted for publication 5 November 2018

Published 23 November 2018



### Abstract

The fabrication and application of a new type of cantilever for atomic force microscopes are presented. The beams of the cantilevers are made from a thin sheet of beryllium copper, featuring a bending stiffness in a wide range of  $2\text{--}1900\text{ N m}^{-1}$ , onto which a ball is cemented, whose diameter can be in the range of 0.1–1 mm. The basic properties of the cantilevers (longitudinal and torsional rigidity, tip diameter and material) can be easily changed. The cost of fabricating the cantilevers is considerably lower compared to their commercial counterparts, whereas their quality is approximately the same. Using these cantilevers, it is possible to perform measurements of the tribological properties of material pairs such as steel–molybdenum disulfide ( $\text{MoS}_2$ ), steel–lead (Pb) and polymer–polymer. The larger radius of the cantilever tip also enables measurements of viscosity, and decreases the contact pressure, which is crucial in measurements of biological samples.

Keywords: atomic force microscopy, cantilever, friction

(Some figures may appear in colour only in the online journal)

### 1. Introduction

Nowadays, atomic force microscopy (AFM), which was developed in the 1980s [1] is considered one of the most important tools for measuring and analyzing samples in the micro- and nano-scale [2], and has been constantly under development with respect to scanning probes [3, 4]. A significant advantage of this technique is the possibility of measuring not only the topography of samples, but also such forces as adhesion, friction and viscosity, which impact the operation of many devices [5].

Along with the development of micro-electro-mechanical systems (MEMS) on a large scale, for example MEMS accelerometers, which have been applied in an ever-growing number of device types [6, 7], the interest in measuring these forces has been increasing due to the larger ratio of the surface area to the volume in those devices, compared to the macro-scale.

Since the ratio is high, friction and adhesion forces dominate over inertial and gravitational ones [8, 9]. However, the

currently used AFM tips simulate a single asperity contact, which results in high contact pressures [10] and an unrealistic contact, which does not exist in MEMS devices at all. These high contact pressures impact friction, adhesion, wear and many other parameters. Soft samples, especially biological samples, are affected the most.

Another issue connected with the standard AFM measurements is a limitation related to the materials that can be used for the tips, what excludes measurements involving various pairs of materials. The paper describes the fabrication and applications of a new type of cantilever with a tip of a higher radius in order to obtain lower contact pressure. This kind of tip can be made of various materials.

### 2. Fabrication procedure

A thin sheet of beryllium copper (Alloy Brush 190 CuBe<sub>2</sub>; Be 1.8%, Co + Ni 0.3% by Lamineries Matthey SA, La

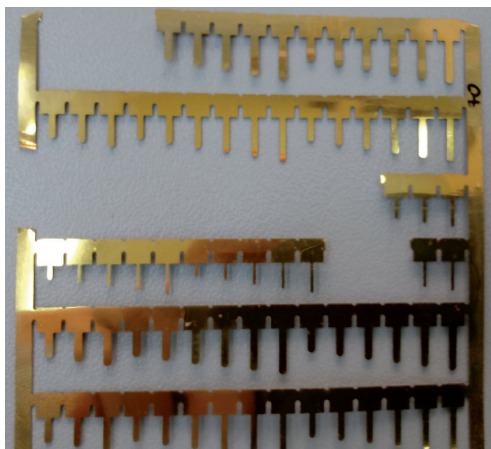


**Figure 1.** Multiple cantilever beams attached to a common base, fabricated by etching from a thin sheet of beryllium–copper.

Neuveville, Switzerland) with a thickness in the range of 40–80  $\mu\text{m}$  was used as a base material for the cantilever.

A photoresist was used for masking in order to create the beams and holders of the cantilever. Afterwards, the sheet was etched by immersion in a solution of  $\text{H}_2\text{SO}_4$ ,  $\text{K}_2\text{Cr}_2\text{O}_7$  and  $\text{NaCl}$ . The reverse side of the sheet was coated with a reflective layer, in this case made of gold, which was done by Physical Vapor Deposition.

The resulting product (figure 1) is a base with multiple cantilevers attached. Dimensions of the presented batch are characterized by the standard deviation of ca.  $\pm 18 \mu\text{m}$ ,  $\pm 13 \mu\text{m}$ ,  $\pm 18 \mu\text{m}$  (length, width, straightness). Single cantilever beams with holders were mechanically cut out of the base using paper scissors—the resultant large error is of no concern, since the holder dimensions do not affect the resulting stiffness of the beam.

Various spherical elements can be used as the tip. In the reported study,  $\text{SiO}_2$  and stainless steel balls for rolling bearing, with diameters ranging from 0.1 mm to 0.7 mm were used. The balls were fixed to the end of the cantilever beam by means of epoxy resin (Epicote 1004 by Shell Chemicals, London, UK).

The obtained cantilever is shown in figure 2. The width and length of the beam can be controlled during the etching process. The thickness of the beam can be changed by using metal sheets of different thicknesses. Controlling those parameters allows both the bending and the torsional stiffness to be changed over a wide range for each cantilever, for example, from 2 to 1900 N  $\text{m}^{-1}$ , and 80 to 32 000 N  $\text{m}^{-1}$ , respectively. A single base can therefore be used to produce cantilevers with various properties. Due to the large diameter of the sphere, as compared to typical cantilever tips, a wide range of materials such as steel, aluminum,  $\text{SiO}_2$ , polymers (e.g. PETP, PS, PC) is available.

### 3. Applications

After fabrication, stiffness of the cantilevers must be calibrated. Owing to the calibration, errors of the geometrical

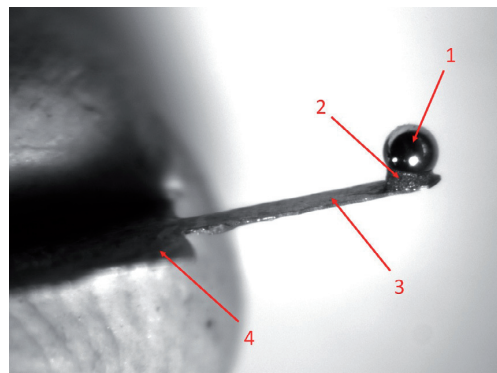


**Figure 2.** Exemplary cantilever made of beryllium–copper with a steel ball tip: length 2500  $\mu\text{m}$ , width 400  $\mu\text{m}$ , thickness 50  $\mu\text{m}$ , ball diameter 400  $\mu\text{m}$ ; 1—cantilever tip, 2—epoxy resin, 3—cantilever beam, 4—cantilever holder.

dimensions do not impact the measurements. Due to the dimensions being larger than in the case of typical cantilevers, it is easier to apply some approaches such as geometric calibration [11] and nanoindenter torsional calibration [12]; at the same time, higher accuracy can be obtained.

Standard methods of calibration, such as the use of a reference spring [13] or MEMS microforce sensors [14], are also applicable for these cantilevers.

The larger radius of the tip increases the contact area between the tip and the surface being studied, what magnifies the pull-off force. Increasing the pull-off force and minimizing the stiffness of the beam, owing to the optimization of its geometrical dimensions, allows adhesion to be measured in cases where its magnitude is too small to be determined, or when the pull-off force should be increased in order to decrease the related error while measuring its small values [15].

The larger radius of the tip also decreases the maximum pressure exerted during contact, which in turn diminishes any deformation of the sample under the tip. This makes it possible to measure the mechanical properties of some biological samples, such as annular ligament, with decreased impact of sample deformation [16]. In the case of such measurements, the possibility of changing the stiffness of the cantilever allows for it to be made almost equal to the stiffness of the sample, what can result in a decrease in measurement errors connected with uncertainty of the cantilever stiffness.

Owing to the larger diameters of the tip, it is easier to coat it with various layers, making it possible to measure the tribological properties between different materials, such as various anti-adhesive coatings in contact with polymers to potentially be used in nano-imprint lithography [17]. Such measurements, as well as those mentioned below, were performed using a commercial NT-206 AFM system.

The presented cantilevers were also used to determine the viscosity of a PDMS film deposited on a silicon dioxide ( $\text{SiO}_2$ ) substrate. The Couette flow model was used after appropriate adaptation to the AFM technique [18]. Assuming a viscous film between two surfaces, one of which is the substrate and the second is the cantilever tip, the viscosity can be calculated as follows:

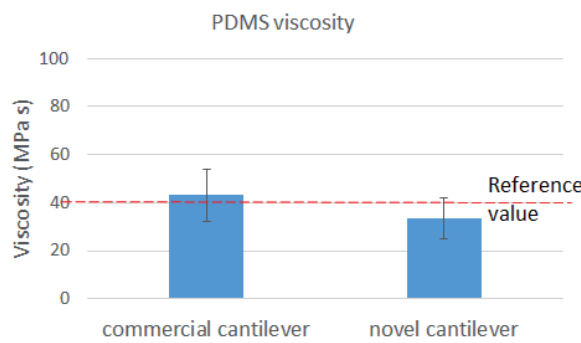


**Figure 3.** Viscosity measurements of PDMS by a commercial cantilever having a spherical tip of  $2\ \mu\text{m}$  in diameter and the novel beryllium copper cantilever with a tip diameter of  $0.7\ \text{mm}$  against the reported standard value (horizontal line); instrumentation: NT-206 AFM system.

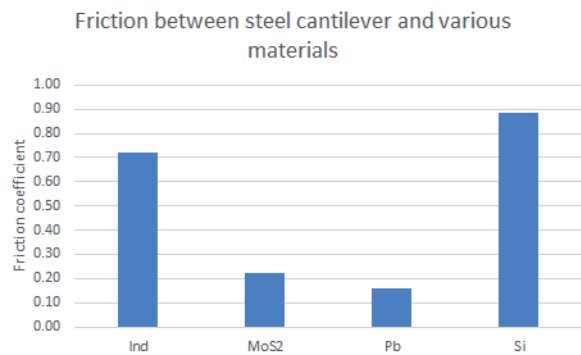


**Figure 4.** Measurements of the friction coefficient between a cantilever with a steel ball of  $0.7\ \text{mm}$  as a tip and a Si wafer with three different layers deposited; instrumentation: NT-206 AFM system.

$$\eta = \frac{F_t \cdot D}{A \cdot v} \quad (1)$$

where:  $\eta$  is the viscosity of the film,  $F_t$  is the friction force,  $D$  is the film thickness and  $v$  is the sliding speed.

The measured values of viscosity are similar to the value reported by the manufacturer of the PDMS, as shown in figure 3.

A larger spectrum of materials used for AFM tips makes it possible to perform measurements of friction for pairs of materials such as steel–molybdenum disulfide ( $\text{MoS}_2$ ), steel–lead (Pb), and polymer–polymer.

A cantilever with a steel ball (diameter of  $0.7\ \text{mm}$ ) as the tip was used to create a sliding pair with a silicon wafer and molybdenum disulfide film on the wafer. At a sliding speed of  $3.5\ \mu\text{m}$  per second and a load of  $30\ \mu\text{N}$ , a friction coefficient of 0.88 was determined for steel–Si, which proves that the result reported by Qing [19] can be obtained in an easier way—without the need to build a dedicated micro-friction test apparatus. Under the same load and sliding speed, a steel– $\text{MoS}_2$  pair (measurements performed in the air at a humidity of 50%) yielded a friction coefficient of 0.22, which agrees with the results of previous research realized at the macro-scale [20, 21].

The presented cantilevers were also used to obtain the friction coefficients of material pairs such as steel–lead film on a Si wafer and steel–indium film on a Si wafer. Both of these films were obtained by physical vapor deposition: evaporative deposition. The results of friction measurements are illustrated in figure 4.

## 4. Conclusions

A new type of AFM cantilever is presented. The applied fabrication process makes it possible to obtain cantilevers featuring various bending and torsional stiffnesses, for example,  $2\text{--}1900\ \text{N m}^{-1}$ , and  $80\text{--}32\,000\ \text{N m}^{-1}$ , respectively.

Even though the large diameters of the spheres used for the tips (in the range of  $0.1\text{--}0.7\ \text{mm}$ ) exclude a high resolution of topography scanning, resolution of force measurements can still be increased.

A wide range of materials can be used for the tip, including steel, silicon dioxide, zirconium silicate, zirconium dioxide, and polymers such as polystyrene, and such a tip can easily be machined in order to change its shape or roughness, according to specific demands. This enables performing measurements adequate to the frictional mating of a real pair of materials, for example in MEMS devices.

The presented cantilevers can be installed in commercial AFM systems such as the NT-206. While applied in other systems, the holding part may have to be manufactured with a different shape.

Another noteworthy feature of the new cantilevers is their dramatically lower cost compared to their commercially available counterparts with spherical tips.

## Acknowledgments

This work was supported by NANOVISC 2014/15/N/ST8/03664 Prelidium grant financed by the National Science Centre. The authors acknowledge a key contribution of Mr Grzegorz Ekiwiński to creating the concept of the presented cantilevers and building the first prototypes, and would like to thank Mr Kamil Bochra for preparing the samples with films deposited on Si wafers.

## ORCID iDs

M Michałowski <https://orcid.org/0000-0002-6946-6840>  
S Łuczak <https://orcid.org/0000-0003-2351-9473>

## References

- [1] Binnig G, Quate C F and Gerber C H 1986 Atomic force microscopy and drug induced degradation *Phys. Rev. Lett.* **56** 930–3
- [2] Eaton P and West P 2010 *Atomic Force Microscopy* (Oxford: Oxford University Press)
- [3] Seokbeom K, Jungki S, Sang-Joon C and Jungchul L 2017 Facile batch fabrication of hydrogel atomic force microscope cantilevers via capillary filling and ultraviolet

- curing in an aligned elastomeric mold pair  
*J. Microelectromech. Syst.* **26** 504–6
- [4] Kwangseok K, Seokbeom K, Taehong K, Wonjung K and Jungchul L 2016 Spray-coated liquid metal reflectors for transparent hydrogel atomic force microscope cantilevers  
*J. Microelectromech. Syst.* **25** 848–50
- [5] Turkowski M 2004 Influence of fluid properties on the characteristics of a mechanical oscillator flowmeter  
*Measurement* **35** 11–8
- [6] Łuczak S, Grepl R and Bodnicki M 2017 Selection of MEMS accelerometers for tilt measurements  
*J. Sensors* **2017** 9796146
- [7] Łuczak S 2016 Tilt measurements in BMW motorcycles  
*Recent Global Research and Education: Technological Challenges* ed R Jabłoński *et al* (Cham: Springer) pp 287–93
- [8] Zhao Y P, Wang L S and Yu T X 2003 Mechanics of adhesion in MEMS—a review  
*J. Adhes. Sci. Technol.* **17** 519–46
- [9] Tas N R, Gui C and Elwenspoek M 2003 Static friction in elastic adhesion contacts in MEMS  
*J. Adhes. Sci. Technol.* **17** 547–61
- [10] Komvopoulos K 2003 Adhesion and friction forces in micro-electromechanical systems: mechanisms, measurement, surface modification techniques, and adhesion theory  
*J. Adhes. Sci. Technol.* **17** 477–517
- [11] Albrecht T R, Akamine S, Carver T E and Quate C F 1990 Microfabrication of cantilever stylus for the atomic force microscope  
*J. Vacuum Sci. Technol. A* **8** 3386–96
- [12] Jarząbek D 2015 Precise and direct method for the measurement of the torsion spring constant of the atomic force microscopy cantilevers,  
*Rev. Sci. Instrum.* **86** 013701
- [13] Sikora A, Bednarz L, Ekwinski G and Ekwinska M 2014 The determination of the spring constant of T-shaped cantilevers using calibration structures  
*Meas. Sci. Technol.* **25** 044015
- [14] Dziekoński C, Dera W and Jarząbek D 2017 Method for lateral force calibration in atomic force microscope using MEMS microforce sensor  
*Ultramicroscopy* **182** 1–9
- [15] Michałowski M, Voicu R, Obreja C, Baracu A, Muller R and Rymuza Z 2017 Influence of deposition temperature during LPCVD on surface properties of ultrathin polysilicon films  
*Microsyst. Technol.* **24** 537–42
- [16] Kwacz M, Rymuza Z, Michałowski M and Wysocki J 2015 Elastic properties of the annular ligament of the human stapes—AFM measurement  
*J. Assoc. Res. Otolaryngol.* **16** 433–46
- [17] Tochino T, Uemura K, Michałowski M, Fujii K, Yasuda M, Kawata H, Rymuza Z and Hirai Y 2015 Computational study of the effect of side wall quality of the template on release force in nanoimprint lithography  
*Japan. J. Appl. Phys.* **54** 06FM06
- [18] Bhushan B 2008 *Nanotribology and Nanomechanics: an Introduction* 2nd edn (Berlin: Springer)
- [19] Tao Q, Tianmin S and Shizhu W 2007 Micro-friction and adhesion measurements for Si wafer and TiB<sub>2</sub> thin film  
*Tsinghua Sci. Technol.* **12** 261–8
- [20] Akbarzadeh M, Zandrahimi M and Moradpour E 2017 Molybdenum disulfide (MoS<sub>2</sub>) coating on AISI 316 stainless steel by thermo-diffusion method  
*Arch. Metall. Mater.* **3** 1741–8
- [21] Rapoport L, Moshkovich A, Perfiliev V, Lapsker I, Halperin G, Itovich Y and Etsion I 2008 Friction and wear of MoS<sub>2</sub> films on laser textured steel surfaces  
*Surf. Coat. Technol.* **202** 3332–40

**Publikacja – P2**

**Simulation model for frictional contact of two  
elastic surfaces in micro/nano scale and its  
validation**

**Michałowski M.**

**Regular article**

Marcin Michałowski\*

# Simulation model for frictional contact of two elastic surfaces in micro/nanoscale and its validation

<https://doi.org/10.1515/ntrev-2018-0075>

Received April 19, 2018; accepted August 20, 2018

**Abstract:** A numerical model is suggested and validated for simulating frictional forces between two samples. The model employs knowledge of surface topographies and values of surface properties provided in the relevant literature and can be applied to contact between complex surfaces. It employs the Lennard-Jones molecular force theory and applies it to a surface segmented into cuboids, which represent separate springs in a Winkler layer. In order to model a contact of two rough surfaces, their asperities are merged into one surface that is put into contact with a perfectly flat surface. Validation, done by atomic force microscopy (AFM), shows that the model can be applied for contacts of rigid samples in the elastic regime of forces.

**Keywords:** atomic force microscopy; friction; simulation.

**Abbreviations:** AFM, atomic force microscopy; LPCVD, low-pressure chemical vapor deposition; MEMS, microelectromechanical systems; NEMS, nanoelectromechanical systems

## 1 Introduction

Reliability is always a significant issue in micro- and nano-electromechanical systems (MEMS and NEMS). Because of scaling effects, volumetric properties of MEMS/NEMS are not the main focus of failure mode analysis [1–6]. In microscale, surface properties and surface-surface contact mostly affect performance and reliability [7]. Adhesion of surfaces and friction between two sliding surfaces result in stiction (sometimes permanent due to low elastic restoring forces) and wear of mechanisms [8–10]. Adhesion of

two surfaces can be modeled based on contact theories such as the Johnson, Kendall, and Roberts (JKR) [11] or Maugis model [12]. With detailed knowledge of both contacting surface topographies, it is possible to predict the adhesion forces between them [13]. Prediction of friction is, however, a more complex issue, and even the measurement of friction forces between two surfaces in microscale is a difficult task [14]. That leads toward a need to develop a way to accurately simulate friction contact of two surfaces. A respective contact model was suggested and validated in this paper.

Previously developed friction models present accurate predictions within limited areas. For example, the Greenwood-Wiliamson statistical approach with Weibull distribution [15] is a good predictor of contact between two surfaces with very limited number of contacting asperities, which comes to very rough surfaces under low loads. Those limitations make it hard to use this model while developing contact surfaces in MEMS and NEMS for minimal friction. There are also models for specific situations such as numerical simulations of rigid body dispersions, which predict frictional behavior during dispersion in solvents [16]; however, they are not applicable to this scale. Molecular dynamics models are also a possibility for predicting contact, but their complexity is still very high. Numerous parameters affect those models, and due to still high error of the results and long computation time, these models still need significant work in order to be applied to the design of MEMS/NEMS devices [17, 18]. Validation of friction models is also a complex task as it might require development of special apparatus to accurately measure nanoscale contact [19]. However, it is possible to use atomic force microscope (AFM) to measure contact parameters with high accuracy, as it was done for other types of simulation models [20–22].

## 2 Simulation model

In this simulation, the Tabor's theory [23], developed further by McClelland [24], is assumed to be a good

\*Corresponding author: Marcin Michałowski, Faculty of Mechatronics, Institute of Micromechanics and Photonics, Warsaw University of Technology, Boboli 8, 02-525 Warsaw, Poland, e-mail: m.michalowski@mchtr.pw.edu.pl.  
<http://orcid.org/0000-0002-6946-6840>

description of two contacting surfaces. This theory suggests that friction can be divided into adhesive friction and mechanical friction. The adhesive part is caused by molecular bonds between atoms of two surfaces moving relatively to each other. The mechanical part, also called load-controlled or deformation component, describes the force needed for those surfaces to deform each other. Another assumption taken in this model is a simplification of elastic deformation by considering the material as a set of parallel springs as in the Winkler mattress model. Each spring in the Winkler layer is a separate point in the simulation approximating area  $S$ . Asperities of two contacting surface topographies are summed to form one rough surface (Figure 1), which is in contact with a flat surface. Additionally, the flat sample is assumed to be rigid, and the Young's modulus of the rough surface is calculated according to Eq. (1) [25].

$$E = \frac{1}{\frac{(1-\nu_1^2)}{E_1} + \frac{(1-\nu_2^2)}{E_2}} \quad (1)$$

where  $E_1, E_2, \nu_1, \nu_2$  are Young's modulus and Poisson's ratio of material surfaces 1 and 2, respectively.

Deformation of the elastic layer can be derived from the force equilibrium Eq. (2):

$$\sum_{i=1}^m P_i(\Delta z_i) + \sum_{i=1}^n F(l_i) = N \quad (2)$$

where  $P_i$  is the contact deformation force acting on the surface layer deforming it elastically over  $\Delta z_i$  [26].  $F(l_i)$

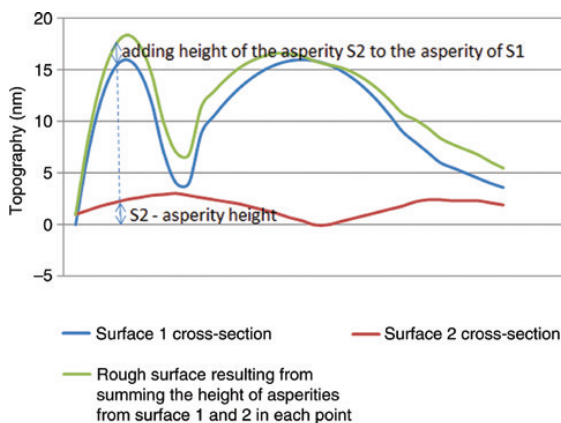


**Figure 1:** An example of a rough surface used for simulation, modeled in contact with a perfectly smooth surface. This rough surface is created by summing of the asperities of two real surfaces into one.

is the molecular force described by the Lennard-Jones theory,  $l_i$  is the distance between the two surfaces in point  $i$  and can be described as  $l_i = d - z_i$ .  $N$  is the external force,  $m$  is the number of springs being in mechanical contact, and  $n$  is the number of springs in strictly adhesive contact. The elementary force opposing the elastic deformation can be described as [26]:

$$P_i(\Delta z_i) = \frac{E}{kh} \Delta z_i \quad (3)$$

where  $h$  is the height of the Winkler's layer, and  $k$  is:

$$k = \frac{(1 + \sqrt{\nu_1 \nu_2}) \cdot (1 - 2\sqrt{\nu_1 \nu_2})}{1 - \nu_1 \nu_2} \quad (4)$$

The molecular force  $F(l_i)$  can be derived from the Lennard-Jones potential energy equation [27]:

$$E_p = \frac{A}{l_i^n} - \frac{B}{l_i^m} \quad (5)$$

Powers  $n$  and  $m$  are taken as 2 and 8 due to the assumption of two half-spaces interacting with each other [28]. Afterward, we differentiate Eq. (5) with respect to distance and calculate constants  $A$  and  $B$  assuming that the force equals 0 when the distance is  $\varepsilon$  and the adhesion energy to be equal to the integral of the force with respect to the distance over  $\varepsilon$  to  $\infty$ .

$$\Delta\gamma = \int_{\varepsilon}^{\infty} F(l_i) dl \quad (6)$$

After these transformations, the force can be calculated as:

$$F(l_i) = \frac{8}{3} \frac{\Delta\gamma}{\varepsilon} \left( \left( \frac{\varepsilon}{l_i} \right)^3 - \left( \frac{\varepsilon}{l_i} \right)^9 \right) \quad (7)$$

where  $\varepsilon$  is the intermolecular distance at which potential energy is minimal,  $\Delta\gamma$  is the adhesion energy equal to  $\Delta\gamma = \sqrt{\gamma_1 \gamma_2}$ , where  $\gamma_1$  and  $\gamma_2$  are surface energies of samples 1 and 2. For points with no initial mechanical contact  $l_i > \varepsilon$ , we can calculate the deformation of the elastic layer by assuming a force equilibrium  $F(l_i) = P_i(\Delta z_i)$  and using Eqs. (3) and (7),

$$\Delta z_i = \frac{8}{3E} \Delta\gamma kh \left( \frac{\varepsilon^2}{(d - z_i)^3} - \frac{\varepsilon^8}{(d - z_i)^9} \right) \quad (8)$$

where  $d$  is the distance between the flat surface and the base of the rough surface, and  $z_i$  is the height of the asperity at point  $i$  from the base level, as can be seen in Figure 2.

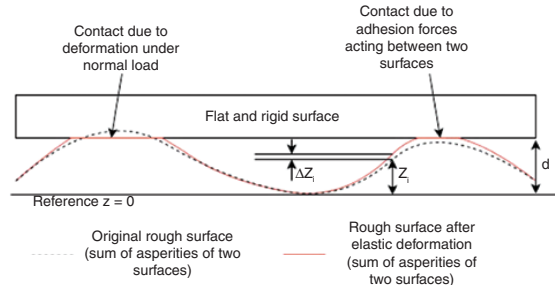


**Figure 2:** Schematic of contact between two real surfaces. Asperities of two real surfaces are merged into one surface called “rough surface”, and the second is presumed to be ideally “flat and rigid surface”. The figure shows deformation of the “rough surface” under load and due to adhesion forces.

Each spring in the model is a cuboid of the surface material with its height being the height of the Winkler’s layer and its upper area is equal to  $S$ . When two surfaces: “rough surface” and “flat and rigid surface” are moving laterally with respect to each other, each cuboid is sheared. A schematic of a sheared element is shown in Figure 3. The work of the shear force is:

$$W = \frac{1}{2} Q_i \Delta s_i \quad (9)$$

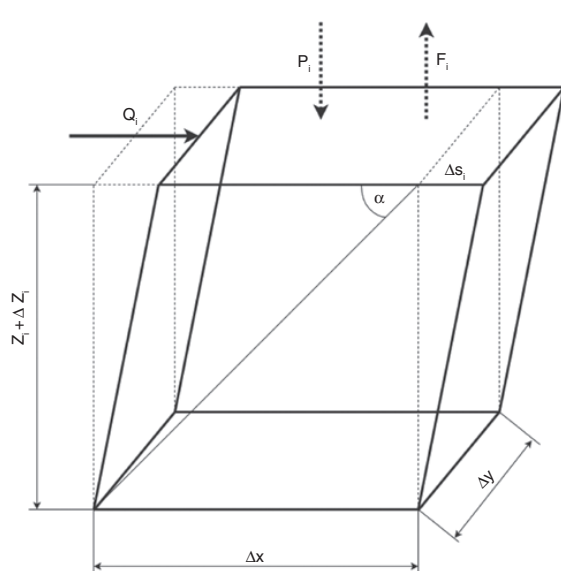


**Figure 3:** With a surface modeled as collection of parallel springs, one spring representing a cuboid of the surface material is shown.  $\Delta x$  and  $\Delta y$  are the dimensions of the cuboid in this model, assumed to be the size of the step set during surface topography measurement.  $Z_i$  is the height of the layer,  $Q$  is the shearing force, while  $P$  and  $F$  are the load and adhesion forces that could stretch or compress  $Z_i$ .

An extension of the diagonal of the cuboid resulting from the shear can be calculated in two ways. Strictly geometrical under an assumption that the angle between the diagonal and the top side ( $\alpha$  in Figure 3) does not change with the shear of the top, due to a low deformation of the cuboid:

$$\Delta l = C \cdot \frac{\Delta s_i}{z_i + \Delta z_i} \quad (10)$$

where  $C = \frac{\tan \alpha}{\tan^2 \alpha + 1}$ ,  $\tan \alpha = \frac{z_i + \Delta z_i}{\Delta x}$ ,  $\Delta x$  is the side of the upper square of the cuboid.

The second way of denoting an extension is to use a well-known equation, due to stretching of the material in the direction and contracts in the direction traverse of the stretching:

$$\Delta l = \frac{\sigma_1}{E} - \nu \frac{\sigma_2}{E} \quad (11)$$

where  $\sigma_1 = \frac{Q}{S}$ , and  $\sigma_2 = -\frac{Q}{S}$ .

From Eqs. (10) and (11), we can calculate:

$$\Delta s_i = \frac{Q_i}{2CGS} (z_i + \Delta z_i) \quad (12)$$

where  $G = \frac{E}{2(1+\nu)}$ ,  $S$  is the upper surface area of one calculated cuboid. Substituting Eq. (12) into Eq. (9), we get an equation for work of the shear force:

$$W = \frac{1}{4} Q_i^2 (z_i + \Delta z_i) \frac{1}{CGS} \quad (13)$$

The energy needed to break contact can be derived from Eq. (7) by assuming the separation of surfaces from distance  $l_{ia}$  to  $\infty$

$$En = \int_{l_{ia}}^{\infty} \frac{8\Delta\gamma}{3\varepsilon} \left( \left( \frac{\varepsilon}{l_i} \right)^3 - \left( \frac{\varepsilon}{l_i} \right)^9 \right) dl_i = \frac{8\Delta\gamma}{3} \cdot \left( \frac{\varepsilon^2}{2l_i^2} - \frac{\varepsilon^8}{8l_i^8} \right) \quad (14)$$

where  $l_{ia} = d - (z_i + \Delta z_i)$ .

Assuming that the work of the shear force has to be equal to the energy needed to break contact, we can use Eqs. (13) and (14) to calculate the lateral force needed to destroy the adhesion bonding at point  $i$ :

$$\begin{aligned} Q_i &= \left( \frac{1}{z_i + \Delta z_i} 4CGS \int_{l_{ia}}^{\infty} \frac{8\Delta\gamma}{3\varepsilon} \left( \left( \frac{\varepsilon}{l_i} \right)^3 - \left( \frac{\varepsilon}{l_i} \right)^9 \right) dl_i \right)^{\frac{1}{2}} \\ &= \left( \frac{1}{z_i + \Delta z_i} 4CGS \cdot \frac{8\Delta\gamma}{3} \cdot \left( \frac{\varepsilon^2}{2l_i^2} - \frac{\varepsilon^8}{8l_i^8} \right) \right)^{\frac{1}{2}} \end{aligned} \quad (15)$$

The lateral force is summed for all points, where adhesive contact occurs. The contact component is calculated using the previously determined force  $P_i$ . Knowing the external force  $N$ , it is possible to calculate the distance  $d$  from Eq. (2) and then  $P_i$  from Eq. (3). Then, we can calculate the distance  $l_{im}$  at which the molecular force  $F(l)$  is equal to  $P_i$ . Afterward, the energy needed to break contact is calculated as the energy needed to separate the initial contact from the distance  $l_{im}$  to  $\varepsilon$  and from that point to  $\infty$ . The calculation of energy needed is similar to that of Eq. (14).

$$Enm = \int_{l_{im}}^{\infty} \frac{8\Delta\gamma}{3\varepsilon} \left( \left(\frac{\varepsilon}{l}\right)^3 - \left(\frac{\varepsilon}{l_i}\right)^9 \right) dl_i \quad (16)$$

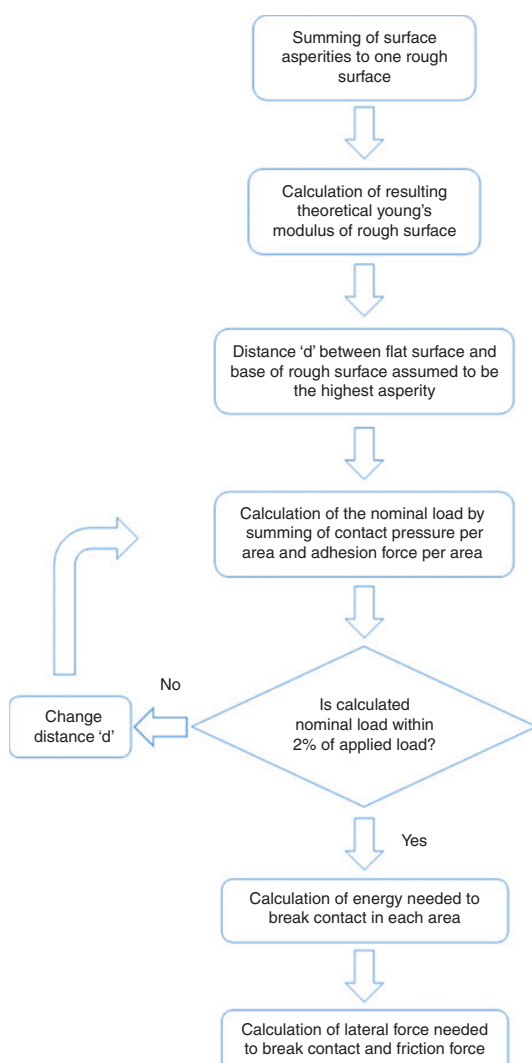


**Figure 4:** Block schematic of the friction simulation algorithm.

The lateral force needed to break the contact can be calculated in a similar way as Eq. (15):

$$Q_i = \left( \frac{1}{d} 4CGS \int_{l_{im}}^{\infty} \frac{8\Delta\gamma}{3\varepsilon} \left( \left(\frac{\varepsilon}{l}\right)^3 - \left(\frac{\varepsilon}{l_i}\right)^9 \right) dl_i \right)^{\frac{1}{2}} \quad (17)$$

The force required to separate a contact is summed for every cuboid in the model, both while in contact due to the deformation of the surface under normal load and while in contact due to adhesion forces.

It is also possible to calculate those values for a situation, where the two contacting surfaces were held in contact for some time prior to movement by assuming a time-dependent elastic modulus [29]. This model for the time being was implemented in Delphi; however, owing to a fairly simple algorithm (Figure 4), it can be transferred to other programming languages.

### 3 Simulation studies

In order to simulate the contact of two surfaces with this method, some parameters of the samples have to be measured or assumed. In the model, we assume the intermolecular distance  $\varepsilon$  to be 2 nm [27] and the Winklers layer thickness as the thickness of the measured layer. The area of a single spring in the model is important as well; it was assumed to be the step of scanning during the AFM measurement of the surface, which was 20 nm  $\times$  20 nm. The AFM was used because it is a widely available and commonly used instrument [30–34]. This could allow for an easy acquisition of model inputs.

Other inputs of the model are surface free energy of samples, elastic modulus, and Poisson's ratio of both materials and detailed topography of surfaces.

#### 3.1 Validation method

The validation of the model was done by assuming one of the contacting surfaces to be a sphere sliding over a flat surface (Figure 5). Because of this assumption, the outputs of the model can be compared with the AFM friction loop measurements. A cantilever with a spherical tip was used on various samples to measure the lateral force and, as the result, the coefficient of friction. One additional simplification was added at this point: the tip sphere was not modeled as a whole sphere, but rather

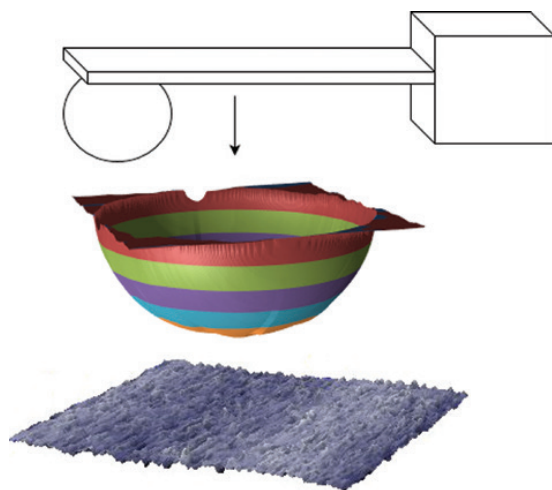


**Figure 5:** Schematics of the simulation validation method. A spherical surface that comes into contact with the sample is moved laterally. The spherical surface in the experiment is a cantilever tip; from the top, we can see a cantilever with a spherical tip; part of the sphere used to calculate the contact; polysilicon sample surface (with 20:1 ratio in the axis z with respect to x and y).

as a half sphere. During the test, no sample with roughness higher than 70 nm Ra was used; therefore, the force between the higher parts of the sphere and the surface sample are negligible. As the exact point of initial contact will, in most cases, not be known in nanometer resolution, validation was done by numerous measurements of topography and friction on the same samples but over different areas, and averaging of both values: measurement of friction and simulated friction for multiple sample surface with the AFM tip.

## 4 Measurements

In order to validate the model, a cantilever with a  $\text{SiO}_2$  tip with a diameter of 2  $\mu\text{m}$  was used. This cantilever was CP-NCH-SiO-A from sQube. Calibration of the cantilever in the z axis was realized by a reference spring with a stiffness of 35.5 N/m and the Si wafer as the hard material for photodiode calibration [35]. In the torsional axis, the calibration was done on the basis of the measurements of the geometrical dimensions of the beam and the assumption of the AFM manufacturer that photodiode sensitivity is equal in both directions. An NT-206 AFM system was used during this study. Friction loop measurements were done on polysilicon samples (Figure 6) produced by low-pressure chemical vapor deposition (LPCVD) with

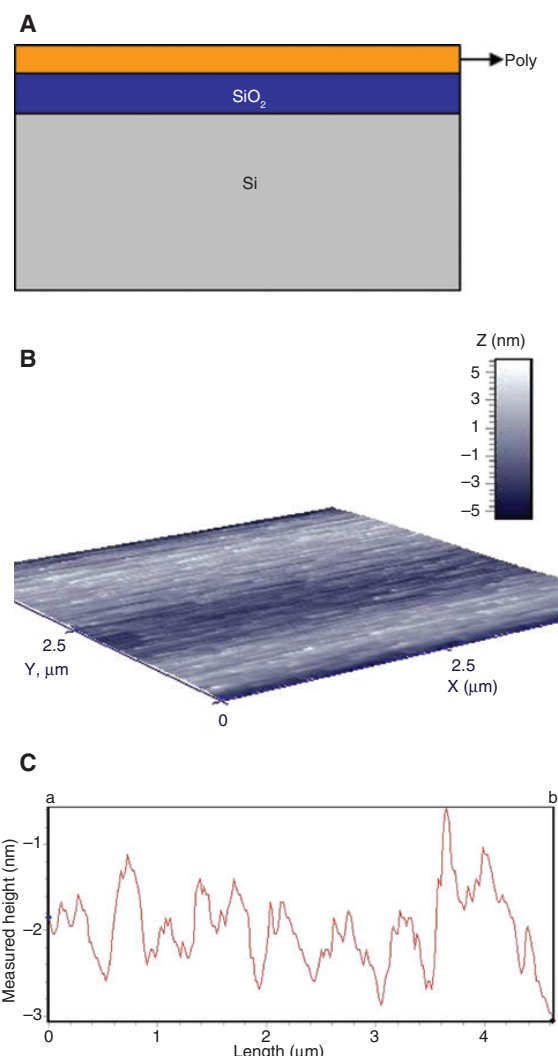


**Figure 6:** Silicon samples measured during validation of the model. (A) Cross section of the silicon sample layers (not to scale). (B) Sample topography. (C) Sample topography cross section.

different deposition temperatures, by thermal decomposition of silane in temperatures of 580°C, 610°C, and 630°C. Layers were produced on  $\text{SiO}_2$ , which was attained through thermal oxidation of <100>-oriented silicon substrate. The  $\text{SiO}_2$  film thickness manufactured in that way was 1.7  $\mu\text{m}$ . Various temperatures of polysilicon deposition resulted in change in the roughness and the grain size of the top layer. The duration of the deposition was controlled in order to achieve a constant thickness of the polysilicon layer of 50 nm for all samples.

The topography of both cantilever tip and samples was measured by the AFM with a step of data acquisition

of  $20 \text{ nm} \times 20 \text{ nm}$ , using a sharp tip CSC17-No Al-15 from MikroMasch. The topography was measured in contact mode with low loads. For polysilicon samples, the measurements were done over an area of  $5 \mu\text{m} \times 5 \mu\text{m}$  at seven separate spots. No significant deformations or differences were spotted between scans. Additionally, scans over a larger area of  $20 \mu\text{m} \times 20 \mu\text{m}$  were done to check if larger deformations exist on the surface of the sample. In the case of the spherical tip CP-NCH-SiO-A, its topography was acquired by repeated scans on the AFM and combining the resulted areas.

Young's modulus of the polysilicon samples was measured on a Tryboscope using the indentation procedure with the application of the Oliver and Pharr model [36]. For these measurements, the Berkovitch tip was used. A trapezoidal loading curve with both loading and unloading time of 5 s and a holding time of 2 s was used. The maximum load during those measurements was  $1500 \mu\text{N}$ . In order to avoid the impact of the substrate during the measurements, samples with a  $2\text{-}\mu\text{m}$  polysilicon layer were prepared utilizing the same fabrication process. The value obtained was  $110 \text{ GPa}$ . During this study, a Hysitron Tryboscope was used. For the purpose of simulation, it was accepted that the Young's modulus of  $\text{SiO}_2$  is  $70 \text{ GPa}$ , according to Ref. [37]. For both samples, literature values of Poisson's ratio were used: 0.22 [38] for polysilicon and 0.17 [37] for  $\text{SiO}_2$ , respectively.

Surface free energy of the LPCVD-prepared samples was measured according to a wettability method [39]. Five microliters of droplets of water and diiodomethane were placed on samples, and their angle with the surface was measured. Afterward, the surface free energy of the samples was calculated [39]. Because of the spherical shape of the cantilever, the wettability procedure was not used for the cantilever tip; in this case, a value of  $72 \text{ mJ/m}^2$  [40] was used in the model.

Friction loop measurements with the use of the simulated cantilever were done on each of these samples seven times at various locations on the sample, and the average value was accepted to be compared with the simulation results. The friction measurements were done under a constant load of  $10 \mu\text{N}$  and a sliding speed of  $3.5 \mu\text{m/s}$ . The constant load was achieved by a feedback loop system with the AFM piezo-element controlling the deflection of the cantilever to be constant at the level at which  $10 \mu\text{N}$  load is exacted on the surface. A  $10\text{-}\mu\text{N}$  load was selected in order to be certain that the contact stays in the elastic regime. The Hertz contact model for a ball with  $2 \mu\text{N}$  in contact with a flat surface for these materials shows that in order to exceed the polysilicon yield strength, a load of  $70 \mu\text{N}$  would have to be applied. Kinematic friction was used for comparison with the simulation. The measurement devices and example results are depicted in Figure 7. All of these measurements were done

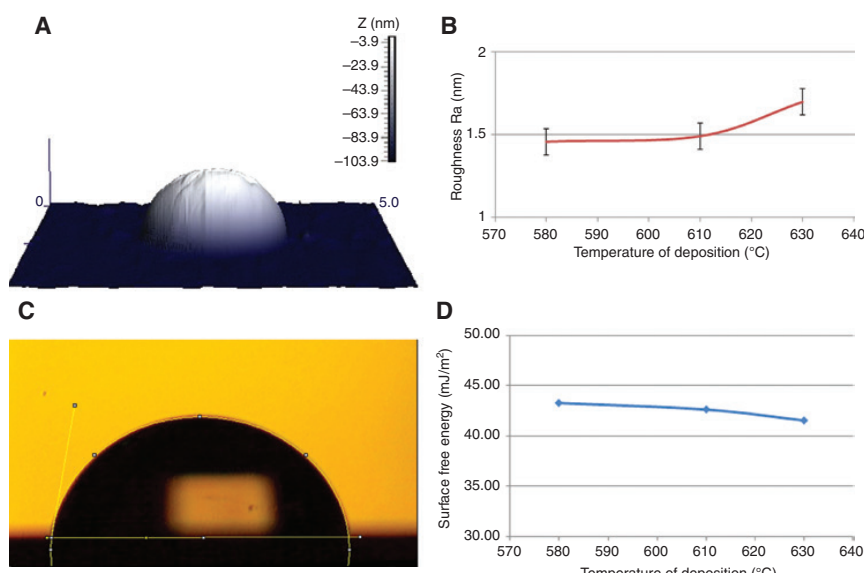


**Figure 7:** Example of the measurement results. (A) Cantilever tip surface. (B) Roughness of the polysilicon samples. (C) Example of a water droplet on a polysilicon sample. (D) Surface free energy of polysilicon samples.

in a clean room with controlled environment, with a temperature of 22.3°C and a humidity of 53.1–56.2%.

## 5 Results

In the simulated samples, the adhesive component of friction is dominating the mechanical part and is roughly 40 times greater for all the  $\text{SiO}_2$ -polysilicon contacts. In both friction measurements and simulation, the same normal load of 10  $\mu\text{N}$  was applied; therefore, the comparison of the friction coefficient is equivalent to the comparison of the lateral force. The average values of the friction coefficient from seven measurements and from seven simulations, one for each topography scan of polysilicon in contact with the cantilever plane, are depicted in Figure 8.

A two-sample t-test was done on each surface pair resulting in p values of 0.13, 0.12, and 0.79 for roughness values of 1.45, 1.49, and 1.7  $\mu\text{m}$ ; each of these values is greater than the assumed threshold of 0.1. Additionally, the R-Pearson correlation between averages was calculated to be 0.96, which is a high strength correlation. Simulation is in line with the measurements giving a good prediction of the values.

Figure 9 depicts the range of friction coefficient values for each simulation compared to the range of values obtained from the measurements. We can see that the scatter of both simulation and experimental values

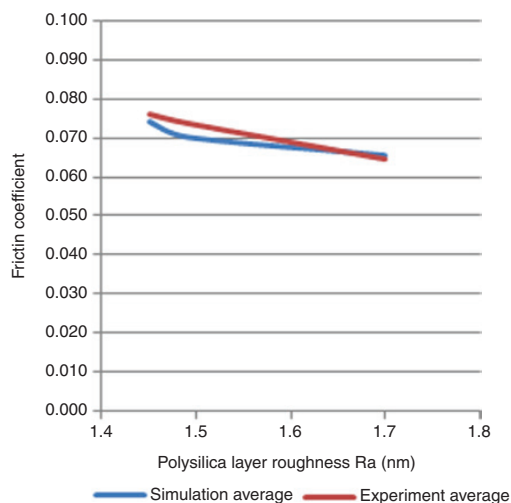


**Figure 8:** Comparison of the coefficient of friction of  $\text{SiO}_2$  friction with polysilicon samples of varied roughness, from simulation and experiment.

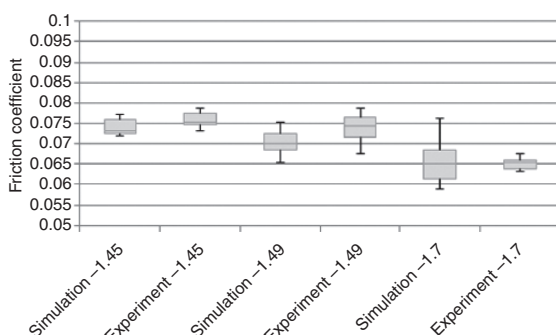


**Figure 9:** Box plots of simulation and experimental values of  $\text{SiO}_2$  and polysilicon contact showing the dispersion range of results, for varied roughness of polysilicon. Boxes denote the range between 1 and 3 quartile, while the whiskers show the range between the minimum and maximum value.

is similar, which further suggests the accuracy of the model.

## 6 Discussion

The simulation model is a good predictor for contacts of two smooth samples. The influence of change in roughness of one surface on the friction is predicted accurately. At this point, the model is accurate for contact between samples when the adhesion contact is dominant as no mechanical locking of two surfaces is taken into account. The adhesive part of friction will be greater than the mechanical one for smooth samples and during low loads. For example, for a simulated sample (Ra of 1.7 nm) in contact with the 2- $\mu\text{m}$  diameter ball tip, the mechanical part exceeds the adhesive part at about 600  $\mu\text{N}$  of load. This model assumes the surface to consist of cuboids with x and y dimensions according to the scan size. This assumption has a negligible effect on smooth surfaces, but surfaces with higher kurtosis, with more spiked asperities, will be affected more by this simplification. By assuming the top of the asperity to be a cuboid of x,y dimensions instead of a sharp end, the contact area will be significantly overestimated at this point, resulting in overestimation of the force needed to break contact, which in turn overestimates the friction force. This was tested on samples with higher roughness and kurtosis (Ra ~50 nm and Rku ~3), and the step of data acquisition for topography had to be 5 nm  $\times$  5 nm or less to correctly simulate the friction force. As this model is meant to be used in conjunction with the topography measured by the AFM, which scans the

sample in particular points and not the highest points of the asperities, the flat cuboid should be statistically indistinguishable from the actual surface for a small-enough measuring mesh. One more noteworthy limitation of the model is that it assumes an elastic contact and no plastic deformation. That means that simulation is only accurate when loads do not exceed the elastic regime of the measured surface material. This limitation is, however, met for majority of the loads existing in MEMS/NEMS and materials such as polymers, silicon, silicon dioxide, or polysilicon [41, 42]. Calculation of friction based on topography and more easily measured properties such as surface free energy can lead toward easier prediction of surface interaction than either uncertain off-chip measurement methods or expensive and time-consuming on-chip measurements [43].

## 7 Summary

A simulation model for the contact of two surfaces is discussed. The model allows the prediction of friction forces with the separation for adhesion friction and mechanical friction. The model uses the Winkler's layer model, Lennard-Jones energy of contact, and Tabor's friction theory as its base. This is a numerical model with a simulation step size possible to be set according to the resolution, with which we measured the simulated surfaces. The inputs of the model are both surface topographies, and their properties such as elasticity, surface free energy, and Poisson's ratio. Simulation outputs were validated for smooth surfaces in which the adhesive part of the friction is dominant. Further validation of rough samples and plastic range of deformation are required to specify the exact range of model application. It is planned to continue the validation of other materials in order to confirm the effects of surface energy and elastic properties on friction results, to ensure accurate prediction over a wide range of values. The proposed model is simpler and faster in calculation than the molecular dynamics models and can be applied to highly patterned surfaces of elements within the elastic regime. The prediction of friction forces in MEMS and NEMS devices can possibly lead toward a more optimized development of NEMS actuators.

**Acknowledgments:** The author would like to thank Sieriusz Łuczak, D.Sc. Ph.D. Eng., for the critical revision of the manuscript.

## References

- [1] Sniegowski JJ, Miller SL, LaVigne G, Rodgers MS, McWhorter PJ. Monolithic geared-mechanisms driven by a polysilicon surface-micromachined on-chip electrostatic engine, In *Technical Digest of the 1996 Solid State Sensor and Actuator Workshop*, Hilton Head Island, SC, June 3–6, 1996, pp. 178–182.
- [2] Rodgers MS, Sniegowski JJ, Miller SL, Barron CC, McWhorter PJ. Advanced micromechanisms in a multi-level polysilicon technology. In *SPIE Micromachined Devices and Components III*, Austin, TX, September 29, 1997, 3224, pp. 120–130.
- [3] Miller SL, LaVigne G, Rodgers MS, Sniegowski JJ, Waters JP, McWhorter PJ. Routes to failure in rotating MEMS devices experiencing sliding friction. In *Proc. SPIE Micromachined Devices and Components III*, Austin, September 29, 1997, 3224, pp. 24–30.
- [4] Komvopoulos K. Surface engineering and microtribology for micromechanical systems. *Wear* 1996, 200, 305–327.
- [5] Romig A, Dugger M, McWhorter P. Materials issues in micro-electromechanical devices: science, engineering, manufacturability and reliability. *Acta Mater.* 2003, 51, 5837–5866.
- [6] Alsem D, van der Hulst R. Wear mechanisms and friction parameters for sliding wear of micron-scale polysilicon sidewalls. *Sens. Actuat. A* 2010, 163, 373–382.
- [7] Miller SL, Rodgers MS, La Vigne G, Sniegowski JJ, Clews P, Tanner DM, Peterson KA. Failure modes in surface micromachined microelectromechanical actuation systems. *Microelectron. Reliab.* 1999, 39, 1229–1237.
- [8] Smallwood S, Eapen K, Patton S, Zabinski J. Performance results of MEMS coated with a conformal DLC. *Wear* 2006, 260(11–12), 1179–1189.
- [9] Tanner D, Miller W, Eaton W, Irwin L, Peterson K, Dugger M, Senfit D, Smith N, Tangyunyong P, Miller S. The effect of frequency on the lifetime of a surface micromachined micro-engine driving a load. In *IEEE Reliability Physics Symposium Proceedings*, 26–35, 1998.
- [10] Zhanshe G, Yonggang M, Hao W, Caijun S, Shizhu W. Measurement of static and dynamic friction coefficient of sidewalls of bulk-microfabricated MEMS devices with an on-chip microtribotester. *Sens Actuat. A Phys.* 2007, 135, 863–69.
- [11] Johnson K, Kendall K, Roberts A. Surface energy and the contact of elastic solids. *Proc. Roy. Soc. London A* 1971, 324, 301.
- [12] Maugis D. Adhesion of spheres: the JKR-DMT transition using a duddale model. *J. Colloid Interface Sci.* 1992, 150, 243.
- [13] Prokopovich P. Adhesion models: from single to multiple asperity contacts. *Adv. Colloid Interface Sci.* 2011, 168(1–2), 210–222.
- [14] Tang XS, Loke YC, Lu P, Sinha SK, O'Shea SJ. Friction measurement on free standing plates using atomic force microscopy. *Rev. Sci. Instrum.* 2013, 84, 013702.
- [15] Lu P, O'Shea S. Mechanical contact between rough surfaces at low load. *J. Phys. D: Appl. Phys.* 2012, 45(47), ID 475303.
- [16] Molina J, Yamamoto R. Direct numerical simulations of rigid body dispersions. I. Mobility/friction tensors of assemblies of spheres. *J. Chem. Phys.* 2013, 139(23). doi: 10.1063/1.4844115.
- [17] Dong Y, Li Q, Martini A. Molecular dynamics simulation of atomic friction: a review and guide. *J. Vac. Sci. Technol. A* 2013, 31(3), ID 30801.

- [18] Ye Z, Martini A. Atomic friction at exposed and buried graphite step edges: experiments and simulations. *Appl. Phys. Lett.* 2015, 106(23), 231603–231603.5.
- [19] Qing T, Shao T, Wen S. Micro-friction and adhesion measurements for Si wafer and TiB<sub>2</sub> thin film. *Tsinghua Sci. Technol.* 2007, 12(3), 261–268.
- [20] Korayem MH, Kavousi A, Ebrahimi N. Dynamic analysis of tapping-mode AFM considering capillary force interactions. *Sci. Iran.* 2011, 18(1), 121–129.
- [21] Korayem MH, Zakeri M. Dynamic modeling of manipulation of micro/nano particles on rough surfaces. *Appl. Surf. Sci.* 2011, 257(15), 6503–6513.
- [22] Korayem MH, Sadeghzadeh S, Rahneshin V. A new multiscale methodology for modeling of single and multi-body solid structures. *J. Comput. Mater. Sci.* 2012, 63, 1–11.
- [23] Tabor D. The role of surface and intermolecular forces in thin film lubrication. *Tribol. Ser.* 1982, 7, 651–682.
- [24] McClelland GM. Friction at weakly interacting interfaces. In *Adhesion and Friction*, Grunze, M, Kreuzer, HJ, Eds., Springer: Berlin, Heidelberg, 1989, pp. 1–16.
- [25] Chen R-H, Weng Y-J, Hung H-Y, Wang Y-L, Tsai C-T. Study of transfer printing using micro-dynamically-regulated micro-structural flexible mold. *Optik – International Journal for Light and Electron Optics* 2016, 127(7), 3590–3596.
- [26] Johnson K. *Contact Mechanics*, Cambridge University Press: Cambridge, UK, 1985.
- [27] Azoroff L. *Introduction to Solids*, Mc Graw-Hill: New York, 1960.
- [28] Israelachvili J. *Intermolecular and Surface Force*, Elsevier: Cambridge, 2011.
- [29] Nolbert D, Rymuza Z. Modelling of frictional and adhesive contacts at silicon/polymer interface for nanotechnological applications. *Tribology – Mater. Surf. Interfaces* 2013, 7(2), 97–102.
- [30] Jarząbek D, Kaufmann A, Schift H, Rymuza Z, Jung T. Elastic modulus and fracture strength evaluation on the nanoscale by scanning force microscope experiments. *Nanotechnology* 2014, 25, 215701–1–9.
- [31] Abetkovskaya S, Chizhik S, Pogoskaya I, Rymuza Z, Jarząbek D, Michałowski M, Linke J. Determining the Young modulus of nanosize thickness coatings for MEMS from the results of static force spectroscopy. *Bull. Russ. Acad. Sci. Phys.* 2012, 76(9), 1009–1011.
- [32] Kucharski S, Jarząbek D, Piątkowska A, Woźniacka S. Decrease of nano-hardness at ultra-low indentation depths in copper single crystal. *Exp. Mech.* 2016, 56(3), 381–393.
- [33] Jarząbek D, Siewert D, Fabianowski W, Schift H, Rymuza Z, Jung T. Influence of alkali ions on tribological properties of silicon surface. *Tribol. Lett.* 2015, 60(2), 1–8.
- [34] Uchihashi T, Watanabe H, Fukuda S, Schibata M, Ando T. Functional extension of high-speed AFM for wider biological applications. *Ultramicroscopy* 2016, 160, 182–196.
- [35] Sikora A, Bednarz L, Ekwīński G, Ekwīńska M. The determination of the spring constant of T-shaped cantilevers using calibration structures. *Meas. Sci. Technol.* 2014, 25(4), ID 044015.
- [36] Oliver WC, Pharr GM. Measurement of hardness and elastic modulus by instrumented indentation: Advances in understanding and refinements to methodology. *J. Mater. Res.* Jan. 2004, 19(1), 3–20.
- [37] Kim MT. Influence of substrates on the elastic reaction of films for the microindentation tests. *Thin Solid Films* 1996, 283, 12–16.
- [38] Sharpe W, Yuan B, Vaidyanathan R, Edwards R. In *Proceedings of the 10th MEMS Workshop*, Nagoya, Japan, 1997, pp. 424–429.
- [39] Andersen W. Wettability literature survey – part 2: wettability measurement. *SPE* 1986, 13933, 1246–1258.
- [40] Chibowski E. Surface free energy and wettability of silyl layers on silicon determined from contact angle hysteresis. *Adv. Colloid Interface Sci.* 2005, 113, 121–131.
- [41] Greenwood J. Contact of nominally flat surfaces. *Proc. R. Soc. A* 1966, 295, 300–319.
- [42] Maugis D. On the contact and adhesion of rough surfaces. *J. Adhes. Sci. Technol.* 1996, 10, 161–175.
- [43] Guo Z, Feng Z. Research development of measuring methods on the tribology characters for movable MEMS devices: a review. *Microsyst. Technol.* 2009, 15, 343–354.

## Bionote



**Marcin Michałowski**

Faculty of Mechatronics, Institute of Micromechanics and Photonics, Warsaw University of Technology, Boboli 8, 02-525 Warsaw, Poland, <http://orcid.org/0000-0002-6946-6840>.  
 m.michalowski@mchtr.pw.edu.pl

Marcin Michałowski MSc, with a degree from Warsaw University of Technology Department of Mechatronics, is a mechanical engineer with experience in micro- and nano-tribology. His expertise involves friction simulations and measurements, protective coatings, and development of measurement procedures. He is the main organizer of the 8th International Colloquium on Micro-Tribology.

## **Publikacja – P3**

**Influence of deposition temperature during  
LPCVD on surface properties of ultrathin  
polysilicon films**

**Michałowski M., Voicu R., Obreja C., Baracu A.,  
Muller R., Rymuza Z.**

## Influence of deposition temperature during LPCVD on surface properties of ultrathin polysilicon films

Marcin Michałowski<sup>1</sup>  · Rodica Voicu<sup>2</sup> · Cosmin Obreja<sup>2</sup> · Angela Baracu<sup>2,3</sup> ·  
Raluca Muller<sup>2</sup> · Zygmunt Rymuza<sup>1</sup>

Received: 29 July 2016 / Accepted: 19 July 2017  
© Springer-Verlag GmbH Germany 2017

**Abstract** The selection of the proper materials for the fabrication of the micro electro mechanical systems (MEMS) is a very important issue in the MEMS research. The materials should be adequate for the fabrication process as well as they have to demonstrate in particular good adhesive (to avoid stiction between contacting/sliding components) and frictional/tribological properties. We fabricated ultrathin (50 nm thick) polysilicon films on single crystal silicon wafers at various deposition process conditions and observed the effect of the process parameters on surface topography and adhesive as well as frictional properties of the produced films. The atomic force microscope was used in these studies equipped with special cantilevers. We identified interesting correlations between the process parameters and adhesive/frictional properties of the studied films which enable to optimize the process to decrease adhesion (stiction) and friction between sliding components of MEMS devices and compared them to previous research done at samples with thicker layer. Topography of both samples and cantilevers has been studied in depth to allow later simulation of the interface. Additional measurements of friction in various humidities should be done next in order to assess the influence of its impact on friction coefficient. Further comparison of adhesion to friction in particular environmental properties

might also increase our understanding of MEMS surface interactions.

### 1 Introduction

The use of the polysilicon films in micro/nanotechnologies is important for the fabrication of the structural elements of micro electro mechanical systems (MEMS) as well as nano electro mechanical systems (NEMS) (Madou 2012; Brand 2005; Hartzell et al. 2011). Such components are critical when they are performing also tribological functions such as sliding components, e.g. in MEMS micromotors or mechanisms. The adhesive/sticking and frictional properties are deciding on the reliability and lifetime of such systems (Zhang et al. 2005; Achanta and Celis 2015; Sinha et al. 2013; Yang et al. 2013). The need for systematic studies of the influence of the fabrication process of polysilicon structural films on their adhesive, nanotribological and nanomechanical properties results from the growing interest of industrial fabrication of such structures. Despite the fact that measuring techniques in this area are known (Jarzabek et al. 2009, 2014), there are no systematic studies performed in this field. Thus, it is important to find the fabrication process parameters, that result in particular tribological properties whether it is minimum or high friction. Those parameters can be used during production of rubbing components of MEMS micromotors as well as other types of MEMS devices.

✉ Marcin Michałowski  
m.michalowski@mchtr.pw.edu.pl

<sup>1</sup> Faculty of Mechatronics, Institute of Micromechanics and Photonics, Warsaw University of Technology, Warsaw, Poland

<sup>2</sup> National Institute for Research and Development in Microtechnologies (IMT Bucharest), Bucharest, Romania

<sup>3</sup> University Politehnica of Bucharest, Bucharest, Romania

### 2 Fabrication process

The polysilicon films have been deposited on a <100>—oriented silicon substrate. The wafers were first thermally oxidized at a temperature of 1000 °C, in order to obtain a

$\text{SiO}_2$  thickness of 1.7  $\mu\text{m}$ . Over this insulator, there were deposited the polysilicon thin films using low-pressure chemical vapor deposition (LPCVD) method. In order to investigate the effect of temperature on grain size and deposition rate, the films have been obtained by thermal decomposition of silane at three different temperatures: 580, 610 and 630  $^{\circ}\text{C}$ . In all our tests the polysilicon thickness was constant, 50 nm (Voicu et al. 2015).

A pattern has been used for the test samples configuration (Fig. 1), one mask has been used for all of the samples. This mask has been prepared for further practical application in MEMS devices. The fabrication process of the samples is described in Fig. 2.

### 3 Experimental details

After fabrication, the samples were tested on scanning electron microscope (SEM) (Fig. 3) and atomic force microscope (AFM) in order to investigate their surface topography. Figures 3 and 4 show examples of SEM and AFM scans. AFM experiments were done with three types of cantilevers depending on the measurement performed. Cantilever with sharp tip has been used for topography scans (CSC17-No Al-15m MikroMasch with a nominal tip radius of <8 nm), the scans were done on a 5  $\times$  5  $\mu\text{m}$  range. A colloidal tip (CP-NCH-SiO-A, sQube) with a ball diameter of 2  $\mu\text{m}$  has been used for friction measurements. This cantilever has been calibrated in both z (vertical) and x (torsional) axis. Calibration in y has not been done as scans were done along x axis of the cantilever and y axis tilt is negligible in this situation. In order to calibrate the cantilever vertically, a special membrane (12Z00073, Nanoidea) has been used along with TGZ03 step-calibrating structure, while torsional stiffness has been obtained by mathematical calculation, they have been as following  $C_{\text{ver}} = 80 \text{ N/m}$  and  $C_{\text{tor}} = 16,000 \text{ N/m}$ . For the adhesion measurements a custom-made (fabricated in Warsaw Institute of Micromechanics and Photonics) beryllium

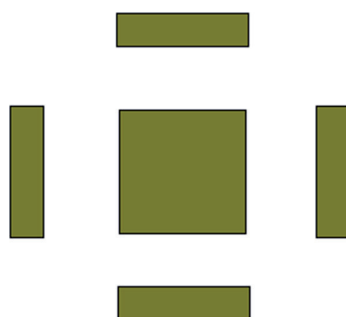


**Fig. 1** Geometry of MEMS sample with islands patterned on silicon chip with 4  $\times$  4 mm in size (central island is 1  $\times$  1 mm in size)

bronze cantilever with a  $\text{SiO}_2$  ball of 0.35 mm diameter has been used. This cantilever has been calibrated vertically in the same way as the one with colloidal tip to be  $C_{\text{ver2}} = 49 \text{ N/m}$ . In order to have a greater understanding of the interface during adhesion of the tip to the sample, the  $\text{SiO}_2$  ball has been measured by AFM. This allows also usage of simulation models for surface–surface interface. Crucial parameters of the measurements are summed up below.

For friction measurements, the applied normal force (contact load) during the friction measurement was 10  $\mu\text{N}$ . The sliding speed during friction measurements was about 3.5  $\mu\text{m/s}$ . For the adhesion measurements, maximum contact pressure did not exceed 0.5  $\text{N/mm}^2$ . The surface topography and friction measurements were performed in a clean room at the following ambient conditions: temperature 22.3  $^{\circ}\text{C}$ , humidity 53.1–56.2%. In order to attain the adhesion in various humidities, the pull-off force tests have been carried out at 20, 40 and 60% to identify the influence of the humidity on the pull-off forces between the probe and the film during detachment of the probe from the tested film.

### 4 Results and discussion

The roughness of the sample deposited at different temperatures varied slightly with the temperature changes. The AFM images of the surface topography of the samples are shown in Fig. 4.

The surface of the films was uniform for all tested samples in various scanning locations. The roughness of the films fabricated at various temperatures is expressed by the  $R_a$  and its kurtosis is indicated by  $R_{ku}$  parameter and it is presented in comparison for the set of the tested samples in Fig. 5.

The roughness of the polysilicon films is increasing at the increase of the temperature of the deposition. What we can also see from both the cross-sections and the kurtosis, with the rise of the temperature the spikiness of the surface increases. The differences here are more significant statistically than in  $R_a$ . The difference in roughness and kurtosis among all tested films has been minor for particular samples in different locations of scanning. The standard deviation of the identification of the  $R_a$  was 0.16, 0.14 and 0.08 nm for the films deposited at 580, 610 and 630  $^{\circ}\text{C}$ , respectively, while kurtosis error was about 12% of the measured value. This measurements show that with the increase of the temperature the surface roughness is caused by higher spikiness instead of waviness.

The adhesive properties of the films were strongly dependent on the surface topography and the humidity. The pull-off force for the tested films is presented in Fig. 6.

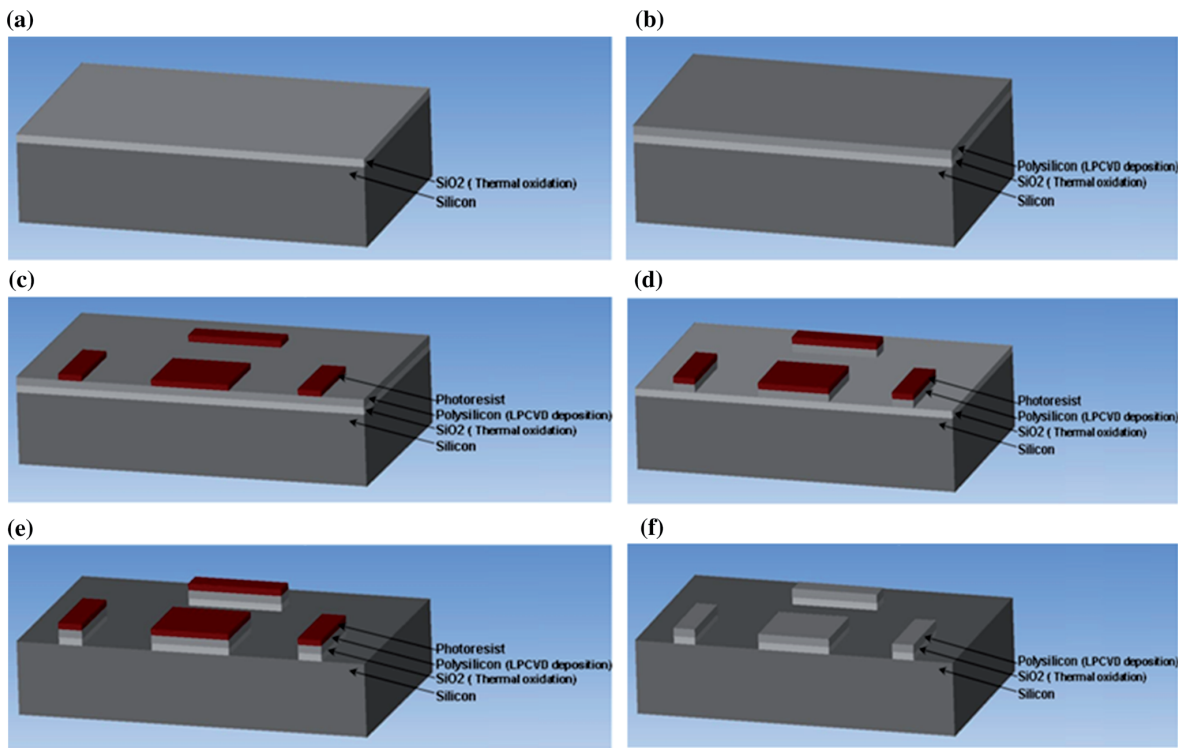


**Fig. 2** Technological process of the test sample configuration: **a** thermal oxidation of the substrate; **b** polysilicon thin films deposition; **c** the photolithographic process; **d** dry etching of the polysilicon thin films; **e** SiO<sub>2</sub> wet etching; **f** photoresist removal

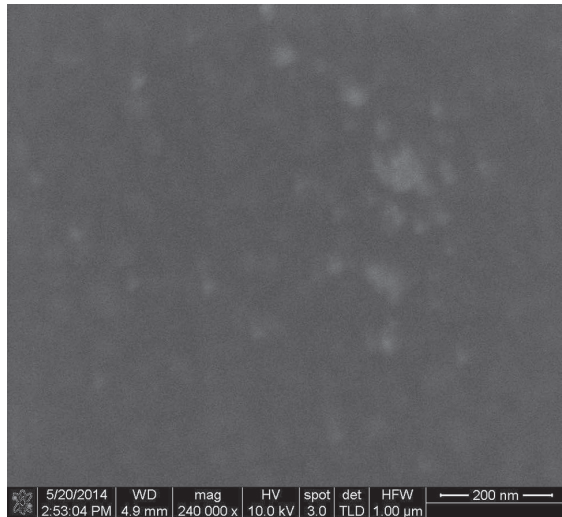


**Fig. 3** SEM image of 50 nm undoped polysilicon deposited at 610 °C

This results compared to samples with 2 µm thickness layer, which were conducted previously (Voicu et al. 2014), are significantly higher. Both sample sets were produced in the same manner, with the same method and

the same fabrication temperature. Different thickness has been achieved by manipulating the deposition time and silane flow, also the same cantilevers were used to avoid any potential impact of tip size or radius (Voicu et al. 2014). The values for 2 µm thick samples were about 600–1000 nN which is about ten times lower than in currently measured samples. Research conducted by Voicu et al. were done in medium humidity environment of about 40%, also the same type of cantilever (beryllium bronze beam with a SiO<sub>2</sub> ball of 0.35 mm diameter) has been used. Different fabrication process resulted in difference in sample roughness, in case of the thicker samples the roughness has been in range of R<sub>a</sub> 30–70 nm, in comparison to 1.45–1.7 nm R<sub>a</sub> for thinner samples.

Multiple scans of the cantilever tip have shown the roughness of about 6.7 nm with standard deviation of 1.7 nm. Topography of the cantilever has been shown on Fig. 7.

The friction is strongly dependent on the roughness of the films. The interdependence of those parameters is illustrated by Fig. 8.

The decrease of the friction coefficient with the increase of the roughness can be explained by the decrease of the real area of contact, which strongly influence the adhesive component of friction force. Also, it is in good correlation with the adhesive properties of the film which can be

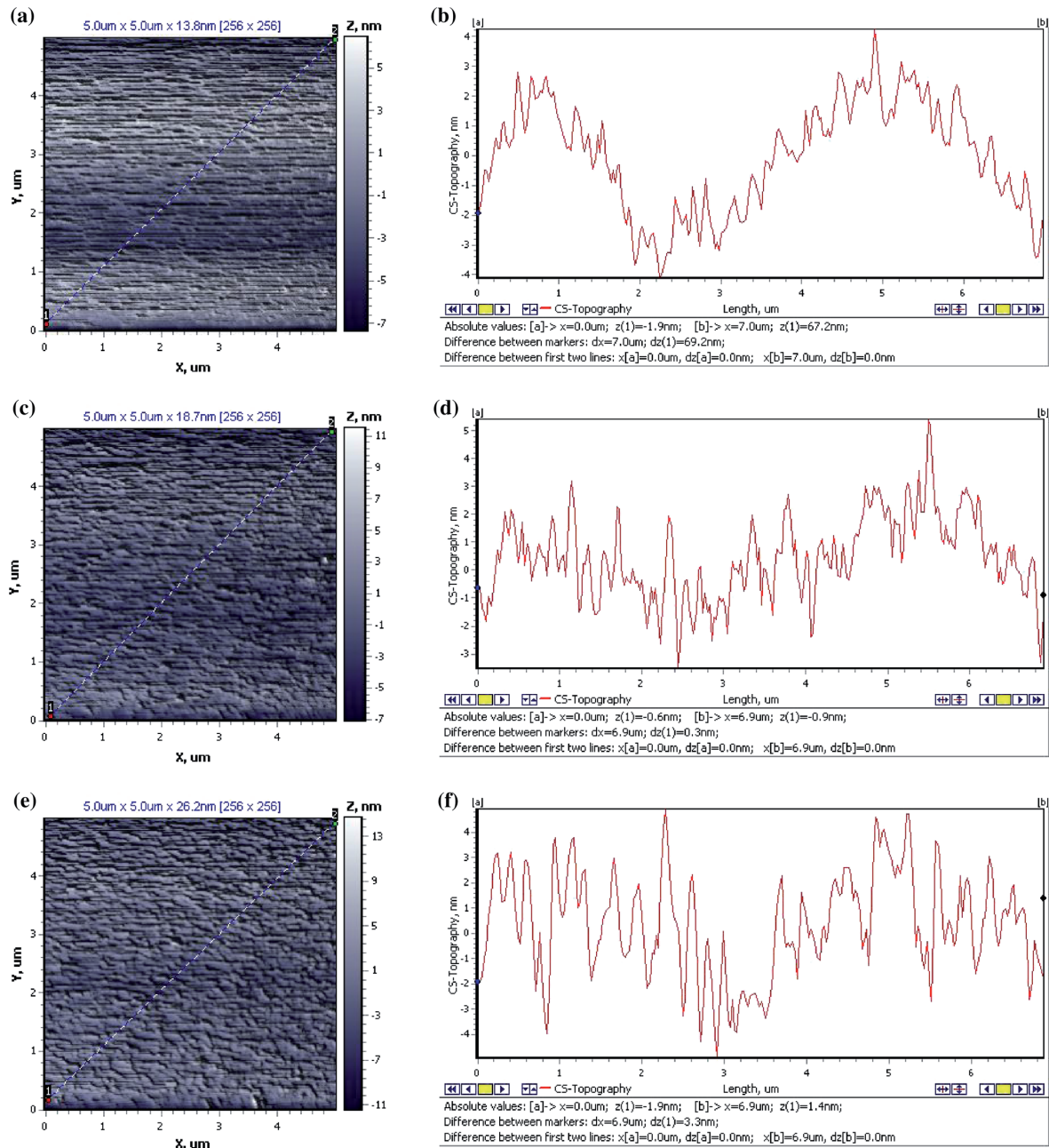


**Fig. 4** Images and cross-sections done using atomic force microscope. **a, c, e** Topography views of samples with surface layer deposited at 580, 610 and 630 °C accordingly. **b, d, f** Cross-sections

of surface topography of polysilicon film deposited at temperature 580, 610 and 630 °C accordingly

observed in Fig. 7. The correlation states here that the lower the adhesion, the lower the friction coefficient as well, while both are presumably connected to the lower real contact area. Previous measurements on thicker samples showed higher friction coefficient of samples that had

higher thickness and higher roughness (Voicu et al. 2014). Those measurement found friction coefficient of about 0.12, which is 1.5 higher than of current samples.

The adhesion and friction for the deposited ultrathin films with the thickness 50 nm is governed mainly by the

**Fig. 5** Surface parameters of fabricated samples: **a**  $R_a$  roughness parameter of polysilicon films vs. temperature (in °C) of their deposition **b**  $R_{ku}$  kurtosis parameter of polysilicon films vs. temperature (in °C) of their deposition

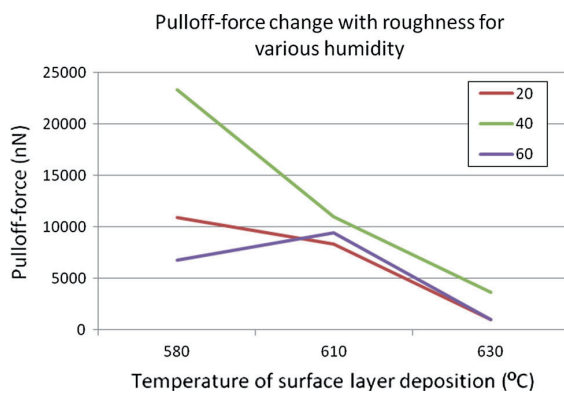
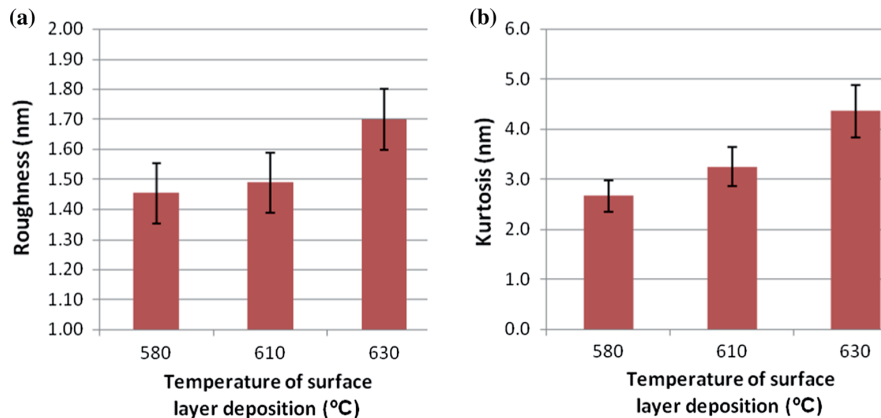


**Fig. 6** Pull-off force (adhesive force) vs. temperature of fabrication (which influenced on roughness, see Fig. 4) and humidity

roughness of the films which is relatively small when the polysilicon films are deposited at the temperature 580, 610 and 630 °C. The differences between surface properties are not very big, but might be significant in production of MEMS and NEMS devices.

## 5 Conclusions

The adhesive and frictional properties of the ultrathin polysilicon films depend on the temperature of their deposition. At higher temperature the roughness of the

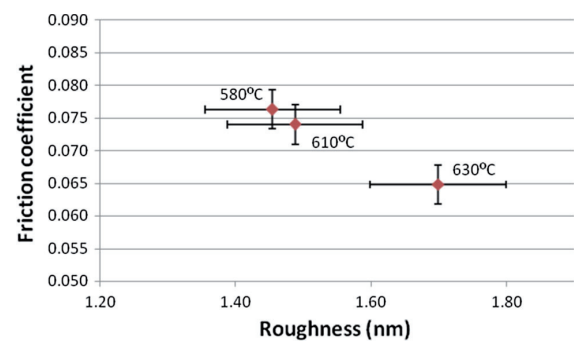
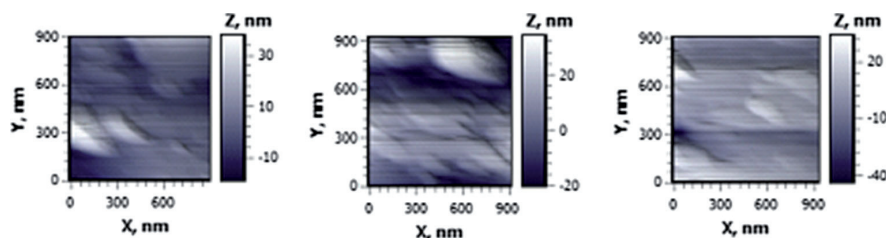


**Fig. 8** Friction coefficient vs. roughness (which depends on temperature of deposition). Points on the chart are samples with surface deposited at various temperatures (marked with *labels*)

films is increasing, which influences strongly the adhesion and friction properties of the surface. The roughness's of the tested ultrathin films were relatively small. Roughness and spikiness of the surface have been increasing along with the increase of the fabrication temperature.

The fact that friction decreases with the increase of roughness and spikiness of the surface suggests that in this range of operation the friction force is governed mainly by the adhesive component of the friction force. To decrease friction and adhesion it is necessary to fabricate the films at higher temperatures which will increase the roughness of the surface and in turn decrease the area of contact. Lower friction coefficient and higher pull off-force in thinner

**Fig. 7** Topography of cantilever ball used for pull-off force measurements in three different locations



samples, with lower roughness, strongly suggests that adhesive component is dominant in new thin samples, but mechanical part of friction is important with samples over 30 nm of Ra. In high roughness contacts the mechanical component of friction is large enough to dominate the friction while at low roughness the real contact area increases and high adhesion occurs which dramatically increasing friction (Rabinowicz 1995). Since at low roughness (up to 1.7 nm Ra) the friction is decreasing with the increasing roughness and at high roughness the friction is increasing with the increase of roughness (Voicu et al. 2014), then it is possible that the minimum of friction coefficient can be achieved with roughness in between 1.7 and 30 nm.

The tested films seem to be good candidates to be used for the fabrication of MEMS devices with sliding components, e.g. vibrating, such as MEMS RF switches. Additional measurements of friction in various humidites should be done in the future in order to assess the influence of its impact on friction coefficient. Further comparison of adhesion to friction in particular environmental properties might also increase our understanding of MEMS surface interactions.

**Acknowledgements** The fabrication of the films carried out by the authors from IMT has been also supported by the Sectoral Operational Programme Human Resources Development 2007–2013 of the Ministry of European Funds through the Financial Agreement POS-DRU/159/1.5/S/132397 and by the Romanian Contract Nucleu No. 15N/2016 TEHNOSPEC (TEHNOlogii generice esențiale pentru priorități ale SPECializării inteligeante).

## References

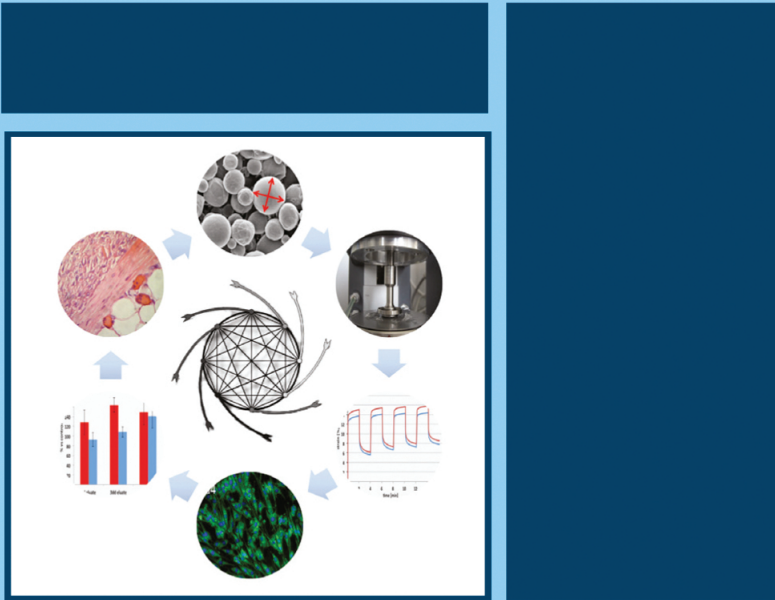
- Achanta S, Celis JP (2015) Nanotribology of MEMS/NEMS. In: Gnecco E, Meyer E (eds) Fundamentals of friction and wear on the nanoscale. NanoScience and technology. Springer, Cham
- Brand O (2005) Fabrication technology. In: Brand O, Fedder GK (eds) CMOS - MEMS. Wiley-VCH Verlag GmbH, Weinheim, Germany
- Hartzell AL, da Silva MG, Shea H (2011) MEMS reliability. Springer, Berlin
- Jarzabek D, Rymuza Z, Ohmae N (2009) Friction and adhesion of carbon nanotube brushes. *Int J Mater Res* 100:973–977
- Jarzabek D, Kaufmann A, Schift A, Rymuza Z, Jung T (2014) Elastic modulus and fracture strength evaluation on the nanoscale by scanning force microscope experiments. *Nanotechnology* 25:21
- Madou MJ (2012) Fundamentals of microfabrication and nanotechnology, vol I–III, 3rd edn. CRC Press, Boca Raton
- Rabinowicz E (1995) Friction and wear of materials, 2nd edn. Wiley, New York, p 315
- Sinha SK, Sujee K, Satyanarayana N, Lim SC (eds) (2013) Nanotribology and materials in MEMS. Springer, Berlin
- Voicu R, Michalowski M, Rymuza Z, Gavrila R, Obreja C, Müller R, Baracu A (2014) Design and analysis of polysilicon thin layers and MEMS vibrating structures. In: Proceedings DTIP 2014—SYMPORIUM on design, test, integration and packaging of MEMS/MOEMS, Cannes Côte d’Azur, France, pp 129–133
- Voicu R, Baracu A, Gavrila R, Obreja C, Danila M, Dinescu A, Bita B, Müller R (2015) Material characterizations for MEMS vibration sensors and biostructures applications. *Dig J Nanomater Biostruct* 10(3):1077–1085
- Yang S, Zhao Y, Jiang Z, Liu Y, Tian B (2013) A micro-force sensor with slotted-quad-beam structure for measuring the friction in MEMS bearings. *Sensors* 13(10):13178–13191
- Zhang W, Meng G, Li H (2005) Electrostatic micromotor and its reliability. *J Microelectron Reliab* 45(7–8):1230–1242



## Monografia – P4

Surface mechanical properties

Jarząbek D., Michałowski M.



# Characterization of Polymeric Biomaterials

Edited by Maria Cristina Tanzi  
and Silvia Farè

# Surface mechanical properties

11

D. Jarząbek\*, M. Michałowski<sup>†</sup>

\*Institute of Fundamental Technological Research, Warsaw, Poland, <sup>†</sup>Institute of Micromechanics and Photonics, Warsaw University of Technology, Warsaw, Poland

## 11.1 Atomic force microscope

Numerous mechanical properties of the surface at the nanoscale can be obtained by the atomic force microscope (AFM). In recent years this measurement device has been widely used in various researches on both classical materials [1–3] and biomaterials [4–6]. AFM allows measuring of surface properties of materials via numerous techniques such as force-distance curves (FDCs), lateral scanning, wear measurements, etc.

### 11.1.1 Force-distance curves

The acquisition of the first FDC was made in order to compare a layered material such as highly oriented pyrolytic graphite (HOPG) and single crystals such as lithium fluoride (LiF) in 1988 [7]. Since then the procedure has been developed both in approach and mathematical analysis. This technique is also called force calibration mode. Its base principle is that the AFM cantilever moves vertically, along the axis perpendicular to the investigated surface, then the contact between the measured sample and cantilever tip occurs and the cantilever retracts from the contact afterward (Fig. 11.1). Vertical movement is governed usually by a piezo-element called piezotube, which allows movement in  $x$ -,  $y$ -, and  $z$ -axis. It should be noted that the range of piezoelement displacement is limited to micrometer scale, therefore the rough positioning of the tip above the sample is done mostly by step motors or a feedback loop controlled constant voltage motors. After the coarse positioning the piezo extends which decreases the distance between the sample and the tip. An example of an FDC can be seen in Fig. 11.2. At the  $x$ -axis of the graph there is the piezo displacement and at the  $y$ -axis the cantilever's deflection. The first part of the curve is called zero line—from point 1 to point 2. It is clear that the cantilever tip is still separated from the sample surface and there is no deflection of the tip with the displacement of the piezo. The next part is noncontact region during which “jump-to-contact” during loading and “jump-off-contact” during unloading occurs, this part is located between points 2 and 3. Knowledge of the cantilever stiffness allows to determine so-called pull-on force and pull-off force. The last part (from 3 to 5) of the curve is the contact line during which the distance between the sample and tip is zero and the deflection of the cantilever and sample deformation occurs. Point 4 is the maximum deflection of the cantilever and point 5 marks the jump-off-contact moment.

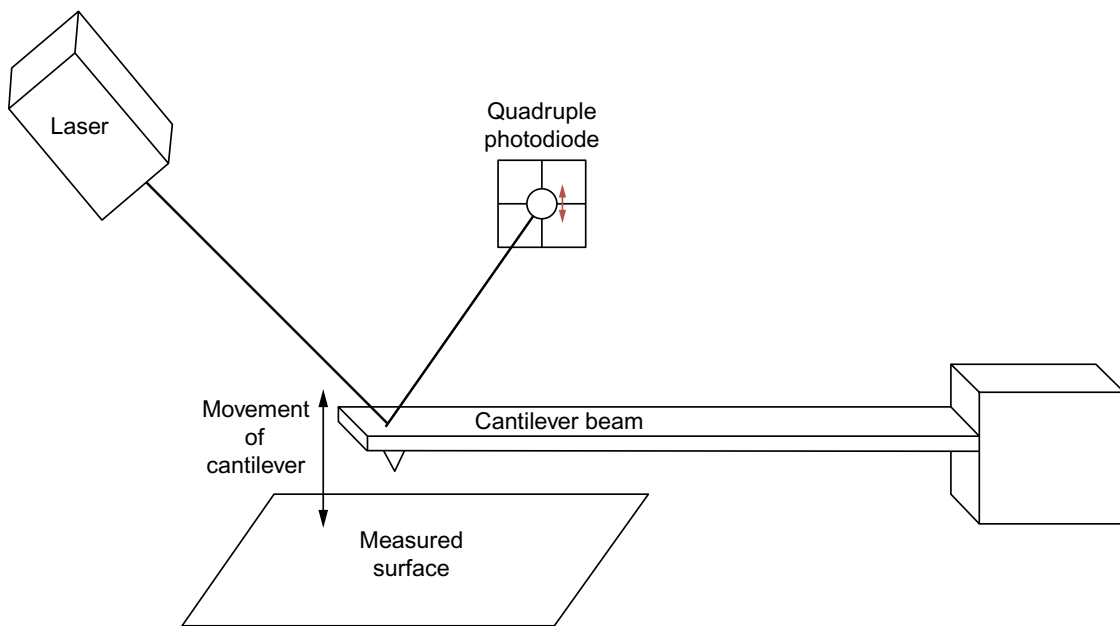


**Fig. 11.1** Schematic of AFM cantilever with a sharp tip during a FDC procedure.

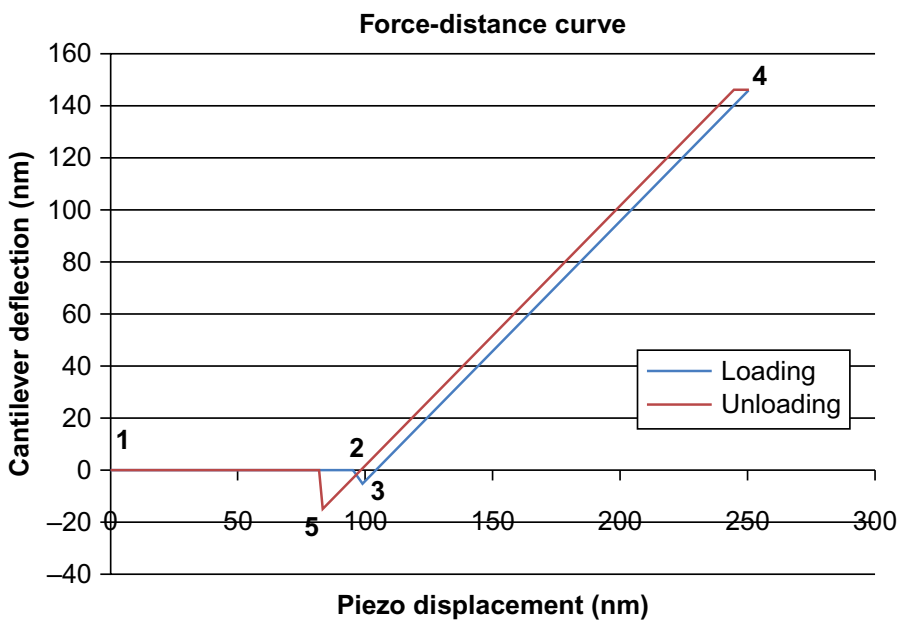


**Fig. 11.2** Sample FDC between a silicon tip and a surface of a silicon wafer. At part from 1 to 2 cantilever's deflection is equal to zero—the approach, 2–3 is the noncontact region during which force between sample surface and cantilever tip exceeds effective elastic constant of the cantilever and the jump-to-contact can be observed. 3–4 is the contact region during which the cantilever deflection rises with the displacement of the piezoelement. The last part is the jump-off-contact at point 5.

Jump-to-contact and jump-off-contact mark the points when the force between the tip and the sample surface is greater than effective elastic constant of the cantilever. Analysis of the zero line, noncontact region, and contact line of the FDC allows to draw numerous information about the tested sample. This procedure has been used in numerous studies on biological samples such as tissues [8], platelets [9], and microbial cells

[10]. Multiple varieties of this procedure have been developed resulting in various application possibilities of measured values. For example, there is a newly developed method of determining surface charge of solid-liquid interface [11].

When one would like to measure FDC, one must perform proper calibration in order to calculate signal from the detector (in volts) to the proper value of a force. The normal force  $F_N$  applied by the cantilever to the measured surface is related to the cantilever's deflection through Hook's law.

$$F_N = k \cdot \alpha \cdot V_{norm} \quad (11.1)$$

where  $V_{norm}$  is the normal deflection of the AFM cantilever expressed in [V] measured by position sensitive diode (PSD),  $\alpha$  is the deflection sensitivity determined from FDC in [V/ $\mu\text{m}$ ], and  $k$  is a spring constant of the cantilever in [N/m], which could be determined using one of the methods described further. Deflection sensitivity  $\alpha$  should be determined as an average of several measurements of the slope in section 3–4 (Fig. 11.2). In order to measure this slope, FDCs should be performed on a rigid sample with high hardness to avoid indentation of the sample's surface. Polished silicon or silicon carbide can be used. In many AFM systems it is possible to adjust the gain of the signal and set the value of sensitivity to 1 V/ $\mu\text{m}$ . It makes the calculations easier and the values of the voltage (in [mV]) at y-axis correspond to nanometers.

It is also worth mentioning that under FDC measurements one can also understand dynamic measurements, in which the cantilever is vibrated by a piezoelement in the AFM head with the known amplitude ( $A$ ) and its oscillations frequency is analyzed. This approach allows to omit some of the problems of the static measurement, for example, the blank spot during jump-to-sample. During the oscillation the effective spring force  $F = kA$  allows to come closer to the sample than during static mode, in which very stiff cantilevers are required, which in turn decreases the horizontal resolution of the measurement. This causes the dynamic modes of surface scanning to give topographies with better resolution, and during FDC measurements allows more detailed measurement of force in the close proximity with the surface, which is important, i.e., during studying of meniscus forces [12]. This procedure, however, requires an additional piezoelement in the head of the AFM that allows vibration of the cantilever. Also the measured output is not a force but a force gradient, which can be calculated into a force afterward. Additionally it is believed that dynamic FDC measurements provide more artifacts than static procedure [12].

### 11.1.1.1 Adhesion measurement

With the use of the FDC technique it is possible to directly measure the adhesion between the surface and the tip of the cantilever (Fig. 11.3). Adhesion is the force that binds the cantilever tip to the sample while retracting and holding it on the surface forcing the cantilever to bend downward (to the sample) until the spring restoring force of the cantilever will not exceed the adhesion force. Therefore adhesion is calculated as a jump-off-contact in the horizontal scale multiplied by a cantilever spring constant  $F_{adh} = k_c \times \delta_c$ . Adhesion energy is related to the adhesion force by  $E = \frac{F}{2\pi R}$  where  $R$  is the radius of the sphere in contact with a surface. However, the actual

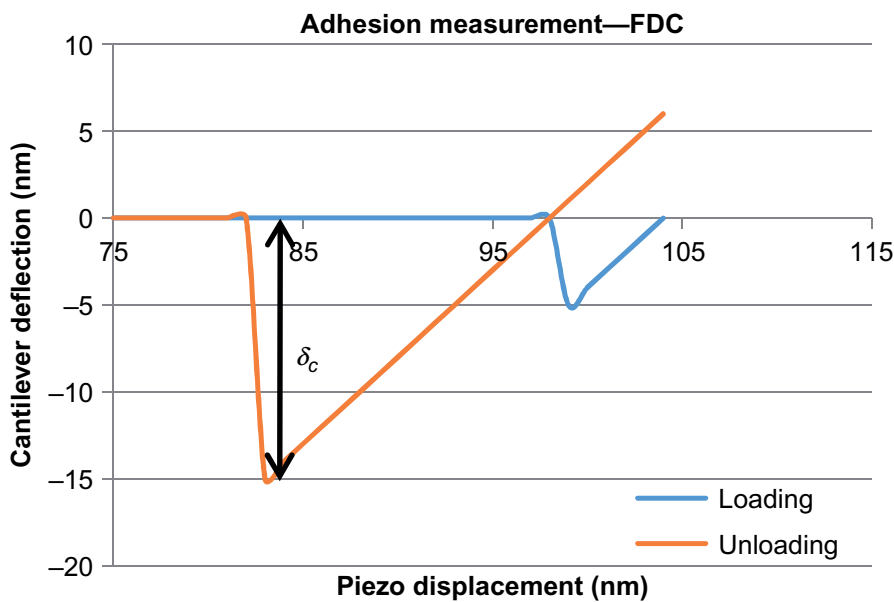


**Fig. 11.3** Chart depicts the adhesion measurement done by FDC. Adhesion force is measured as the jump-off-contact multiplied by cantilever spring constant, during a FDC procedure.

contact area is not as simple to determine as at the macroscale. In order to get the actual contact, we need to use one of the contact models such as Hertz [13]; Johnson-Kendall-Roberts [14]; or Derjaguin, Muller, and Toporov [15]. These models are described further in more details. Additionally, hysteresis can be observed as the distance between the approach and retraction curve. Adhesion measurements have been used with multiple biomaterials studies such as leukocytes [16], cell surface receptors [17], and human endothelial cells [18]. Thin layers of materials such as graphene [19] can be measured as well. Furthermore, the adhesion measurements are performed often in the biomaterials field, for example, adhesion has been found to be influenced by surface roughness of wood surface and natural fiber [20]. Adhesion measurements were conducted in liquid environments as well, which allowed to produce adhesive materials working underwater [21]. Detail protocol has been developed for quantifying cell adhesion forces by AFM measurements [22]. Liu [19] and others have measured the adhesive properties of thin layers of grapheme (FLG—few-layer graphene) by this method and found that the adhesive properties are independent of the number of graphene layers and equal to  $0.23 \pm 0.11 \text{ J/m}^2$ . They have also researched if there is a correlation between number of layers and adhesive force of contact. Interestingly, there has been no correlation for pull-off forces in situations when there has been no previous sliding movement of tip over the surface. However, for thinner layers sliding movement caused an increase in adhesive forces of about 15%. This effect is caused due to the delamination of surface under tensile load.

#### 11.1.1.2 Contact models

The contact radius at the nanoscale is not a direct relation of contacting surfaces like at the macroscale. The actual contact takes place only at a few asperities from both of the surfaces. Those surfaces are deformed by forces that appear between them. The

question of what are those forces is answered differently in various contact models. In the case of AFM measurements, where there is a small, mostly spherically ended tip interacting with a flat surface, it is reasonable to analyze different models for a situation of a sphere in contact with a flat surface.

The most basic contact model was introduced in 1881 by Hertz (Fig. 11.4). It considers two surfaces that elastically deform under an outside force  $F$ . It does not take into account any surface forces or adhesion between two elements. Without these inputs it takes a base point of contact radius  $a_0$  at zero load equal to 0. The crucial parameters can be summed up to:

$$a = \sqrt[3]{\frac{3RF}{4E^*}} \quad (11.2)$$

$$\delta_c = \frac{a^2}{R} \quad (11.3)$$

$$P(x) = \frac{3F\sqrt{1-x^2}}{2\pi a^2} \quad (11.4)$$

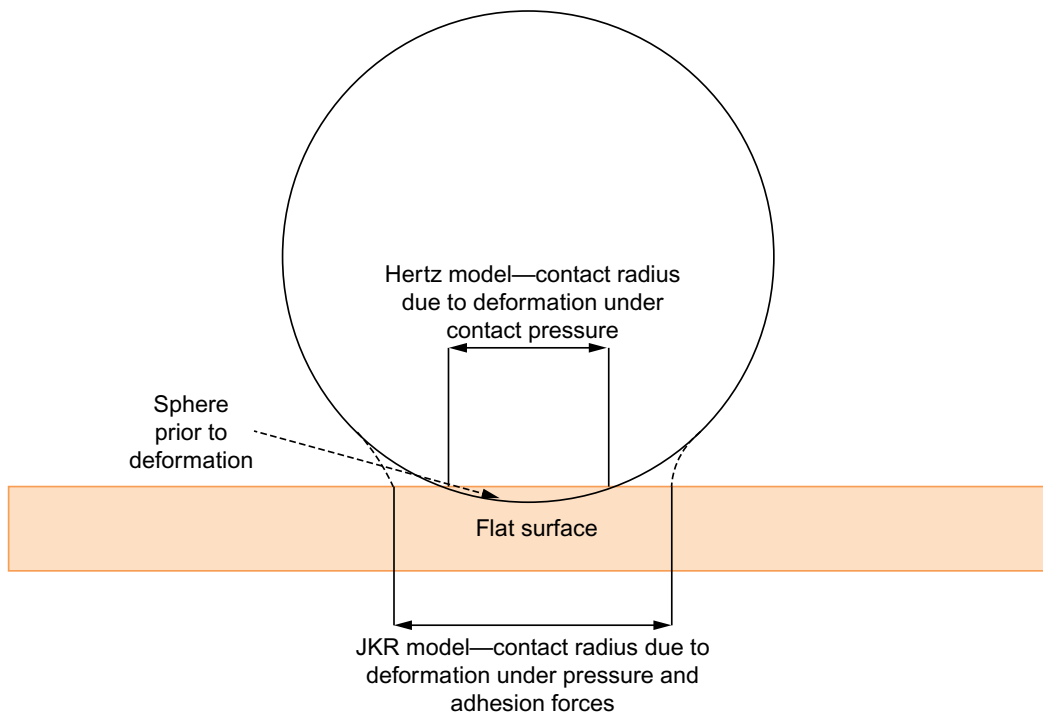


**Fig. 11.4** Schematic shows the actual contact area of a sphere contacting with a flat surface. Deformation and contact radius are presented by calculation with two contact models Hertz (without the impact of adhesion forces) and Johnson-Kendall-Roberts (with the effect of adhesion on contact area).

where  $a$  is the contact radius,  $R$  is the radius of the sphere,  $x = \frac{y}{a}$  and  $y$  is the distance from the center of the contact circle,  $E^*$  is the effective Young's modulus, which is defined by the following equation:

$$\frac{1}{E^*} = \frac{1 - \nu_1^2}{E_1} + \frac{1 - \nu_2^2}{E_2} \quad (11.5)$$

where  $E_1$ ,  $E_2$ ,  $\nu_1$ , and  $\nu_2$  are Young's moduli and Poisson's ratios of the surface and the indenter, respectively. In the case of AFM measurement the cantilever tip is the indenter. In the case of an assumption of a rigid tip with a deformable surface Sneddon analysis has to be employed [23] and Oliver-Pharr method can be used [24]. Since the Hertz model does not take into account surface forces and adhesion it is accurate only for situations when these forces are negligible, for example, in the case of very high loads and materials with low surface energy. Unfortunately, it is rarely the case in AFM measurements, hence, more complex models have to be applied.

There are three more complex models that are currently used in order to calculate the actual contact area from AFM FDC, namely, Johnson-Kendall-Roberts (JKR) [14]; Derjaguin, Muller, Toporov (DMT) [15]; and Maugis [25] model (Fig. 11.4). The DMT model assumes the deformation according to Hertz model but also takes into account the forces acting between two bodies outside of the contact region. The summarized crucial parameters are as follows [15]:

$$F_{ad} = 2\pi RW \quad (11.6)$$

$$a = \sqrt[3]{(F + 2\pi RW) \frac{3R}{4E^*}} \quad (11.7)$$

$$\delta_c = \frac{a^2}{R} \quad (11.8)$$

$$P(x) = \frac{3F\sqrt{1-x^2}}{2\pi a^2} \quad (11.9)$$

where  $F_{ad}$  is the adhesion force and  $W$  stands for the adhesion work at the contact. Taking into account only the forces outside of the contact region, the DMT is accurate for situations of low adhesion and small tip radii, which corresponds to sharp needle tips. In the case of a larger radius of contact and highly adhesive materials, JKR model [14] is more accurate. On the other hand, it neglects the forces outside of the contact area [14]:

$$F_{ad} = \frac{3}{2}\pi RW \quad (11.10)$$

$$a = \sqrt[3]{\left( F + 3\pi RW + \sqrt{6\pi RWF + (3\pi RW)^2} \frac{3R}{4E^*} \right)} \quad (11.11)$$

$$\delta_c = \frac{a^2}{R} - \frac{2}{3} \sqrt{\frac{(6\pi Wa)}{E^*}} \quad (11.12)$$

$$P(x) = \frac{2E^*a}{\pi R} \left(1 - \frac{x^2}{a^2}\right)^{1/2} - \sqrt{\frac{2E^*W}{\pi a}} \left(1 - \frac{x^2}{a^2}\right)^{-1/2} \quad (11.13)$$

Since these two models are suitable for two extreme situations a question arises what to do in the situations in between these two and also where the boundary between them should be set. In this case the Maugis model [25] can be helpful. It introduces a dimensionless parameter  $\lambda$  given by the following equation:

$$\lambda = \frac{2.06}{\xi_0} \sqrt[3]{\frac{RW^2}{\pi \left(\frac{4}{3}\right)^2 E^{*2}}} \quad (11.14)$$

where  $\xi_0$  is the interatomic distance.  $\lambda$  is larger for more compliant, adhesive bodies and smaller for rigid materials with low surface energies. In the case of this model the contact equations are as follows:

$$h = \frac{a^2}{R} - \frac{4\lambda a}{3} \sqrt[3]{\frac{\pi W}{\frac{4}{3} RE^*}} \sqrt{m^2 - 1} \quad (11.15)$$

$$F = \frac{\frac{4}{3} E^* a^3}{R} - \lambda a^2 \sqrt[3]{\left(\frac{\pi W \left(\frac{4}{3}\right)^2 E^{*2}}{R}\right)^2} \times \left(\sqrt{m^2 - 1} + m^2 \arctan \sqrt{m^2 - 1}\right) \quad (11.16)$$

$$1 = \frac{\lambda a^2}{2} \sqrt[3]{\left(\frac{\frac{4}{3} E^*}{\pi W R^2}\right)^2} \times \left(\sqrt{m^2 - 1} + (m^2 - 2) \arctan \sqrt{m^2 - 1}\right) \\ + \frac{4\lambda a^2}{3} \sqrt[3]{\frac{\frac{4}{3} E^*}{\pi W R^2}} \times \left(1 - m + \sqrt{m^2 - 1} \times \arctan \sqrt{m^2 - 1}\right) \quad (11.17)$$

where  $m = \frac{c}{a}$  and  $c$  is the area to which the adhesive forces are extended, and  $a$  is the contact radius. It is worth to note that the value of contact radius is different than calculated in other models. From Eqs. (11.15) to (11.17) it is possible to calculate crucial parameters of the contact. Assuming  $\lambda$  is equal to 0, after some algebraic transformations one can obtain the DMT model and when  $\lambda$  goes to the infinity the Maugis model results in JKR model. Having that in mind, it is possible to use Maugis

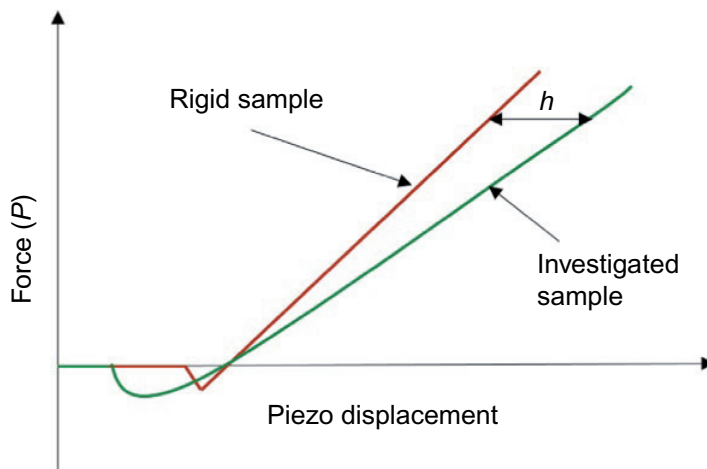
model for all situations of contact. Unfortunately, due to the fact that it is the most complex and one can apply simpler models in many situations: Hertz for high load and low adhesion, DMT for low radius of contact with rigid materials, and JKR for high radius of contact with high surface energies. For value  $\lambda$  below 0.1 the DMT model is suggested, between 0.1 and 10 Maugis model, while above 10 the JKR model [26].

Calculation of the contact area plays a significant role in numerous experiments such as the adhesion measurement of graphene [27] or a study of onion abaxial epidermis walls [28]. Its application with cells has also been studied [29]. During the measurements of cells by the FDC procedure Efremov et al. studied the applicability of contact models for biological samples. They have used a tipless cantilever with glued sphere with diameter of 5  $\mu\text{m}$ . Low stiffness of the cantilever which was equal to about 0.03 N/m allowed the detection of extremely low forces with high resolution. The indentation curves showed that measurements on cells are done in nonequilibrium conditions due to the local interfacial viscoelasticity and complex nature of surface interactions. They did however state that the JKR model can be used to calculate the retraction curve during low holding times (under 10 s). This allows to study cell mechanical properties such as adhesion forces, elastic properties, and the point of zero indentation of cells.

#### 11.1.1.3 Young's modulus and hardness measurement

Due to the acquisition of FDC it is also possible to evaluate mechanical properties of the surfaces. Both hardness and elastic modulus can be calculated from the FDC. There are a few methods to determine the elasticity of the sample with the use of AFM. One of them is to use the previously described contact models. Sometimes it is also possible to use the unloading curve and apply the Oliver-Pharr approach used in the nanoindentation method described in the following chapter and in Ref. [24]. In both cases, one should obtain a force-depth ( $P-h$  curve) from FDCs. In order to obtain the  $P-h$  curve one must compare FDC obtained at a rigid material (i.e., curves from sensitivity measurement) with FDC obtained at an investigated sample. Then the depth  $h$ , which corresponds to a particular value of force is determined according to Fig. 11.5. Finally, in the case of purely elastic contact one can fit one of the previously described contact models (i.e., Hertz or JKR) to the plot of  $P-h$  curve. On the other hand, in the case of an elastic-plastic contact, one should apply Oliver-Pharr method,

**Fig. 11.5**  $P-h$  curve is obtained by subtraction of both plots: FDC performed at rigid, reference sample and FDC performed at an investigated sample.



in which in order to establish the contact area, a contact area function  $A(h)$  must be known. The contact area function needs to be calibrated for each cantilever tip before measurements, which in the case of AFM measurement may be difficult. The most popular method for determination of  $A(h)$  for AFM tips was proposed by Villarrubia [30]. It is also described in details in Ref. [31] where AFM was applied for determining the micromechanical properties of EPDM elastomers. Firstly, one should perform a topography measurement at the reference sample. It is popular to use special calibration grids, i.e., TGX series. Next, one should apply the theory described in Ref. [30]. One can try to write his own script for determination of the contact area function or it is also possible to use ready scripts (i.e., provided by Image Nanometrology). However, it must be remembered that the small radius of the tip may change over the time of use. One should then calibrate the tip shape as often as possible, especially in the case of hard samples measurement.

Another approach toward establishment of Young's modulus in the case of elastic-plastic contact has been proposed by Hoffman et al. [32]. Similar to Oliver and Pharr method, it uses the slope of the unloading curve. However, in this approach a tip without shape calibration can be used. Vertical tip deflection  $\delta_c$  can be related to the electrical signal from AFM photodiode  $D$ , by the following equation:

$$\delta_c = A(D - D_0) \quad (11.18)$$

where  $A$  is cantilever sensitivity and  $D_0$  is the initial deflection signal. Due to the fact that the interaction is modeled as a spring, the deflection is directly related to the applied force  $P$  by Hook's Law. For the tip:

$$P = k_c \delta_c \quad (11.19)$$

and for the sample:

$$P = S(\delta_p - \delta_c) \quad (11.20)$$

where  $k$  is the cantilever spring constant,  $S$  is the contact stiffness, and  $\delta_p$  is the vertical change in the piezo actuator. Combination of these equations gives:

$$\delta_c = A(D - D_0) \left( 1 + \frac{k}{S} \right) \quad (11.21)$$

Using Sneddon definition of contact [23]:

$$S = 2E^* a \quad (11.22)$$

We get:

$$E^* = \frac{\alpha}{\frac{K}{A} - 1} \quad (11.23)$$

where  $K = A \left( 1 + \frac{k}{S} \right)$  and  $\alpha = \frac{k}{2a}$ .

It is possible to obtain parameters  $A$  and  $\alpha$  by measuring two samples with a known elasticity. This method allows to determine the Young's modulus without the contact area function calibration. On the other hand, it requires the measurements of two samples with known Young's modulus. Similarly to other methods, it requires also the knowledge of the Poisson's ratio of the measured sample.

It should be noted that there are many different, nontrivial applications of the measurement of elastic properties by AFM in biomaterials and biology. For instance, it has been used to find the glass transition temperature of polymers [33] or to recognize two different dendritic molecules [34,35] during which researchers mapped the stiffness and elasticity of the molecules. This procedure allowed to state that the generation 4 (G4) dendritic molecules are much more elastic ( $350 \pm 70$  MPa) than generation 3 (G3) molecules ( $190 \pm 30$  MPa) which reflects the higher molecular stiffness of G4. Elastic properties of cells are also measured very often [36–38]. For example, FDC measurements were used to show that cancer cells can be distinguished by nanomechanical testing due to the fact that they display a lower stiffness than benign cells [37].

There are also less popular methods that use more sophisticated models, finite element modeling, or samples with specially designed geometry. For example, in Ref. [39] researchers used FDC procedure to load and unload the stapes annular ligament which attaches the stapes footplate in the human middle ear (Fig. 11.6). Cantilever with a stainless steel ball as a tip was used in order to measure the stiffness of the annular ligament which operates as a flat spring. During normal operation stapes footplate oscillations are within 100-nm amplitude, which makes it impossible to measure with macroscale devices. AFM cantilever allowed measuring its stiffness in physiological range of displacement. Measurements found that the system response is linear in this range and its stiffness, which can be calculated by analysis of a two-spring system (one of which is the cantilever and the second is the annular ligament), is about 120 N/m. From the stiffness of the annular ligament with the knowledge of its dimensions its elastic properties have been derived by assumption that the annular ligament is a homogenous material [39]. This experiment allowed the further work on inner ear prosthetics. The knowledge of

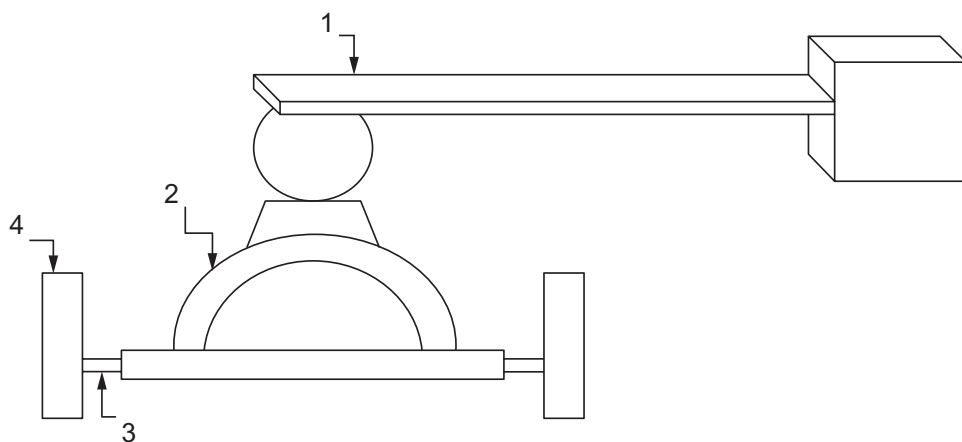


**Fig. 11.6** Figure depicts measurement setup for annular ligament of stapes footplate measurement, where (1) is the cantilever with spherical tip, (2) is the stapes, (3) is the annular ligament, and (4) is the oval window.

elastic properties of the real annular ligament allowed selection of a proper material for the prosthetics and the knowledge of stiffness selects the proper dimensions.

#### 11.1.1.4 Calibration of normal load

Most of the research conducted on AFM requires the knowledge of forces used in the experiment. In order to know the vertical force applied, one can measure the deflection of the cantilever tip. Unfortunately, the exact value of cantilever's normal stiffness is required. Measurement of stiffness or calibration of normal load is one of the first and also one of the most discussed topic in AFM measurement methodology. Numerous papers have been published on various methods of calibration [40–45] and still in different laboratories different methods are used. We will discuss only four of the most popular of them.

The earliest and most basic method of calibration is the calculation of the normal stiffness of the cantilever directly from its dimensions. Normal stiffness is derived from the following equation:

$$k = \frac{Eh^3w}{4l^3} \quad (11.24)$$

where  $h$ ,  $w$ , and  $l$  are dimensions of the cantilever as shown in Fig. 11.7.

This equation is valid only for a rectangular cantilever. However, more complex equations can be derived for V-shaped cantilevers as well. The method is very simple and easy—dimensions can be easily measured by optical or electron microscope, or they are given by the manufacturer. Furthermore, most of the cantilevers are made from materials, which Young's modulus is well known. Therefore it is easy to determine the required calibration constant. Unfortunately, this method makes an assumption that the cantilever is uniform and that the Young's modulus of the thin layer of the material (in this case a thin cantilever) is the same as that of the bulk and has not been influenced by the process of production. Moreover, the most often used technologies of cantilever production do not offer very precise control of the cantilever's dimensions. In particular, thickness  $h$ , which is cubed in the equation, cannot be uniform along the cantilever's length. These problems result in a high error of this calibration method.

Furthermore, an often used method of calibration is performing an FDC measurement on reference probe sample. Various samples are used for this purpose, for

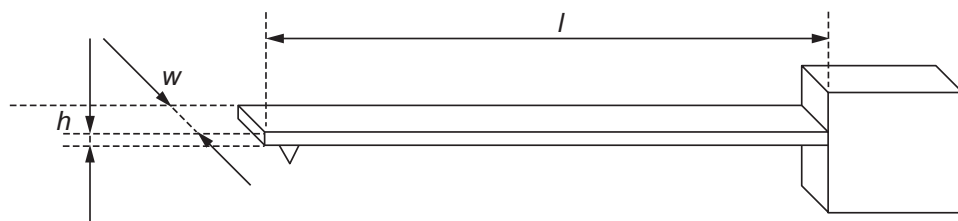
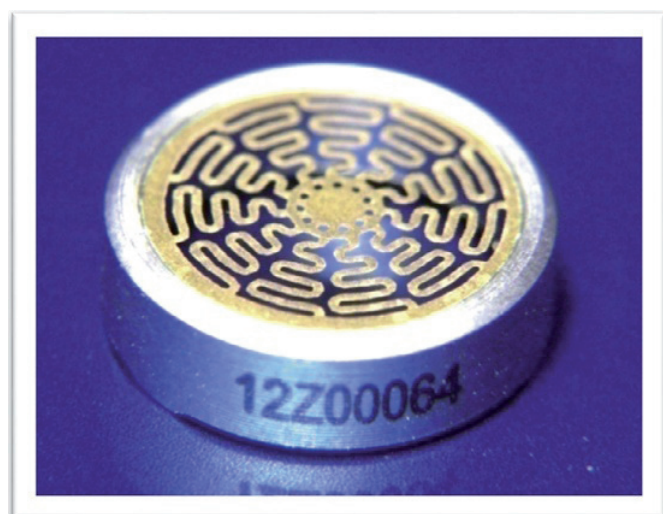


**Fig. 11.7** Cantilever dimensions diagram,  $h$  is the height or thickness of the cantilever,  $w$  is the width, and  $l$  is the length.

**Fig. 11.8** Example of a reference spring used to calibrate normal load of a cantilever used in atomic force microscopy. The spring is made of brass and designed as a flat spring with dimensions such as its spring constant would be stable at the middle of the spring, in this case equal to 35.5 N/m.



instance, piezoelectric cantilevers [46], cantilevers previously calibrated by other means [43] or specifically prepared for this purpose, reference sample which usually is a flat spring [47]. In this approach we consider the whole setup as two sequentially connected springs and we derive the spring constant from the slope of the FDC curve after contact of the two samples. An example of the reference sample is shown in Fig. 11.8.

First advantage of this method is it can be used to calibrate cantilevers without the knowledge of its dimensions and regardless of its shape. Most of the commercially used cantilevers are rectangular shape, however V-shaped are also produced and any cantilevers made with a special geometry for particular purposes can be calibrated by this approach. Second advantage is that it is not necessary to assume uniformity of the cantilever structure. The main disadvantage of this method is the need to use a reference sample and that the measurement error depends strongly on the difference between the spring constant of the cantilever and the reference sample. That requires usage of multiple samples for wide range of different cantilevers.

Another method has been developed by Hutter and Bechhoefer [37] and this approach is based on the fact that cantilever oscillates due to thermal noise. These oscillations can be measured by means of laser interferometry and it is used to calculate the normal stiffness of the cantilever. For rectangular cantilevers the equation is as follows:

$$k = \frac{k_b T}{\langle q^2 \rangle} \quad (11.25)$$

where  $k_b$  is the Boltzmann's constant,  $T$  is the temperature of the cantilever in kelvins, and  $\langle q^2 \rangle$  is the mean squared displacement of the end of the cantilever. This approach is very fast and does not require any dimensions of the measured cantilever. Unfortunately, a very precise method of cantilever displacement determination is necessary. The amplitude of oscillations is in pico-meter range, and while the laser photodiode system has high accuracy, in most cases, it is not able to measure the

oscillations with so small amplitude. Therefore costly laser interferometry is required, which can significantly increase the cost of purchasing AFM. Furthermore, the thermal noise is assumed to be the only source of noise in the system, which is not always true and can produce additional error [38].

The most popular method, which is standardly available in most of AFMs, has been developed by Sader [41,42]. This method enables the normal spring constant to be determined using only the plain view dimensions of the cantilever, its fundamental resonant frequency and quality factor in air. The plain dimensions are easy to measure even by an optical microscope.

$$k_z = 0.1906 \rho b^2 L Q_f \omega_f^2 \Gamma_i^f (\omega_f) \quad (11.26)$$

where  $L$  and  $b$  are the length and width of the cantilever, respectively;  $\rho$  is the density of the fluid (usually air);  $\omega_f$  and  $Q_f$  are the radial resonant frequency and quality factor of the fundamental resonance peak, respectively, and  $\Gamma_i^f$  is the imaginary part of the hydrodynamic function given by Eq. (20) of Ref. [48].

To sum up it should be noted that numerous methods of normal stiffness calibration are available and the choice of which one to use is mostly that of available equipment and time spent on calibration procedure.

### Force-distance curves step by step

1. Perform a few force-distance curves at a rigid sample (i.e., polished silicon)
2. Calculate sensitivity, if possible set it to  $1 \text{ V}/\mu\text{m}$
3. Determine the normal stiffness coefficient (Sader method or other)
4. Perform force-distance curves at your sample
5. If you are interested in adhesion:
  - a. Measure the height of the jump-off-contact according to Fig. 11.3
  - b. Apply one of the contact models, in the case of polymers JKR is the most popular
6. If you are interested in Young's modulus or hardness:
  - a. Perform the tip shape calibration in order to obtain  $A(h)$  function
  - b. Perform FDC at the investigated sample
  - c. Obtain  $P-h$  curves from FDC performed at the investigated sample and at a rigid sample (i.e., those obtained at point 1)
  - d. Fit the suitable contact model to  $P-h$  curve or apply Oliver-Pharr method or Hoffman's method. In the case of Hoffman's method, point c is not necessary. However, one must perform FDC at two other samples with known Young's modulus
  - e. Determine the Young's modulus and hardness from the applied model

#### 11.1.2 Friction and wear

Since the development of lateral force microscope (LFM) mode of AFM it has been possible to measure friction forces at the nanoscale. The base procedure involves contact scanning with a known load of the cantilever tip on the measured surface.

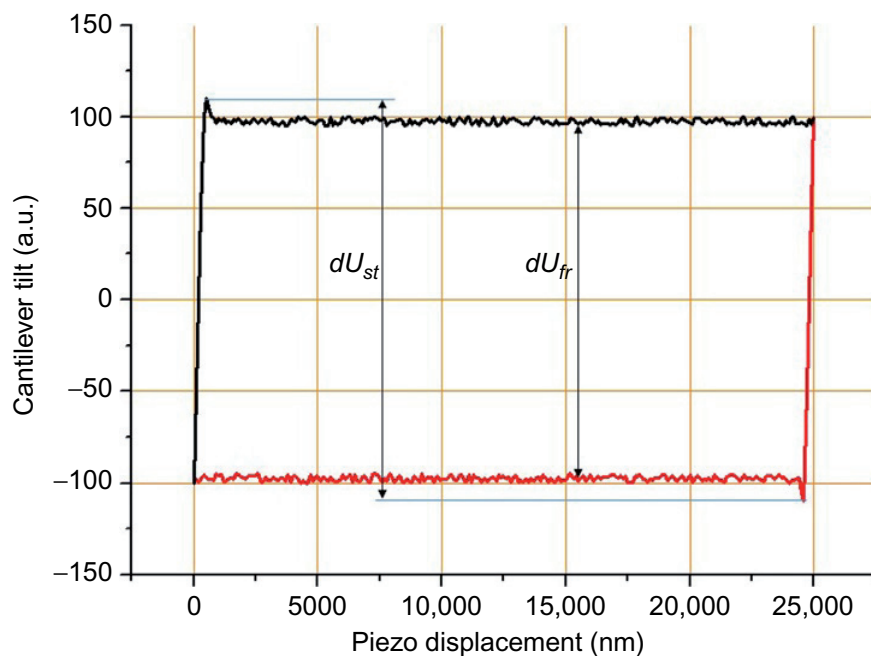


**Fig. 11.9** Chart presents a friction loop, *x*-axis is the horizontal displacement of the piezoelement in the scanning direction, *y*-axis is the cantilever tilt.  $dU_{st}$  represents the double static friction, while  $dU_{fr}$  represents the double dynamic friction. Point is the starting moment of the measurement, cantilever tilts without sliding until point 2, when the tip slips along the surface until its spring constant is in equilibrium with the dynamic friction in point 3. After that dynamic friction occurs until point 4, when measurement in the second direction starts.

Direction of this scan is perpendicular to the length of the cantilever. In order to measure the friction typically a spherical tip is used in order to minimize the scratching of the sample. A spherical tip also allows for a more controlled contact area since its wear affects the contact radius less significantly than the wear of low radius tip. After calibration of the torsional stiffness (methods are described further) it is possible to measure the force that twists the cantilever during scanning; however, the torsion of the cantilever during the scan is not only the result of friction forces but also the topography influences the results. In order to avoid this influence, a scan in both directions along the same line is done. The torsion of the cantilever recorded in both directions is called the friction loop (Fig. 11.9). The distance between the lines corresponds to the sum of the cantilever's torsions in both directions, which in turn means that the friction force is proportional to  $\frac{dU_{fr}}{2}$ , where  $U_{fr}$  is the distance between forward scanning line and backward scanning line on the friction loop chart.

Moreover, both the static friction and the dynamic friction can be determined from a friction loop. In order to measure strictly dynamic friction only the middle part of the loop has to be used ( $U_{fr}$  at Fig. 11.9). The beginning of a friction loop ( $U_{st}$  at Fig. 11.9) depicts the static friction after which a short slip of the cantilever can be seen as a drop in the friction force which occurs when the dynamic friction begins. This procedure measures the total friction between two elements without separation to mechanical

friction and adhesive friction. Due to the low load applied by AFM cantilever it is possible to measure friction at extremely thin films even monolayers [49]. There has been also a method proposed recently to measure friction and elastic properties simultaneously [50].

### 11.1.2.1 Viscosity measurements

AFM can be also used to measure rheological properties (viscosity) of thin films and other samples. There are methods for determination of viscosity of fluids or viscoelastic and viscoplastic solids, i.e., polymers such as PDMS. Here, a simple method which allows to calculate the viscosity from friction loop is shown. Basically, in order to calculate the effective viscosity from friction loop we use the equation for friction of a Newtonian liquid:

$$F_f = \frac{\eta A \nu}{D} \quad (11.27)$$

where  $F_f$  is the friction force;  $\nu$  is the scanning velocity;  $D$  is the measured film thickness; and  $A$  is the actual contact area described as  $A = \pi a^2$ , where  $a$  is the actual contact radius of the contacting asperity. The radius of contact can be estimated according to one of the contact models. If the contact is elastic-plastic then the tip shape calibration should be performed. In the case of viscoelastic solids it is reasonable to assume that the surface forces are significant and the JKR model can be applied. According to this model,  $a$  can be derived according to the following equation:

$$a^3 = \frac{R}{K} \left( F + 6\pi R \gamma + \sqrt{12\pi R \gamma F + (6\pi R \gamma)^2} \right) \quad (11.28)$$

where  $K$  is the bulk elastic modulus given as  $K = \frac{4}{3}E$ ;  $\gamma$  is the surface energy that can be calculated from FDC measurements as  $\gamma = \frac{F_{adh}}{-3R\pi}$ , where  $F_{adh}$  is the pull-off force; and  $R$  is the reduced radius defined as  $R = \frac{R_1 R_2}{(R_1 + R_2)}$ , where  $R_1$  and  $R_2$  are radii of two contacting surfaces. It should be noted that the method is valid only for Newtonian liquids.

### 11.1.2.2 Torsional stiffness calibration

During the precise measurements of lateral forces by AFM it is particularly important to know an accurate value of the cantilever's torsional spring constant and the PSD lateral sensitivity. The combination of these two parameters gives the AFM lateral force calibration constant (LFCC). There are many different methods described in the literature, which can be used to determine LFCC. Unfortunately, it is still challenging to calibrate an AFM system to interpret an LFM signal as a quantifiable surface force (i.e., friction force).

Many LFM calibration methods have been proposed but unfortunately none of them have become the leading method widely accepted by the community. One key reason for this is that straightforward determination of the calibration constant is pretty difficult. Hence, many proposed methods apply some assumptions and simplifications. Therefore the comparison of the different methods and the results obtained due to them is hard or almost impossible. Furthermore, it is even more challenging to produce an agreed methodology for LFM calibration. Basically, due to the fact that it is relatively difficult to implement certain methods weighed against their perceived accuracy. In addition, some methods can exhibit undesirable side effects during implementation, for example, damage to the AFM tip and/or surface. First methods for LFCC determination were based on the geometry of cantilever [51]. They determine LFCC from precisely measured cantilever's dimensions. Unfortunately, classic geometrical approximations can be highly erroneous, partially due to large variances in the materials used for cantilevers.

Modern LFCC determination methods can be grouped into two categories. In the first approach, the lateral sensitivity of PSD and the torsional spring constant of the cantilever are determined separately. For example, in Ref. [52] the nanoindentation tester was used to determine the torsional spring constant of the investigated cantilevers. They were then mounted in AFM and a special calibration grid was applied to calibrate the lateral sensitivity of PSD. On the other hand, in a more common approach LFCC is measured directly, without any separation [53–56]. One of the most accepted methods for LFCC determination is the wedge method developed by Ogletree et al. [53], which was further modified by Varenberg et al. [54]. In this method, LFCC is obtained by analyzing the lateral response of AFM cantilever when scanned across a commercially available trapezoidal calibration grating (Fig. 11.10A). Two chemically identical surfaces at the grating, which are arranged by a given angle  $\theta$  (in radians) to each other, are scanned (Fig. 11.10B). For each surface the friction loop is obtained. In this case, friction loops are not centered so for both of them offsets can be evaluated. According to Ref. [54] the following expression can be used:

$$\sin\theta(L \cos\theta + A)\mu_s^2 - \frac{\Delta_s - \Delta_f}{W_s}(L + \cos\theta)\mu_s + L \sin\theta \cos\theta = 0 \quad (11.29)$$

where  $L$  stands for the load;  $A$  for adhesion; and  $\Delta_s$ ,  $\Delta_f$ , and  $W_s$  are illustrated in Fig. 11.10C. The quadratic equation has two solutions but only the one that satisfies the  $\mu < \tan\theta$  condition is usable. With the derived friction coefficient for the sloped surface, LFCC can then be calculated according to the following equation:

$$\text{LFCC} = \frac{\mu_s(L + A \cos\theta)}{W_s(\cos^2\theta - \mu_s^2 \sin^2\theta)} \quad (11.30)$$

With LFCC every single scan point signal can be converted into a friction force  $F_L$  as long as the setup was not changed. It should be noted that obtained LFCC is valid only

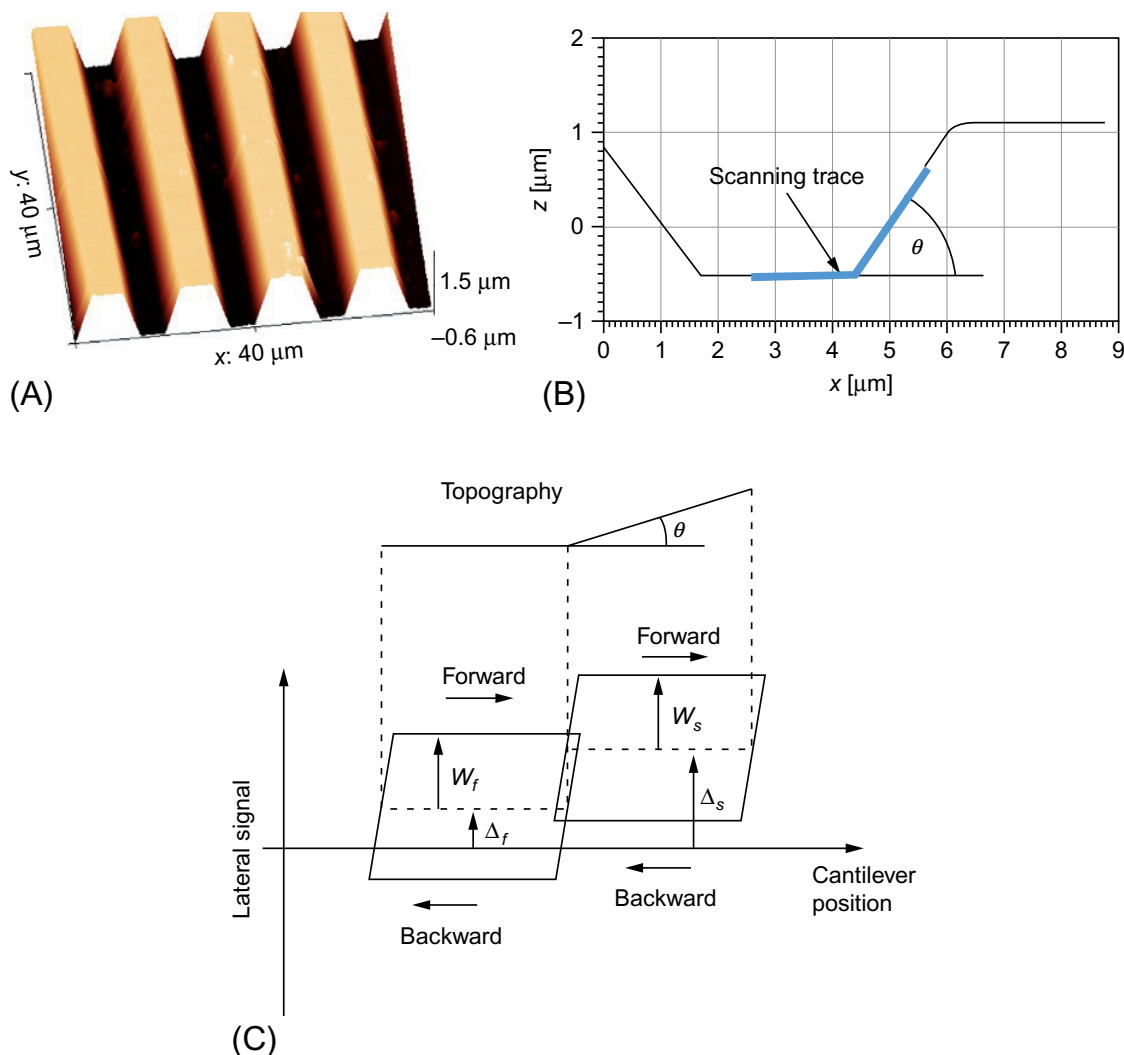


**Fig. 11.10** Calibration grating for the wedge method. Lateral force calibration method. (A) TGZ11 calibration structure, which provides two chemically identical surfaces, one flat and one angled. (B) Forces and moments, which act on AFM tip while scanning the angled surface. (C) Schematic of friction loops gained from the calibration experiment.

for the currently used setup, i.e., the used cantilever and the position of the laser spot on it. If the scanning setup has changed, the system must be calibrated again.

Although, the wedge method is one of the most popular and accepted methods, it still has some disadvantages and inaccuracies. Systematic errors are typically problematic. For example, an often made assumption is that the load exerted on a sloped facet of the calibration grating during trace and retrace scans is the same. However, the feedback system of the AFM can lead to differences in trace and retrace loads. One should then realize that the LFCC is usually determined with inaccuracy equal to about 10%.

It is also possible to purchase a special calibration device for LFCC (i.e., TetraX provided by Tridec). It is costly, but it gives the inaccuracy equal to less than 5% (usually about 1%).

### Friction loops step by step

1. Perform the calibration of the normal load (points 1–3 from FDC table)
2. Perform the calibration of the lateral force according to one of the described methods (i.e., Varenbergh method or apply a LFCC calibration device)
3. Set the AFM into lateral force mode and perform friction loops at the investigated samples
4. If you are interested in the coefficient of friction:
  - a. Use a dedicated computer program or a simple spreadsheet program to determine  $dU$ . Then in order to determine the friction force it must be multiplied by LFCC. Finally, the coefficient of friction is determined by division of the friction force by the normal load
5. If you are interested in viscosity:
  - a. Perform the tip shape calibration and determine the penetration depth according to points 6a–6c from FDC table or use the JKR model
  - b. Use a dedicated computer program or a simple spreadsheet program to determine  $dU$ . Then in order to determine the friction force it must be multiplied by LFCC. Finally, the viscosity can be determined from Eq. (11.28)
6. If you are interested in wear, you should perform a few friction loops at the same place, with high normal load, and then measure the wear trace in a topography mode with low normal load (or in the tapping mode)

### 11.1.3 Nanopillars

One of the newest techniques, which allows the determination of mechanical properties, i.e., Young's modulus and interface strength at the nanoscale is the method described in Ref. [3]. Authors used AFM to exert forces by the cantilever tip onto sample pillars with dimensions of a few tens of nanometers. In this method the cantilever deformations are monitored quantitatively by AFM (Fig. 11.11A). It is then possible to bend the pillars and determine the Young's modulus of the pillars material. Furthermore, force can be raised until the threshold for triggering fracture is reached, which allows the determination of the fracture strength. In Ref. [3] the authors have used this technique to determine the Young's modulus of nanopillars made of single crystal silicon and to measure the interface strength between silicon and silicon dioxide made by LPCVD technique.

During the experiments with nanopillars the cantilever moves across the sample surface along a line forming a 90 degree angle with the cantilever axis—exactly as in the LFM mode. In this method the cantilever exerts the vertical force to the pillars. Due to the third law of dynamics the force bends the cantilever which undergoes torsion flexure during the scanning motion of the cantilever tip across the sample. The force exerted by the cantilever is the predominant cause of nanopillar deformation and fracture. Hence, the accurate calibration of the perpendicular and lateral forces exerted and measured by the AFM is of particular importance for reproducible experiments. It is possible to adjust the normal force via the set point controlled by the feedback which holds the cantilever deflection constant. Unfortunately it is not possible to set the constant lateral force. It is influenced by the value of the normal force as well as

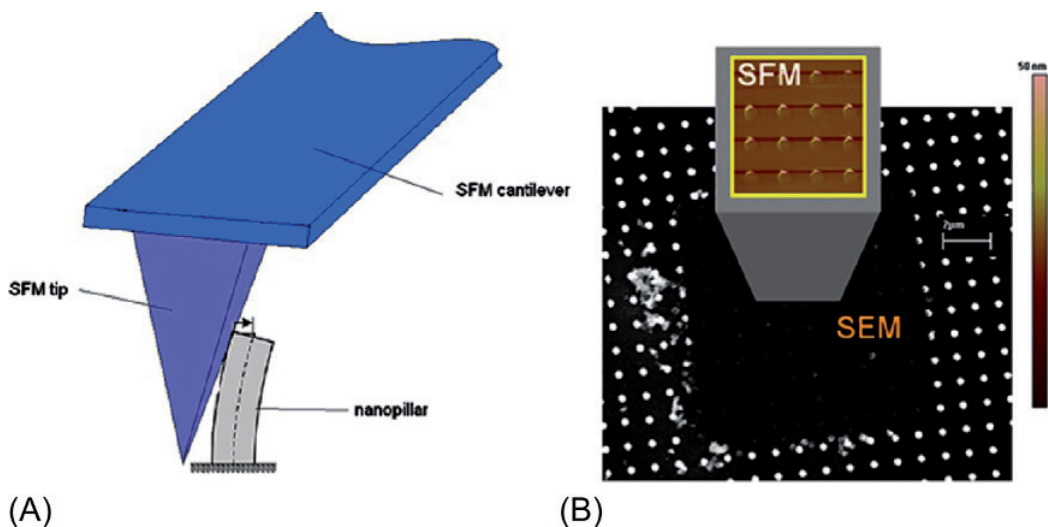


**Fig. 11.11** The method of fracture strength examination by AFM. (A) Sketch of the experimental approach and setup. (Not drawn to scale.) The AFM tip exerts well-defined forces on nanometer scale pillars. The pillars are bent until fracture occurs. (B) A  $10 \times 10 \mu\text{m}^2$  field with one hundred nanopillars is depicted in AFM and SEM micrographs. Some nanopillar debris can be recognized in the SEM micrograph outside of the border of the AFM scan field [3].

the scan velocity and feedback parameters. The scanning parameters should be then obtained empirically and optimized by studying the effect of their variation. The proper calibration of the normal and torsional stiffness should also be performed.

The experiments with nanopillars allow determining two important mechanical properties of materials: Young's modulus and fracture strength. The Young's modulus can be measured from the spring constant associated to cantilever's bending. It can be extracted from the slope of the bending curve. Furthermore, the fracture strength can be determined from the threshold values for the fracture force—the highest force sustained by the pillar. Due to the fact that the aspect ratio of the nanopillars usually is lower than 10 the deflection  $\delta$  of bottom-fixed pillar in response to a lateral force  $F$  at the pillar top can be described by the equation obtained from Timoshenko beam theory [3]:

$$\delta = \frac{64FL^3}{3E\pi D^4} + \frac{4(7+6\nu)FL}{E3\pi D^2} \quad (11.31)$$

where  $E$  stands for the Young's modulus of the pillar's material and  $D$  and  $L$  for its diameter and height, respectively.  $\nu$  is the Poisson's ratio. In order to increase the accuracy of the results, one should measure as many pillars as possible. In Fig. 11.11B, a field of fractured nanopillars ( $100 \times 100$ ) is shown. The statistical analysis allows the accurate determination of the Young's modulus and the fracture strength.

The previously described technique was used in Ref. [3], in order to measure fracture strength and Young's modulus of nanopillars made of silicon. The measured modulus was equal to 130 GPa. Furthermore, the fracture strength of nanopillars made of

pure silicon and containing Si/SiO<sub>2</sub> interface was investigated. Nanopillars of different sizes between 100 and 300 nm in diameter, 200 nm in height, and the interface at 50 nm above the base have been studied in this work. The experimentally determined threshold stress to induce fracture in silicon nanopillars was about 8 GPa, similar to the fracture strength of bulk silicon of about 7 GPa as it has been determined from macroscopic experiments [32,33]. In the case of the fracture strength measurements for the second experimentally probed system, the Si/SiO<sub>2</sub> nanopillars, the fracture initiation always occurs at threshold stresses of about 3 GPa, which is significantly lower than observed for bulk silicon nanopillars of similar diameter. Furthermore, the breakage always occurred at the interface and not, as in the case of crystalline Si pillars, at the pillar base. It is also possible to produce the pillars made of other materials, i.e., polymers and apply this method [57].

## 11.2 Classical instrumented nanoindentation

### 11.2.1 Basics of instrumented nanoindentation

During a well-established, traditional indentation test (macro or micro indentation), a hard tip penetrates into a sample. The tips are often made of a very hard material, i.e., diamond and the tip's properties are known. The test allows to determine the mechanical properties (hardness, Young's modulus) of the investigated sample. The load exerted on the indenter tip is increased and due to this load the tip penetrates into the sample until it reaches a user-defined value. The maximum load may be held constant for some time or removed with accurately set velocity. Next, the area of the residual indentation in the sample is measured and the hardness,  $H$ , is defined as the maximum load,  $P_{max}$ , divided by the residual indentation area,  $A_r$ :

$$H = \frac{P_{max}}{A_r} \quad (11.32)$$

The residual indentation area (projected area) can be measured directly using optical microscopy.

With the progress of the miniaturization, different methods have been developed to measure hardness and Young's modulus at the nanometer scale (i.e., surface layers less than a few micrometers thick). The most common is the nanoindentation technique developed by Oliver and Pharr [24]. Similarly to the classical indentation, an indenter, usually a diamond of known geometry, is pressed into the tested surface. As a result of the nanoindentation the drawing of a loading and unloading curve of the applied load as a function of the penetration depth is obtained (so-called  $P$ - $h$  curve). From the slope of the unloading curve so-called stiffness can be determined:

$$S = \frac{dP}{dh} \quad (11.33)$$

This value includes a contribution from the material being tested as well as the response of the test device. It is possible then to determine the reduced Young's modulus  $E^*$  from the stiffness of the contact:

$$E^* = \frac{1}{\beta} \frac{\sqrt{\pi}}{2} \frac{S}{\sqrt{A_p(h_c)}} \quad (11.34)$$

where  $A_p(h_c)$  is the projected area of the indentation at the contact depth  $h_c$ , and  $\beta$  is a geometrical constant on the order of unity.  $A_p(h_c)$  is often approximated by a fitting polynomial, i.e., for a Berkovich tip:

$$A_p(h_c) = C_0 h_c^2 + C_1 h_c^1 + C_2 h_c^{1/2} + C_3 h_c^{1/4} + \dots + C_8 h_c^{1/128} \quad (11.35)$$

where  $C_0$  for a Berkovich tip is equal to 24.5. The tip shape calibration should be performed in order to obtain  $A_p(h_c)$  function. One should use a sample with a known Young's modulus (i.e., fused silica) and perform indentations for different penetration depths. Then from the reversed Oliver-Pharr method equations one should calculate the value of  $A_p$  for a particular penetration depth. Finally, Eq. (11.35) should be fitted to the obtained data. In most modern nanoindentation devices the tip shape calibration can be performed automatically. The reduced modulus  $E^*$  is related to Young's modulus  $E_S$  of the test specimen through Eq. (11.5).

In order to determine hardness, the area can be measured after the indentation by AFM, optical or electron microscope. An example indentation image is shown in Fig. 11.12. Some indenters use an area function based on the geometry of the tip, compensating for elastic load during the test. Use of this area function provides a method gaining real-time nanohardness values from a  $P$ - $h$  curve.

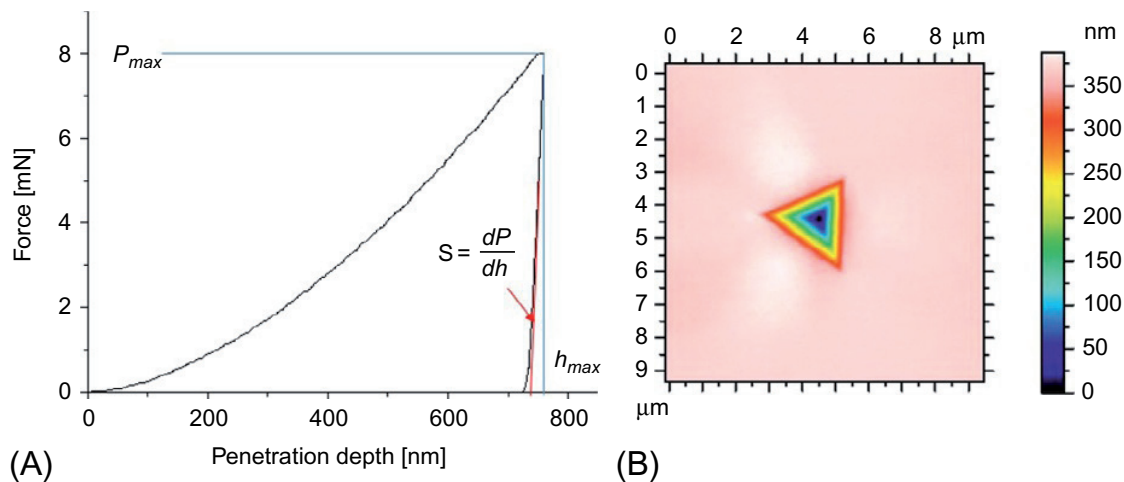


**Fig. 11.12** (A) A force-depth curve obtained from nanoindentation in copper single crystal. (B) A micrograph of a nanoindentation imprint obtained with atomic force microscope.

### 11.2.2 Oliver-Pharr method

From  $P-h$  curves one can determine three important quantities: the maximum load  $P_{max}$ , the maximum displacement  $h_{max}$ , and the elastic unloading stiffness  $S$ . From these parameters it is possible to determine hardness and Young's modulus of the investigated surface without measuring the indentation imprint. The most often used method for determination of the mechanical properties of surfaces by nanoindentation without imaging was developed by Oliver and Pharr in their famous paper [24]. They have modified the method described by Doerner and Nix [58]. Basically, in the Oliver-Pharr (O-F) method, the unloading curves are approximated by the power law relation:

$$P = \alpha(h - h_f)^m \quad (11.36)$$

where  $\alpha$  and  $m$  are power law fitting constants. The value of  $m$  usually ranges from 1.2 to 1.6. Then, assuming that the effect of pileups is negligible, O-F method determines the contact depth  $h_c$  from the following equation:

$$h_c = h_{max} - \epsilon \frac{P_{max}}{S} \quad (11.37)$$

where  $\epsilon$  is a constant that depends upon the geometry of the indenter. The projected area can be then determined from Eq. (11.35). Due to O-F method, nanoindentation is a fast, simple, fully automated, and independent of human bias method for determination of hardness and Young's modulus of the surface layer and thin coatings.

### 11.2.3 Indentation size effect and experimental practice

Mechanical properties of materials at the nanoscale have generated considerable recent research interest because of the fact that some of these properties, i.e., hardness can change significantly when the dimensions of the samples decrease toward the atomistic scale. One should be aware that this effect has been also observed in numerous nano and microindentation experiments—hardness increases usually with decreasing penetration depth. This phenomenon is known as the indentation size effect (ISE). It has been reported that ISE is easily observed for single crystals. The significant increase of hardness in these materials occurs for depths less than 1  $\mu\text{m}$  [59]. The model for ISE was developed by Nix and Gao. It is based on geometrically necessary dislocations (GND). According to this model, the dependence between the hardness and the indentation depth can be described as follows:

$$H^2 = H_0^2 \left( 1 + \frac{h_0}{h} \right) \quad (11.38)$$

where  $H_0$  is the hardness for the indefinitely large indentation depth  $h$  and  $h_0$  is a length scale, which depends on the indenter geometry and the dislocation structure.

It should be noted that if one would like to perform nanoindentation tests, in particular, ISE investigation, the surface layer of samples must be properly prepared. For instance in Ref. [60,61], where copper single crystals were investigated, in order to achieve surface with low roughness ( $R_a < 10 \text{ nm}$ ), the samples were polished and then carefully electropolished. Electropolishing is necessary due to the fact that cutting and polishing the sample can significantly influence the surface layer, i.e., it may introduce stress. It should be noted that even cutting by spark erosion or a precise wire saw may introduce stress into a thin surface layer of an investigated sample, which can significantly influence the nanoindentation results. Finally one should carefully and rigorously clean the samples before nanoindentation. Distilled water, alcohol, and acetone should be used in order to remove any organic and inorganic impurities (i.e., fats). This procedure can be applied to any metal or ceramic samples. On the other hand, in the case of polymers the surface is usually ready for indentation without any additional steps. It is due to the fact that thin polymer films are usually prepared by spin coating, which results in low roughness. Polymers and polymer-matrix composites are also usually much softer than metals or ceramics, therefore roughness can be higher because of the fact that indentation depths are much deeper. For example in Ref. [62], where particle-reinforced silicone-rubber matrix composites were investigated, it was possible to indent samples as they were obtained from production.

#### 11.2.4 Dynamic mechanical analysis by nanoindenters

At the macroscale it is possible to evaluate rapidly complex, storage, and loss modulus as well as phase angle or damping ratio of viscoelastic samples by special dynamic mechanical analysis (DMA). Basically, viscoelastic properties are determined with steady-state oscillation or vibration tests using small tensile (compressive) bars, cylinders, beams in bending or strips in torsion. A modification of this method can be introduced at the nanoscale due to nanoindentation devices. It is usually called dynamic nanoindentation (Fig. 11.13).

In this method a quasi-static force is applied to the indenter probe (like in a classical nanoindentation) while simultaneously a small oscillatory force is superimposed. The dynamic mechanical response of the material can be then modeled by Kelvin-Voigt, Maxwell, or other models of viscoelasticity. For example in Ref. [62] a flat-ended,

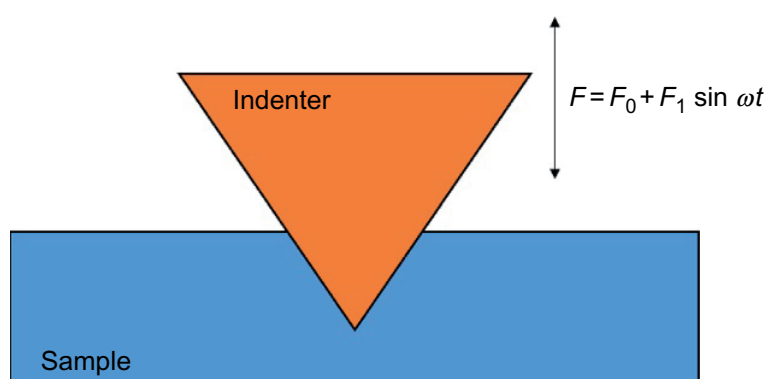


**Fig. 11.13** A scheme of dynamic nanoindentation. A small oscillatory force is superimposed to quasi-static force applied to the indenter.

100- $\mu\text{m}$ -radius tip was used to apply 5- $\mu\text{m}$  pretest compression and a 50-nm oscillation amplitude to particle-reinforced silicone-rubber matrix composites. The oscillation frequency ranged from 1 up to 45 Hz. In this case a complex modulus  $E^c$ , which describes the capacity of storing and consuming energy was defined as follows:

$$E^c = E' + iE'' \quad (11.39)$$

where the real part  $E'$  is the storage modulus that represents the stiffness and it quantifies the ability to store energy elastically, and the imaginary part  $E''$  is the loss modulus that quantifies the ability to dissipate energy. According to Ref. [63] the storage modulus and the loss modulus can be determined from the following equations:

$$E' = \frac{k}{2} \sqrt{\frac{\pi}{A}} \quad (11.40)$$

$$E'' = \frac{\omega C}{2} \sqrt{\frac{\pi}{A}} \quad (11.41)$$

where  $k$  and  $C$  are the stiffness and the damping coefficients of investigated sample, respectively, and  $\omega$  is the loading frequency.  $A$  denotes the projected contact area. This technique has been applied in many different papers. For example in Ref. [64] the viscoelastic properties of epoxy were investigated with a Berkovich and a conospherical tip. Furthermore, in Ref. [65] cellulose nanocrystals were applied in order to reinforce electrospun fibers made of PMMA. The dynamic mechanical properties of the fibers were measured by dynamic indentation.

### Nanoindentation step by step

1. Prepare the sample surface. In the case of metals, the samples should be polished and electropolished. Other samples should also be polished to reduce the roughness if necessary
2. Perform the tip shape calibration with, i.e., fused silica
3. Perform nanoindentation at the investigated samples
4. Measure the imprints with AFM or in the case of bigger imprints with profilometer or optical microscope

## 11.3 Conclusion

Surface mechanical properties play an essential role in the development of nanotechnology and novel materials, i.e., biocomposites. Hardness, Young's modulus, adhesion friction, and wear resistance determine in many cases the possible applications of a new material. Therefore it is of particular importance to measure these parameters qualitatively and quantitatively. It is possible due to modern techniques, i.e., AFM and nanoindentation described in this chapter. However, it should be noted that this topic is extremely broad and also it is developing immensely fast. For instance, new, more

**Table 11.1 The summary of described techniques**

<b>Technique</b>		
<b>Materials</b>	<b>Hardness</b>	<b>Young's modulus</b>
Hard materials, i.e., ceramics Metals	Micro and nanoindentation with diamond indenters.  Micro and nanoindentation with hard (i.e., diamond or sapphire) indenters	Micro and nanoindentation with diamond indenters.  AFM nanopillars  Micro and nanoindentation with hard (i.e., diamond or sapphire) indenters  AFM nanopillars  AFM force-distance curves Nanoindentation Nanoindentation with diamond indenters  AFM force-distance curves
Soft materials, i.e., polymers Thin ceramic or metal films Thin polymer films	AFM force-distance curves Nanoindentation Nanoindentation with diamond indenters  AFM force-distance curves	AFM force-distance curves AFM nanopillars  Nanoindentation with diamond indenters  AFM force-distance curves
	<b>Friction</b>	<b>Adhesion</b>
All materials	AFM friction loops  <b>Viscosity</b>	AFM force-distance curves  <b>Storage and loss modulus</b>
Viscoelastic materials (bulk and thin films)	AFM friction loops	DMA by nanoindentation

precise AFM calibration techniques are being constantly developed. Therefore the knowledge described here is just a basis for further investigation. [Table 11.1](#) sums up the information described in this chapter.

## References

- [1] Kucharski S, Jarząbek D, Piątkowska A, Woźniacka S. Decrease of nano-hardness at ultra-low indentation depths in copper single crystal. *Exp Mech* 2016;56(3):381–93. ISSN: 0014-4851, <http://dx.doi.org/10.1007/s11340-015-0105-2>.
- [2] Birleanu C, Pustan M, Muller R, Dutescu C, Merie V, Voicu R, et al. Experimental investigation by atomic force microscopy on mechanical and tribological properties of thin films. *Int J Mater Res* 2016;107:429–38.
- [3] Jarzabek DM, Kaufmann AN, Schift H, Rymuza Z, Jung TA. Elastic modulus and fracture strength evaluation on the nanoscale by scanning force microscope experiments. *Nanotechnology* 2014;25:215701-1–215701-9. ISSN: 0957-4484, <http://dx.doi.org/10.1088/0957-4484/25/21/215701>.
- [4] Alam F, Balani K. Adhesion force of *staphylococcus aureus* on various biomaterial surfaces. *J Mech Behav Biomed Mater* 2017;65:872–80.

- [5] Wang CY, Zhao YQ, Zheng SN, Xue J, Zhou JL, Tang Y, et al. Effect of enamel morphology on nanoscale adhesion forces of streptococcal bacteria: an AFM study. *Scanning* 2015;37:313–21.
- [6] Valle J, Burgui S, Langheinrich D, Gil C, Solano C, Toledo-Arana A, et al. Evaluation of surface microtopography engineered by direct laser interference for bacterial anti-biofouling. *Macromol Biosci* 2015;15:1060–9.
- [7] Meyer E, Heinzelmann H, Grutter P, Jung T, Weisskopf T, Hidber HR, et al. Comparative-study of lithium-fluoride and graphite by atomic force microscopy (AFM). *J Microsc (Oxford)* 1988;152:269–80.
- [8] Engler AJ, Richert L, Wong JY, Picart C, Discher DE. Surface probe measurements of the elasticity of sectioned tissue, thin gels and polyelectrolyte multilayer films: correlations between substrate stiffness and cell adhesion. *Surf Sci* 2004;570:142–54.
- [9] Lee I, Marchant RE. Force measurements on platelet surfaces with high spatial resolution under physiological conditions. *Colloids Surf B Biointerfaces* 2000;19:357–65.
- [10] Touhami A, Nysten B, Dufrene YF. Nanoscale mapping of the elasticity of microbial cells by atomic force microscopy. *Langmuir* 2003;19:4539–43.
- [11] Zhao CL, Ebeling D, Siretanu I, van den Ende D, Mugele F. Extracting local surface charges and charge regulation behavior from atomic force microscopy measurements at heterogeneous solid-electrolyte interfaces. *Nanoscale* 2015;7:16298–311.
- [12] Fontaine P, Guenoun P, Daillant J. A critical look at surface force measurement using a commercial atomic force microscope in the noncontact mode. *Rev Sci Instrum* 1997;68:4145–51.
- [13] Hertz H. Über die Berührung fester elastischer Körper. *J Reine Angew Math* 1881;92:156–71.
- [14] Johnson KL, Kendall K, Roberts AD. Surface energy and contact of elastic solids. *Proc R Soc London Ser A Math Phys Sci* 1971;324:301–13.
- [15] Derjaguin BV, Muller VM, Toporov YP. Effect of contact deformations on adhesion of particles. *J Colloid Interface Sci* 1975;53:314–26.
- [16] Zhang XH, Wojcikiewicz E, Moy VT. Force spectroscopy of the leukocyte function-associated antigen-1/intercellular adhesion molecule-1 interaction. *Biophys J* 2002;83:2270–9.
- [17] Chen A, Moy VT. Cross-linking of cell surface receptors enhances cooperativity of molecular adhesion. *Biophys J* 2000;78:2814–20.
- [18] Pfister G, Stroh CM, Perschinka H, Kind M, Knoflach M, Hinterdorfer P, et al. Detection of HSP60 on the membrane surface of stressed human endothelial cells by atomic force and confocal microscopy. *J Cell Sci* 2005;118:1587–94.
- [19] Liu XZ, Li QY, Egberts P, Carpick RW. Nanoscale adhesive properties of graphene: the effect of sliding history. *Adv Mater Interfaces* 2014;1:9.
- [20] Jin X, Kasal B. Adhesion force mapping on wood by atomic force microscopy: influence of surface roughness and tip geometry. *Roy Soc Open Sci* 2016;3:7.
- [21] Zhong C, Gurry T, Cheng AA, Downey J, Deng ZT, Stultz CM, et al. Strong underwater adhesives made by self-assembling multi-protein nanofibres. *Nat Nanotechnol* 2014;9:858–66.
- [22] Beaussart A, El-Kirat-Chatel S, Sullan RMA, Alsteens D, Herman P, Derclaye S, et al. Quantifying the forces guiding microbial cell adhesion using single-cell force spectroscopy. *Nat Protoc* 2014;9:1049–55.
- [23] Sneddon IN. The relation between load and penetration in the axisymmetric Boussinesq problem for a punch of arbitrary profile. *Int J Eng Sci* 1965;3:47–57.

- [24] Oliver WC, Pharr GM. An improved technique for determining hardness and elastic-modulus using load and displacement sensing indentation experiments. *J Mater Res* 1992;7:1564–83.
- [25] Maugis D. Adhesion of spheres – the JKR-DMT transition using a Dugdale model. *J Colloid Interface Sci* 1992;150:243–69.
- [26] Johnson KL, Greenwood JA. An adhesion map for the contact of elastic spheres. *J Colloid Interface Sci* 1997;192:326–33.
- [27] Jiang T, Zhu Y. Measuring graphene adhesion using atomic force microscopy with a microsphere tip. *Nanoscale* 2015;7:10760–6.
- [28] Xi XN, Kim SH, Tittmann B. Atomic force microscopy based nanoindentation study of onion abaxial epidermis walls in aqueous environment. *J Appl Phys* 2015;117.
- [29] Efremov YM, Bagrov DV, Kirpichnikov MP, Shaitan KV. Application of the Johnson-Kendall-Roberts model in AFM-based mechanical measurements on cells and gel. *Colloids Surf B Biointerfaces* 2015;134:131–9.
- [30] Villarrubia JS. Algorithms for scanned probe microscope image simulation, surface reconstruction, and tip estimation. *J Res Natl Inst Stand Technol* 1997;102:425–54.
- [31] Ferencz R, Sanchez J, Blumich B, Herrmann W. AFM nanoindentation to determine Young's modulus for different EPDM elastomers. *Polym Test* 2012;31:425–32.
- [32] Hoffman D, Miskioglu I, Drelich J, Aifantis K. Measuring the elastic modulus of polymers by nanoindentation with an atomic force microscope. In: EPD congress 2011; 2011. p. 243–51.
- [33] Cappella B, Stark W. Adhesion of amorphous polymers as a function of temperature probed with AFM force-distance curves. *J Colloid Interface Sci* 2006;296:507–14.
- [34] Shulha H, Zhai XW, Tsukruk VV. Molecular stiffness of individual hyperbranched macromolecules at solid surfaces. *Macromolecules* 2003;36:2825–31.
- [35] Tsukruk VV, Shulha H, Zhai XW. Nanoscale stiffness of individual dendritic molecules and their aggregates. *Appl Phys Lett* 2003;82:907–9.
- [36] Bushell GR, Cahill C, Clarke FM, Gibson CT, Myhra S, Watson GS. Imaging and force-distance analysis of human fibroblasts in vitro by atomic force microscopy. *Cytometry* 1999;36:254–64.
- [37] Cross SE, Jin YS, Rao J, Gimzewski JK. Nanomechanical analysis of cells from cancer patients. *Nat Nanotechnol* 2007;2:780–3.
- [38] Rotsch C, Jacobson K, Radmacher M. Dimensional and mechanical dynamics of active and stable edges in motile fibroblasts investigated by using atomic force microscopy. *Proc Natl Acad Sci U S A* 1999;96:921–6.
- [39] Kwacz M, Rymuza Z, Michalowski M, Wysocki J. Elastic properties of the annular ligament of the human stapes—AFM measurement. *J Assoc Res Otolaryngol* 2015;16:433–46.
- [40] Hutter JL, Bechhoefer J. Calibration of atomic-force microscope tips. *Rev Sci Instrum* 1993;64:1868–73.
- [41] Sader JE, Larson I, Mulvaney P, White LR. Method for the calibration of atomic-force microscope cantilevers. *Rev Sci Instrum* 1995;66:3789–98.
- [42] Sader JE, Chon JWM, Mulvaney P. Calibration of rectangular atomic force microscope cantilevers. *Rev Sci Instrum* 1999;70:3967–9.
- [43] Gibson CT, Watson GS, Myhra S. Determination of the spring constants of probes for force microscopy/spectroscopy. *Nanotechnology* 1996;7:259–62.
- [44] Gibson CT, Weeks BL, Abell C, Rayment T, Myhra S. Calibration of AFM cantilever spring constants. *Ultramicroscopy* 2003;97:113–8.

- [45] Slattery AD, Blanch AJ, Quinton JS, Gibson CT. Accurate measurement of atomic force microscope cantilever deflection excluding tip-surface contact with application to force calibration. *Ultramicroscopy* 2013;131:46–55.
- [46] Aksu SB, Turner JA. Calibration of atomic force microscope cantilevers using piezolevers. *Rev Sci Instrum* 2007;78. Article Number: 043704.
- [47] Sikora A, Bednarz L, Ekwinski G, Ekwinska M. The determination of the spring constant of T-shaped cantilevers using calibration structures. *Meas Sci Technol* 2014;25. Article Number: 044015.
- [48] Sader JE. Frequency response of cantilever beams immersed in viscous fluids with applications to the atomic force microscope. *J Appl Phys* 1998;84:64–76.
- [49] Yang Y, Singh J, Ruths M. Friction of aromatic thiol monolayers on silver: SFA and AFM studies of adhesive and non-adhesive contacts. *RSC Adv* 2014;4:18801–10.
- [50] Tran DK, Chung KH. Simultaneous measurement of elastic properties and friction characteristics of nanowires using atomic force microscopy. *Exp Mech* 2015;55:903–15.
- [51] Ruan JA, Bhushan B. Atomic-scale friction measurements using friction force microscopy. 1. General-principles and new measurement techniques. *J Tribol Trans ASME* 1994;116:378–88.
- [52] Jarzabek DM. Precise and direct method for the measurement of the torsion spring constant of the atomic force microscopy cantilevers. *Rev Sci Instrum* 2015;86:6.
- [53] Ogletree DF, Carpick RW, Salmeron M. Calibration of frictional forces in atomic force microscopy. *Rev Sci Instrum* 1996;67:3298–306.
- [54] Varenberg M, Etsion I, Halperin G. An improved wedge calibration method for lateral force in atomic force microscopy. *Rev Sci Instrum* 2003;74:3362–7.
- [55] Wang HB, Gee ML. AFM lateral force calibration for an integrated probe using a calibration grating. *Ultramicroscopy* 2014;136:193–200.
- [56] Mullin N, Hobbs JK. A non-contact, thermal noise based method for the calibration of lateral deflection sensitivity in atomic force microscopy. *Rev Sci Instrum* 2014;85:9.
- [57] Jarząbek DM. A method for investigation of fracture on the nanometer scale by use of SFM and its applications [PhD thesis]. Warsaw: Warsaw University of Technology; 2013.
- [58] Doerner MF, Nix WD. A method for interpreting the data from depth-sensing indentation instruments. *J Mater Res* 1986;1:601–9.
- [59] Elmustafa AA, Stone DS. Nanoindentation and the indentation size effect: kinetics of deformation and strain gradient plasticity. *J Mech Phys Solids* 2003;51:357–81.
- [60] Kucharski S, Jarzabek D. Depth dependence of nanoindentation pile-up patterns in copper single crystals. *Metall Mater Trans A Phys Metall Mater Sci* 2014;45A:4997–5008.
- [61] Kucharski S, Jarzabek D, Piatkowska A, Wozniacka S. Decrease of nano-hardness at ultra-low indentation depths in copper single crystal. *Exp Mech* 2016;56:381–93.
- [62] Wang KQ, Gao W, Wang XZ, He HL. Quasi-static and dynamic nanoindentation of particle-reinforced soft composites. *J Appl Polym Sci* 2017;134:9.
- [63] Wang ZX, Volinsky AA, Gallant ND. Crosslinking effect on polydimethylsiloxane elastic modulus measured by custom-built compression instrument. *J Appl Polym Sci* 2014;131:4.
- [64] Zhang YF, Bai SL, Yang DY, Zhang Z, Kao-Walter S. Study on the viscoelastic properties of the epoxy surface by means of nanodynamic mechanical analysis. *J Polym Sci B Polym Phys* 2008;46:281–8.
- [65] Dong H, Strawhecker KE, Snyder JF, Orlicki JA, Reiner RS, Rudie AW. Cellulose nanocrystals as a reinforcing material for electrospun poly(methyl methacrylate) fibers: formation, properties and nanomechanical characterization. *Carbohydr Polym* 2012;87:2488–95.

## Publikacja – P5

Impact of graphene coatings on nanoscale  
tribological properties of miniaturized mechanical  
objects

**Michałowski M., Tomasik J., Wiśniewska M.**

# **Impact of graphene coatings on nanoscale tribological properties of miniaturized mechanical objects**

Marcin Michałowski<sup>1</sup>, Jan Tomaszik<sup>2</sup>, and Marta Wiśniewska<sup>2</sup>

<sup>1</sup>Institute of Micromechanics and Photonics, Faculty of Mechatronics, Warsaw University of Technology, Warsaw, Poland

[m.michalowski@mchtr.pw.edu.pl](mailto:m.michalowski@mchtr.pw.edu.pl)

<sup>2</sup>Institute of Metrology and Biomedical Engineering, Faculty of Mechatronics, Warsaw University of Technology, Warsaw, Poland

[{j.tomasik,martwissn}@mchtr.pw.edu.pl](mailto:{j.tomasik,martwissn}@mchtr.pw.edu.pl)

**Abstract.** Impact of graphene coatings on nanoscale tribological properties of miniaturised mechanical objects has been examined. In order to do so, a set of steel, copper-plated specimens has been used, upon which graphen coating has been deposited. Their mechanical and tribological properties such as friction coefficient, hardness and Young's modulus, before and after covering of these samples with graphene layer, have been compared. The results are outlined in the paper, some interesting properties have been found.

**Keywords:** Graphene · nanotechnology · tribology · friction

## **1. Introduction**

Due to its unique features [1,2], graphene has been staying in scientific limelight since its discovery in 2002. It is claimed that the deposition of graphene layer on surfaces of industrial elements may significantly improve their mechanical properties and lead to decline in friction coefficient or increase in hardness and elasticity [3]. Therefore, graphene coatings may become an attractive alternative to the ones that are already used in the manufacturing. However, no attempt has been made to investigate, and quantitatively describe, graphene performance in practical industrial applications yet. In order to overcome this barrier and, in effect, make graphene coatings conducive to manufacture on a mass scale, the GRAPH-TECH research project was introduced. Its aim is to evaluate impact of graphene coatings on tribological properties of miniaturized industrial objects, i.e. bearings or gearwheels. To do this, values of

hardness, Young's modulus, friction coefficient and roughness parameters [4], both before and after graphene deposition, have been estimated and compared.

The core findings of the research, referring to nanoscale mechanical properties of these objects, are presented in the paper.

## 2. Materials and Methods

### 2.1 Test Specimens

Three sets of test specimens, differing in the steel grade they were made of (40HM, 35HGS and MS45), have been used to assess an influence of graphene layer on nanoscale tribological properties of mechanical elements. All these sets consist of three samples, each with test surface of (20x20) mm. First, the test surfaces were milled and grinded. Then, there was an electrolytic copper plated on them. Only the surfaces prepared this way were graphene-covered.

### 2.2 Measurement Equipment

The test specimens have been measured after copper- and graphene- plating respectively.

In order to evaluate their friction coefficient values the NT-206 AFM by Microtestmachines was used. AFM's are often used for a wide range of nano-scale studies in recent years [5, 6]. This microscope is equipped with a beryllium bronze cantilever with a tip of a steel bearing ball that has a diameter of 0.35 mm. Before conducting the measurements the NT-206 system had been calibrated with stiff reference surfaces, silicon wafer and Nanoidea membranes consecutively. Then, the friction loops (Fig. 1) were created for each and every test specimen before and after graphene deposition. The measurement data obtained this way was used to estimate friction coefficient values.

In the same time, the hardness-indentation depth characteristics were obtained using Hystiron UBi-1 with Berkovi nanoindenter. Then, the Oliver and Pharr formula [7] was used to identify hardness and Young's modulus of the test surfaces.

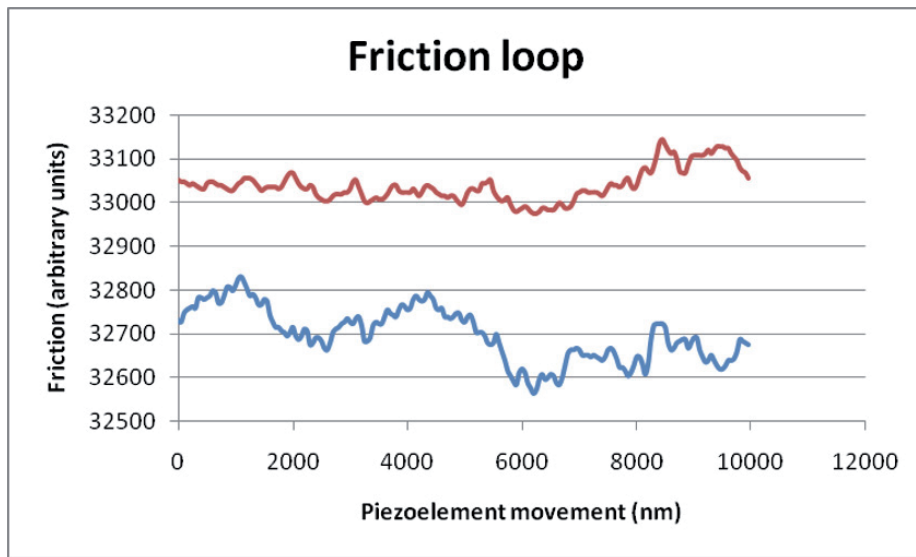


**Fig. 1.** Sample friction loop obtained using AFM (forward movement – red line; backward movement – blue line)

### 3. Results

#### 3.1 Hardness

In order to evaluate impact of graphene coating on a nanoscale hardness of industrial elements, 30 indentations of every specimen were done, both before and after graphene deposition, performed. The maximum load of  $1500 \mu\text{N}$  has been applied for two seconds each time. It is also worth mentioning that both loading and unloading the specimens have lasted for five seconds.

Sample hardness measurement results are presented in Fig. 2 and Fig. 3. They clearly show that hardness is strongly dependent on indentation depth. It may be due to the fact that during experiments indentation process is strongly affected by the geometrical features of the investigated surface (peak, valley or slope).

Also, there are two levels of hardness for the same indentation depth value acquired during the measurements of the test specimens without graphene coating. However, when the graphene-coated samples considered only one level of hardness is visible.

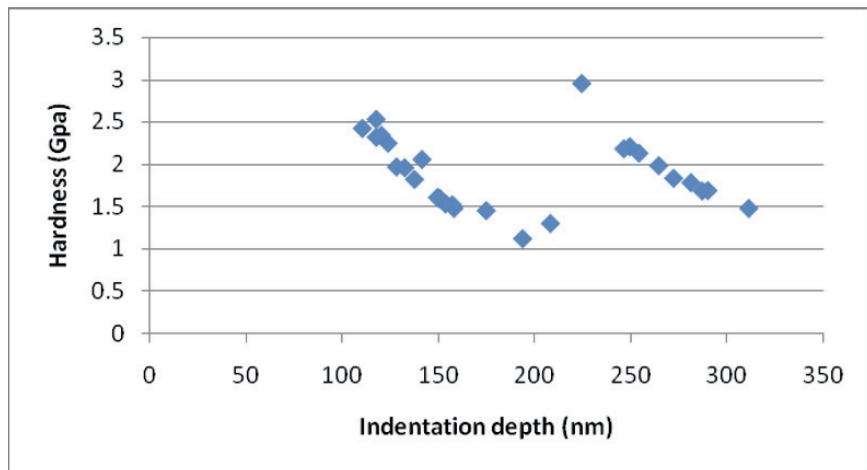


**Fig. 2.** Sample hardness vs. indentation depth - specimen before graphene deposition (40HM-1)

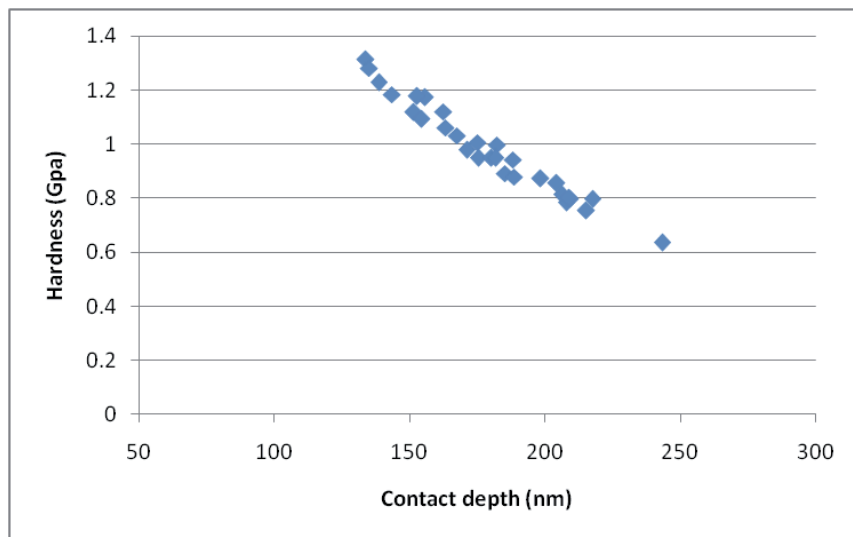


**Fig. 3.** Sample hardness vs. indentation depth - graphene-coated specimen (MS45-1)

Sample hardness measurement results for constant indentation depth are presented in Fig. 4. The chart proves that hardness of measured surface becomes stable after deposition of a graphene layer, but the values of hardness are smaller than the ones obtained before graphenecoating. However, it must be taken into account that during hardness measurements of layers as thin as graphene ones, an impact of the base surface on the results is crucial. Therefore, the decrease of nanoscale hardness is not a result of a graphene layer itself, but is dependent on a choice of an electrolytic copper as a base material.

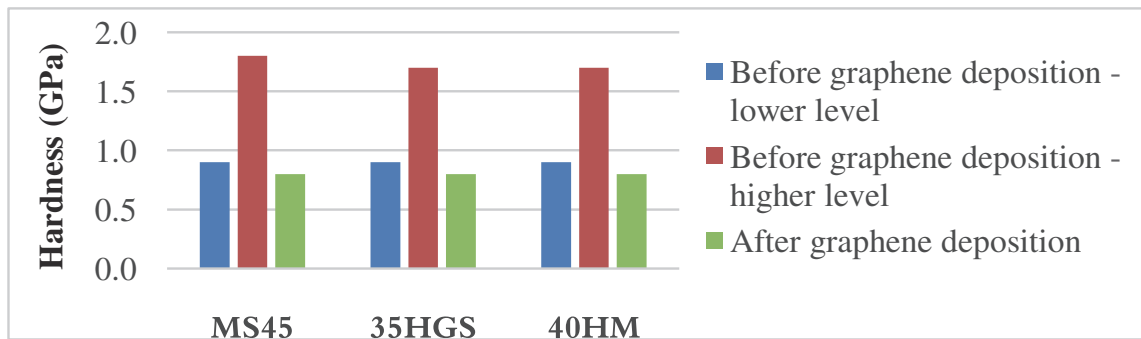


**Fig. 4.** Hardness measurement results obtained for indentation depth of 200 nm

### 3.2 Friction Coefficient

Friction coefficient values of the specimens before and after graphene deposition are presented in Fig. 5.

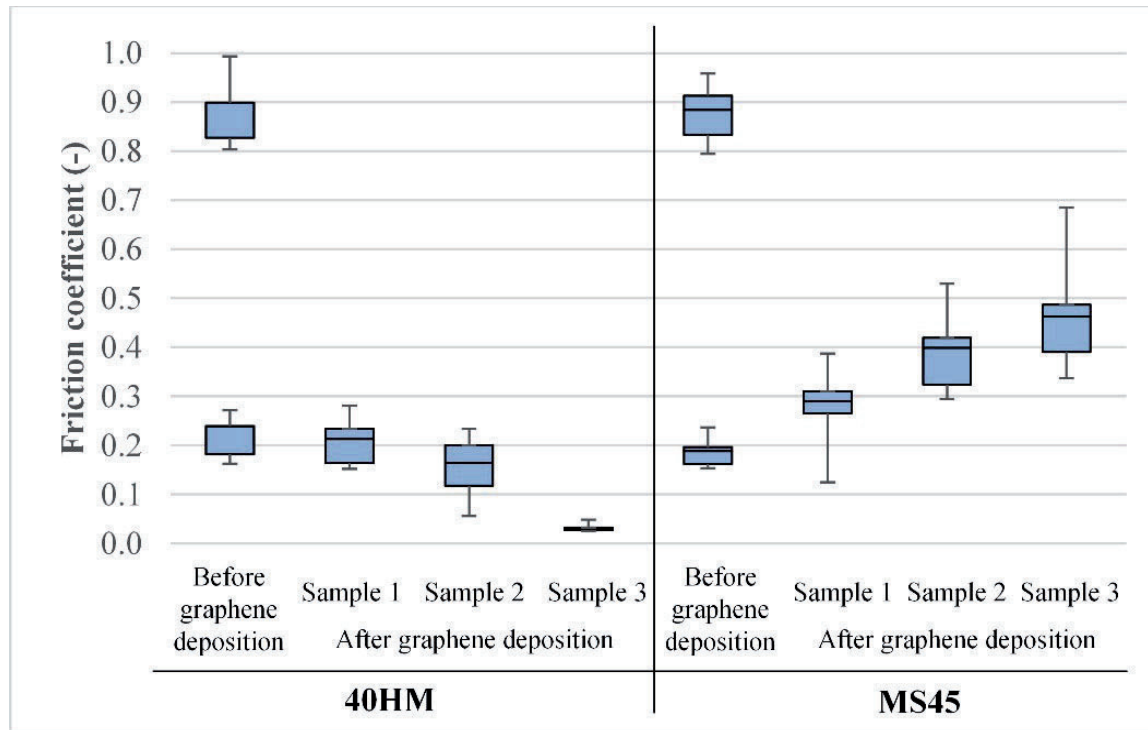


**Fig. 5.** Sample friction coefficient measurement results

Each data set in box-whiskers chart refers to ten measurement results. Every measurement consisted of 256 scanning lines with 256 measurement points each, along the specimen surface. Similarly to the hardness measurement results, there had been a significant variability of measurement results observed before the specimens were graphene-covered. The results can even be divided in two separate groups with medians of about 0.2 and 0.9 respectively, as it is shown in Fig. 5.

Such an extreme variability of the estimated friction coefficient values is not discerned when graphene-plated surfaces are considered. However, the repeatability of the results is slightly dependent on the steel grade the specimens are made of. Also, even with the same base material applied, the variability of results may differ, probably as an effect of divergent quality of graphene coatings. In spite of these, slight improvement of nanoscale frictional properties may be observed, when graphene is deposited on the coppered 40HM steel.

### 3.3 Young's Modulus

Young's modulus was measured by thirty indentations of each specimen. Sample results given in the research are presented in Fig. 6.

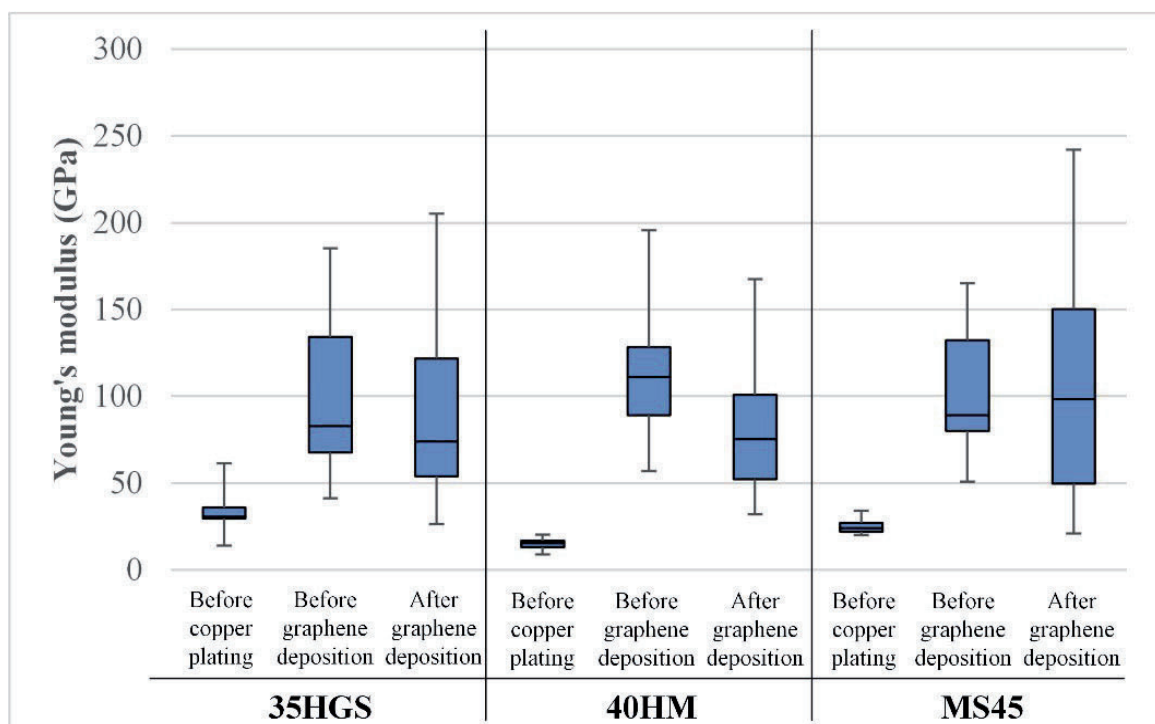


**Fig. 6.** Sample Young's modulus values obtained in the research

There is a significant improvement of nanoscale Young's modulus of the test samples just after plating copper on the steel base. However, there are no differences between values of this parameter that are important from practical point of view.

## 4. Conclusion

The results achieved in the research indicate that graphene coatings may improve the nanoscale tribological properties of steel, copper-plated mechanical objects. Firstly, in spite of their initial variability, hardness and friction coefficient values become

uniform within range of the whole graphene-plated surface. However, depending on the choice of base material, Young's modulus values are not improved by using graphene coatings. In order to minimise an influence of base material on the assessment of tribological features of graphene-coated industrial elements lower loads can be used in the future researches.

## Acknowledgements

This work was supported by grant Graf-Tech/NCBR/05/13/2012 from the National Centre for Research and Development, Poland.

## References

1. A. Geim "Graphene:status and prospects" Science 324 (2009).
2. U. K. Sur "Graphene: a rising star on the horizon of materials science" International Journal of Electrochemistry 2012.
3. A. Klemenz, L. Pastewka, S. G. Balakrishna[et al.] "Atomic Scale Mechanisms of Friction Reduction and Wear Protection by Graphene" Nano Lett.14 (2014).
4. J. Tomasik, M. Wiśniewska "Badania wpływu powłok grafenowych na mikrogeometrię powierzchni" Mechanik 88 (2015).
5. R. Voicu, Z. Rymuza, M. Michałowski [et al.] "Investigations of surface properties of SiO<sub>2</sub> and Si<sub>3</sub>N<sub>4</sub> thin layers used for MEMS vibrating structures applications" CAS 2013 Proceedings / Conference Committee, 2013.
6. D. M. Jarząbek, A. N. Kaufmann, H. Schift [et al.] "Elastic modulus and fracture strength evaluation on the nanoscale by scanning force microscope experiments", Nanotechnology 25 (2014).
7. W.C. Oliver, G.M. Pharr „Measurement of hardness and elastic modulus by instrumented indentation: Advances in understanding and refinements to methodology”, J. Mater. Res. 19 (2004).

## Publikacja – P6

### Annular Ligament of the Human Stapes—AFM Measurement

Kwacz M., Rymuza Z., Michałowski M.,  
Wysocki J.

# *Elastic Properties of the Annular Ligament of the Human Stapes—AFM Measurement*

**Monika Kwacz, Zygmunt Rymuza,  
Marcin Michałowski & Jarosław Wysocki**

**Journal of the Association for  
Research in Otolaryngology**

ISSN 1525-3961

JARO  
DOI 10.1007/s10162-015-0525-9



 Springer

**Your article is protected by copyright and all rights are held exclusively by Association for Research in Otolaryngology. This e-offprint is for personal use only and shall not be self-archived in electronic repositories. If you wish to self-archive your article, please use the accepted manuscript version for posting on your own website. You may further deposit the accepted manuscript version in any repository, provided it is only made publicly available 12 months after official publication or later and provided acknowledgement is given to the original source of publication and a link is inserted to the published article on Springer's website. The link must be accompanied by the following text: "The final publication is available at [link.springer.com](http://link.springer.com)".**



## Research Article

# Elastic Properties of the Annular Ligament of the Human Stapes—AFM Measurement

MONIKA KWACZ,<sup>1</sup> ZYGMUNT RYMUZA,<sup>1</sup> MARCIN MICHAŁOWSKI,<sup>1</sup> AND JAROSŁAW WYSOCKI<sup>2</sup>

<sup>1</sup>*Faculty of Mechatronics, Institute of Micromechanics and Photonics, Warsaw University of Technology, ul. św. A. Boboli 8, 02-525, Warsaw, Poland*

<sup>2</sup>*Department of Otolaryngology, Medical University of Warsaw, Warsaw, Poland*

Received: 12 April 2014; Accepted: 17 May 2015

## ABSTRACT

Elastic properties of the human stapes annular ligament were determined in the physiological range of the ligament deflection using atomic force microscopy and temporal bone specimens. The annular ligament stiffness was determined based on the experimental load-deflection curves. The elastic modulus (Young's modulus) for a simplified geometry was calculated using the Kirchhoff-Love theory for thin plates. The results obtained in this study showed that the annular ligament is a linear elastic material up to deflections of about 100 nm, with a stiffness of about 120 N/m and a calculated elastic modulus of about 1.1 MPa. These parameters can be used in numerical and physical models of the middle and/or inner ear.

**Keywords:** annular ligament, stapes, elastic modulus, atomic force microscopy

**Abbreviations:**  $A$ ,  $b$ ,  $h$ —Dimensions of the annular ligament circular plate (outer radius, inner radius, and thickness, respectively); AFM—Atomic force microscope; AL—Annular ligament;  $\delta f_c$ —Deflection of the cantilever;  $E$ —Elastic (Young's) modulus of the annular ligament of the human stapes;  $F$ —Force acting between the sample and the tip;  $F-d$ —Force-distance curve; FE—Finite element;  $K$ —Deflection sensitivity factor;  $k_c$ —Real spring constant (stiffness) of the cantilever;  $k_n$ —Nominal spring constant of the cantilever;  $k_{ref}$ —Spring constant of the reference

cantilever;  $L_{ow}$ ,  $W_{ow}$ —Length and width of the oval window;  $L_{sf}$ ,  $W_{sf}$ —Length and width of the stapes footplate;  $v$ —The Poisson's ratio; SF—Stapes footplate; SPL—Sound pressure level; SVJ—Stapediovestibular joint;  $V$ —Voltage of the photodiode;  $V_{rigid}$ —Voltage of the photodiode for the rigid sample;  $w$ —Deflection of the annular ligament plate;  $z$ —Displacement of the piezoactuator;  $z_{al}$ —Displacement of the piezoactuator on the AL sample;  $z_{rigid}$ —Displacement of the piezoactuator on the rigid sample

## INTRODUCTION

The annular ligament (AL) of the stapes attaches the stapes footplate (SF) to the vestibular window (Brunner 1954, Bolz and Lim 1972). This attachment is known as the stapedio-vestibular joint (SVJ). The SVJ enables the stapes to vibrate (Wolff and Bellucci 1956, Whyte et al. 2002). The movement of the SF causes pressure changes within the fluid, consequently stimulating the cochlea's sensory hair cells. The bending of the hair cells leads to the conversion of mechanical vibration to action potentials in the auditory nerve fibers. Transmission electron microscopy has shown that the AL of the SVJ is mainly composed of thicker elastic fibers and thinner transverse micro-fibrils (Ohashi et al. 2006). The elastic ligament fibers are regularly arranged in a parallel array and inserted into the cartilaginous matrices. The fibers transversely cross the SVJ between the SF and the vestibular window. The elastic properties of the AL affect the SF displacement amplitude and thus directly affect the middle ear transfer function. It is well known that the vibration amplitude of the SF is dependent on both the frequency and the sound

*Correspondence to:* Monika Kwacz · Faculty of Mechatronics, Institute of Micromechanics and Photonics · Warsaw University of Technology · ul. św. A. Boboli 8, 02-525, Warsaw, Poland. Telephone: +48 22 234 8447; email: m.kwacz@mchtr.pw.edu.pl

pressure level (SPL) at the tympanic membrane. Several authors have observed linear growth of the SF displacement with the SPL, which indicates that the system is linear (Merchant et al. 1996, Asai et al. 1999). Experiments in healthy human ears have also shown that the SF displacement rises slowly from the low frequencies to near the peak ( $\sim$ 10–20 nm at about 0.8–1.0 kHz for 80 dB SPL) (Asai et al. 1999, Heiland et al. 1999, Hato et al. 2001, Huber et al. 2001, 2003; Stenfelt et al. 2004, Chien et al. 2009) and falls off as frequency increases above the peak.

Knowledge of the mechanical properties of the AL is necessary for modeling sound transmission from the middle ear to the cochlear fluid. Theoretical modeling approaches have been reported for the middle ear mechanics in normal (e.g., Wada et al. 1992, Sun et al. 2002, Gan et al. 2006, Gentil et al. 2011), diseased (e.g. Dai et al. 2007, Gan and Wang 2007, Gan et al. 2009, Zhao et al. 2009) and reconstructed (e.g., Ladak and Funnell 1996, Zahnert et al. 1997, Prendergast et al. 1999, Koike et al. 2000, Ferris and Prendergast 2000, Kelly et al. 2003, Yao et al. 2012) states. However, it is difficult to validate these models. In particular, development of an accurate finite element (FE) model requires assuming a specific value for the stiffness of the AL. Researchers generally estimate the value using a cross-calibration process. However, this has resulted in large differences in the obtained values: for example, Young's moduli of 0.01 MPa (Sun et al. 2002), 0.065 MPa (Wada et al. 1992, Kelly et al. 2003), 0.2 MPa (Gan et al. 2006), and 5.5 MPa (Gan et al. 2007).

The mechanical properties of the AL have been investigated directly by an electromagnetic probe (Cancura 1979, human temporal bones), the Mössbauer technique (Lynch et al. 1982, living cats), an image analysis system (Gan et al. 2011, fresh human temporal bones), and a laser Doppler vibrometer (Lauxmann et al. 2014, human temporal bone). Although these methods allow the measurement of displacement at the nanometer level, the experiments in temporal bones were conducted for forces above 1 mN. Therefore, the measured displacement of the stapes was significantly larger than the normal displacement induced in healthy ears at, e.g., 100 dB SPL. This means that the AL stiffness obtained from the force-displacement curves may differ from the actual AL stiffness during normal sound transmission.

Thus, there is a need to develop a new technique allowing the measurement of the stiffness of the AL at much smaller displacements. The measurements should be conducted in the physiological range of elongations of the AL elastic fibers, i.e., for SF displacements from 0 to  $\sim$ 100 nm. Such small displacements are extremely difficult to achieve using

a conventional micro-mechanical testing system (e.g., MTS with SMT-1 capacity load cell developed by Interface Inc. or FemtoTools FT-FS100 by Nanoscience Instruments, Inc.).

Atomic force microscopy (AFM) (Binnig et al. 1986) is nowadays commonly used for measuring the mechanical properties of biological samples at the nanoscale (Radmacher 1997, Sugawara et al. 2002, Ikai et al. 2003, Takai 2005, Darling et al. 2006, Murakoshi et al. 2006, Thurner 2009). The AFM technique enables the manipulation of the samples by a precisely controlled piezo-scanner and a micro-cantilever probe. The piezo-scanner can be designed for nanomanipulation with about 50 picometers resolution. The micro-cantilever probe is composed of a soft beam with reflective coating and a tip attached to the end of the beam. In the contact AFM mode, force between the tip and the sample causes the beam to bend. A laser beam is reflected off the beam, small changes in beam deflection are detected by a sensitive photodetector. The analysis of the force-displacement curve recorded by the AFM allows the calculation of the stiffness (Doerner and Nix 1986, Oliver and Pharr 1992). During the analysis, deflection of the cantilever and the tip-sample interaction are treated as two springs in series. So far, the AFM technique has not been used to measure the stiffness of the AL.

The aim of this study is to develop new experimental method for determining the elastic properties of the stapes AL in the physiological range of its deflection. To this end, the AFM technique and fresh human temporal bone specimens were used.

## MATERIALS AND METHODS

### Measurement System

The measurements were performed in two human temporal bone specimens of the stapes AL. Neither ethics nor IRB approval was required for the use of cadaveric temporal bones under Polish law. In each specimen, we repeated the measurement 30 times. The AFM instrument was used to mechanically load the AL and quantitatively characterize its elastic properties in the physiological range of deformations. In the measurements, the maximum deflection of the AL was limited to 100 nm. The force-displacement curves were recorded by an AFM NT-206 system (Microtestmachines Ltd, Gomel, Belarus). The system consists of a scanning unit, a controller, and software for AFM-data processing, visualization, and analysis.

The scanning unit comprises a base platform and a detachable measuring head. A piezo-mechanism and motors, mounted inside the base platform, provide both approach (loading) and withdrawal (unloading)

actions of the sample platform. The range of the vertical motion is 20 mm with steps down to about 200 nm. The measuring head allows high-precision movement (vertical resolution of about 0.3 nm) of the removable cantilever holder. The laser source, the photodiode, and the video camera are integrated with the measuring head. The video camera is focused on the cantilever beam and connected to the controller. The controller allows the control of laser beam placement and positioning on the sample.

The AFM system was equipped with a rectangular cantilever (Fig. 1) made especially for our measurements in the Institute of Micromechanics and Photonics at the Warsaw University of Technology. The cantilever beam was etched out of a thin (60  $\mu\text{m}$ ) beryllium copper plate (Alloy Brush 190 CuBe2; Be 1.8 %, Co+Ni 0.3 %, Lamineries Matthey SA, La Neuveville, Switzerland) with a polished reflective upper surface. The nominal spring constant  $k_{c,\text{nom}}$  of the cantilever was 186 N/m (see Section 2.3). As a tip, a stainless steel bearing ball with a diameter of 0.7 mm was used. The ball was glued with epoxy resin (Epicote 1004, Shell Chemicals, London UK) onto the end of the cantilever beam. The real spring constant ( $k_c$ ) of the cantilever was measured using the calibration method described by Ekwinska and Rymuza (2009). After the calibration, the cantilever was mounted in the cantilever holder of the measuring head.

#### Data Acquisition

The AFM optical system consists of a digital camera with an attached lens focused on the cantilever. The output of the camera is sent to the computer to allow viewing of the sample during measurement. Using the manual drive, the sample was brought closer to the cantilever until a distance of about 1 mm between the sample and the cantilever was reached. Next, remote-

controlled displacements were used to bring the sample into contact with the cantilever. Finally, force-distance ( $F-d$ ) curves were acquired using the closed-loop force mode with a maximum displacement of  $\sim 100$  nm applied at a rate of about 100 nm/s. For each AL specimen, we performed the measurements at different locations on the specimen surface. At the beginning, the tip was placed above the middle of the stapes head (Fig. 2C) and the first curve was recorded. Then, the cantilever was lifted and subsequent measurements were done at 28 other locations in a regular pattern of 5- $\mu\text{m}$  steps within a 15- $\mu\text{m}$  radius around the starting point. The horizontal displacement between measurement points was controlled by the AFM piezo-scanner. Each curve was recorded over 3 s. Finally, the measurement results were calibrated to get the data in nN/nm.

#### Sample Preparation

Two fresh cadaveric temporal bones, obtained from donors with ages of 24 and 32 years, were used in this study. The donors had no evidence of otologic disease. The temporal bones were removed from human corpses selected in the Forensic Medicine Institute of Warsaw Medical University no later than on the third day following death. The bodies were stored at 4 °C. The bones were harvested according the standard practice developed by Schuknecht (1968) with the use of a Stryker oscillating saw. During preparation of the specimen, the condition of the AL of the stapes was examined to confirm that otosclerosis in the oval window niche was absent. After being collected, the bones were kept in normal saline at 5 °C until the following day.

#### The Procedure for Preparation

Temporal bones were dissected under an operating microscope using a standard set of micro-otosurgical equipment and a saw blade mounted on dentist drill tool. First, the temporal bone was washed and wax was removed from the external ear. Then, an anterior tympanotomy was performed and the oval window location was identified relative to the external structures of the temporal bone. The tympanic membrane was carefully removed to expose the ossicles. The incudo-stapedial joint was disarticulated with the use of surgical micro-scissors, and the malleus-incus complex was removed. Subsequently, much of the petrous portion of the temporal bone, including the semicircular canals and the cochlea, was cut off. After size reduction, only the whole stapes and the SVJ with a thin bony rim of the oval window niche were left intact. The bony block also included the beginning of both scala vestibuli and scala tympani as well as the

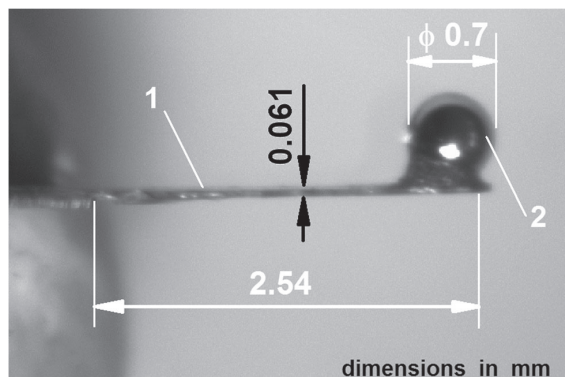


**FIG. 1.** The cantilever used in our measurement. 1 cantilever beam (length 2.54 mm, width 0.41 mm, thickness 0.061 mm), 2 tip of the cantilever (a steel ball of 0.7-mm diameter).

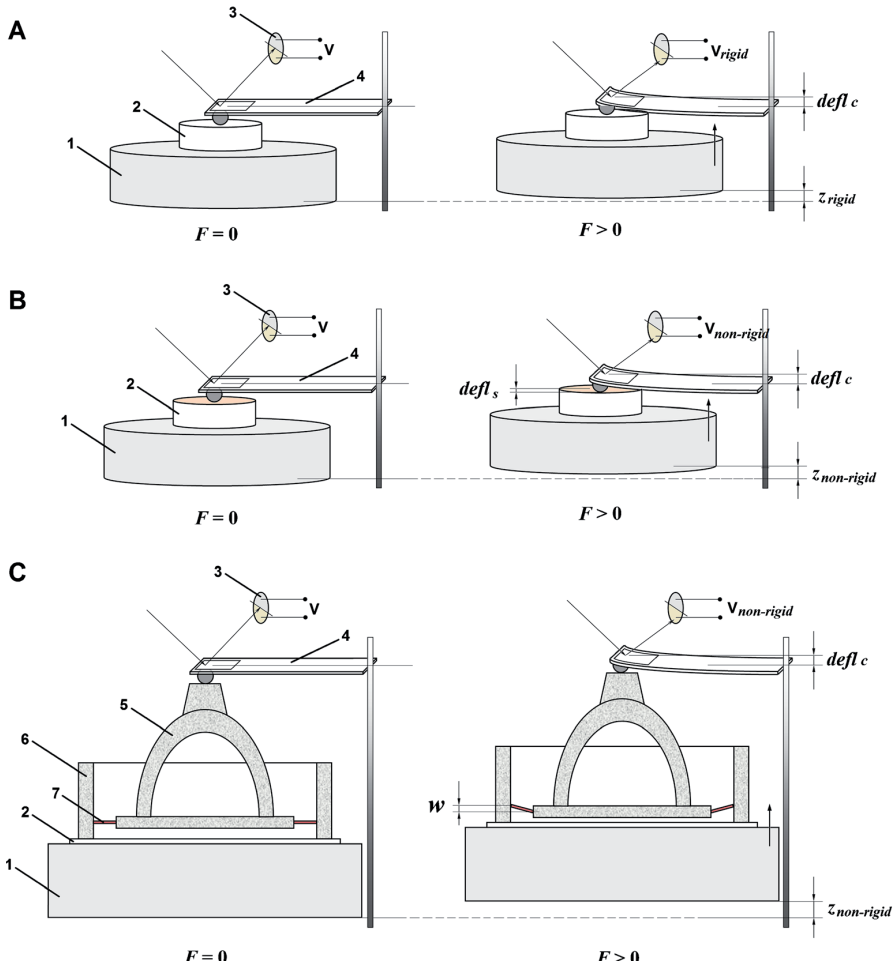


**FIG. 2.** AFM-based nanomechanics measurements.  $F$  force acting between the sample and the tip,  $V$  voltage of the photodiode,  $defl_c$  deflection of the cantilever,  $defl_s$  deflection of the sample,  $w$  deflection of the AL of the stapes,  $z$  displacement of the piezoactuator. **A** Measurements on a rigid reference sample. The rigid surface acted as an infinitely stiff sample, i.e., a sample that cannot deform and only the cantilever bends. The resulting cantilever deflection is the same as the piezoactuator displacement

( $defl_c = z_{\text{rigid}}$ ). 1 piezoactuator, 2 sample, 3 photodiode, 4 cantilever. **B** Measurements on a non-rigid sample. For the non-rigid samples, the measured deflection ( $defl_c$ ) of the cantilever is not the same as the piezoactuator displacement ( $z_{\text{non-rigid}}$ ), but  $defl_c = z_{\text{non-rigid}} - defl_s$ . 1 piezoactuator, 2 sample, 3 photodiode, 4 cantilever. **C** Measurements on the AL sample. 1 piezoactuator, 2 glass cover slip, 3 photodiode, 4 cantilever, 5 stapes, 6 oval window bone, 7 annular ligament of the stapes.

proximal portions of the semicircular canals. The total volume of the specimen was approximately  $1 \text{ cm}^3$ . Finally, the specimens were glued to thin glass coverslips using universal instant adhesive (Loctite 401, Henkel Ltd, UK). The AL specimen is schematically shown in Figure 2C. To prevent drying, the specimens were wrapped in gauze moistened with saline solution. The AFM measurements were performed on the same day.

#### AFM-Based Nanomechanics Measurements

In AFM measurements (Fig. 2), the cantilever (4) is the element that converts the force ( $F$ ) acting between

sample and tip to the deflection ( $defl_c$ ) at the tip. For small forces, the relationship between  $F$  and the optically measured  $defl_c$  is given by Hooke's law:

$$F = -k_c \cdot defl_c \quad (1)$$

where  $k_c$  is the spring constant of the cantilever,  $defl_c$  is the deflection at the cantilever tip, and  $F$  is the force acting between the sample and the tip. The same force ( $F$ ) causes deflection ( $defl_s$ ) of the sample depending on the stiffness ( $k_s$ ) of the sample:

$$defl_s = -\frac{F}{k_s} \quad (2)$$

where  $k_s$  is the stiffness of the sample,  $\text{defl}_s$  is the deflection of the sample, and  $F$  is the force acting between the sample and the tip.

#### Calibration and Real Stiffness (Spring Constant) of the Cantilever

Knowledge of the real spring constant  $k_c$  of the cantilever is essential for quantitative measurements. Nominal spring constants estimated from the dimensions are not accurate enough since the real value can vary drastically with small variations in the thickness and due to defects in the material. For this reason, it is better to measure rather than calculate this constant. To determine  $k_c$ , we conducted a series of calibration tests on two reference samples.

First, we performed the calibration of the sensitivity of the deflection sensor using the AFM NT-206 control software “SurfaceScan”. To that end, the force-displacement curves were recorded on a rigid reference sample (2 in Fig. 2A). This sample was made of a polished silicon wafer. We assumed that the silicon surface acted as an infinitely stiff sample ( $k_s=\infty$ ), i.e., the sample cannot deform and only the cantilever bends. In that case, the cantilever deflection is equal to the piezoactuator (1) displacement ( $\text{defl}_c=z_{\text{rigid}}$ ). From the curve slope obtained for the region of linear compliance, we determined the deflection sensitivity factor  $K$  (in nm/V) as

$$K = \frac{\Delta z_{\text{rigid}}}{\Delta V_{\text{rigid}}} \quad (3)$$

where  $K$  is the deflection sensitivity factor (in nm/V),  $z_{\text{rigid}}$  is the displacement of the piezoactuator (1, in nm), and  $V_{\text{rigid}}$  is the voltage of the photodiode (3, in V) recorded for the rigid reference sample (2).

Subsequently, we performed the calibration of the cantilever stiffness. To that end, the force-displacement curves were recorded on a non-rigid reference sample with known stiffness ( $k_{s-\text{ref}}$ ) (2 in Fig. 2B). As a reference sample, we used the calibration structure 12Z00010 (Nanoidea Ltd., Warsaw, Poland, <http://www.nanoidea.pl>) with a stiffness of 35 N/m (traceability certificate attached to the structure). After determining the sensitivity factor  $K$ , the deflection ( $\text{defl}_c$ ) of the cantilever can be calculated as

$$\text{defl}_c = K \cdot \Delta V_{\text{non-rigid}} \quad (4)$$

In Eq. 4, the  $\Delta V_{\text{non-rigid}}$  is equal to the difference between the photodiode output voltage at the first contact point and the voltage at any location in the

contact region of the force-distance curve. It should be noted that for the non-rigid samples, the measured deflection ( $\text{defl}_c$ ) of the cantilever is not the same as the piezoactuator (1) displacement ( $z_{\text{non-rigid}}$ ), but

$$\text{defl}_c = z_{\text{non-rigid}} - \text{defl}_s \quad (5)$$

#### Data Analysis and Elastic Modulus Calculation

For the AL sample, the measured deflection ( $\text{defl}_c$ ) of the cantilever depends on both the  $k_c$  of the cantilever and the  $E$  of the AL. We neglected the indentation of the stapes head caused by the cantilever tip. This is justified because the bone stiffness is much higher than the AL stiffness. In order to calculate the deflection of the AL ( $w$ ), the deflection of the cantilever ( $\text{defl}_c$ ) should be subtracted from the piezoactuator displacement ( $z_{\text{non-rigid}}=z_{\text{AL}}$ ) (Fig. 2C). Using Eqs. 5 and 1, the AL deflection ( $w$ ) can be calculated as

$$w = \text{defl}_s = z_{\text{AL}} - \text{defl}_c = z_{\text{AL}} + F/k_c \quad (7)$$

where  $w$  is the AL deflection,  $z_{\text{AL}}$  is the piezoactuator displacement for the AL sample,  $\text{defl}_c$  is the measured cantilever deflection (on the AL sample),  $F$  is the force applied, and  $k_c$  is the cantilever spring constant.

Note that  $F/k_c$  corresponds to the deflection of the cantilever on a hard surface at the same force  $F$ . Thus, the force-displacement ( $F-d$ ) curves are converted to the force-deflection ( $F-w$ ) curves.

Our measurement method requires that the stapes head should not be deformed. To that end, we used a stainless sphere with an extremely large diameter (0.7 mm), as mentioned above. Calculations based on Hertz theory (Young and Budynas 2002, p. 702) showed that the indentation depth (at the maximal force  $F=22$   $\mu$ N) is about 1.2 nm. This value corresponds to about 1.2 % of the AL deflection. Therefore, the data analysis based on Eq. 7 is justified.

To estimate a value of  $E$  for the AL, we used the Kirchhoff–Love theory for small deformations of thin plates under pure bending (Reddy 2007). For a circular, isotropic, and transversely loaded plate of constant thickness, the governing differential equation in cylindrical coordinates ( $r, \theta, z$ ) can be written in the form

$$\frac{d}{dr} \left[ \frac{1}{r} \frac{d}{dr} \left( r \frac{dw}{dr} \right) \right] = -\frac{t(r)}{B} \quad (8)$$

where  $w$  is the plate deflection (in m),  $t$  is the shear force (in N/m),  $B = \frac{Eh^3}{12(1-v^2)}$  is the bending stiffness of the plate,  $h$  is the thickness of the plate, and  $v$  is the Poisson's ratio.

The AL plate was assumed to be simply supported on the outer periphery and subjected to a uniformly distributed load  $F$  around the edge of a central hole (Fig. 3). For this load, the shear force is

$$t(r) = \frac{F}{2\pi r} \quad (9)$$

Substituting Eq. 9 into Eq. 8, the solution for the deflection function  $w(r)$  is

$$w(r) = \frac{F \cdot r^2}{8\pi B} (\ln r - 1) - \frac{C_1 r^2}{4} - C_2 \ln r + C_3 \quad (10)$$

The constants  $C_1$ ,  $C_2$ , and  $C_3$  in Eq. 10 can be determined from the boundary conditions at the outer ( $r=a$ ) and inner ( $r=b$ ) edges. For analytical simplicity, we assume that the boundary conditions can be written as

$$w(r=a) = 0, M_r(r=a) = 0, M_r(r=b) = 0 \quad (11)$$

where  $M_r(r) = B \left( \frac{d^2 w}{dr^2} + v \frac{1}{r} \frac{dw}{dr} \right)$  is the radial bending moment.

Using the above boundary conditions (Eq. 11) and the expressions for  $w(r)$  and  $M_r(r)$ , we have calculated the constants  $C_1$ ,  $C_2$ , and  $C_3$  to be

$$\begin{aligned} C_1 &= \frac{P}{4\pi B} \left( \frac{1-v}{1+v} \frac{2b^2}{a^2-b^2} \ln \frac{b}{a} \right) \\ C_2 &= -\frac{P}{4\pi B} \frac{1+v}{1-v} \frac{a^2 b^2}{a^2-b^2} \ln \frac{b}{a} \\ C_3 &= \frac{Pa^2}{8\pi B} \left( 1 + \frac{1}{2} \frac{1-v}{1+v} \frac{b^2}{a^2-b^2} \ln \frac{b}{a} \right) \end{aligned} \quad (12)$$

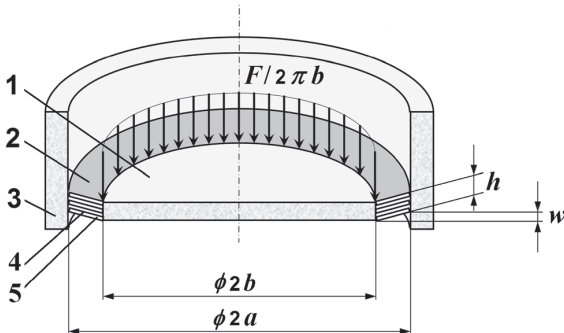


**FIG. 3.** The AL plate. The AL plate is a circular plate of diameter  $2a$  with a central hole of diameter  $2b$ . The AL plate is composed of  $n$  elastic fiber plates separated by amorphous substance. On the outer periphery, the AL plate is simply supported. The AL plate is subjected to a uniformly distributed load  $F/2\pi b$  (in N/m) around the edge of the central hole. 1 central hole (where the SF is placed), 2 annular ligament plate, 3 oval window bone, 4 single elastic fiber plate, 5 amorphous substance.

Substituting the above constants  $C_1$ ,  $C_2$ , and  $C_3$  in Eq. 10 and then simplifying, the AL plate deflection at  $r=b$  can be written in the form

$$\begin{aligned} w &= w(r=b) = \frac{3F \cdot (1-v^2)}{4\pi Eh^3} \left[ \frac{(a^2-b^2) \cdot (3+v)}{1+v} + \frac{4a^2b^2(1+v)}{(a^2-b^2) \cdot (1-v)} \left( \ln \frac{a}{b} \right)^2 \right] \\ &= C \cdot \frac{F}{E} \end{aligned} \quad (13)$$

where  $C$  is a constant, given by

$$C = \frac{3 \cdot (1-v^2)}{4\pi h^3} \left[ \frac{(a^2-b^2) \cdot (3+v)}{1+v} + \frac{4a^2b^2(1+v)}{(a^2-b^2) \cdot (1-v)} \left( \ln \frac{a}{b} \right)^2 \right] \quad (14)$$

where  $a$ ,  $b$ , and  $h$  are the dimensions of the AL plate and  $v$  is the Poisson's ratio of the AL plate.

Comparing Eq. 13 with Eq. 7, the elastic modulus ( $E$ ) of the AL can be obtained as

$$E = C \cdot \frac{\frac{F}{z_{AL}} \cdot k_c}{k_c + \frac{F}{z_{AL}}} = C \cdot \frac{\alpha \cdot k_c}{k_c + \alpha} \quad (15)$$

where  $\alpha = \frac{F}{z_{AL}}$  is the slope of the force-deflection curve recorded for the AL sample and  $k_c$  is the real spring constant of the cantilever.

### Measurements of AL Dimensions

The AL dimensions are needed to calculate the  $E$  of the AL based on Eq. 15. Therefore, after the AFM measurements, we scanned the AL samples using a SkyScan 1076 micro-CT System (Bruker-microCT, formerly Skyscan, Kontich, Belgium, [www.skyscan.be](http://www.skyscan.be)) according to the methodology described in detail in Kwacz et al. (2012). Briefly, the voxel size was 9  $\mu\text{m}$  and the scans were performed with a source voltage and source current of 100 kV and 100  $\mu\text{A}$ , respectively. An aluminum filter with a thickness of 1 mm was used to reduce the low-energy content of the X-ray energy spectrum, thus reducing beam hardening. The scanning exposure time per frame was 220 ms. The images were acquired at a step angle of 0.7° for a total circular orbit of 360°. In order to improve the quality of the final images, averaging of five frames collected at each angular position was done. The cone beam acquisitions save all of the projection images as 16-bit TIFF files. The SkyScan's volumetric reconstruction software "NRecon 1.5.1.1" was used to create a set of cross section slices through the object. The output files were saved in 8-bit grayscale BMP format with a

size of  $2000 \times 2000$  pixels. The stack of slice images was then used for segmentation and 3D volume reconstruction of the AL using the ScanIP software (Simpleware Ltd, UK, [www.simpleware.com](http://www.simpleware.com)). Because the grayscale differences between the AL and the SF were small, the automatic contouring could not be used, and manual segmentation was required. The morphological and smoothing filters, available in the ScanIP software, were used to reduce the noise in the images. After smoothing and segmentation, 3D reconstruction and morphometric measurements of the AL, the SF, and the OW were performed (Fig. 4). The following dimensions were measured: (1) the OW length ( $L_{OW}$ ), (2) the OW width ( $W_{OW}$ ), (3) the SF length ( $L_{SF}$ ), (4) the SF width ( $W_{SF}$ ), and (5) the SF thickness at the outer edge. The thickness of the AL was taken to be as the same as the SF thickness on the outer edge (Ohashi et al. 2006).

## RESULTS

### Dimensions of the AL Plate

The results of the morphometric measurements (Fig. 4) for two temporal bone specimens are listed in Table 1.

Based on the measured dimensions, we calculated the outer radius ( $a$ ) and inner radius ( $b$ ) of the assumed AL circular plate model as  $a=^{1/4} (L_{OW} + W_{OW})$  and  $b=^{1/4} (L_{SF} + W_{SF})$ . For Specimen 1 and

Specimen 2, respectively, the outer radius is  $a_1=1.09$  mm and  $a_2=1.03$  mm, and the inner radius is  $b_1=0.99$  mm and  $b_2=0.94$  mm. The thickness at points 1 to 4 for Specimens 1 and 2 ranged from 0.16 to 0.31 mm and from 0.15 to 0.28 mm, respectively. For use as the constant thickness ( $h$ ) of the AL circular plate model, we calculated the averages of the measurements at point 1 to 4 for Specimens 1 and 2, giving  $h_1=0.24$  mm and  $h_2=0.22$  mm, respectively.

### Calibration of Deflection Sensor and Cantilever Stiffness

The two reference samples mentioned in Section 2.3 (*Calibration and real stiffness (spring constant) of the cantilever*) are a rigid sample (Si) and a calibration membrane 12Z00010 (Nanoidea Ltd.). Both Si and membrane were tested 15 times, and the standard deviations of the slopes from the multiple curves were less than 3 % of the average values.

Figure 5A shows the calibration curves recorded on the rigid sample (Si) as described in Section 2.3. At the beginning (point 1), we start the measurement and the cantilever approaches the sample. At point 2, the cantilever comes into contact with the sample and then applies a load to it. The maximum load is at point 3. After that, we reduce the load until the cantilever comes out of contact (point 4). The slope of  $\text{defl}_c/z_{\text{rigid}}$  is 1 for the range of cantilever displacement up to 1000 nm. Higher displacement than 1  $\mu\text{m}$  might

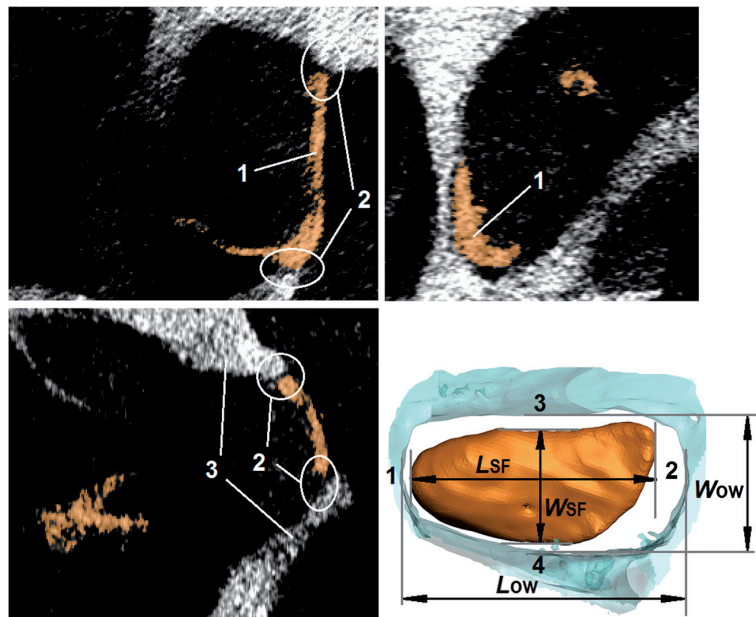


**FIG. 4.** Morphometric measurements of the stapes footplate (SF) and the oval window (OW) based on micro-CT imaging with the use of the Measure Tool in ScanIP software (Simpleware Ltd, UK). 1

stapes footplate (SF), 2 annular ligament (AL), 3 oval window (OW) bone.  $L_{OW}$  length of the OW,  $W_{OW}$  width of the OW,  $L_{SF}$  length of the SF,  $W_{SF}$  width of the SF (dimensions are listed in Table 1).

**TABLE 1**

Dimensions of the AL measured in two human specimens (Specimen 1 and Specimen 2) used in our study. The  $L_{SF}$ ,  $W_{SF}$ ,  $L_{OW}$ , and  $W_{OW}$  dimensions and the measurement points 1–4 are shown in Figure 4

	Specimen 1	Specimen 2
Length of the SF, $L_{SF}$ (mm)	2.76	2.58
Width of the SF, $W_{SF}$ (mm)	1.22	1.18
Length of the oval window, $L_{OW}$ (mm)	2.95	2.82
Width of the oval window, $W_{OW}$ (mm)	1.41	1.31
Thickness of the AL, $h$ (mm)		
At measurement point 1	0.31	0.28
At measurement point 2	0.16	0.15
At measurement point 3	0.23	0.22
At measurement point 4	0.25	0.23

result in nonlinearity of the photodiode. The shift between the unloading and loading curve is caused by the elastic hysteresis of the cantilever beam. Nevertheless, the slope is similar to the one of loading phase. At the end of the measurement, the tip is pulled off from the surface.

Figure 5B shows the calibration curves obtained with a calibration structure as described in Section 2.3. The shapes of the curves are actually quite different, exhibiting not just a change of slope due to non-rigidity of the calibration structure, but also force drift during unloading. The force drift

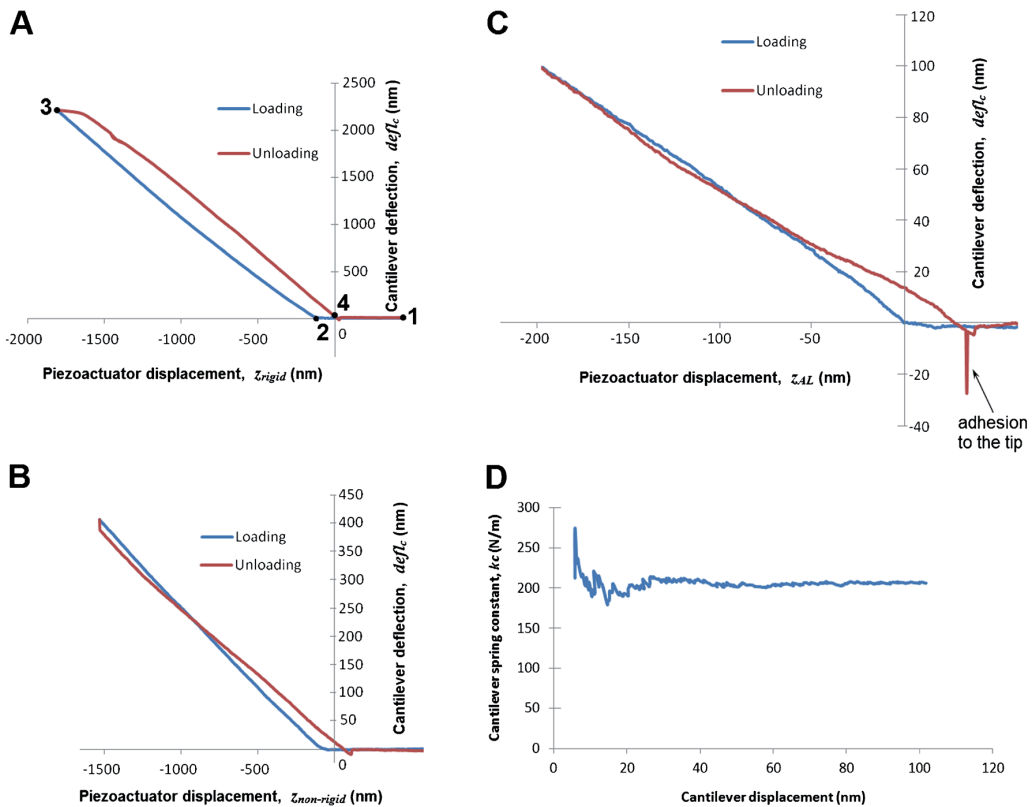


**FIG. 5.** A Calibration curves (the calibration of the deflection sensor) recorded on the rigid reference sample (silicon wafer). 1 start point, 2 contact point, 3 maximum load, 4 out of contact. B Force-distance curves recorded on the reference sample (calibration structure 12Z00010, Nanoidea Ltd., Piaseczno nearby Warsaw, Poland, <http://www.nanoidea.pl>). C Measurement curves recorded

on the AL sample. D Real spring constant ( $k_c$ ) of the self-made cantilever determined based on the calibration curves. The cantilever beam (length 2.54 mm, width 0.41 mm) etched out of the 60- $\mu$ m beryllium copper plate (Alloy Brush 190 CuBe2, Lamineries Matthey SA, La Neuveville, Switzerland).

causes the cantilever displacement to decrease during the short hold between loading and unloading, which results in a vertical segment. During unloading, the deflected calibration structure interacts with the cantilever, which results a smaller slope of the unloading curve. The slopes of the curves were calculated by the method of least squares. Based on the calibration curves, the real spring constant ( $k_c$ ) of the self-made cantilever used in our study (Fig. 1) was found to be 200.0 N/m (Fig. 5D). The standard deviation was less than 3 % of the average value. The slope was always calculated after the first 30 nm to avoid the early irregularities and up to 1000 nm or till the end of the measurement.

#### Spring Constant of the AL of the Human Stapes

Figure 5C shows one set of loading and unloading curves recorded on the AL sample (see Fig. 2C). The curve shape is similar to those of the curves recorded on the calibration samples. This indicates that a similar process occurs during the measurement of the AL sample. Please note that the curves shown in Figure 5C were recorded for piezoactuator displacements less than 200 nm. Therefore, the lower smoothness and departures from straight lines are more obvious than in Figure 5A, B. It can also be seen that the AL sample has a higher adhesion force than the calibration membrane. At the end of unloading on the AL sample, there is a large pull-off force (notation “adhesion to the tip” in Fig. 5C), which is caused by adhesion to the sample. This force is significantly larger than the pull-off force on the calibration samples (Fig. 5A, B). The higher adhesion of the AL sample is caused by the fact that the specimen was kept moist until the measurement, which was necessary to prevent drying and stiffening of the AL. The damp surface had some surface tension effects that were not seen in the dry calibration loads.

Based on the measurement curves (Fig. 5C) and the calibration data, we determined the force-

deflection ( $F-w$ ) curves for the AL (Fig. 6). The colored lines correspond to single measurements, and each black line represents the average slope for that sample. Most of the curves do not pass through the origin because the surface of the stapes head is not flat. For this reason, the value of  $z_{AL}$  in Eq. 7 at  $F=0$  N is different in each of the measurement points on the stapes head. The slope of the average  $F-w$  curve is almost the same for the two specimens. This slope corresponds to the AL stiffness ( $k_{AL}$ ). Our measurement results (Table 2) showed that for Specimen 1 and Specimen 2, the  $k_{AL}$  was 115.8 N/m (SD 30.4) and 124.6 N/m (SD 24.5), respectively.

#### Elastic Modulus of the AL

Finally, we determined the elastic modulus ( $E$ ) of the AL based on Eq. 13 and the measurement data. In Eq. 13, we adopted the dimensions of the AL plate given in Section 3.1, a Poisson's ratio  $\nu=0.4$ , the real spring constant of the cantilever  $k_c=200$  N/m (see Section 3.2), and the slope of the force-deflection curve  $\alpha_1=115.8$  N/m and  $\alpha_2=124.6$  N/m. The calculations for Specimen 1 and Specimen 2 gave values for  $E$  of 1.05 and 1.22 MPa, respectively.

Additionally, to demonstrate the strong effect of the AL thickness ( $h$ ) on the AL elastic modulus ( $E$ ), we calculated  $E$  not only for the average values of  $h$  but also for values ranging from 0.15 to 0.31 mm. The results of this calculation are shown in Figure 7.

## DISCUSSION

The objective of this study was to develop a new experimental method for determining the elastic properties of the stapes AL in the physiological range of its deflection. To this end, the AFM technique and fresh human temporal bone specimens were used. One of the major applications of AFM is the

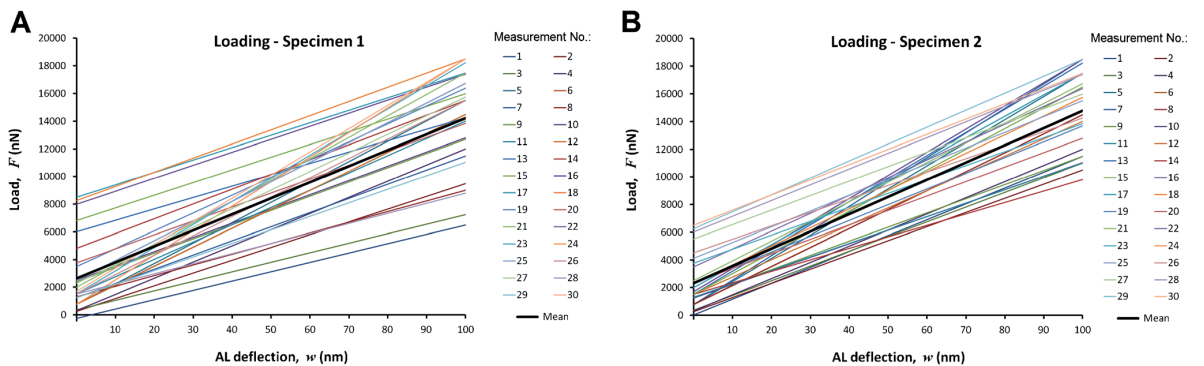


**FIG. 6.** The force-deflection ( $F-w$ ) curves for the two AL specimens.  $F$  force acting between the sample and the cantilever,  $w$  the AL deflection (where  $w=z_{AL}-\text{defl}$ , according to Eq. 7 and Figure 5C). Colored lines—the curves for single measurements, black lines—the approximated curves.

**TABLE 2**

Stiffness ( $k_{AL}$ ) and elastic modulus ( $E$ ) for the two AL specimens (Specimen 1 and Specimen 2) determined in this study

Measurement no.	Specimen 1		Specimen 2	
	Stiffness, $k_{AL}$ (N/m)	Elastic modulus, $E$ (MPa)	Stiffness, $k_{AL}$ (N/m)	Elastic modulus, $E$ (MPa)
1	67.5	0.72	115.0	1.16
2	92.5	0.91	102.5	1.08
3	69.0	0.74	106.5	1.10
4	117.0	1.06	117.0	1.17
5	147.5	1.22	167.5	1.45
6	137.5	1.17	137.5	1.29
7	102.5	0.97	177.5	1.49
8	77.0	0.80	137.0	1.29
9	103.0	0.98	102.5	1.08
10	103.0	0.98	98.0	1.04
11	125.0	1.10	97.0	1.04
12	137.0	1.17	125.0	1.22
13	82.5	0.84	167.5	1.45
14	107.0	1.00	83.0	0.93
15	92.0	0.90	150.0	1.36
16	94.0	0.92	168.0	1.45
17	90.0	0.89	155.0	1.39
18	102.5	0.97	134.5	1.28
19	129.0	1.13	114.0	1.15
20	101.0	0.96	104.5	1.09
21	155.0	1.25	142.5	1.32
22	142.5	1.19	129.0	1.25
23	167.5	1.31	101.0	1.07
24	177.5	1.35	114.0	1.15
25	142.5	1.19	114.0	1.15
26	140.0	1.18	197.5	1.58
27	134.5	1.15	105.0	1.09
28	73.0	0.77	114.0	1.15
29	98.0	0.94	122.5	1.21
30	168.0	1.31	110.0	1.13
Mean	115.8	1.05	124.6	1.22
Standard deviation	30.4	0.17	24.5	0.26

quantitative measurement of interaction forces between the sample and the probe tip. This technique

has been widely employed to examine the mechanical properties of materials in both the micro- and the

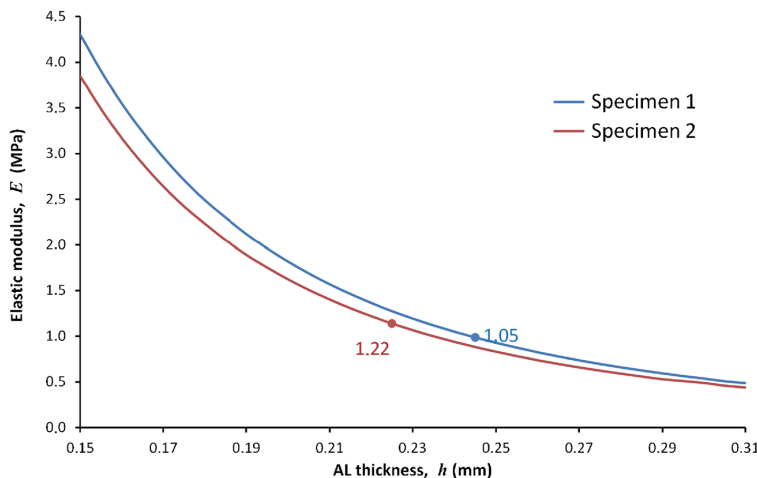


**FIG. 7.** The AL elastic modulus ( $E$ ) calculated for various values of the AL thickness ( $h$  from 0.2 to 0.3 mm). The calculations based on Eq. 12. For Specimen 1 and Specimen 2, the following values were adopted:  $a_1=1.09$  mm,

$b_1=0.99$  mm,  $\alpha_1=115.8$  N/m and  $a_2=1.03$  mm,  $b_2=0.94$  mm,  $\alpha_2=124.6$  N/m, respectively. On the graph, the  $E$  values for the average  $h_1=0.24$  mm and  $h_2=0.22$  mm are shown.

nanoscale. However, to measure the elastic modulus of the annular ligament of the human stapes, AFM has not been used until now.

### Sample Preparation and the Measurement Technique

The measurements were performed in two human cadaveric temporal bone specimens of the stapes AL. Fresh cadaveric temporal bones have been commonly used in experimental measurements of middle- and inner-ear mechanics. It has been experimentally shown that the functioning of the middle ear structures is similar between live and cadaveric ears (Rosowski et al. 1990). In our study, we have used specimens harvested from human cadavers within 48 h after death, protected from drying, and stored without freezing until the measurement. We have performed the AFM measurement in the fourth day after death. The same procedure is widely used by many researchers.

### Cantilever Stiffness and Tip Geometry

Proper choice of both cantilever stiffness and tip geometry are necessary to obtain accurate measurement results by AFM. For the measurement of the AL elastic modulus, we have chosen a cantilever with a nominal spring constant of about 200 N/m. However, because the thickness of AFM cantilevers is difficult to control during manufacture, the nominal spring constant for cantilevers from two different batches can vary by almost a factor of two (Cumpson et al. 2003). Therefore, the accurate calibration of the real spring constant of the cantilever is essential for limiting uncertainties and achieving reliable measurement results.

In the literature, a number of different calibration methods have been described. These methods can be divided into three principal classes: dynamic response methods, theoretical methods, and static response methods. Typical accuracies, advantages, and disadvantages of these methods were discussed by Myhra (1998).

### Elastic Modulus of the AL of the Human Stapes

Our estimation of the AL elastic modulus was based on a number of simplifying assumptions. In fact, the real FP is not circular, the thickness and width of the AL are not uniform, and the ligament itself does not appear to be either homogeneous or isotropic, having highly oriented fibers and having thicker bands on the medial and lateral sides (Whyte et al. 2002, Ohashi et al. 2006, 2008). Therefore, the resulting

Young's modulus is applicable only if the same simplified model is used.

In our model, the boundary conditions for the AL plate were chosen assuming that the plate is simply supported at the outer periphery (the connection between the AL and OW bone) and the load is axially applied and uniformly distributed at the inner periphery (the connection between the AL and the SF). This allowed us to use plate-bending theory for deriving the load-deflection ( $F-w$ ) relationship (Eq. 13, Section 2.3). Then, the  $F-w$  relationship can be compared with the experimentally obtained force-deflection characteristics (Fig. 6). This comparison allowed us to obtain Eq. 15 for the calculation of the AL elastic modulus.

The boundary conditions (Eq. 11) result from our assumption that the AL fibers act like springs and remain straight when the stapes moves, that is, the AL fibers do not become curved either close to the SF or close to the OW bone. However, there is no literature clearly showing how the AL fibers are deformed during stapes movement. Thus, it is also possible to adopt other boundary conditions, for example,  $w(a)=0$ ,  $M_r(a)=0$ ,  $\frac{dw}{dr}(r=b)=0$  or  $w(a)=0$ ,  $\frac{dw}{dr}(r=a)=0$ ,  $\frac{dw}{dr}(r=b)=0$ . In this work, we did not repeat our modeling for different boundary conditions.

In this study, the deflections were up to only 100 nm, much less than the plate thickness, thus justifying the use of the Kirchhoff-Love theory for thin plates.

The shapes of both the OW niche and the SF are very irregular and vary among individuals (e.g., Hagr et al. 2004; Sim et al. 2013). Numerous authors have treated the AL as an elliptical ring in finite element modeling of the middle ear (Ladak and Funnell 1996; Sun et al. 2002, Gan et al. 2011, Gentil et al. 2011). However, an elliptical shape for the AL plate leads to considerable difficulties in finding an analytical solution for the differential equation describing the plate bending. Therefore, in this study, we have replaced the elliptical shape of the AL rim with a circular shape. Such an approach will certainly affect the calculation of the AL elastic modulus.

It is known that the stapes AL contains a collection of individual elastic fibers that are "regularly arranged in a linear fashion and form a laminated array parallel to the horizontal plane of the SVJ" (Ohashi et al. 2006). Therefore, the AL may display direction-dependent properties caused by structural anisotropy. Due to the radial arrangement of the elastic fibers running from the SF toward the OW, the radial elastic modulus could be smaller than the circumferential elastic modulus. Nevertheless, in this study, we treated the AL as a homogeneous and isotropic structure. The same assumption was made by Lynch et al. (1982) to estimate the AL elastic modulus based on a

measured AL compliance. Moreover, AL isotropy has been assumed in most FE models (Sun et al. 2002, Wada et al. 1992, Kelly et al. 2003, Gan et al. 2006, 2007, Kwacz 2013). In this study, we obtained a value for the AL elastic modulus of approximately 1.1 MPa. This value is much higher than the value of 0.01 MPa obtained by Lynch et al. (1982) and lower than the value of 5.5 MPa estimated by Gan et al. (2007). Presumably, the enormous discrepancy between the values given by individual researchers reflects, at least in part, the differences among the models used to make the estimates, which are useful only in the context of their own models.

#### Spring Constant of the AL of the Human Stapes

Our measurement results indicate that the AL is a linear elastic material, at least up to static deflections of 100 nm. A similar conclusion was reported by Lynch et al. (1982) for stimuli up to 140 dB SPL. Other measurements of stapes motion (Guinan and Peake 1967; Goode et al. 1994) suggest that stapes motions as large as 1  $\mu\text{m}$  are still within the linear regime. The individual lines in Figure 6A, B seem to belong to two different families, one with a slope similar to the average slope and another with a steeper slope. This may be related to the inhomogeneous stiffness distribution of the AL around the SF (Lauxmann et al. 2014), caused by variation in both the AL thickness and the gap width between the SF and the OW. Near point 1 (Fig. 4, Table 1), the elastic fibers of the AL are significantly shorter than those near point 2. Moreover, the AL thickness near point 1 is almost twice as large as the thickness near point 2. This is consistent with the literature (Hagr et al. 2004; Ohashi et al. 2006; Sim et al. 2013). Such an anatomical structure leads to a higher AL stiffness at the SF posterior edge (point 1) than at the anterior edge (point 2). This causes a force applied to the stapes head to induce not only piston-like movement of the SF, but also rotations about its short and long axes (Huber et al. 2008; Sim et al. 2010, Eiber et al. 2012). It may be expected that the SF rotation affects the value of the force recorded by the AFM (Fig. 4). Since the rotation angle depends on the location of the measurement point, the individual  $F_w$  curves (Fig. 6) could have different slopes.

We measured a AL spring constant of approximately 120 N/m for SF displacements from 0 to 100 nm, comparable to the range of displacements observed during stapes vibration in normal human ears. Because of measurement difficulties, the AL stiffness in the range below 100 nm has never been reported in the literature.

Cancura (1979) described static measurements of the AL stiffness in nine human temporal bone

preparations. He showed that the force-displacement characteristic is linear in the 5–20 mN range with an average stiffness of about 250 N/m. However, the smallest force (5 mN) used by Cancura induces displacements of 20–40  $\mu\text{m}$  (see Cancura 1979, Fig. 5), which is about 200–400 times larger than the largest displacement that we used. This may cause the difference between the AL stiffnesses reported by Cancura and by us.

Lynch et al. (1982) reported dynamic measurements in anesthetized cats with the Mössbauer method. The AL stiffness derived from their data is 430 N/m. This value is about 3.5 times higher than the AL stiffness resulting from our measurement. However, the differences in anatomy between the cat and human ears may explain the difference in the obtained values.

Gan et al. (2011) described measurements in nine fresh human specimens. They applied the load to the stapes head using a 10-N load cell. In their measurement, a preload of 1 mN was used and then the load cell was moved to the maximum displacement of 0.2 mm. They used a constant displacement rate of 2.0  $\mu\text{m}/\text{s}$ . Based on the stress-strain relationship (Gan et al. 2011, Fig. 7b, mean value), the AL displacement of 70  $\mu\text{m}$  (recalculated for the shear strain of 1) corresponds to the loading force of 17.5 mN. The AL stiffness derived from this data is 250 N/m, which is about 2 times higher than the value determined in our study. However, both the displacement and the displacement rate are significantly higher than those used in our AFM measurement.

Recently, the AL stiffness in a human temporal bone was reported by Lauxmann et al. (2014). They applied a force from 1 to 50 mN at different points on the SF and measured the induced SF displacement using a laser Doppler vibrometer (LDV). Based on the force-displacement curve (Lauxmann et al. 2014, Fig. 11, green line), the AL stiffness determined from the slope of the curve is 1050 N/m. This value is much higher than the stiffness of 120 N/m obtained in our measurements. A reason for this discrepancy may be differences in measurement procedures. In Lauxmann's measurement, the force is applied at the center of the SF and an initial force of 1 mN is used at the starting position. In our measurement, the force is applied at the stapes head and it does not exceed the value of 20  $\mu\text{N}$  (Fig. 6). For forces below 20  $\mu\text{N}$ , a lower stiffness may be expected than for forces above 1000  $\mu\text{N}$ . Lauxmann et al. (2014) measured the spatial displacement of the stapes head using a LDV, which required velocities above 0.5  $\mu\text{m}/\text{s}$ . The loading velocity in our study (0.1  $\mu\text{m}/\text{s}$ ) is significantly lower. This may also contribute to the lower value of AL stiffness obtained in our measurement.

# Author's personal copy

KWACZ ET AL.: Elastic Properties of the Annular Ligament of the Human Stapes

The AL spring constant ( $\sim 120$  N/m) reported here, obtained for small displacements using AFM, is intended to be used in numerical (FE) models of the human middle ear mechanics and to design a suitable membrane for our new chamber stapes prosthesis (Kwacz et al. 2014).

## ACKNOWLEDGMENTS

We gratefully acknowledge the valuable comments from the reviewers and the section editor.

### Conflict of Interest

The authors declare that they have no competing interest.

## REFERENCES

- ASAI M, HUBER A, GOODE R (1999) Analysis of the best site on the stapes footplate for ossicular chain reconstruction. *Acta Otolaryngol (Stockh)* 119(5):356–361
- BINNIG G, QUATE CF, GERBER C (1986) Atomic force microscope. *Phys Rev Lett* 56:930–933
- BOLZ EA, LIM DJ (1972) Morphology of the stapediovestibular joint. *Acta Otolaryngol* 73:10–17
- BRUNNER H (1954) Attachment of the stapes to the oval window in man. *AMA Arch Otolaryngol* 59:18–29
- CHIEN W, ROSOWSKI JJ, RAVICZ ME, RAUCH SD, SMULLEN J, MERCHANT SN (2009) Measurement of stapes velocity in live human ears. *Hear Res* 249:54–61
- CANCURA W (1979) On the elasticity of the ligamentum annulare. *Arch Otorhinolaryngol* 107:27–32
- CUMPSON PJ, HEDLEY J, ZHDAN P (2003) Accurate force measurement in the atomic force microscope: a microfabricated array of reference springs for easy cantilever calibration. *Nanotechnology* 14:918–924
- DAI C, CHENG T, WOOD MW, GAN RZ (2007) Fixation and detachment of superior and anterior malleolar ligaments in human middle ear: experiment and modeling. *Hear Res* 230(1–2):24–30
- DARLING EM, ZAUSCHER S, GUILAK F (2006) Viscoelastic properties of zonal articular chondrocytes measured by atomic force microscopy. *Osteoarthritis Cartilage* 14(6):571–579
- DOERNER MF, NIX WD (1986) A method for interpreting the data from depth-sensing indentation instruments. *J Mater Res* 1(4):601–609
- EIBER A, HUBER AM, LAUXMANN M, CHATZIMICHALIS M, SEQUEIRA D, SIM JH (2012) Contribution of complex stapes motion to cochlea activation. *Hear Res* 284(1):82–92
- EWINSKA M, RYMUZA Z (2009) Normal force calibration method used for calibration of atomic force microscope. *Acta Phys Pol A* 116:S78–S81
- FERRIS P, PRENDERGAST PJ (2000) Middle ear dynamics before and after ossicular replacement. *J Biomech* 33:581–590
- GAN RZ, CHENG T, DAI C, YANG F, WOOD MW (2009) Finite element modeling of sound transmission with perforations of tympanic membrane. *J Acoust Soc Am* 126(1):243–253
- GAN RZ, REEVES BP, WANG X (2007) Modeling of sound transmission from the ear canal to cochlea. *Ann Biomed Eng* 35(12):2180–2195
- GAN RZ, SUN Q, FENG B, WOOD MW (2006) Acoustic-structural coupled finite element analysis for sound transmission in human ear—pressure distributions. *Med Eng Phys* 28:395–404
- GAN RZ, WANG X (2007) Multifield coupled finite element analysis for sound transmission in otitis media with effusion. *J Acoust Soc Am* 122(6):3527–3538
- GAN RZ, YANG F, ZHANG X, NAKMALI D (2011) Mechanical properties of stapedial annular ligament. *Med Eng Phys* 33:330–339
- GENTIL F, PARENTE M, MARTINS P, GARBE C, JORGE RN, FERREIRA A, TAVARES JM (2011) The influence of the mechanical behavior of the middle ear ligaments: a finite element analysis. *Proc Inst Mech Eng H* 225(1):68–76
- GOODE RL, KILION M, NAKAMURA K, NISHIHARA S (1994) New knowledge about the function of the human middle ear: development of an improved analog model. *Am J Otol* 15(2):145–154
- GUINAN JJ JR, PEAKE WT (1967) Middle-ear characteristics of anesthetized cats. *J Acoust Soc Am* 41(5):1237–1261
- HAGE AA, FUNNELL WRJ, ZEITOUNI AG, RAPPAPORT JM (2004) High-resolution X-ray computed tomographic scanning of the human stapes footplate. *J Otolaryngol* 33(4):217–221
- HATO N, WELSH JT, GOODE RL, STENFELT S (2001) Acoustic role of the buttress and posterior incudal ligament in human temporal bones. *Otolaryngol Head Neck Surg* 124:274–278
- HEILAND K, GOODE R, ASAI M, HUBER A (1999) A human temporal bone study of stapes footplate movement. *Am J Otol* 20:81–86
- HUBER A, KOIKE T, WADA H, NANDAPALAN V, FISH U (2003) Fixation of the anterior malleolar ligament: diagnosis and consequences for hearing results in stapes surgery. *Ann Otol Rhinol Laryngol* 112:348–355
- HUBER A, LINDER T, FERRAZZINI M, SCHMID S, DILLIER N, STOECKLI S, FISCH U (2001) Intraoperative assessment of stapes movement. *Ann Otol Rhinol Laryngol* 110(1):31–35
- HUBER AM, SEQUEIRA D, BREUNINGER C, EIBER A (2008) The effects of complex stapes motion on the response of the cochlea. *Otol Neurotol* 29(8):1187–1192
- IKAI A, AFRIN R, SEKIGUCHI H, OKAJIMA T, ALAM MT, NISHIDA S (2003) Nano-mechanical methods in biochemistry using atomic force microscopy. *Curr Protein Pept Sci* 4(3):181–193
- KELLY DJ, PRENDERGAST PJ, BLAYNEY AW (2003) The effect of prosthesis design on vibration of the reconstructed ossicular chain: a comparative finite element analysis of four prostheses. *Otol Neurotol* 24:11–19
- KOIKE T, WADA H, KOBAYASHI T (2000) Analysis of the finite-element method of transfer function of reconstructed middle ears and their postoperative changes. In: Rosowski JJ, Merchant SN (eds) *The function and mechanics of normal, diseased and reconstructed middle ears*. Kugler, The Hague, pp 309–320
- KWACZ M, WYSOCKI J, KRAKOWIAN P (2012) Reconstruction of the 3D geometry of the ossicular chain based on micro-CT imaging. *Biocybernetics Biomed Eng* 32(1):27–40
- KWACZ M (2013) A three-dimensional finite element model of round window membrane vibration before and after stapedotomy surgery. *Biomech Model Mechanobiol* 12:1243–1261
- KWACZ M, MAREK P, BORKOWSKI P, GAMBIN W (2014) Effect of different stapes prostheses on the passive vibration of the basilar membrane. *Hear Res* 310:13–26
- LADAK HM, FUNNELL WR (1996) Finite element modeling of the normal and surgically repaired cat middle ear. *J Acoust Soc Am* 100:933–944
- LAUXMANN M, EIBER A, HAAG F, IHRLE S (2014) Nonlinear stiffness characteristics of the annular ligament. *J Acoust Soc Am* 136:1756–1767

## Author's personal copy

KWACZ ET AL.: Elastic Properties of the Annular Ligament of the Human Stapes

- LYNCH TJ, NEDZELNITSKY V, PEAKE WT (1982) Input impedance of the cochlea in cat. *J Acoust Soc Am* 72:108–130
- MERCHANT SN, RAVICZ ME, ROSOWSKI JJ (1996) Acoustic input impedance of the stapes and cochlea in human temporal bones. *Hear Res* 97:30–45
- MURAKOSHI M, YOSHIDA N, IIDA K, KUMANO S, KOBAYASHI T, WADA H (2006) Local mechanical properties of mouse outer hair cells: atomic force microscopy study. *Auris Nasus Larynx* 33(2):149–157
- MYHRA S (1998) in: JC Riviere, S Myhra (eds.) *Handbook of surface and interface analysis methods for problem solving*, Marcel Dekker, New York, 1998, pp. 52
- OHASHI M, IDE S, KIMITSUKI T, KOMUNE S, SUGANUMA T (2006) Three-dimensional regular arrangement of the annular ligament of the rat stapediovestibular joint. *Hear Res* 213:11–16
- OHASHI M, IDE S, KIMITSUKI T, SAWAGUCHI A, KIMITSUKI T, KOMUNE S, SUGANUMA T (2008) Histochemical localization of the extracellular matrix components in the annular ligament of rat stapediovestibular joint with special reference to fibronectin, 36-kDa microfibril-associated glycoprotein (MAGP-36), and hyaluronic acid. *Med Mol Morphol* 41:28–33
- OLIVER WC, PHARR GM (1992) An improved technique for determining hardness and elastic modulus using load and displacement sensing indentation measurements. *J Mater Res* 7(6):1564–1583
- PRENDERGAST PJ, FERRIS P, RICE HJ, BLAYNEY AW (1999) Vibro-acoustic modeling of the outer and middle ear using the finite-element method. *Audiol Neuro Otol* 4:185–191
- RADMACHER M (1997) Measuring the elastic properties of biological samples with the AFM. *IEEE Eng Med Biol Mag* 16(2):47–57
- REDDY JN (2007) Theory and analysis of elastic plates and shells. CRC Press, Taylor & Francis
- ROSOWSKI JJ, DAVIS PJ, MERCHANT SN, DONAHUE KM, COLTRERA MD (1990) Cadaver middle ears as models for living ears: comparisons of middle ear input immittance. *Ann Otol Rhinol Laryngol* 99:403–412
- SCHUKNECHT H (1968) Temporal bone removal at autopsy. Preparation and uses. *Arch Otolaryngol* 87(2):129–137
- SIM JH, CHATZIMICHALIS M, LAUXMANN M, RÖÖSLI C, EIBER A, HUBER AM (2010) Complex stapes motions in human ears. *J Assoc Res Otolaryngol* 11(3):329–341
- SIM JH, RÖÖSLI C, CHATZIMICHALIS M, EIBER A, HUBER AM (2013) Characterization of stapes anatomy: investigation of human and guinea pig. *J Assoc Res Otolaryngol* 14(2):159–173
- STENFELD S, HATO N, GOODE RL (2004) Fluid volume displacement at the oval and round windows with air and bone conduction stimulation. *J Acoust Soc Am* 115(2):797–812
- SUN Q, GAN RZ, CHANG KH, DORMER KJ (2002) Computer-integrated finite element modeling of human middle ear. *Biomech Model Mechanobiol* 1(2):109–122
- SUGAWARA M, ISHIDA Y, WADA H (2002) Local mechanical properties of guinea pig outer hair cells measured by atomic force microscopy. *Hear Res* 174(1–2):222–229
- TAKAI E (2005) Osteoblast elastic modulus measured by atomic force microscopy is substrate dependent. *Ann Biomed Eng* 33(7):963–971
- THURNER PJ (2009) Atomic force microscopy and indentation force measurement of bone. *Wiley Interdiscip Rev Nanomed Nanobiotechnol* 1(6):624–649
- WADA H, METOKI T, KOBAYASHI T (1992) Analysis of the dynamic behavior of the human middle ear using a finite-element method. *J Acoust Soc Am* 92:3157–3168
- WHYTE JR, GONZALEZ L, CISNEROS AI, YUS C, TORRES A, SARRAT R (2002) Fetal development of the human tympanic ossicular chain articulations. *Cells Tissues Organs* 171:241–249
- WOLFF D, BELLUCCI R (1956) The human ossicular ligaments. *Ann Otol Rhinol Laryngol* 65:895–909
- YAO W, LI B, HUANG X, GUO C, LUO X, ZHOU W, DUAN M (2012) Restoring hearing using total ossicular replacement prostheses—analysis of 3D finite element model. *Acta Otolaryngol* 132(2):152–159
- YOUNG WC, BUDYNAS RG (2002) Formulas for stress and strain, 7th edn. McGraw-Hill, New York, **Table 14.1, p. 702**
- ZAHNERT T, SCHMIDT R ET AL (1997) FE-simulations of vibrations of the Dresden middle ear prosthesis. In: Huttenbrink K-B (ed) *Middle ear mechanics in research and otosurgery*. Technical University of Dresden, Dresden, pp 200–206
- ZHAO F, KOIKE T, WANG J, SIENZ H, MEREDITH R (2009) Finite element analysis of the middle ear transfer functions and related pathologies. *Med Eng Phys* 31(8):907–916



## Publikacja – P7

Computational study of the effect of side wall  
quality of the template on release force in  
nanoimprint lithography

Tochino T., Uemura K., **Michałowski M.**, Fujii  
K., Yasuda M., Kawata H., Rymuza Z., Hirai Y.

Computational study of the effect of side wall quality of the template on release force in nanoimprint lithography

This content has been downloaded from IOPscience. Please scroll down to see the full text.

[View the table of contents for this issue](#), or go to the [journal homepage](#) for more

Download details:

IP Address: 194.29.141.127

This content was downloaded on 24/06/2015 at 11:31

Please note that [terms and conditions apply](#).

## Computational study of the effect of side wall quality of the template on release force in nanoimprint lithography

Takamitsu Tochino<sup>1</sup>, Kimiaki Uemura<sup>1</sup>, Marcin Michalowski<sup>2</sup>, Kazuo Fujii<sup>1</sup>, Masaaki Yasuda<sup>1</sup>, Hiroaki Kawata<sup>1</sup>, Zygmund Rymuza<sup>2</sup>, and Yoshihiko Hirai<sup>1</sup>

<sup>1</sup>Department of Physics and Electronics Engineering, Graduate School of Engineering, Osaka Prefecture University, Sakai 599-8531, Japan

<sup>2</sup>Institute of Micromechanics and Photonics, Warsaw University of Technology, Sw. A. Boboli 8, 02-525 Warsaw, Poland

Received December 8, 2014; revised February 9, 2015; accepted February 19, 2015; published online May 29, 2015

A template release force is one of the important factors for a low-defect template release process in nanoimprint lithography. In this work, the origin of the template release force is investigated by computational study of side wall quality characteristics such as the critical separation forces between the template and the resist interface, and the slope angle of the side wall. The critical separation forces in the normal and shear directions, which are related to adhesion and friction characteristics are experimentally evaluated for the computational study. The computational results show that the shear separation force, which is related to the static friction between the template surface and the resist, strongly affects the release force characteristics. On the other hand, the side wall slope angle also affects the template release force above the critical side wall slope angle. The computational results show good agreement with experimental results. © 2015 The Japan Society of Applied Physics

### 1. Introduction

Nanoimprint lithography<sup>1)</sup> has high resolution and is a cost-effective method for fabricating various micro- and nano-devices. One of the important issues in nanoimprint lithography is the template release (de-molding) process. Owing to adhesion between the template and the resist, the resist is stuck on the surface of the template, and the resist becomes stretched, which sometimes forms defects at the template release process. To prevent defect formation, several approaches to reduce the template release force have been developed. One of the effective methods is to decrease the surface energy of the template and to prevent the sticking of the resist by applying an antisticking layer<sup>2-4)</sup> or a segregation agent on resists.<sup>5,6)</sup> In addition, some mechanical approaches have been reported for the smooth release using peeling or novel release methods.<sup>7-11)</sup>

On the other hand, evaluation of the materials or processes for template release has been reported.<sup>12-20)</sup> Also, several analyses of the defect factors or mechanisms have been carried out by experiments and simulation works.<sup>21-28)</sup> We have conducted the computational analysis of the basic mechanisms of the template release process and clarified the template separation mechanisms on the basis of the critical stress model and fracture mechanics model.<sup>29-31)</sup>

One of the important parameters for verifying the template release process is the maximum release force, because inner stress is induced by the release force, and the resulting stress causes resist breakdown or damage. In this study, we focused on the dependence of template release force on the slope angle of the pattern and the stresses critical for template separation from the resist. To investigate the release process, critical stress is newly evaluated by experiments, and the release force is measured experimentally at various slope angles of the patterns. The experimental results are compared with computational results, and the mechanism of template release is discussed in this paper.

### 2. Numerical model and experimental methods

#### 2.1 Numerical model

To investigate the template release force, a simple schematic model shown in Fig. 1 is applied. A resist on a rigid substrate

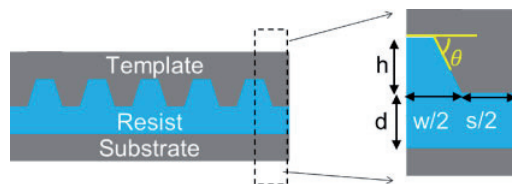


**Fig. 1.** (Color online) Left: Schematic of the analytical model of resist separation from the mold. Right: The details of the model. The pattern height is  $h$  and the residual thickness of the resist is  $d$ . The pattern width is  $w$ , the space is  $s$ , and the slope angle is  $\theta$ .

was pressed with a rigid template, where the side wall of the template pattern was inclined at a side wall slope angle  $\theta$ . The pattern height is  $h$  and the residual thickness of the resist is  $d$ . The resist was fixed on the rigid substrate and the residual stress due to pressing was not taken into consideration in the investigation of the template release effect itself. The template was moved in the vertical direction and stress was induced at the interface between the template and the resist. The critical stress model<sup>29,32)</sup> was applied to express the template separation from the resist in numerical simulation. When the induced stress exceeds the critical stress, the template separates from the resist. When the normal stress  $\sigma_n$  and the shear stress  $\sigma_s$  at the interface satisfy the relation

$$(\sigma_n/P_n)^2 + (\sigma_s/P_s)^2 > 1, \quad (1)$$

the template separates from the resist, where  $P_n$  is the critical normal stress and  $P_s$  is the shear stress at the interface.  $P_n$  is the adhesion force between the resist and the template and  $P_s$  is the static friction force due to surface roughness. The side wall slope angle and critical stress are varied to investigate their impact on the side wall quality of the template pattern. In this work, the ratio  $P_s/P_n$ , which we call a side wall quality factor, is varied. Therefore, the quantitative values of these parameters are important for actual systems.

The release load is calculated by a finite element method based on conventional continuum mechanics using MSC-MARC software. The template is lifted and the induced force is calculated. Then, force curves are obtained under various

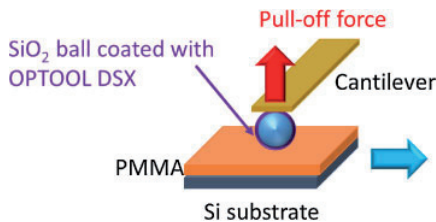


**Fig. 2.** (Color online) Schematics of the critical stress measurement using SPM.

**Table I.** Experimental extraction of the critical stresses for template separation.

Sample	$P_n$ (kPa)	$P_s$ (kPa)	$P_s/P_n$
A	25.6	180	7.0
B	15.6	313	20
C	10.7	20	18

conditions. In the computation, we varied the side wall quantity factor  $P_s/P_n$  from 1.0 to 20.0. The elastic modulus of the resist is 3.0 GPa, Poisson's ratio is 0.35, and the residual layer is 2.0  $\mu\text{m}$ . The pattern height and the space width of the template are 2.0  $\mu\text{m}$ .

## 2.2 Parameter extraction by experiment

For the discussion on the critical stresses  $P_n$  and  $P_s$ , the side wall quality factor  $P_s/P_n$  is important for simulation. In order to verify their values, the critical stresses are investigated by experimental work. Figure 2 shows the schematics of the verification method by scanning probe microscopy (SPM). We use a  $\text{SiO}_2$  ball tip coated with an antisticking layer, OPTOOL DSX (Daikin Chemical),<sup>2)</sup> to simulate a template surface. The diameter of the  $\text{SiO}_2$  ball is 0.35 mm. The tip is indented on a poly(methyl methacrylate) (PMMA) resist surface coated on the substrate. The critical normal stress  $P_n$  is extracted from the pull-off force from the resist per unit area, and the critical shear force  $P_s$  is extracted from the static friction force evaluated from the stick-slip force in lateral force when the normal force is 15  $\mu\text{N}$ .

The results of the extracted critical stresses are shown in the Table I. The molecular weight of the PMMA is 120 kg/mol. The results are distributed, but the side wall quality factor  $P_s/P_n$  is in the range from 7 to 20, which indeed depends on roughness, antisticking layer, and resist elasticity among others.

## 2.3 Experimental methods

To verify the computational results, the release forces are experimentally measured using specific templates having various slope angles of the patterns. The templates are prepared by conventional dry etching of a Si chip. Figure 3 shows the cross-sectional views of the templates obtained by scanning electron microscopy (SEM). The pitch of the line and space pattern is 4.0  $\mu\text{m}$ . The slope angle of the side wall is varied from 90 to 63°, the pattern height is designed to be 2.0  $\mu\text{m}$ ; however, it was very difficult to control the pattern height and the slope angle of the side wall simultaneously. Using these templates, the release force is measured for

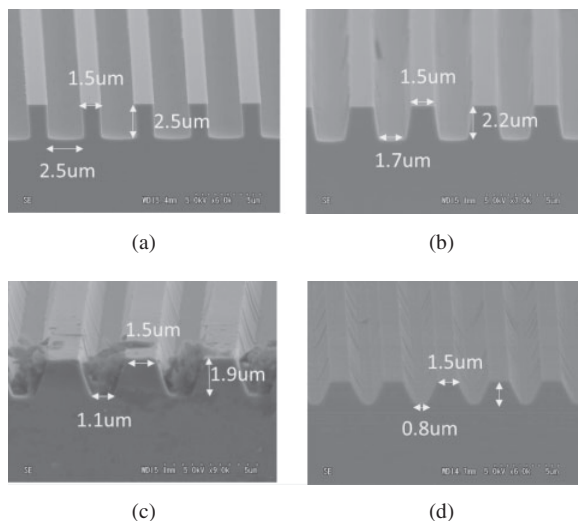


**Fig. 3.** Cross-sectional views of the templates examined at various side wall slope angles: (a) 90, (b) 80, (c) 70, and (d) 62°.

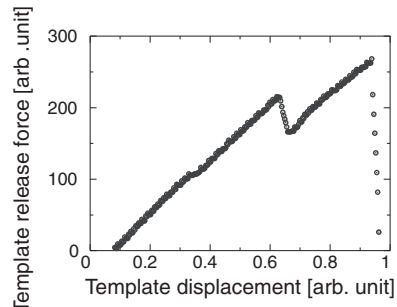


**Fig. 4.** Example of the measured force curve in template release process.

PMMA, where the thicknesses of the residual layers are all 2.0  $\mu\text{m}$ .

Figure 4 shows typical results of the force curve in the template release process for a side wall slope angle of 80°. The results show multiple peaks of the release force.

## 3. Results and discussion

### 3.1 Dependence of release force on the critical stresses $P_s$ and $P_n$

The release force strongly depends on the critical release stresses  $P_n$  and  $P_s$ , with low values favorable for release. In this section, the dependence of release force on the side wall quality factor  $P_s/P_n$  is investigated in detail by computational work. Figure 5(a) shows typical displacement force characteristics (force curve) in the template release process when  $P_s/P_n$  is 1.0.

The release force per unit area of the back side of the template linearly increases owing to elastic deformation caused by resist stretching. The stress induced at the bottom boundary of the template to the residual layer is larger than that at the top boundary to the pattern cavity under displacement in the vertical direction owing to the template release. Then, the bottom of the template firstly separates from the residual layer and the release force decreases. As a result, the first peak appears in the release force curve. The

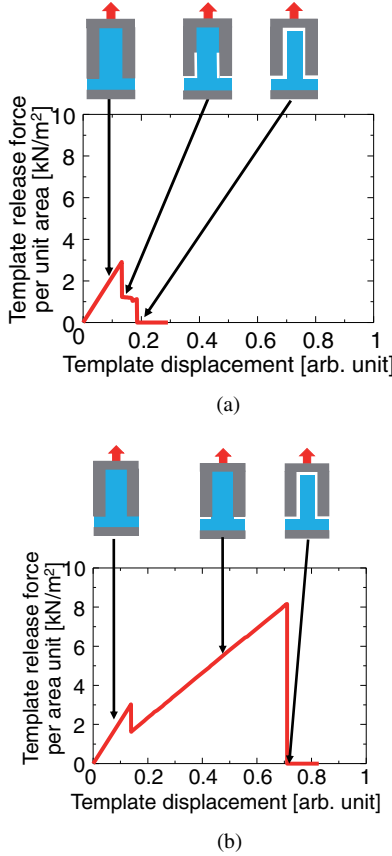


**Fig. 5.** (Color online) Computational results of force curves at various side wall quality factors ( $P_s/P_n$ ): (a)  $P_s/P_n = 1$  and (b)  $P_s/P_n = 20$ .

first peak depends on the critical normal stress  $P_n$  because the interface between the resist and the bottom of the template separates owing to the normal stress on the interface. After the separation from the residual layer, the separation proceeds along the side wall as the template is pulled up. The adhering area decreases owing to the separation and the release force remains nearly constant. Then, the side wall of the template separates from the resist and finally the upper side of the template separates. After the separation, the release force decreases to zero. As a result, the release force curve shows multiple local peaks.

On the other hand, Fig. 5(b) shows a typical release force characteristic when  $P_s/P_n$  is 20. In this case, the critical shear stress  $P_s$  is larger than the normal critical stress  $P_n$ , and the resist strongly sticks to the side wall of the template. The release force increases linearly owing to the elastic stretching of the resist until the side wall is separated from the resist, and the second peak appears. Then, the separation of the resist from the side wall immediately occurs under large shear stress and the top wall of the template pattern is also separated. As a result, the release force decreases down immediately to zero. As demonstrated above, the maximum release force and the force characteristics depend on the  $P_s/P_n$  ratio, which restates the side wall quality. When the  $P_s/P_n$  ratio increases, the release force has multipeaks due to the separation of the resist from the residual layer and the side wall of the pattern.

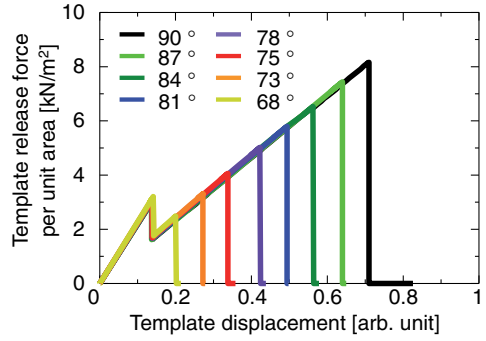


**Fig. 6.** (Color online) Computational results of the force curve at various side wall slope angles at  $P_s/P_n$  ratio of 20.

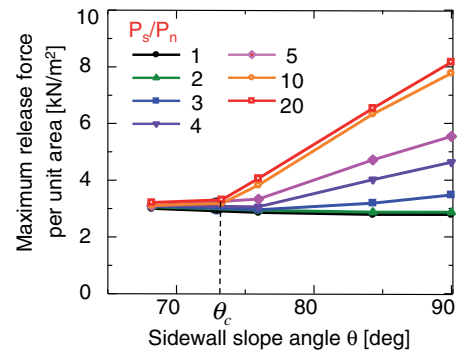


**Fig. 7.** (Color online) Computational results of the relationship between the side wall slope angle  $\theta$  and the maximum release force at various  $P_s/P_n$  ratios.

### 3.2 Dependence of maximum release force on the side wall slope angle release

Next, we discuss the dependence of the maximum release force on the side wall slope angle as an indicator of template quality. The side wall slope angle  $\theta$  is varied and the release force is investigated. Figure 6 shows the dependence of release force characteristics on the side wall slope angle when  $P_s/P_n$  is 20. There are multiple local peaks. The first peak remains the same regardless of the modification of the slope angle; however, the second peak decreases with the decreasing slope angle  $\theta$ . In this example, the values of the first and second peaks become identical at a side wall slope angle of approximately 73°, which we call the critical slope angle  $\theta_c$ . The value of  $\theta_c$  depends on the pattern height,  $P_s/P_n$  ratio, and resist material among others. When the slope angle exceeds the critical angle, the second local peak in the release force exceeds the first peak in the release force.

Figure 7 shows the relationship between the side wall slope angle  $\theta$  and the maximum release force at various  $P_s/P_n$  ratios. As the slope angle  $\theta$  decreases, the release force decreases. Nevertheless, the release loads converge on a constant value when the slope angle  $\theta$  is below the critical slope angle  $\theta_c$  for any  $P_s/P_n$  ratios. This is because the contribution of normal stress increases and the separation is accelerated, which makes it easy to release the template at a low release force. This finding is easily understandable but has not been refined by theoretical investigations. If the slope angle is allowed to be less than 90° in a specific application,

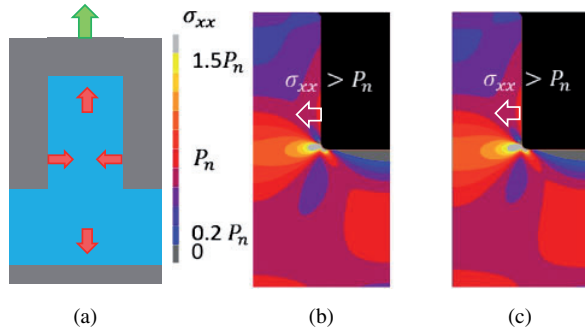


**Fig. 8.** (Color online) Induced lateral stress in the resist due to release force. (a) Schematics of the induced stress, (b) lateral stress distribution before resist separation at  $P_s/P_n$  ratio of 10, and (c) lateral stress distribution before resist separation at  $P_s/P_n$  ratio of 20.

the slope angle of the pattern cavity should be less than the critical angle  $\theta_c$  to suppress the maximum release force for the successful release. The maximum release force depends on both the  $P_s/P_n$  ratio and the slope angle  $\theta$ , which are related to the fabrication of the mold pattern, surface treatment to prevent sticking, and resist characteristics.

On the other hand, the release force saturates when the  $P_s/P_n$  ratio increases to approximately over 10. This is because the lateral force is induced in the resist pattern owing to vertical stretching, and the normal stress  $\sigma_n$  at the interface on the side wall exceeds the critical normal stress  $P_n$  before the shear stress  $\sigma_s$  exceeds the critical  $P_s$  shear stress. Figure 8(a) shows a schematic of the stress induced in the resist in the case of the vertical wall template. Figures 8(b) and 8(c) demonstrate lateral stress distributions in resists  $\sigma_{xx}$  before resist separations occur for the  $P_s/P_n$  ratios of 10 and 20, respectively. Both the stress distributions are almost the same and the resist separations occur at almost the same release forces. The same situations occur even in the sloped templates owing to stress laterally induced by elastic deformation of the resists.

### 3.3 Comparison with experiments and discussion

The impact of the critical stress and the side wall slope angle of the template on the release force is verified by computational works and compared with that verified by experiments. Figure 9 shows the dependence of the maximum release force on the side wall slope angle. The cross marks indicate the measured release forces and the triangles indicate the average of the experiments at a specific slope angle. The circles indicate the experimental results reported by Kawata et al.<sup>11)</sup> The solid, dots, and dashed lines indicate computational results at various  $P_s/P_n$  ratios. All of the release forces are normalized by the force at a slope angle of 90°. The experimental results show that the force released converges on a constant value with decreasing slope angle, as in the computational works. The reduction ratio is almost 0.5, which is in good agreement with the computational results. On the other hand, the critical slope angle in the experiments is approximately 80° or greater, as it is approximately 73° in the computational works. At present, we were unable to explain this difference clearly. One of the possible reasons for the computational works is the underestimation of the normal stress contribution on the side wall interface for the

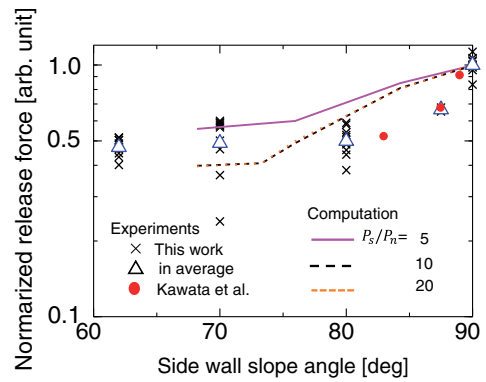


**Fig. 9.** (Color online) Computational and experimental results of maximum release force at various side wall slope angles. The  $\times$  marks indicate the measured release forces and the triangles indicate the average of the experiments at a specific slope angle. The circles indicate the experimental results reported by Kawata et al.<sup>11)</sup> The solid, dotted, and dashed lines indicate computational results at various  $P_s/P_n$  ratios. All of the release forces are normalized by the force at a slope angle of 90°.

separation model. Nevertheless, the computational works well express the template release processes and clarify the template release mechanism for sloped patterns.

### 4. Conclusions

The impact of the side wall quality of template patterns on template release force is investigated by computational works. The origin of the template release force is the elastic stretching of the resist due to the adhesion and static friction between the resist and the template. The maximum release force per unit area is investigated by computational study of the side wall qualities such as the critical separation stress between the template and the resist interface, and the slope angle of the side wall. The critical separation forces in the normal and shear directions, which are related to adhesion and friction parameters, are experimentally evaluated for the computational study. The computational results for a typical case study show that the shear separation force, which is related to the static friction between the template surface and the resist, affects the release force characteristics when the ratio of the critical shear separation stress to the normal separation stress is below 10. On the other hand, the slope angle of the side wall also affects the template release force above the critical side wall slope angle, at which the maximum separation force is induced owing to side wall separation by the shear force at the resist and template interface. In this case study, the reduction effect induced by the slope angle of the side wall shows about 50% reduction in the release force. The computation results show a rather good agreement with experimental results.

- 1) S. Y. Chou, P. Krauss, and P. Renstrom, *J. Vac. Sci. Technol. B* **14**, 4129 (1996).
- 2) Y. Hirai, S. Yoshida, A. Okamoto, Y. Tanaka, M. Endo, S. Lrie, H. Nakagawa, and M. Sasago, *J. Photopolym. Sci. Technol.* **14**, 457 (2001).
- 3) T. Bailey, B. Choi, M. Colburn, A. Grot, M. Meissl, S. Shaya, J. Ekerdt, S. Sreenivasan, and C. Willson, *J. Vac. Sci. Technol. B* **18**, 3572 (2000).
- 4) G. Y. Jung, Z. Li, W. Wu, Y. Chen, D. L. Olynick, S. Y. Wang, W. M. Tong, and R. S. Williams, *Langmuir* **21**, 1158 (2005).
- 5) H. Atasoy, M. Vogler, T. Haatainen, A. Schleunitz, D. Jarzabek, H. Schift, F. Reuther, G. Grützner, and Z. Rymuza, *Microelectron. Eng.* **88**, 1902

- (2011).
- 6) N. Nakamura, T. Yamashita, T. Kitagawa, H. Kawata, M. Shirai, and Y. Hirai, *J. Photopolym. Sci. Technol.* **27**, 111 (2014).
  - 7) H. Mekaru, O. Koizumi, A. Ueno, and M. Takahashi, *Microsyst. Technol.* **16**, 1323 (2010).
  - 8) T. Nishino, N. Fujikawa, H. Kawata, and Y. Hirai, *Jpn. J. Appl. Phys.* **52**, 06GJ05 (2013).
  - 9) T. Kitagawa, N. Nakamura, H. Kawata, and Y. Hirai, *Microelectron. Eng.* **123**, 65 (2014).
  - 10) J. S. Wi, R. J. Wilson, R. M. White, and S. X. Wang, *J. Vac. Sci. Technol. B* **29**, 033001 (2011).
  - 11) H. Kawata, M. Matsue, K. Kubo, M. Yasuda, and Y. Hirai, *Microelectron. Eng.* **86**, 700 (2009).
  - 12) J.-C. Heo, K.-S. Kim, and K.-W. Kim, *Microelectron. Eng.* **98**, 64 (2012).
  - 13) M. Okada, Y. Haruyama, S. Matsui, H. Miyake, S. Iyoshi, T. Yukawa, and H. Takeuchi, *J. Vac. Sci. Technol. B* **29**, 06FC04 (2011).
  - 14) A. Francone, C. Ilojoi, C. Poulain, C. Lombard, B. P. Donat, J. Boussey, and M. Zelsmann, *J. Vac. Sci. Technol. B* **28**, C6M72 (2010).
  - 15) J. Takahashi, J. Taniguchi, and Y. Kamiya, *J. Vac. Sci. Technol. B* **28**, C6M23 (2010).
  - 16) B. Gates and G. Whitesides, *J. Am. Chem. Soc.* **125**, 14986 (2003).
  - 17) J. Gao, L. Yeo, M. Chan-Park, J. Miao, Y. Yan, J. Sun, Y. Lam, and C. Yue, *J. Microelectromech. Syst.* **15**, 84 (2006).
  - 18) J. Taniguchi, T. Kawasaki, T. Yasuno, Y. Kogo, I. Miyamoto, M. Komuro, H. Hiroshima, N. Sakai, and K. Tada, *Jpn. J. Appl. Phys.* **41**, 4194 (2002).
  - 19) D. Truffier-Boutry, A. Beaurein, R. Galand, B. Pelissier, J. Boussey, and M. Zelsmann, *Microelectron. Eng.* **87**, 122 (2010).
  - 20) Y. Otsuka, S. Hiwasa, and J. Taniguchi, *Microelectron. Eng.* **123**, 192 (2014).
  - 21) T. Balla and S. M. Spearing, *Microelectron. Eng.* **103**, 49 (2013).
  - 22) H. Hiroshima, *J. Vac. Sci. Technol. B* **27**, 2862 (2009).
  - 23) Y. Hirai, S. Yoshida, and N. Takagi, *J. Vac. Sci. Technol. B* **21**, 2765 (2003).
  - 24) S. Park, Z. Song, L. Brumfield, A. Amirsadeghi, and J. Lee, *Appl. Phys. A* **97**, 395 (2009).
  - 25) A. Amirsadeghi, J. J. Lee, and S. Park, *Appl. Surf. Sci.* **258**, 1272 (2011).
  - 26) A. Amirsadeghi, J. J. Lee, and S. Park, *Langmuir* **28**, 11546 (2012).
  - 27) H. Kawata, J. Ishihara, T. Tanabe, M. Yasuda, and Y. Hirai, *J. Photopolym. Sci. Technol.* **25**, 747 (2013).
  - 28) N. Fujikawa, H. Kawata, M. Yasuda, and Y. Hirai, *J. Photopolym. Sci. Technol.* **25**, 245 (2012).
  - 29) T. Shiotsu, N. Nishikura, M. Yasuda, H. Kawata, and Y. Hirai, *J. Vac. Sci. Technol. B* **31**, 06FB07 (2013).
  - 30) T. Shiotsu, K. Uemura, T. Tochino, S. Ooi, Y. Onishi, M. Yasuda, H. Kawata, T. Kobayashi, and Y. Hirai, *Microelectron. Eng.* **123**, 105 (2014).
  - 31) T. Tochino, T. Shiotsu, K. Uemura, M. Yasuda, H. Kawata, and Y. Hirai, *J. Vac. Sci. Technol. B* **32**, 06FG08 (2014).
  - 32) M. Ortiz and A. Pandolfi, *Int. J. Numer. Methods Eng.* **44**, 1267 (1999).

Warszawa, 09.11.2018

dr inż. Jan Tomaszik

## OŚWIADCZENIE

Jako współautor artykułu:

*Michałowski M., Tomaszik J., Wiśniewska M. (2016) Impact of graphene coatings on nanoscale tribological properties of miniaturized mechanical objects*

opublikowanego w:

Advanced Mechatronics Solutions. Advances in Intelligent Systems and Computing, tom 393

Oświadczam, że mój indywidualny wkład w jego powstanie polegał na krytycznej korekcie tekstu manuskryptu oraz skomentowaniu jego intelektualnej treści.

Procentową wartość mojego wkładu szacuję na **10%**.



Jan Tomaszik

Warszawa, 24.04.2019

dr hab. inż. Sergiusz Łuczak, prof. uczelni

## OŚWIADCZENIE

Jako współautor artykułu:

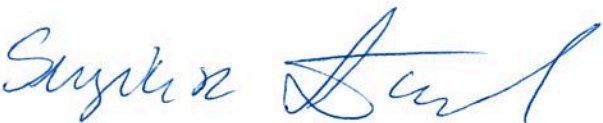
*Michałowski M., Sergiusz Ł., Cantilevers with spherical tips of millimeter magnitude*

opublikowanego w czasopiśmie:

*Journal of Micromechanics and Microengineering (2019), tom 29, numer 1*

Oświadczam, że mój indywidualny wkład w jego powstanie polegał na krytycznej korekcie tekstu manuskryptu oraz skomentowaniu jego intelektualnej treści.

Procentową wartość mojego wkładu szacuję na **10%**.



Sergiusz Łuczak

Warszawa, 24.04.2019

dr inż. Dariusz Jarząbek

## OŚWIADCZENIE

Jako współautor rozdziału monografii:

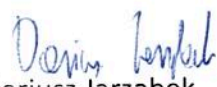
*Jarząbek D., Michałowski M., 11 Surface mechanical properties*

opublikowanego w:

*Characterization of Polymeric Biomaterials, Woodhead Publishing (2017), str. 255-282*

Oświadczam, że mój indywidualny wkład w jego powstanie polegał na zaplanowaniu kształtu ogólnego rozdziału oraz napisaniu połowy tekstu końcowego.

Procentową wartość mojego wkładu szacuję na 50%.

  
Dariusz Jarząbek

Warszawa, 24.04.2019

dr hab. inż. Monika Kwacz

## OŚWIADCZENIE

Jako współautor artykułu:

*Kwacz, M., Rymuza, Z., Michałowski, M., Wysocki J., Elastic Properties of the Annular Ligament of the Human Stapes—AFM Measurement*

opublikowanego w czasopiśmie:

*Journal of the Association for Research in Otolaryngology (2015) 16: 433.*

Oświadczam, że mój indywidualny wkład w jego powstanie polegał na udziale w zredagowaniu treści i stworzeniu ilustracji, opracowaniu metodyki i przeprowadzeniu obliczeń modułu sprężystości więzadła oraz na pełnieniu roli autora korespondującego.

Procentową wartość mojego wkładu szacuję na **40%**.



Monika Kwacz

Warszawa, 06.05.2019

prof. dr hab. med. Jarosław Wysocki

## OŚWIADCZENIE

Jako współautor artykułu:

*Kwacz, M., Rymuza, Z., Michałowski, M., Wysocki J., Elastic Properties of the Annular Ligament of the Human Stapes—AFM Measurement*

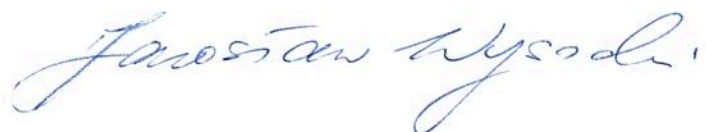
opublikowanego w czasopiśmie:

*Journal of the Association for Research in Otolaryngology (2015) 16: 433.*

Oświadczam, że mój indywidualny wkład w jego powstanie polegał na przygotowaniu preparatów, które były obiektem badań eksperymentalnych, oraz krytycznej korekcie tekstu manuskryptu.

Procentową wartość mojego wkładu szacuję na **10%**.

Jarosław Wysocki



Warszawa, 09.11.2018

mgr inż. Marta Wiśniewska

## OŚWIADCZENIE

Jako współautor artykułu:

*Michałowski M., Tomaszik J., Wiśniewska M. (2016) Impact of graphene coatings on nanoscale tribological properties of miniaturized mechanical objects*

opublikowanego w:

Advanced Mechatronics Solutions. Advances in Intelligent Systems and Computing, tom 393

Oświadczam, że mój indywidualny wkład w jego powstanie polegał na krytycznej korekcie tekstu manuskryptu, przygotowaniu części ilustracji oraz skomentowaniu jego intelektualnej treści.

Procentową wartość mojego wkładu szacuję na **15%**.

*Marta Wiśniewska*  
Marta Wiśniewska

As the co-author of the article:

Michałowski, M., Voicu, R., Obreja, C., **Baracu A.**, Muller R., Rymuza Z., Influence of deposition temperature during LPCVD on surface properties of ultrathin polysilicon films

published in the Journal:

Microsystem Technologies (2017), vol. 24, str. 537-542

I declare that my contribution consisted of preparation of part of the figures, critical analysis of the text intellectual content and its general revision.

I evaluate my contribution at 5%.

Dr. Angela Baracu



National Institute for R&D in Microtechnologies - IMT Bucharest

126A Erou Iancu Nicolae St., 077190 Bucharest, Romania

Phone: +40.21.269 07 77; +40.21.269 07 78

Mobile +40 722 383 075; Fax: +40.21.269 07 72;

Website: [www.imt.ro](http://www.imt.ro)

As the co-author of the article:

Michałowski, M., Voicu, R., Obreja, C., Baracu A., Muller R., Rymuza Z., Influence of deposition temperature during LPCVD on surface properties of ultrathin polysilicon films

published in the Journal:

Microsystem Technologies (2017), vol. 24, str. 537-542

I declare that my contribution consisted in a general revision of the manuscript and critical analysis of the text intellectual content.

I evaluate my contribution at 2%.

Dr. Cosmin Obreja

Signature



[cosmin.obreja@imt.ro](mailto:cosmin.obreja@imt.ro)

National Institute for Research and Development in Microtechnologies (IMT-Bucharest)

126A, Erou Iancu Nicolae Street, 077190, Bucharest, Romania

phone: (+40) 21 269 07 74; (+40) 21 269 07 78;

fax: +40.21.269.07.72

mobile @0040) 723 502 876

[www.imt.ro](http://www.imt.ro)

As the co-author of the article:

Michałowski, M., Voicu, R., Obreja, C., Baracu A., Muller R., Rymuza Z., Influence of deposition temperature during LPCVD on surface properties of ultrathin polysilicon films

published in the Journal:

Microsystem Technologies (2017), vol. 24, str. 537-542

I declare that my contribution consisted in a general revision of the manuscript and critical analysis of the text intellectual content.

I evaluate my contribution at 4%.

Dr.Raluca Müller



National Institute for R&D in Microtechnologies - IMT Bucharest  
126A Erou Iancu Nicolae St., 077190 Bucharest, Romania  
Phone: +40.21.269 07 77; E-mail: raluca.muller@imt.ro

<http://www.imt.ro>

As the co-author of the article:

Michałowski, M., Voicu, R., Obreja, C., Baracu A., Muller R., Rymuza Z., Influence of deposition temperature during LPCVD on surface properties of ultrathin polysilicon films

published in the Journal:

Microsystem Technologies (2017), vol. 24, str. 537-542

I declare that my contribution consisted of involvement in preparation of the samples, reviewing the figures 1 and 2 and the text of the fabrication process, critical analysis of the text intellectual content and its general revision of the manuscript.

I evaluate my contribution at 7%.

Dr. Rodica Voicu



National Institute for R&D in Microtechnologies - IMT Bucharest  
Laboratory of Modeling, Simulation and CAD  
126A, Erou Iancu Nicolae street, 077190, Bucharest, ROMANIA  
Tel: +40-21-269.07.70; +40-21-269.07.74; +40-21-269.07.78; +40-21-269.07.79  
Fax: +40-21-269.07.72; +40-21-269.07.76  
<http://www.imt.ro>  
E-mail: rodica.voicu@imt.ro

As the co-author of the article:

Tochino T., Uemura K., Michalowski M., Fujii K., Yasuda M., Kawata H., Rymuza Z., Hirai Y.,  
*Computational study of the effect of side wall quality of the template on release force in  
nanoimprint lithography*

published in the Journal:

Japanese Journal of Applied Physics (2015), vol 54, Number 6S1

I declare that my contribution consisted of conceptualization of the model used in the article  
and calculation of the model simulation results.

I evaluate my contribution at **8%**.

Date: November 20, 2018

Co-author's name: Yoshihiko Hirai

Authorized signature :

A handwritten signature in black ink, appearing to read "Hirai Yoshihiko".

As the co-author of the article:

Tochino T., Uemura K., Michalowski M., Fujii K., Yasuda M., Kawata H., Rymuza Z., Hirai Y.,  
*Computational study of the effect of side wall quality of the template on release force in  
nanoimprint lithography*

published in the Journal:

Japanese Journal of Applied Physics (2015), vol 54, Number 6S1

I declare that my contribution consisted of conceptualization of the model used in the article  
and calculation of the model simulation results.

I evaluate my contribution at 5%.

Data: November 20, 2018

Co-author's name: Kawata Hiroaki

Authorized signature :

A handwritten signature in black ink, appearing to read "Hiroaki Kawata".

As the co-author of the article:

*Tochino T., Uemura K., Michalowski M., Fujii K., Yasuda M., Kawata H., Rymuza Z., Hirai Y., Computational study of the effect of side wall quality of the template on release force in nanoimprint lithography*

published in the Journal:

Japanese Journal of Applied Physics (2015), vol 54, Number 6S1

I declare that my contribution consisted of conceptualization of the model used in the article and calculation of the model simulation results.

I evaluate my contribution at **15%**.

Date: November 20, 2018

Co-author's name: Tochino Takamitsu

Authorized signature : 

As the co-author of the article:

*Tochino T., Uemura K., Michalowski M., Fujii K., Yasuda M., Kawata H., Rymuza Z., Hirai Y., Computational study of the effect of side wall quality of the template on release force in nanoimprint lithography*

published in the Journal:

Japanese Journal of Applied Physics (2015), vol 54, Number 6S1

I declare that my contribution consisted of conceptualization of the model used in the article and calculation of the model simulation results.

I evaluate my contribution at **15%**.

Data: November 20, 2018

Co-author's name: Uemura Kimiaki

Authorized signature : *Uemura Kimiaki*